

MULTISCALE MODELING AND SIMULATION  
OF CROSSLINKED POLYMERS

BY

Jacob D. Davidson

A dissertation submitted in partial fulfillment  
of the requirements for the degree of  
Doctor of Philosophy  
(Aerospace Engineering)  
in the University of Michigan

2014

Doctoral Committee:

Assistant Professor Nakhiah Goulbourne, Chair  
Professor Ellen Arruda  
Professor John Kieffer  
Associate Professor Veera Sundararaghavan  
Professor Anthony Waas

## ACKNOWLEDGMENTS

---

Writing a dissertation does not happen overnight, and there were a lot of people who provided help and support in the process. First of all I would like to thank my advisor Nakhiah Goulbourne for her guidance and support in my research during graduate school, and for her readings of this manuscript which have greatly helped to improve the work. I would also like to thank my committee members for their review and input on the work in this dissertation.

My family has provided unconditional love and support for me through the journey of graduate school. Thanks for this. It definitely has not been easy at times. I would also like to acknowledge all of the great people I've been around at Mary Washington, Virginia Tech, and Michigan. There are too many to name all, but Jessie Ruff, Jeremy and Melissa Moore, Simon Vazquez, Alex Cusick, Eric Eckstein, Brent Dreaver, Kahlil Detrich, Josh Stenzler, Steve Anton, Lauren Tusso, Robert Hughes, Riddhiman Bhattacharya, Alyssa Skulborstad, and others - I'm glad to have been around you for the many years I've been a student. In Ann Arbor, it has been great to be a part of Michigan Cooperative House and the surrounding community. Without all the music, bushels of apples, woodworking, bike riding, and kitchen organization, my time here would certainly have been less enjoyable.

*Jacob Davidson*

*Ann Arbor, MI, USA, January 2014*

## CONTENTS

---

Acknowledgments	ii
List of Figures	vi
List of Tables	xviii
List of Appendices	xx
Abstract	xxi
Chapters:	
1 INTRODUCTION AND MOTIVATION	1
1.1 The polymer age meets high-performance computing . . . . .	1
1.2 Polymers at the molecular level . . . . .	4
1.3 Crosslinked polymers as engineering materials . . . . .	7
1.4 Outline of content . . . . .	10
2 INTRODUCTION TO POLYMER PHYSICS	14
2.1 Single chain statistical treatment . . . . .	14
2.2 Distribution of end-to-end vectors . . . . .	19
2.3 Many chain systems . . . . .	25
3 MODELING RUBBER ELASTICITY	31
3.1 Modeling large deformation limiting extensibility . . . . .	52
3.2 Comprehensive physics-based models of elasticity . . . . .	59
4 A NONAFFINE NETWORK MODEL FOR THE LARGE DEFORMATION MECHANICAL RESPONSE OF ELASTOMERS	68
4.1 Model development . . . . .	70
4.2 Experimental data analysis . . . . .	79
4.3 Discussion of results . . . . .	85
4.4 Conclusions . . . . .	88

5	MOLECULAR DYNAMICS SIMULATIONS OF POLYMERS: INTRODUCTION AND SIMULATION METHODS	90
5.1	Molecular dynamics: basics	91
5.2	Coarse-grained simulations of polymer materials	94
5.3	Simulation methods	98
5.4	Primitive path analysis	107
5.4.1	Primitive path analysis in crosslinked polymer networks	111
6	MICRO-MACRO CHAIN AND PRIMITIVE PATH DEFORMATION IN CROSSLINKED POLYMER NETWORKS	114
6.1	Undeformed network properties	116
6.2	Average chain and primitive path deformation	119
6.2.1	Theoretical background	120
6.2.2	Simulation results: average deformation	123
6.3	Distribution of chain lengths	127
6.3.1	Angular dependence of end-to-end length distribution	133
6.4	Phase space and time-dependent conformations	140
6.5	Discussion	145
6.6	Conclusions	148
7	CONNECTING CHAIN BEHAVIOR AND MECHANICAL PROPERTIES	150
7.1	Simulated mechanical test results	151
7.2	Modulus depends on nonaffine deformation	156
7.3	Limiting extensibility: simulation results vs. model predictions	163
7.4	Discussion	168
7.5	Summary and conclusions	170
8	THE SHAPE MEMORY EFFECT	172
8.1	Thermal SMP's and the glass transition	175
8.2	SMP cycling procedure	177
8.3	Temperature-dependent simulation of polymers	179
8.4	SMP Simulation methods	180
8.5	Ensemble and pairwise potential comparison	186
8.6	Molecular properties of the different chain models	191
8.7	Temperature-dependent modulus	199
8.8	Simulated shape memory cycling	205
8.9	Visualization of temperature-dependent chain conformations	209
8.10	Discussion	214
8.11	Conclusions	215
9	SUMMARY AND MAIN CONTRIBUTIONS	217

9.1	Main contributions of work . . . . .	218
9.2	Future work and extensions of current projects . . . . .	220
APPENDICES		222
BIBLIOGRAPHY		241

## LIST OF FIGURES

---

Figure 1	Multiscale modeling of polymer materials seeks to connect chain chemistry and polymer network structure with the macroscopic material properties. This is done by building models to connect the behavior at different length scales. . . . .	3
Figure 2	The monomer repeat structures of polyethylene and polypropylene, the two most commonly used synthetic polymer materials. . . . .	4
Figure 3	A polyethylene chain of 15 monomers in two different configurations. . . . .	5
Figure 4	A schematic showing the bending angle $\theta$ between successive monomers, and the torsional angle $\phi$ for a group of 3 monomers. . . . .	5
Figure 5	The torsional angle energy landscape for a sequence of three monomers, showing the energy minima and the energy difference between the different torsional states. . . . .	6
Figure 6	The characteristic behavior of a rubber elastic material is demonstrated by the classic data of Treloar [1]. A line is drawn through the original data to make this plot. . . . .	8
Figure 7	Crosslinked polymers display viscoelasticity when deformation at different strain rates. This is demonstrated with data on the VHB 4905 elastomer from Ref. [2]. . . . .	9
Figure 8	The modulus of a polymer changes by several orders of magnitude across the glass transition. This is demonstrated here by the data of Qi et al. [3], who measured the modulus of tBA-PEGDMA as a function of temperature by performing mechanical deformation tests. . . . .	10
Figure 9	A random walk consisting of $n$ steps, each of length $l$ . Each monomer is represented by the vector $\mathbf{r}_i$ , where $i = 1..n$ . The end to end vector is $\mathbf{R}$ . . . . .	15
Figure 10	The freely-rotating chain model considers a constant angle of $\theta_0$ between monomers. . . . .	16

Figure 11	A chain with one end fixed at the origin having a charge $q_1$ , and the other end having a charge $q_2$ . The charges act to apply a force $f$ . The chain end-to-end vector is labeled $\mathbf{R}$ . . . . .	21
Figure 12	The Gaussian ( $\Psi_G$ ) and Langevin ( $\Psi_L$ ) probability functions, shown with (a) regular and (b) logarithmic scaling on the vertical axis. The functions are similar for small $R/Nb$ , but differ for large values: $\Psi_L \rightarrow 0$ as $R/Nb \rightarrow 1$ , but $\Psi_G$ stays finite. . . . .	24
Figure 13	A schematic of different polymer solution densities, classified relative to the overlap concentration $\rho^*$ . . . . .	26
Figure 14	A chain confined by fixed obstacles (a) will undergo thermal fluctuations which are restricted by the obstacles (b). If the chain is “reeled-in” to minimize the path length from one end to the other the resulting path is still restricted by the obstacles (c) [4]. . . . .	27
Figure 15	A schematic of quantities involved in primitive path-tube theory. The primitive path shown has $N_{pp} = 3$ steps of constant length $b_{pp}$ , and the thermal fluctuations of the chain are restricted by a ‘tube’ with dimension $a$ . . . . .	28
Figure 16	Schematic of an elastomer at the molecular level, showing crosslinks and entanglements between polymer chains. . . . .	32
Figure 17	The characteristic stress-stretch response of vulcanized natural rubber, showing strain softening, hardening, and the difference between uniaxial and equi-biaxial deformation states for loadings applied in the 1 direction. The lines are drawn through the data of Treloar [1] to guide the eye. . . . .	32
Figure 18	An ideal freely-jointed chain with $N$ Kuhn monomers, each of length $b$ . The chain follows random walk statistics and has end-to-end vector $\mathbf{R}$ . . . . .	33
Figure 19	The affine network model. A chain is decomposed into 3 chains in orthogonal directions, and each chain deforms affinely with the applied deformation. . . . .	35

Figure 20	The single chain description of network connectivity proposed by Rubinstein and Panyukov [5]. A chain with $N$ monomers is coupled to the applied deformation via 2 effective chains of length $n_p$ . For Gaussian chains, this is decomposed into a sum over 3 chains aligned with the principal directions of stretch, each with length $N/3$ and coupled to the applied deformation via 2 effective chains of length $n_p/3$ . . . . .	37
Figure 21	The magnitude of monomers fluctuations varies with stretch, and this is modeled by a deformation-dependent 'tube' potential. . . . .	42
Figure 22	The free energy of a crosslinked, entangled network is determined by Rubinstein and Panyukov [5] by assuming a decomposition into crosslinked and entangled components. . . . .	44
Figure 23	A schematic of the representation used in the solution of the nonaffine tube model [5]. Chains with $q$ monomers are attached in series (i.e. a junction functionality of $\phi = 2$ ), and a virtual chain of $m_i$ monomers attaches each junction point to the nonfluctuating elastic background. This representation is mapped onto the combined chain picture where a chain of $q$ monomers is attached to effective chains of $n_i$ monomers at each end. . . . .	45
Figure 24	The stress-stretch modeling capabilities of the nonaffine tube model [5, 6] are demonstrated by (a) plotting stress with different values of the softening ratio $G_e^{NA}/G_c^{NA}$ , and (b) showing the difference in stress-stretch behavior of uniaxial and biaxial deformation states for parameter values $G_e^{NA} = G_c^{NA}$ . Stress is plotted for each by normalizing with respect to the shear modulus of $G_c^{NA} + G_e^{NA}$ . . . . .	51
Figure 25	Model fits to uniaxial and biaxial deformations of the natural rubber data of Treloar [1]. (a) The 3-chain model [7] with best fit parameters $G = 0.34$ MPa and $N = 95$ , and (b) the 8-chain model [8] with best fit parameters $G = 0.29$ MPa and $N = 28$ . . . . .	56
Figure 26	The effect of varying the finite extensibility parameter $N$ in the 8-chain model [8]. . . . .	57



Figure 27	Fits of the Arruda and Boyce [8] 8-chain model and the Rubinstein and Panyukov [5, 6] nonaffine tube model to two data sets. (a) VHB 4905 data from Fox and Goulbourne [9] was fit by optimizing parameters of the 8-chain model to all of the data, and optimizing fit parameters for the nonaffine tube model to data with $\lambda_1 < 3.5$ . Best fit parameters are $G = 0.037$ , $N = 38$ for the 8-chain model, and $G_c = 0.026$ , $G_e = 0.044$ for the nonaffine tube model. (b) b186 rubber data from Lulei and Miehe [10] was fit by optimizing parameters of the 8-chain model to all of the data, and optimizing fit parameters for the nonaffine tube model to data with $\lambda_1 < 1.8$ . Best fit parameters are $G = 1.59$ , $N = 29$ for the 8-chain model, and $G_c = 0.40$ , $G_e = 1.35$ for the nonaffine tube model. . . . .	58
Figure 28	The result of fitting the 8-chain model [8] to b186 rubber [10] by optimizing parameters to data only with $\lambda > 1.8$ . With this restriction, best fit parameters are $G = 0.62$ , $N = 2.2$ , and the model captures limiting extensibility but not small deformation behavior. . . . .	59
Figure 29	In the Edwards and Vilgis [11] slip-link model, deformation is transferred to an individual chain (curved lines) through a deformation of the primitive path (straight lines). Finite extensibility occurs when the primitive path length equals the contour length of the chain. This is a different physical mechanism for finite extensibility effects than the other models in this section, which consider limiting chain extensibility when the chain end-to-end distance equals the contour length. The slip-link model definition of $\alpha$ , the limiting extensibility parameter, will be used in Chapter 7 to analyze trends in limiting extensibility for different simulated polymer networks. . . . .	62

Figure 30	The slip-link [11], extended tube [12], ABGI [13], and micro-sphere [14] models applied to (a) vulcanized natural rubber [1], including uniaxial (blue circles) and biaxial (red squares) data, (b) silicone rubber [8], including uniaxial (blue circles) and pure shear (red squares) data, (c) VHB 4905 uniaxial data [9], and (d) b186 rubber uniaxial data [10]. The curves are shifted on the $x$ -axis in order to display all on a single plot: the shift in (a) and (c) is a stretch of 4, and the shift in (b) and (d) is a stretch of 1 for each curve. . . . .	65
Figure 31	A schematic of the polymer network model, represented as a sum of (a) crosslinked and (b) entangled components. Each is then mapped onto a single chain description to determine the stress. . . . .	71
Figure 32	The effect of varying the model parameters on predictions for stress for an applied uniaxial deformation. (a) a range of strain softening behavior, shown by setting $\lambda_{\max} = 4$ and varying the softening ratio $G_e/G_c$ , (b) different strain hardening behavior, shown by setting $G_e/G_c = 1$ and varying the hardening parameter $\lambda_{\max}$ . . . . .	80
Figure 33	Model predictions for stress with $G_e/G_c = 1$ and $\lambda_{\max} = 4$ for different loading conditions in (a) tension, (b) compression. . . . .	81
Figure 34	Eq. 108 with the best fit parameters from Table 2 applied to (a) natural rubber [1], (b) silicone rubber [8], (c) VHB 4905 [9], (d) b186 rubber [10]. . . . .	83
Figure 35	The Lennard-Jones 12-6 pair potential (Eq. 111) plotted with the parameter values $\epsilon = \sigma = 1$ . The cutoff of $r_c = 2^{1/6}$ includes only the repulsive part of the potential, while $r_c = 2 \times 2^{1/6}$ includes repulsive and attractive parts. . . . .	92
Figure 36	An example of particles placed in a simulation box with periodic boundaries; particles that go out one side come back in the other side. . . . .	93
Figure 37	(a) An all-atomistic representation of a polyethylene (PE) chain. (b) Atoms in the PE chain grouped together to form a united-atom model. (c) The bead-spring model of Kremer and Grest [15]. . . . .	95

Figure 38	The mean-square distance between beads separated by $m$ steps, $\overline{R^2[m]}$ , plotted as a function of $m$ at different times during equilibration for two different systems: (a) $N = 100$ , $\rho_{cl} = 0.85$ , shown in comparison to the reference equilibrium curve for long chains obtained by Auhl et al. [16], (b) $N = 100$ , $\rho_{cl} = 0.45$ . . . . .	102
Figure 39	Uniaxial stress-stretch results for simulated tests cases crosslinked at $\rho_{cl} = 0.85$ with different chain lengths: (a) The averaging process used to estimate equilibrium stress-stretch results for the simulations, (b) A comparison of stress-stretch results for uniaxial tension and compression obtained via averaging with those from Svaneborg [17]. . . . .	106
Figure 40	An example of a chain in a polymer network reduced to its primitive path using the Z1 code [18, 19, 20]. . . . .	109
Figure 41	(a) A selection around a test chain in the $N = 100$ , $\rho_{cl} = 0.85$ system is shown here at various levels of uniaxial deformation. (b) Snapshots of the system are used as input to the Z1 code [18, 19, 20] to extract the primitive paths at a given level of the applied deformation. . . . .	113
Figure 42	The single chain description of network connectivity proposed by Rubinstein and Panyukov [5, 6]. A chain with $N_K$ monomers is coupled to the applied deformation via 2 effective chains of length $n_p$ . For Gaussian chains, this is decomposed into a sum over 3 chains aligned with the principal directions of stretch, each with length $N_K/3$ and coupled to the applied deformation via 2 effective chains of length $n_p/3$ . . . . .	120
Figure 43	The generalized single-chain description of polymer network deformation [21]. The two effective chains which couple the test chain to the applied deformation may be functions of the applied stretch. The chains are no longer Gaussian so they cannot be simply decomposed into three orthogonal directions. . . . .	121
Figure 44	Changes in mean-square end-to-end chain length and primitive path length for uniaxial, biaxial, and pure shear deformations. (a)-(b) Short, unentangled chains: $N = 20$ , $\rho_{cl} = 0.45$ . (c)-(d) Long, entangled chains: $N = 200$ , $\rho_{cl} = 0.85$ . . . . .	125

Figure 45	The probability distribution of chain lengths (a) and primitive path lengths (b) for the $N = 20$ , $\rho_{cl} = 0.45$ system with an applied uniaxial stretch. A normal distribution defined by the mean and standard deviation of each distribution (lines) is shown with the data (points) in order to visualize the trends. The standard deviation of each distribution as a function of deformation is shown in (c). . . . .	129
Figure 46	The probability distribution of chain lengths (a) and primitive path lengths (b) for the $N = 200$ , $\rho_{cl} = 0.85$ system with an applied uniaxial stretch. A normal distribution defined by the mean and standard deviation of each distribution (lines) is shown with the data (points) in order to visualize the trends. The standard deviation of each distribution as a function of deformation is shown in (c). . . . .	130
Figure 47	3D plots of the distribution of chain end-to-end vectors in undeformed and uniaxially deformed states of the $N = 20$ , $\rho_{cl} = 0.45$ system. The half-ellipsoid has axes defined by the RMS chain stretch in each direction and is overlaid for reference. The colors of each point are defined by the end-to-end length of a chain ( $R$ ) divided by its contour length ( $L$ ). . . . .	131
Figure 48	3D plots of the distribution of chain end-to-end vectors in undeformed and uniaxially deformed states of the $N = 200$ , $\rho_{cl} = 0.85$ system. The half-ellipsoid has axes defined by the RMS chain stretch in each direction and is overlaid for reference. The colors of each point are defined by the end-to-end length of a chain ( $R$ ) divided by its contour length ( $L$ ). . . . .	132
Figure 49	A unit sphere (a) deforms into an ellipsoid (b), with axes defined by the principal stretches. . . . .	135
Figure 50	1001 points placed quasi-uniformly on the surface of (a) a unit sphere, and (b) an ellipsoid. . . . .	136

Figure 51	RMS end-to-end chain lengths for the $N = 20$ , $\rho_{cl} = 0.45$ system as a function of the angle of orientation with respect to the axis of elongation. The standard deviation of end-to-end chain lengths in a given “bin” is shown on each plot, and calculated results from the simulations (points) are compared with the nonaffine ellipsoid defined Eq. 132 (lines). The plots are for different levels of a uniaxial applied stretch: (a) $\lambda_1 = 1$ , (b) $\lambda_1 = 2.35$ , and (c) $\lambda_1 = 3.75$ . . . . .	138
Figure 52	Results for the $N = 200$ , $\rho_{cl} = 0.85$ system in the same manner as Figure 51. The different levels of the uniaxial applied stretch are (a) $\lambda_1 = 1$ , (b) $\lambda_1 = 3.75$ , (c) $\lambda_1 = 6.5$ , and (d) $\lambda_1 = 10$ . . . . .	139
Figure 53	The time averaged chain conformations, primitive paths determined using the Z1 algorithm [18, 20], and phase space of 2 representative chains in the $N = 20$ , $\rho_{cl} = 0.45$ system at various levels of uniaxial deformation: $\lambda_x = 1$ , $\lambda_x = 2.35$ , and $\lambda_x = 3.75$ . The dark shading (shadow) represents the phase space of each chain, i.e. the region in space the chain explores over time. . . . .	141
Figure 54	(Color online) The time averaged chain conformations, primitive paths determined using the Z1 algorithm [18, 20], and phase space of 2 representative chains in the $N = 100$ , $\rho_{cl} = 0.85$ system at various levels of uniaxial deformation: $\lambda_x = 1$ , $\lambda_x = 4.5$ , and $\lambda_x = 8$ . The dark shading (shadow) represents the phase space of each chain, i.e. the region in space the chain explores over time.	141
Figure 55	A “deformation map” for the short vs. long chain systems. The uniaxial stress-stretch curve is shown for the short system $N = 20$ , $\rho_{cl} = 0.45$ , and the long chain system $N = 100$ , $\rho_{cl} = 0.85$ . A representative chain is shown at different stretch levels for each system; the chain images are taken from Figures 53 and 54. . . . .	143
Figure 56	Nonaffine deformation parameters $\beta_{ee}$ (for chain end-to-end length changes) and $\beta_{pp}$ (for primitive path length changes) determined from each simulation plotted versus the average number of kinks per chain ( $\bar{Z}$ ). . . . .	147

Figure 57	Large deformation stress-stretch results obtained via MD, showing (a) uniaxial deformation of samples with different chain lengths crosslinked at the same density of $\rho_{cl} = 0.65$ , (b) uniaxial and biaxial deformations of samples with the same chain length ( $N = 100$ ) crosslinked at different densities. . . . .	152
Figure 58	The Young's modulus was determined by fitting a straight line to the initial linear part of the curve for Cauchy (true) stress versus stretch for a uniaxial deformation. This shows the best fit line for samples with different chain lengths, each case crosslinked at $\rho_{cl} = 0.65$ . . . . .	153
Figure 59	Stress-stretch data with the nonaffine network model fit to two simulated systems with very different mechanical properties. The model parameters are optimized to simultaneously fit uniaxial and biaxial extension and compression data. Fit results are shown for extension (a) and compression (b). . . . .	154
Figure 60	The departure of the measured modulus values from the classical prediction shows a correlation with the affineness of deformation of chain end-to-end distance. . . . .	157
Figure 61	A comparison of the measured to the predicted modulus values for the nonaffine tube and nonaffine network models. A linear fit is shown on each to highlight the predicted trend. The simulation data points are shown for chain lengths of 20 (blue circles), 35 (red squares), 100 (green diamonds), and 200 (purple triangles), each crosslinked at the different densities: $\rho_{cl} = 0.45$ (open symbols), 0.65 (half-filled), and 0.85 (filled symbols). . . . .	161
Figure 62	A comparison of the limiting extensibility parameter value $\lambda_{max}$ obtained by curve fitting to the predicted value for (a) the 8-chain model [8], (b) the nonaffine network model [21], and (c) the slip-link model [11]. A linear fit is shown on each to highlight the predicted trend. The simulation data points are shown for chain lengths of 20 (blue circles), 35 (red squares), 100 (green diamonds), and 200 (purple triangles), each crosslinked at the different densities: $\rho_{cl} = 0.45$ (open symbols), 0.65 (half-filled), and 0.85 (filled symbols). . . . .	167
Figure 63	The typical shape memory cycling procedure, with stress-free heating to recover the initial shape. . . . .	173

Figure 64	A schematic of the temperature-dependent storage modulus ( $G'$ ) and loss tangent ( $\tan \delta$ ) of a crosslinked polymer, showing the glass transition temperature ( $T_g$ ) and the glassy and rubbery regions . . . . .	176
Figure 65	A schematic of the temperature-dependent deformation of a material during shape memory cycling, showing both fixed and stress-free heating boundary conditions. . . . .	177
Figure 66	A schematic of the angular potentials included for each chain model. . . . .	182
Figure 67	A plot of the torsional angle potential $U_T(\phi)$ from Eq. 140 with the parameters listed in Table 10. . . . .	184
Figure 68	The modulus is determined as the slope of a line fit to the linear region of the stress-stretch curve. The result of this procedure is shown here for the FJC system (a) above $T_g$ , and (b) below $T_g$ . . . . .	188
Figure 69	The modulus-temperature results for the FJC system simulated with the different ensembles and pairwise potential cutoff values. . . . .	188
Figure 70	Volumetric thermal expansion data of the shape memory polymer tBA-PEGDMA from Nguyen et al. [22]. Lines are fit to the glassy and rubbery regions to determine thermal expansion coefficients. In Ref. [22], $T_g$ was determined by the intersection of these lines. . . . .	189
Figure 71	The volume-temperature curves of the FJC system using both A-NPT and R-NPT. Volume is normalized by the initial volume of the simulation box during equilibration and crosslinking. . . . .	190
Figure 72	The $C_\infty$ values as a function of temperature for each chain model in (a) crosslinked, and (b) uncrosslinked forms. . . . .	193
Figure 73	The average primitive path length ( $\overline{L}_{pp}$ ) as a function of temperature for each chain model in (a) crosslinked, and (b) uncrosslinked forms. . . . .	195
Figure 74	The average number of kinks per chain ( $\overline{Z}$ ) as a function of temperature for each chain model in (a) crosslinked, and (b) uncrosslinked forms. . . . .	196
Figure 75	The cohesive energy density, $E_{CED}$ , calculated as a function of temperature for each chain model in (a) crosslinked, and (b) uncrosslinked forms. . . . .	198

Figure 76	The modulus-temperature results for the different chain models in crosslinked form, along with the uncrosslinked FJC system. All are simulated with the NPT ensemble with $P = 0$ and $r_c = 2 \times 2^{1/6}$ . . . . .	200
Figure 77	The glass transition temperature ( $T_g$ ) was determined as the steepest part of the modulus-temperature curve. High (above $T_g$ ) and low (below $T_g$ ) reference temperatures for simulated cycling and a comparison of properties were chosen relative to $T_g$ . . . . .	201
Figure 78	The pair-distance correlation function at $T = 0.1$ for the FJC, FRC, and RIS models simulated using A-NPT. . .	203
Figure 79	Volume as a function of temperature for the FJC, FRC, and RIS models simulated using A-NPT. . . . .	204
Figure 80	The modulus-temperature behavior of the different systems, plotted by non-dimensionalizing the modulus as $G(T)/(\rho_m(T)\epsilon)$ . Figure 77 shows the same result using the non-dimensionalization $G(T)/(\rho_0\epsilon)$ . . . . .	204
Figure 81	Potential energy as a function of deformation for the crosslinked FJC system at two different temperatures, simulated using A-NPT. At $T_{\text{high}}$ the potential energy fluctuates about a mean, and the system displays entropic elasticity. At $T_{\text{low}}$ the potential energy changes with deformation, and the system displays energetic elasticity. . . . .	205
Figure 82	Uniaxial tension mechanical behavior (the first step of the simulated shape memory cycling procedure) for the different chain models. The uncrosslinked system undergoes viscous flow, with a stress that remained near zero for the deformation rate that was used. . . . .	206
Figure 83	Stretch relaxation at $T_{\text{low}}$ after cooling for the different systems. . . . .	207
Figure 84	Stretch recovery upon stress-free heating to $T_{\text{high}}$ for the different systems. . . . .	208
Figure 85	Stress during shape memory cycling after initial tensile and compressive deformations for (a) the simulated FJC-A-NPT system, and (b) the DP5.1 shape memory polymer material [23] tested by Liu et al. [24]. Each plot also shows the thermal cycling response for the tensile case when the deformation was held during the entire procedure (i.e. the stress was not set to zero at $T_{\text{low}}$ ). . .	210



Figure 86

A visualization of time-dependent conformations for each chain model at different temperatures from  $T_{\text{low}}$  to  $T_{\text{high}}$  increments of 0.1. The “same” chain is shown for each system, i.e. this chain has the same bonded connections and intermolecular entanglements for each case. The time-averaged conformation (the connected beads) is shown along with the time-dependent conformations (i.e. the phase space: shown as the shaded region) for each chain at each temperature. . . . . 212

## LIST OF TABLES

---

Table 1	Best fit parameters for the slip-link [11], extended tube [12], ABGI [13], and micro-sphere [14] models applied to (a) vulcanized natural rubber [1], (b) silicone rubber [8], (c) VHB 4905 uniaxial data [9], and (d) b186 rubber uniaxial data [10]. . . . .	66
Table 2	Best fit parameters for Eq. 108 applied to the different large deformation data sets. . . . .	84
Table 3	Parameters used in the simulations of Chapters 6-7. . .	99
Table 4	The number of simulation timesteps used in equilibrating and crosslinking the networks along with the percentage completion of the crosslinking reaction. A second equilibration was performed on the samples with $\rho_{cl} = 0.45$ and $\rho_{cl} = 0.65$ after compressing to the test density of 0.85. A timestep of $\Delta t = 0.012$ was used in all simulation steps shown here; the simulation time for $n$ timesteps is simply $n \times 0.012\tau$ . . . . .	104
Table 5	Tabulated data on undeformed chain end-to-end and primitive path statistics for the different simulation test cases. . . . .	117
Table 6	The average isotropic pressure on each simulation box in the undeformed configuration. The values were calculated by averaging pressure values over time after equilibrating each system at the test density of 0.85. . .	118
Table 7	Non-phantom and nonaffine parameters for the different simulation test cases. . . . .	126
Table 8	Tabulated properties for the different systems. The modulus $\tilde{G}$ was determined by fitting to the linear region of uniaxial stress-stretch, and the model parameters were determined via a fit to uniaxial and biaxial stress-stretch curves. . . . .	155

Table 9	The values of rheological entanglement length, $N_e^{S\text{-coil}}$ , and topological entanglement length, $N_e^{S\text{-kink}}$ , for each simulation test case. The S-coil and S-kink measures of entanglement length were proposed by Hoy et al. [25].	160
Table 10	Parameters used in the SMP simulations. . . . .	183
Table 11	A list of the different ensemble and pairwise potential simulations considered in this section. . . . .	187
Table 12	Each chain model is considered in both crosslinked and uncrosslinked form for the comparison of molecular properties in Section 8.6. Each is simulated using the NPT ensemble with $r_c = 2 \times 2^{1/6}$ , i.e. attractive LJ interactions enabled (A-NPT). . . . .	192
Table 13	Simulation cases considered for the modulus comparison of Section 8.7. Each is simulated using the NPT ensemble with $r_c = 2 \times 2^{1/6}$ , i.e. attractive LJ interactions enabled (A-NPT). . . . .	199
Table 14	Tabulated values for the approximate glass transition temperature, high and low reference temperatures, and the modulus values at the reference temperatures for each system. . . . .	201
Table 15	Tabulated values of the modulus non-dimensionalized using the temperature-dependent density $\rho_m(T)$ at the reference temperatures for each system. These values show the same trends as those in Table 14, where modulus was non-dimensionalized using the constant density of $\rho_0$ . . . . .	204
Table 16	The Poisson ratio ( $\nu$ ) of each system, calculated using the uniaxial deformation result. . . . .	207

## LIST OF APPENDICES

---

Appendix A	Monte Carlo fitting procedure . . . . .	222
Appendix B	Codes for generating simulation setups and running in LAMMPS . . . . .	223
Appendix C	Complete set of stress-stretch data for the simulated polymer networks . . . . .	236

## ABSTRACT

---

The combination of physics-based modeling and coarse-grained molecular dynamics simulations is a powerful tool to understand how molecular properties and processes affect the mechanical properties of crosslinked polymers. In this dissertation polymer network structure and chain behavior are analyzed in order to connect these microscopic characteristics and deformation mechanisms to the macroscopic material properties of nonlinear elasticity and the shape memory effect. A new physics-based model of rubber elasticity is constructed which can capture the strain softening, strain hardening, and deformation-state dependent response of rubber materials undergoing finite deformations. This model is unique in its ability to capture large-stretch mechanical behavior with only three parameters that are each connected to the polymer chemistry and the important characteristics of the macroscopic stress-stretch response. Coarse-grained molecular dynamics simulations are used to analyze chain behavior during deformation. This work is the first to track primitive path length changes in a deformed polymer network. The primitive path of a polymer chain is defined as the shortest path from one end of the chain to the other which preserves the topological state of the network (i.e. retaining all inter-chain entanglements). Through a comparison of simulated networks with different structures, it is demonstrated that changes in average primitive path length are always nonaffine, even for long, entangled chain networks. A visualization of time-dependent chain conformations and the restraining “tube” in deformed networks demonstrates the viability of using primitive path analysis to quantify micro-macro deformation in crosslinked polymers. The shape memory effect in crosslinked polymers is the ability of a material to hold a deformed shape, then subsequently recover the initial shape when heated above the glass transition temperature. This work is the first to construct a suitable coarse-grained model for examining shape memory polymer behavior via molecular dynamics simulation. It is found that simply including monomer-monomer attraction in the simulation model is sufficient to reproduce the nonlinear thermomechanical trends seen experimentally. Because of the simplicity of the simulation model, these results give important information as to how to model and understand these systems.

## CHAPTER 1

### INTRODUCTION AND MOTIVATION

---

#### 1.1 THE POLYMER AGE MEETS HIGH-PERFORMANCE COMPUTING

The prevalence of polymers as commonplace materials in the last 100 years is such that Rubinstein and Colby [4] refer to our modern era as the “Polymer Age”. Indeed, many of the aspects of modern life we now take for granted would be practically impossible without polymeric materials. The most common synthetic polymers are polyethylene and polypropylene. Of course, examples of polymers are abundant in nature as well. Proteins and DNA are considered biopolymers; they consist of many repeating base units. Natural latex rubber is a polymer that is produced by several plants, most notably the Pará rubber tree native to South America, and has been used for centuries for things such as shoes, containers and as a means of waterproofing. The elastin in the Dermis layer of the skin is a biopolymer which serves to provide elasticity to skin.

Staudinger [26] proposed in the 1920’s that long-chain molecules exist as collections of repeat units joined by covalent bonds. He termed these structures “macromolecules”. Although polymer materials had been used for many years before this, this time marks the beginning of the field of polymer science. Early experimental work demonstrated that many properties of long-chain molecules (such as molecular size and solution rheology) depend mainly on the number of repeat units. Paul Flory is credited as the founder of polymer physics, and was the first to apply concepts from statistical mechanics to understand the behavior of polymer solutions and materials [27, 28]. Later, Edwards [29, 30, 31] and de Gennes [32] applied path integral methods and introduced field theory techniques and scaling methods from theoretical physics to study polymer

materials. This led to the successful ‘tube’ theory of polymer dynamics [33]. Currently, polymer physics is undergoing a third ‘revolution’ through the use of molecular simulations made possible by recent advances in computing technology [34]. Some of the pioneering work in simulating polymer materials was done by Kremer and Grest [15]. Computer simulations and methods have been developed which allow for the direct observation of microscopic phenomena and analysis of the underlying chemical structure [20].

The use of computer simulations is changing the methods of problem solving in polymer physics, and is also leading to new and expanding areas of research. One of these areas is multiscale modeling; the basic concept is illustrated in Figure 1. The overall goal of multiscale modeling of polymer materials is to connect chain chemistry and polymer network structure with the material properties. Being able to make such a connection is advantageous for many reasons, including material development and engineering design. The combination of physics-based modeling and coarse-grained molecular dynamics simulations is a powerful tool to understand how molecular properties and processes affect the mechanical properties of polymer materials. The central goal of this dissertation is to apply these concepts to analyze nonlinear elasticity, micro-macro deformation, and the shape memory effect in crosslinked polymers. It is demonstrated that, if constructed properly, coarse-grained simulations can be used to inform behavior all the way up to the level of engineering models. Whereas current engineering models are mainly phenomenological, multiscale modeling can be used to connect macroscopic behavior with microscopic processes. The nonlinear properties of crosslinked polymers present a challenging case. One cannot construct a phenomenological model of the nonlinear time, temperature, and deformation dependent properties of a crosslinked polymer material without introducing assumptions about mechanical behavior, and a large number of parameters. The result is often restricted to a limited number of materials, or contains too many parameters to be of practical use. The conclusion is that a useful model cannot be constructed without a basis in the underlying physics. In this dissertation I will demonstrate that coarse-grained molecular dynamics simulations are an essential tool in forming such a model.

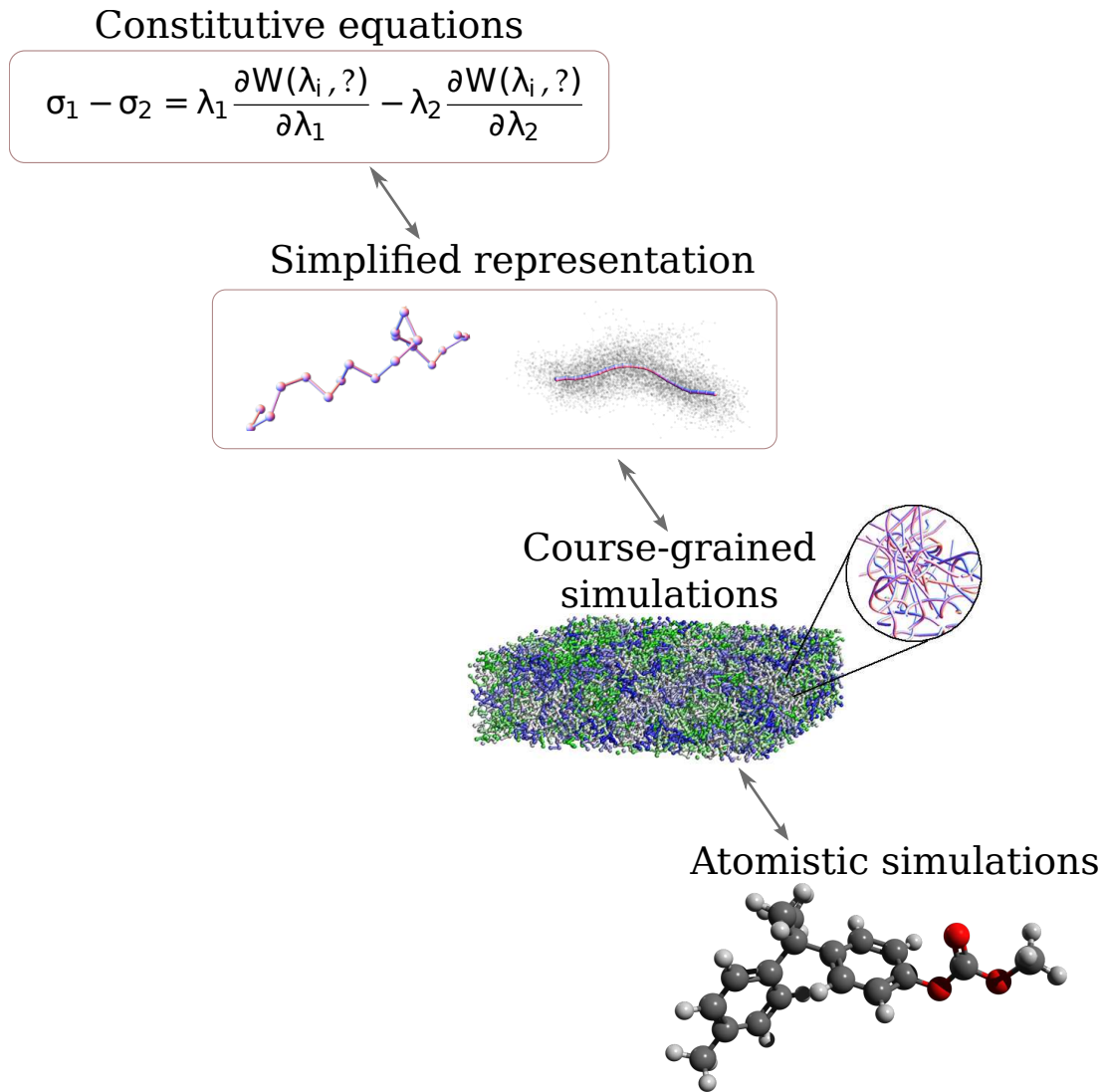


Figure 1: Multiscale modeling of polymer materials seeks to connect chain chemistry and polymer network structure with the macroscopic material properties. This is done by building models to connect the behavior at different length scales.



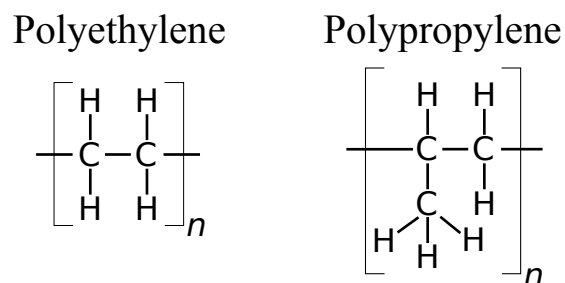


Figure 2: The monomer repeat structures of polyethylene and polypropylene, the two most commonly used synthetic polymer materials.

## 1.2 POLYMERS AT THE MOLECULAR LEVEL

The word polymer comes from the Greek *polus*, meaning many, and *meros*, meaning part; literally, "many parts". A simple polymer consists of a single repeat unit, called a monomer, that is repeated many times. Figure 2 shows the repeat structures of polyethylene and polypropylene; these are the two most commonly-used synthetic polymers. Other important synthetic polymers include polystyrene, polyvinyl chloride, polycarbonate, and polyurethane. All of these materials are produced through a polymerization reaction that converts monomers into long chain polymers (chain polymerization and step-growth polymerization [4, 35] are the two most common).

In a single polymer chain, the monomer unit is repeated  $n$  times. The molecular weight (or molar mass) is typically reported instead of an average value of  $n$ . The most common measure of the value of  $n$ . Common molecular weight values range from approximately  $10^3$  g/mol to  $10^7$  for polymers [35], leading to values of  $n$  from approximately 20 to over  $2 \times 10^5$ .

The covalent bonds between monomers are strong and require a large amount of energy to break. These bonds make up the largest part of the internal energy of a polymer chain. An individual chain also has an associated entropy; since it is long and flexible, it can assume many different conformations. Conformational fluctuations form a significant contribution to the free energy of a polymer chain (for example, the elasticity of an isolated polymer chain is almost entirely entropic). Other polymer properties are also a consequence of chains being long, and being able to assume many different configurations in a statistical manner.

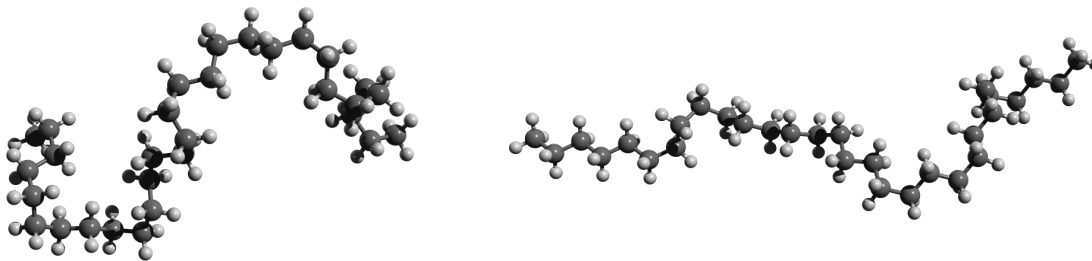


Figure 3: A polyethylene chain of 15 monomers in two different configurations.

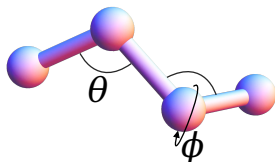


Figure 4: A schematic showing the bending angle  $\theta$  between successive monomers, and the torsional angle  $\phi$  for a group of 3 monomers.

Figure 3 shows two different configurations of a (relatively short) chain of polyethylene, containing only 15 monomers. The bond length between atoms on the chain backbone can be considered fixed. The most important degrees of freedom of a chain are the bending angle between successive monomers ( $\theta$ ) and the torsional angle for a group of 3 monomers ( $\phi$ ). Figure 4 shows a schematic which identifies these angles. Bending motion between monomers is very rigid; the angle  $\theta$  is nearly constant for polymers with carbon-carbon backbone bonds. Variations in the torsional angle are the main source of chain flexibility. For the two configurations of the chain shown in Figure 3, each has a different sequence of torsional angles along the chain backbone.

Different inter-atomic distances cause different torsional configurations to be energetically favorable. A sequence of three monomers typically has 3 local minima in the torsional angle energy landscape. Figure 5 shows a schematic of a typical torsional angle energy landscape. The lowest energy state is called the *trans* state, and the two others are called *gauche<sub>-</sub>* and *gauche<sub>+</sub>*. For polyethylene, the *trans* state has  $\phi = 180^\circ$  and the two *gauche* states have  $\phi = 180 \pm 120^\circ$ . The difference in energy between *trans* and *gauche* states is  $\Delta E \approx 0.8kT$  at room temperature [4], where  $k$  is Boltzmann's constant and  $T$  is temperature. At sufficient temperature (i.e. around room temperature for polyethylene), a large fraction of the dihedral angles exist in the *gauche*

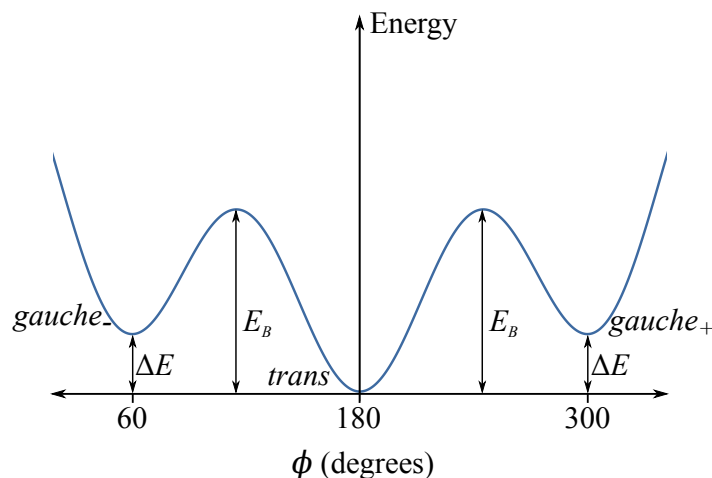


Figure 5: The torsional angle energy landscape for a sequence of three monomers, showing the energy minima and the energy difference between the different torsional states.

states. The energy difference between *trans* and *gauche* states determines the equilibrium population of these states, but the dynamics depends on the height of the energy barrier between states (labeled  $E_B$  in Figure 5) [4]. When thermal energy is high enough to overcome the energy barrier the chain will take on many different configurations in a short amount of time. This behavior is fundamental in determining the properties of individual polymer chains as well as polymer solutions and melts. To illustrate the number of possible configurations available, consider a chain consisting of 20 monomer units. To make a simple estimate, consider the bond angle to be fixed and that each of the dihedral angles exists in either *gauche*<sup>-</sup>, *trans*, or *gauche*<sup>+</sup> states with equal probability. There are then  $3^{18} = 3.9 \times 10^8$  available configurations. For a chain with 100 repeat units, the same calculation leads to  $5.7 \times 10^{46}$  configurations. One can see that this number increases very quickly! The next chapter is concerned with calculating the statistics of the different configurations a chain may take.

Many chains placed together in a solution become entangled, and these entanglements are the dominant factor in determining the rheological properties of the solution. To illustrate, first consider a box of short ropes, each less than a foot long. It is not too difficult to reach in and pull out a few ropes. Now imagine that the box is full of 50ft ropes. To pull out a single

rope requires untangling it from all other others. That may take awhile! This is essentially the reason why long-chain polymer solutions or melts have a high viscosity. When studying polymer materials, it is important to consider interchain entanglements.

Chains in a polymer melt or solution can be crosslinked together to form a single giant molecule. With these added bonds the polymer network exhibits elasticity instead of just viscous flow. Consider again the box of ropes example. The crosslinking procedure is analogous to taking one end of a rope in the box and burning it together with a few other ends of ropes. If you leave them all in the box while doing this, randomly choosing the sets of rope ends to burn together, the ropes will all still be very tangled up. After repeating this procedure until no rope ends are left it will be nearly impossible to remove a rope from the box - you could not just untangle it, you would have to cut it. Unless you pulled on the giant ball of ropes *really* hard, it would continue to be just that: a giant ball of ropes. At the molecular level, this is exactly what the crosslinking procedure does to a collection of polymer chains, and the reason why the resulting network exhibits elasticity.<sup>1</sup> The focus of this dissertation is on crosslinked polymers; different examples and the important properties of crosslinked polymer materials will be described in the next section. This section was meant to give the reader a brief introduction to polymers at the molecular level. A more detailed account can be found in books on the subject (e.g. Refs. [4, 27]). The statistical treatment of polymer chain conformations will be introduced in Chapter 2.

### 1.3 CROSSLINKED POLYMERS AS ENGINEERING MATERIALS

For engineering purposes, polymer materials can be placed into two categories: thermoplastics and thermosets. Thermoplastic materials can be molded into different forms using heat. When heated above the glass transition temperature ( $T_g$ ), a thermoplastic material behaves as a viscous liquid and can be reformed to a different shape (i.e. it undergoes a *plastic* deformation). When cooled below  $T_g$ , the material behaves as an elastic solid which can also undergo plastic

---

<sup>1</sup> The example here described an end-linking reaction; crosslinking bonds can also be added randomly at different locations along each chain instead of only at the ends.

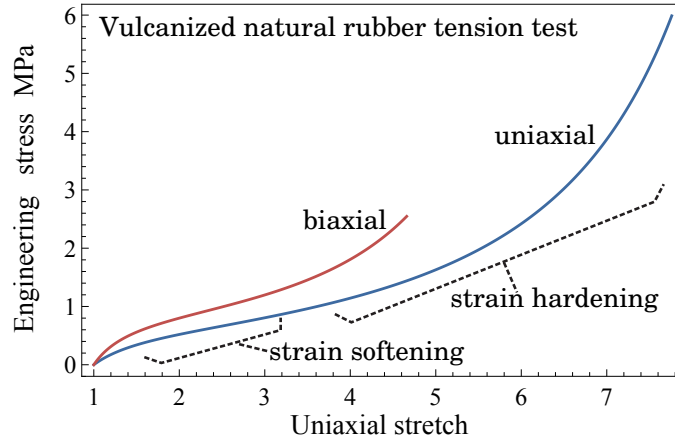


Figure 6: The characteristic behavior of a rubber elastic material is demonstrated by the classic data of Treloar [1]. A line is drawn through the original data to make this plot.

deformation if stretched very far. Most common thermoplastic materials (e.g. polyethylene and polypropylene) have glass transition temperatures above room temperature and therefore behave as solids unless heated. Thermoplastic materials consist of many long chains entangled together. When crosslinks are added to connect the chains, the material is known as a thermoset. Thermosets are therefore crosslinked polymers. The crosslinking procedure is also referred to as vulcanization. In the rest of this section the term “crosslinked polymer” will be used instead of “thermoset” for consistency.

Crosslinked polymer materials have a permanent molecular network structure set by the crosslinks, and have the ability to undergo large, reversible deformations. This is referred to as rubbery-like behavior. The representative uniaxial mechanical stress-stretch behavior of a crosslinked polymer material is demonstrated in Figure 6 using the classic data of Treloar [1] for natural rubber vulcanized with sulfur. There is an initial linear response, followed by a decrease in the tangent modulus (strain softening), and then an increase (strain hardening). The material can be stretched vary far while still retaining the ability to recover the initial shape (the example in Figure 6 can be stretched to a length nearly 8 times the initial length). Most crosslinked polymers (e.g. vulcanized natural rubber) are used above their glass transition temperature (i.e. in the “rubbery” state). Typical modulus values at temperatures above  $T_g$  range from less than 100 kPa to tens of MPa. The material shown in Figure 6

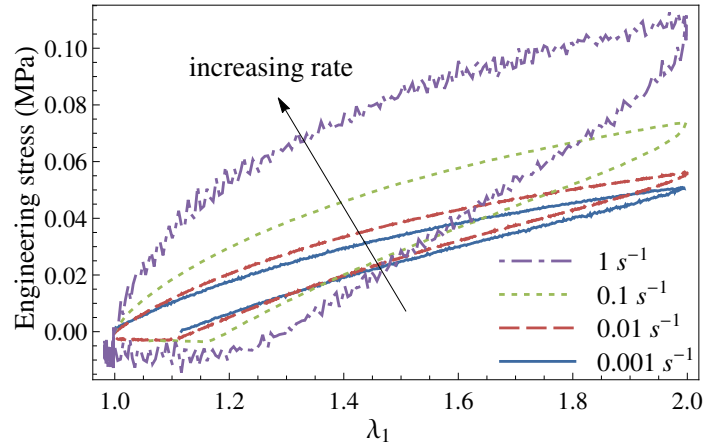


Figure 7: Crosslinked polymers display viscoelasticity when deformation at different strain rates. This is demonstrated with data on the VHB 4905 elastomer from Ref. [2].

was tested above its glass transition temperature. Softer materials that are able to be stretched very far are sometimes called elastomers. The modulus of a crosslinked polymer material can be increased by adding filler particles such as carbon black and silica.

The stretch-stress response of a crosslinked polymer is nonlinear and also rate dependent. The rate-dependent response is called viscoelasticity. Figure 7 shows an example of viscoelasticity for the VHB 4905 elastomer (a polyacrylate material); data is from Stenzler [2]. All crosslinked polymers display viscoelastic behavior to some degree. The size of the hysteresis loop decreases with the applied strain rate. When the rate is sufficiently slow so that the size of the hysteresis loop is negligible the behavior is called *quasistatic*. The uniaxial stress-stretch behavior shown in Figure 6 for vulcanized natural rubber is from a quasistatic tension test.

Cooling a crosslinked polymer material below  $T_g$  leads to a large increase in modulus. The characteristic change in mechanical properties with temperature is demonstrated by the data of Qi et al. in Figure 8, where the modulus of tBA-PEGDMA was measured as a function of temperature via small deformation mechanical testing. Below  $T_g$ , modulus values are of a crosslinked polymer material on the order of GPa or higher.

Historically, the main use of crosslinked polymer materials has been for car tires, which are commonly made from crosslinked styrene-butadiene and/or

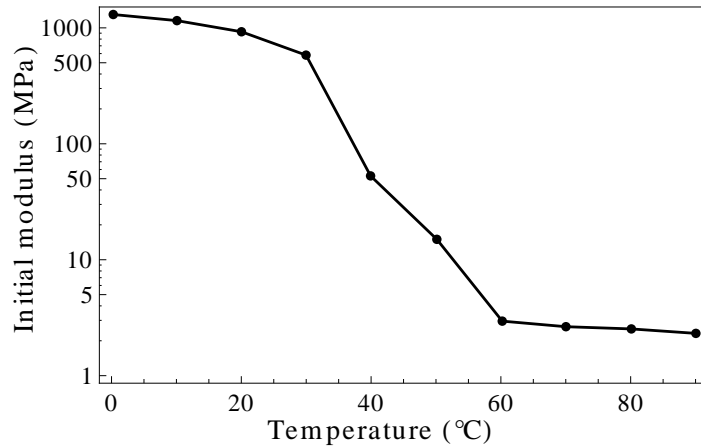


Figure 8: The modulus of a polymer changes by several orders of magnitude across the glass transition. This is demonstrated here by the data of Qi et al. [3], who measured the modulus of tBA-PEGDMA as a function of temperature by performing mechanical deformation tests.

natural rubber (polyisoprene) filled with carbon black. However, recent work has found many new uses for crosslinked polymer materials. Some examples include shape memory polymers [36, 37, 38], self-healing materials [39], stretchable electronics [40, 41, 42], bio-compatible medical devices such as stents [43] and neuronal probes [44], and electroactive polymers [9, 45]. Many new developments are based on biomimetic design principles; crosslinked polymers are found in abundance in nature, such as elastin in the dermis layer of the skin, crosslinked actin in the cellular cortex [46], and spider silk [47, 48].

Although these examples vary in their properties and uses, they all share a common molecular structure of long-chain molecules linked together to form a polymer network. To use crosslinked polymers in new applications requires knowledge of the nonlinear mechanical properties. This dissertation focuses on nonlinear elasticity, micro-macro chain deformation, and the temperature-dependent shape memory effect.

#### 1.4 OUTLINE OF CONTENT

This chapter has thus far presented a brief introduction to crosslinked polymer materials. It is not well understood how the molecular network structure of a crosslinked polymer material leads to its mechanical properties; making

this connection will facilitate material selection in the design process and lead to new material developments. In this dissertation, physics-based modeling and coarse-grained molecular dynamics simulations will be used to analyze nonlinear elasticity, micro-macro chain deformation, and the shape memory effect in crosslinked polymers. The following is a brief summary of the content of each following chapter:

2. **Introduction to polymer physics.** This chapter introduces the single chain statistical treatment and calculations for the end-to-end distance of chains with different levels of bending and torsional rigidity. The Langevin and Gaussian probability functions for the distribution of end-to-end vectors are derived. For many chain systems, the concepts of overlap, entanglements, and the primitive path are introduced and discussed.
3. **Modeling rubber elasticity.** The characteristic nonlinear elastic mechanical properties of crosslinked polymers are introduced. The affine and phantom network models are reviewed, followed by the nonaffine tube model [5, 6]. These models apply to small to intermediate deformations; large deformation modeling is then introduced and reviewed. Models which can capture all characteristic features of rubber elasticity and have a basis in the underlying physics are reviewed in the last section. These include the micro-sphere [14], slip-link [11], extended tube [12], and ABGI [13] models.
4. **A nonaffine network model for the large deformation mechanical response of elastomers.** A new model of large deformation nonlinear elasticity is derived. This model is based on generalizing the Rubinstein and Panyukov [5, 6] nonaffine tube model to include non-phantom deformation and Langevin chain statistics. The model contains parameters that are all linked to the polymer network structure and the behavior of chains in the network, and it is demonstrated that the model can fit data for different rubber-like materials with only 3 parameters. Other models which cover the same scope of material behavior contain 4 or 5 parameters. This model is used to analyze simulation results in the subsequent chapters.



5. **Molecular dynamics simulations of polymers: introduction and simulation methods.** The basics of the molecular dynamics (MD) simulation method is introduced, followed by a review of how MD simulations have been applied to polymers. The simulation methods used in Chapters 6 and 7 are outlined in detail. Primitive path analysis is described and reviewed as a method to analyze the output of a polymer simulation and quantify the effects of interchain entanglements.
6. **Micro-macro deformation in crosslinked polymer networks.** The simulated polymer networks contain test cases ranging from short, untangled chains, to long, entangled chains. The undeformed network properties are tabulated. Chain end-to-end length and primitive path length changes are tracked as each simulated material is deformed, and the affineness of these deformations is shown to depend on the network topology. The movement of individual chains is visualized by tracking over time. It is shown that the primitive path provides an accurate description of the molecular mechanisms of deformation for both short and long chain systems. Although chain end-to-end length deformation is affine in the limit of very long chains, the simulation results suggest that primitive path deformation is always nonaffine.
7. **Connecting chain behavior and mechanical properties.** The mechanical behavior of the simulation test cases is presented, and the different properties are quantified by fitting to simulation results. It is demonstrated that the modulus of each simulated material depends on the level of affineness of chain deformation. The large deformation limiting extensibility behavior is quantified by model fitting, and these values are compared to predictions from several different theoretical models. These results are discussed in the context of connecting molecular behavior with mechanical properties.
8. **The shape memory effect.** The temperature-dependent shape memory effect is introduced, and simulations of the temperature-dependent behavior of polymers are reviewed. The simulation methods used in Chapters 5-7 are modified to capture temperature-dependent behavior. It is shown that including attractive interactions and using the NPT ensemble is

an appropriate simulation setup to represent a shape memory polymer (SMP) via coarse-grained molecular dynamics. The molecular properties and mechanical properties of the simulated polymer networks with different levels of bending and torsional chain mobility are compared. The simple freely-joined chain simulation model has the “best” shape holding and recovery abilities due to its ability to maximize favorable attractive interactions. Simulated results display the same nonlinear trends for thermomechanical cycling as seen in experiments. The molecular chain conformations occurring at different temperatures are visualized, and these results are discussed in relation the basic molecular mechanisms responsible for SMP behavior.

9. **Summary and conclusions.** The main results and conclusions from this dissertation are presented, including a list of the main contributions of this work. Several avenues for future research are also discussed.

## CHAPTER 2

### INTRODUCTION TO POLYMER PHYSICS

---

In polymer physics one wishes to construct a model from the ground up that begins with only the most basic characteristics common to all polymers. Then, beyond this, one can add more detail when needed to explain a broader range of physical phenomena. For a single polymer chain, the most essential characteristics are that chains consist of many repeat units and experience large conformational fluctuations due to thermal energy. In this chapter we begin with the random walk chain model and the statistics of end-to-end chain distances (Section 2.1). The Gaussian and Langevin chain probability functions are derived and discussed in Section 2.2. The characteristics of many-chain systems are introduced in Section 2.3, along with the concepts of overlap, entanglement, and the primitive path.

#### 2.1 SINGLE CHAIN STATISTICAL TREATMENT

The statistical treatment of a polymer chain begins with the 3D random walk model. The random walk consists of a collection of  $n$  steps of length  $l$  as shown in Figure 9. Each step is represented by the vector  $\mathbf{r}_i$ , and the end-to-end vector is calculated as

$$\mathbf{R} = \sum_{i=1}^n \mathbf{r}_i. \quad (1)$$

The monomers are taken to be fixed-length, non-interacting rods, and all bond and torsional angles are equally probably. This corresponds to the freely-

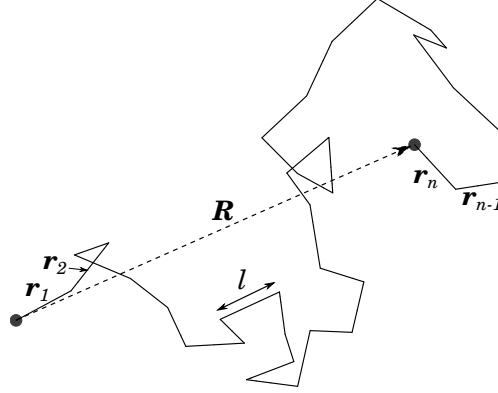


Figure 9: A random walk consisting of  $n$  steps, each of length  $l$ . Each monomer is represented by the vector  $\mathbf{r}_i$ , where  $i = 1..n$ . The end to end vector is  $\mathbf{R}$ .

jointed chain (FJC) model. The mean-square end-to-end distance for the FJC model is a simple calculation:

$$\begin{aligned}
 \langle \mathbf{R} \cdot \mathbf{R} \rangle_{\text{FJC}} &= \left\langle \left( \sum_{i=1}^n \mathbf{r}_i \right) \cdot \left( \sum_{j=1}^n \mathbf{r}_j \right) \right\rangle \\
 &= \left\langle \left( \sum_{i=1}^n \mathbf{r}_i \cdot \mathbf{r}_i \right) \right\rangle \\
 &= n l^2,
 \end{aligned} \tag{2}$$

where  $\langle \cdot \rangle$  represents an average over thermal fluctuations.<sup>1</sup> For chains with a different number of monomers the mean-square end-to-end distance scales according to  $R^2 \propto n$ . In Eq. 2 this behavior was derived for the freely-jointed chain. The proportionality  $R^2 \propto n$  holds for all flexible chains, but the constant of proportionality depends on molecular restrictions for bond bending, torsion, monomer-monomer excluded volume interactions, and solvent interactions. To generalize, the mean-square end-to-end distance can be written as

$$\langle R^2 \rangle = C_n n l^2, \tag{3}$$

<sup>1</sup> Averaging over thermal fluctuations means that an average is taken over all possible configurations.

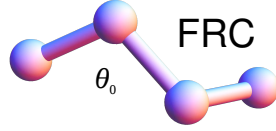


Figure 10: The freely-rotating chain model considers a constant angle of  $\theta_0$  between monomers.

where  $C_n$  is a function of  $n$  and represents deviations from ideal random walk behavior.  $C_n$  becomes independent of  $n$  for long chains [4]:

$$\lim_{n \rightarrow \infty} C_n = C_\infty. \quad (4)$$

The constant  $C_\infty$  is called the characteristic ratio and is typically reported as a measure of the tendency of a chain to coil [4, 27]. A chain in a poor solvent may have  $C_\infty < 1$ , while a chain in a good solvent or with rigid bending constraints will have  $C_\infty > 1$  [4]. For the theoretical development here, we neglect monomer interactions and excluded volume and therefore will always have  $C_\infty > 1$ . A treatment of these interactions is beyond the scope of this introductory chapter but can be found elsewhere [4, 33].

Here we consider the freely rotating chain (FRC) rotational isomeric state (RIS), and hindered rotation chain (HRC) models in addition to the FJC model already described. The constant  $C_\infty$  can be calculated exactly for the FRC and HRC models. The freely-rotating chain model considers a constant angle of  $\theta_0$  between monomers. The value of this angle is due to specific details of the chemical bonding. Figure 10 shows a schematic of monomers separated by an angle  $\theta_0$ . To calculate  $\langle R^2 \rangle$  and  $C_\infty$  for this model we need to determine the projection of the monomer vector  $\mathbf{r}_i$  onto another monomer vector  $\mathbf{r}_j$  existing farther down the chain. To do this, first consider the projection of the unit vector  $\hat{\mathbf{r}}_1$  onto  $\hat{\mathbf{r}}_3$ . This can be calculated as the projection of  $\hat{\mathbf{r}}_1$  onto  $\hat{\mathbf{r}}_2$  times the projection of  $\hat{\mathbf{r}}_2$  onto  $\hat{\mathbf{r}}_3$ , i.e.

$$\hat{\mathbf{r}}_1 \cdot \hat{\mathbf{r}}_3 = (\hat{\mathbf{r}}_1 \cdot \hat{\mathbf{r}}_2) (\hat{\mathbf{r}}_2 \cdot \hat{\mathbf{r}}_3) = [\cos(\pi - \theta_0)]^2. \quad (5)$$

For monomers  $i$  and  $j$  at different places in the chain this generalizes to

$$\hat{\mathbf{r}}_i \cdot \hat{\mathbf{r}}_j = [\cos(\pi - \theta_0)]^{|j-i|}. \quad (6)$$

The mean-square end-to-end distance is then calculated as follows (using  $\alpha = \cos(\pi - \theta_0)$  to shorten the notation):

$$\begin{aligned} \langle R^2 \rangle_{\text{FRC}} &= \left\langle nl^2 + 2l^2 \sum_{i=1}^n \sum_{j=i+1}^n \alpha^{|j-i|} \right\rangle \\ &= \left\langle nl^2 + 2l^2 \left( \frac{n\alpha}{1-\alpha} + \frac{\alpha^{n+1} - \alpha}{(1-\alpha)^2} \right) \right\rangle \end{aligned} \quad (7)$$

The second term in parenthesis can be neglected for large  $n$ . With this (and plugging back in for  $\alpha$ ), we have

$$\langle R^2 \rangle_{\text{FRC}} \approx \left( \frac{1 - \cos \theta_0}{1 + \cos \theta_0} \right) l^2 n. \quad (8)$$

The characteristic ratio is then

$$C_\infty = \frac{\langle R^2 \rangle}{nl^2} = \frac{1 - \cos \theta_0}{1 + \cos \theta_0}. \quad (9)$$

For polyethylene, which has all carbon-carbon backbone bonds, the angle between monomers  $\theta_0 = 109.5^\circ$  [4]. Other polymers with carbon-carbon backbone bonds have values of  $\theta_0$  which are similar to this. Using  $\theta_0$  in Eq. 9 leads to  $C_\infty \approx 2$ .

The freely-rotating chain model neglects restrictions on torsional bending, and therefore predicts a  $C_\infty$  value that is less than determined experimentally for real polymers. For example, polyethylene has  $C_\infty = 7.4$ , and polypropylene has  $C_\infty = 6.0$  [4]. The rotational isomeric state (RIS) model is the most successful model to include torsional bending restrictions. In addition to constant bond lengths and bond angles, this model assumes that there is a relatively high energy barrier between *trans* and *gauche* states (see Figure 5) so that each torsional angle exists in one of the discrete energy minima. For example, a sequence of 3 torsional angles can exist in  $3^3$  possible states: *trans-trans-trans*, *trans-trans-gauche<sup>+</sup>*, *trans-trans-gauche<sup>-</sup>*, *trans-gauche<sup>+</sup>-gauche*, etc. Each

sequence of angles is not equally probable and the probability must be defined for each individual case [4].

The hindered rotation chain (HRC) model assumes that each successive torsional angle is independent. Bond lengths and bond angles are taken to be constant. The torsional angle  $\phi$  is restricted by an energy landscape  $U_T(\phi)$ , and the probability of  $\phi$  taking on a certain value is proportional to the Boltzmann factor,  $e^{-U_T(\phi)/kT}$ . The  $C_\infty$  value predicted by this model is [4]

$$C_\infty = \left( \frac{1 - \cos \theta_0}{1 + \cos \theta_0} \right) \left( \frac{1 + \langle \cos \phi \rangle}{1 - \langle \cos \phi \rangle} \right), \quad (10)$$

where  $\langle \cos \phi \rangle$  is the Boltzmann-weighted average of  $\cos \phi$ :

$$\langle \cos \phi \rangle = \frac{\int_0^{2\pi} \cos \phi e^{-U_T(\phi)/kT} d\phi}{\int_0^{2\pi} e^{-U_T(\phi)/kT} d\phi}. \quad (11)$$

Plugging in for an energy landscape leads to a  $C_\infty$  prediction larger than that for the FRC model (at low temperatures). However, the HRC model predictions are still generally less than those observed experimentally since the theoretical treatment neglects excluded volume and monomer interaction effects [4]. Additional work attempts to include these effects (see, for example, Ref. [33]).

Many polymer properties can be understood without the detailed consideration of bond angle bending, torsion, excluded volume, etc [4, 27, 33, 49]. It has been found that it is useful to define an equivalent freely-jointed chain for calculations of chain properties. The equivalent freely-jointed chain consists of  $N$  monomers of length  $b$ . These quantities are referred to as the number of Kuhn monomers ( $N$ ) and the Kuhn monomer length ( $b$ ). To define  $N$  and  $b$ , let the equivalent freely-jointed chain have the same average end-to-end distance and the same contour length as the actual chain. This leads to

$$\begin{aligned} b &= C_\infty l \\ N &= \frac{n}{C_\infty}. \end{aligned} \quad (12)$$

Any chain can be mapped onto an equivalent freely-jointed chain. Therefore, one can consider freely-jointed chains in calculations of chain properties without loss of generality in the theoretical treatment. This is the approach taken in polymer physics since the FJC model is amenable to theoretical treatment. Indeed, many polymer properties can be understood in terms of the FJC model [4, 27, 33, 49].

## 2.2 DISTRIBUTION OF END-TO-END VECTORS

The last section featured calculations for the thermally averaged end-to-end length of a chain. Thermal fluctuations cause the chain to take on many different configurations, with some being more probable than others. In this section we review the Gaussian and Langevin probability functions for describing the distribution of end-to-end vectors of an ideal freely-jointed chain.

Gaussian chain statistics can be derived by considering a random walk in 3-dimensional space (see, for example, Ref. [4]). The result is a function representing the probability that a chain has an end-to-end vector  $\mathbf{R}$ :

$$\Psi_G(\mathbf{R}) = C_G \exp\left[-\frac{3R^2}{2Nb^2}\right], \quad (13)$$

where  $C_G$  is an associated constant. Applying the normalization condition and integrating over all space yields the value

$$C_G = \left(\frac{3}{2\pi Nb^2}\right)^{3/2}.$$

Note that the probability function only depends on the distance  $R$ . For a chain of  $N$  monomers with one end at the origin, the probability that the other end exists in the spherical shell with radius between  $R$  and  $R + dR$  is

$$4\pi R^2 \Psi_G(R) dR.$$

The Gaussian chain probability function can be used to perform analytical calculations of chain statistics. In the last section we calculated the mean-square



end-to-end distance for a freely-jointed chain (Eq. 2). The calculation can also be done analytically using  $\Psi_G$ :

$$\langle R^2 \rangle = \int_0^\infty R^2 \left( 4\pi R^2 \Psi_G(R) \right) dR = Nb^2. \quad (14)$$

This is the same result obtained by simpler means in Eq. 2. Higher moments can also be calculated. For example,

$$\langle R^4 \rangle = \int_0^\infty R^4 \left( 4\pi R^2 \Psi_G(R) \right) dR = \frac{5}{3} N^2 b^4.$$

The most probable end-to-end distance is found by solving

$$\frac{\partial}{\partial R} \left( 4\pi R^2 \Psi_G(R) \right) = 0.$$

This yields a most probable end-to-end distance of  $\sqrt{\frac{2}{3}} b \sqrt{N}$ . Note that this is different from the root-mean-square (RMS) end-to-end length of  $b\sqrt{N}$ . Many other statistical calculations are possible (see, for example, Doi and Edwards [33]).

Although it is useful for performing calculations, the Gaussian chain probability function does not represent all features of the freely-jointed chain model. Recall that a freely-jointed chain consists of  $N$  segments, each of fixed length  $b$ . The maximum outstretched length of such a chain is its contour length,  $Nb$ . The fact that a chain cannot be stretched farther than its contour length is called limiting extensibility. The Gaussian probability function does not capture limiting extensibility effects since it has a nonzero value for  $R > Nb$ . Limiting extensibility is important to represent for chains that are stretched very far. The Langevin probability function is the exact solution to the freely-jointed chain model. It was first derived by Kuhn and Grun [50]. Here, we present an alternative derivation for the Langevin probability function that is based on material from Treloar [49] and Rubinstein and Colby [4].

Consider a chain with one end fixed at the origin. There is a force applied that acts to push the free end away from the fixed end. This can be accomplished, for example, by placing a charge  $q_2$  at the free end, and varying a charge  $q_1$  placed at the origin in order to vary the applied force. This force acts in the

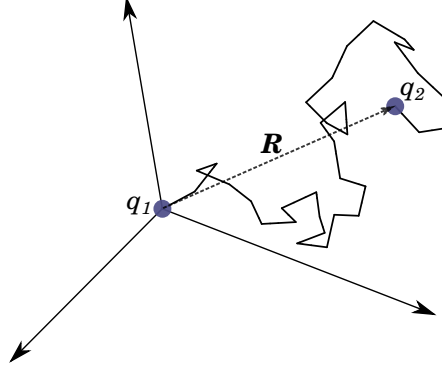


Figure 11: A chain with one end fixed at the origin having a charge  $q_1$ , and the other end having a charge  $q_2$ . The charges act to apply a force  $f$ . The chain end-to-end vector is labeled  $R$ .

radial direction. A schematic of this setup is shown in Figure 11. If the force acting on the chain ends is  $\mathbf{f}$ , then the work required to separate the two ends a distance  $R$  is  $\mathbf{f} \cdot R\hat{\mathbf{r}}$ , where  $\hat{\mathbf{r}}$  is the unit vector in the radial direction. The force is also in the radial direction, so the work is simply  $fR$ . The energy of this configuration is  $U = -fR$ .

The relative probability that a system occupies a given state at temperature  $T$  is

$$P = \frac{1}{Z} \exp\left(-\frac{U}{kT}\right),$$

where  $k$  is Boltzmann's constant and the quantity  $\exp(-U/kT)$  is known as the Boltzmann factor. The quantity  $Z$  is the partition function of the system and is defined as the sum of the Boltzmann factor over all possible states:

$$Z = \sum_{\text{all states}} \exp\left(-\frac{U}{kT}\right) = \sum_{\text{all states}} \exp\left(\frac{fR}{kT}\right)$$

This calculation is performed by an integral over all possible orientations of all  $N$  bond vectors (i.e. an integral over the surface area of a unit sphere):

$$Z = \int \int \exp\left(\frac{fR}{kT}\right) \prod_{i=1}^N \sin \theta_i d\theta_i d\phi_i.$$

Since the force  $f$  acts radially, the probability of a specific chain configuration is spherically symmetric. A single orientation of the end-to-end vector can

therefore be considered without loss of generality. Choosing the z-direction, the end-to-end length is

$$R = \sum_{i=1}^N b \cos \theta_i.$$

With this, the partition function is evaluated as the product of N identical integrals:

$$\begin{aligned} Z &= \left[ \int_0^{2\pi} d\phi \int_0^{\pi} d\theta \exp\left(\frac{fb \cos \theta}{kT}\right) \sin \theta \right]^N \\ &= \left[ \frac{4\pi \sinh\left(\frac{fb}{kT}\right)}{\frac{fb}{kT}} \right]^N. \end{aligned} \quad (15)$$

The Gibbs free energy of this single chain system is the internal energy calculated using the partition function plus any pressure-volume work. The Gibbs free energy is used since a constant force applied to the chain is considered (in contrast to a constant chain end-to-end distance). The work to separate the two ends a distance R apart is analogous to pressure-volume work on this system. The Gibbs free energy is

$$G = fR - kT \ln Z, \quad (16)$$

where Z is given in Eq. 15. The equilibrium condition for a constant applied force is

$$\frac{\partial G}{\partial f} = 0.$$

Solving for the end-to-end length yields

$$R = Nb \left( \coth\left(\frac{fb}{kT}\right) - \frac{kT}{fb} \right),$$

which can be rewritten as

$$\frac{R}{Nb} = \mathcal{L}\left(\frac{fb}{kT}\right),$$

where  $\mathcal{L}$  is the Langevin function. This is inverted to determine force versus chain end-to-end length,

$$\frac{fb}{kT} = \beta\left(\frac{R}{Nb}\right) \quad (17)$$

where  $\beta$  is the inverse Langevin function. Using Eq. 17 in Eq. 16 and writing out the terms leads to

$$G = kT \frac{R}{b} \beta\left(\frac{R}{Nb}\right) - kTN \ln \left[ \frac{4\pi \sinh \beta\left(\frac{R}{Nb}\right)}{\beta\left(\frac{R}{Nb}\right)} \right]. \quad (18)$$

The force  $f$  considered in this calculation of the Gibbs free energy is artificial; we wish to determine the free energy of a single polymer chain undergoing only thermal fluctuations. The free energy in terms of the chain probability function can be written as

$$G = -kT \ln \Psi_L, \quad (19)$$

where  $\Psi_L$  is termed the Langevin probability function. Solving Eqs. 18 and 19 for the probability function leads to

$$\Psi_L(R) = C_L \exp \left[ -\frac{R}{b} \beta\left(\frac{R}{Nb}\right) - N \ln \frac{\beta\left(\frac{R}{Nb}\right)}{\sinh \beta\left(\frac{R}{Nb}\right)} \right], \quad (20)$$

where  $C_L$  is a constant. Eq. 20 is the Langevin probability function, representing the probability that a freely-jointed chain has an end-to-end vector with length  $R$ . Kuhn and Grun [50] first derived Eq. 20 as the exact solution to the freely-jointed chain model.

When the end-to-end vector length is much less than the chain contour length, the Langevin probability function simplifies to a Gaussian function. The Padé approximation to the inverse Langevin function is [51]

$$\beta(x) \approx x \frac{3 - x^2}{1 - x^2}. \quad (21)$$

Plugging this into Eq. 20 and keeping leading order terms in the expansion for  $R \ll Nb$  leads to Eq. 13.

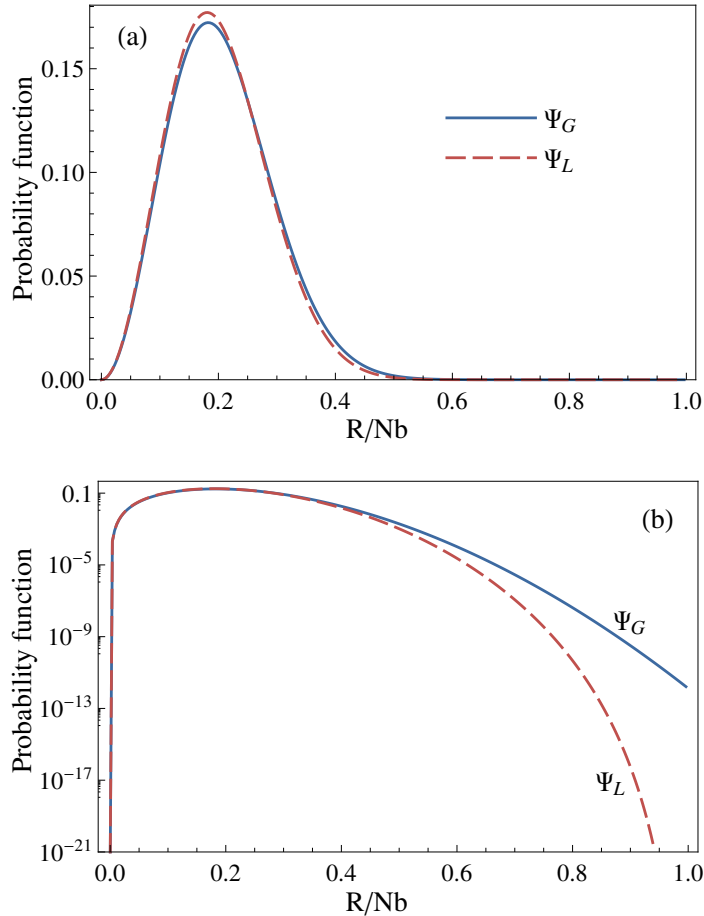


Figure 12: The Gaussian ( $\Psi_G$ ) and Langevin ( $\Psi_L$ ) probability functions, shown with (a) regular and (b) logarithmic scaling on the vertical axis. The functions are similar for small  $R/Nb$ , but differ for large values:  $\Psi_L \rightarrow 0$  as  $R/Nb \rightarrow 1$ , but  $\Psi_G$  stays finite.

Figure 12 shows the probability that a chain has an end-to-end distance  $R$ , according to both the Gaussian (Eq. 13) and Langevin (Eq. 20) functions. The radial probability distribution of each is plotted as a function of chain end-to-end length relative to contour length. Plots with both normal and logarithmic scaling on the vertical axis are shown in order to compare the two functions. For  $R \ll Nb$ , the Langevin and Gaussian probability functions are nearly identical, as can be seen in Figure 12a. However, they become different as  $R/Nb$  approaches 1, as can be seen in Figure 12b. The Langevin function goes to zero for  $R \rightarrow Nb$ , and reflects the fact that a chain cannot be extended beyond its contour length without breaking bonds. The Gaussian

probability function stays nonzero for all  $R$  values and becomes a non-physical representation of chain behavior as  $R/Nb$  approaches 1.

The Gaussian and Langevin probability functions have been used to form physics-based models of rubber elasticity. These are reviewed in Chapter 3. In Chapter 4 we derive a new model of large deformation elasticity using the Langevin probability function.

### 2.3 MANY CHAIN SYSTEMS

The statistical functions discussed thus far were derived by considering a *single* chain free to fluctuate and sample many different configurations. For an ideal freely-jointed chain, the mean-square end-to-end distance is  $\langle R^2 \rangle = Nb^2$ , and it was discussed how other chains can be mapped onto the FJC model. Now consider multiple chains placed in a solution. Each samples many different configurations and has a mean-square end-to-end distance of  $\langle R^2 \rangle$ . The pervaded volume refers to the solution volume occupied by the chain via conformational fluctuations [4]. The average pervaded volume can be calculated as

$$V_p = \left\langle \frac{4\pi}{3} R^3 \right\rangle. \quad (22)$$

Let the chain number density for a solution be  $\rho$ . The critical density for chain overlap ( $\rho^*$ ) occurs when

$$\rho^* \approx \frac{1}{V_p},$$

Using Eq. 22 and neglecting numerical factors,

$$\rho^* \approx \frac{1}{N^{3/2}b^3}. \quad (23)$$

This expression will be used to explain qualitative solution behavior. A solution of chains with  $\rho < \rho^*$  is called dilute. The case  $\rho > \rho^*$  is called semidilute, and  $\rho \gg \rho^*$  is called concentrated. Figure 13 shows a schematic of these different cases. A concentrated system with zero solvent is called a polymer melt.

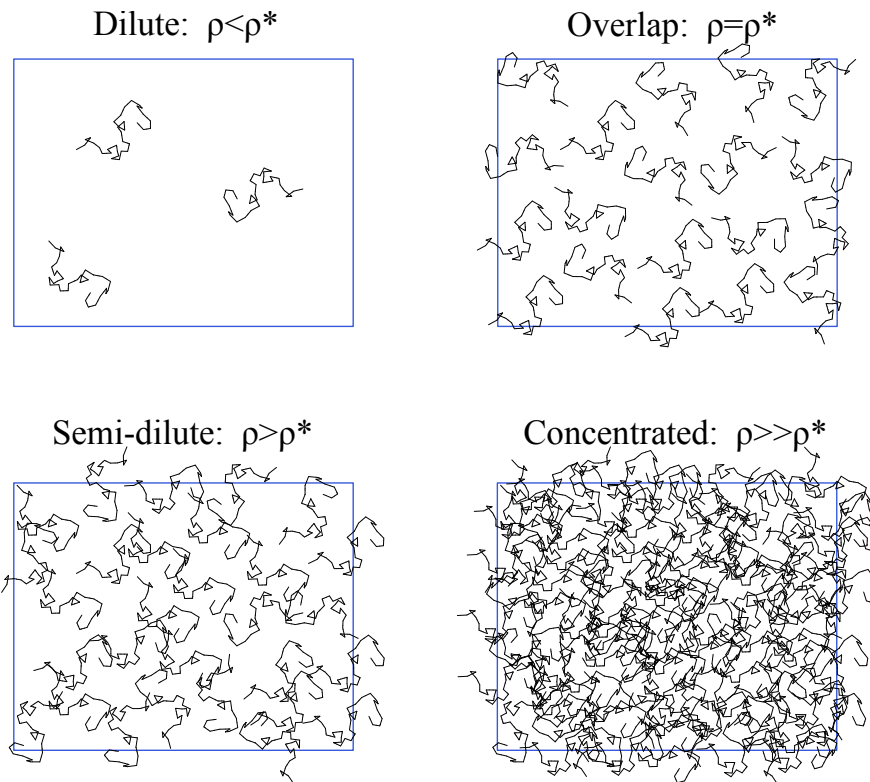


Figure 13: A schematic of different polymer solution densities, classified relative to the overlap concentration  $\rho^*$ .

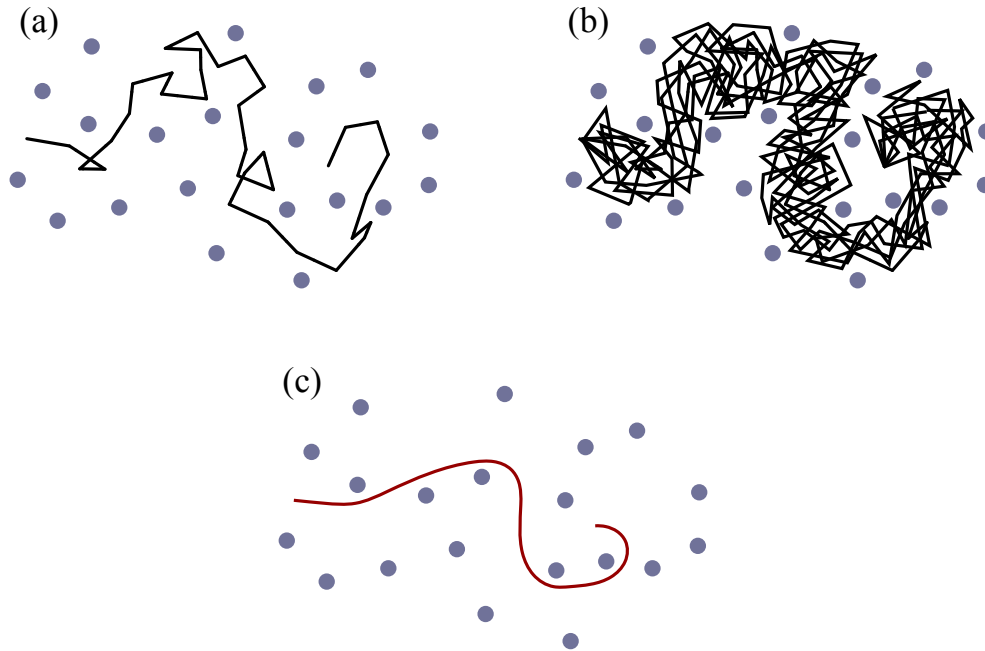


Figure 14: A chain confined by fixed obstacles (a) will undergo thermal fluctuations which are restricted by the obstacles (b). If the chain is “reeled-in” to minimize the path length from one end to the other the resulting path is still restricted by the obstacles (c) [4].

Here, we will consider the concentrated regime where chains strongly overlap ( $\rho \gg \rho^*$ ). A chain in a concentrated solution experiences many interactions with other chains, such that it is reasonable to describe its conformational fluctuations via a mean-field theory. This is the approach of Doi and Edwards [33] in the famous “tube” model. To proceed, consider a chain which has its motion confined by the presence of fixed obstacles, as shown in Figure 14a. The obstacles represent other chains in the solution. For simplicity, the ends of the chain are fixed. The chain will undergo excursions due to thermal fluctuations, and the fluctuations will be restricted by the presence of the obstacles (Figure 14b). If the chain is “reeled-in” at each end, the resulting path must still make its way around the obstacles (Figure 14c). The path shown in Figure 14c is called the primitive path of the chain [4, 33]. The magnitude of the thermal fluctuations in Figure 14b defines an effective “tube” potential in the mean-field theory [33]. The thermal fluctuations occur approximately about the primitive path of the chain. An alternative definition of the primitive path is the time-averaged path of the chain. With this definition the fluctu-



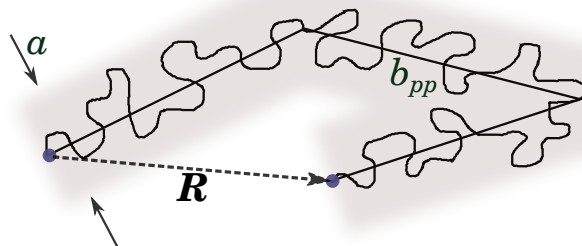


Figure 15: A schematic of quantities involved in primitive path-tube theory. The primitive path shown has  $N_{pp} = 3$  steps of constant length  $b_{pp}$ , and the thermal fluctuations of the chain are restricted by a 'tube' with dimension  $a$ .

ations occur exactly about the primitive path. The average-path definition is more natural when considering monomer fluctuations. The shortest-path definition is simpler to determine from a simulation and is more natural to use to determine the topological state of a system of many polymer chains. Since the primitive path is a theoretical concept, not a material entity, either definition may be used.

Figure 15 illustrates the quantities involved in primitive path-tube theory. The simplest version of the theory considers a constant primitive path step length of  $b_{pp}$ . The number of steps in the primitive path is  $N_{pp}$ , and the primitive path contour length is  $L_{pp} = N_{pp}b_{pp}$ . The magnitude of monomer fluctuations is quantified by the tube dimension  $a$ . The quantities  $a$  and  $b_{pp}$  are often set equal in approximate calculations since they are of the same order. The end-to-end distance of the primitive path is the same as the end-to-end distance of the chain.

The obstacles restrict the motion of a chain and cause its primitive path to have multiple steps. A chain with zero obstacles (e.g. a single chain in solution) will have a primitive path consisting of a single step ( $N_{pp} = 1$ ). A chain with  $k$  obstacles binding its path from one end to the other will have  $N_{pp} = k + 1$ . The obstacles represent intermolecular entanglements with other chains in the system. The number of entanglements a chain experiences is approximately  $N_{pp} - 1$ . The entanglement length,  $N_e$ , refers to the approximate number of

monomers between entanglements. For long chains with many entanglements, the entanglement length is estimated to be

$$N_e \approx \frac{N}{N_{pp}}, \quad (24)$$

where  $N$  is the number of Kuhn monomers in the chain. In relation to the schematic in Figure 15, this definition says that  $N_e$  monomers of the chain exist within each of the  $N_{pp}$  primitive path segments of length  $b_{pp}$ . Although simple, this definition is problematic for all but very long chain systems. Hoy et al. [25] and Karayiannis and Kroger [20] include a thorough discussion of methods to calculate  $N_e$ , along with new calculations that behave as expected in the limits of short and long chains. Further details regarding the calculation of  $N_e$  can be found in Ref. [25]. Here, we note that  $N_e$  is a quantity that is related to the number of entanglements per chain. A system with few entanglements will have a large value of  $N_e$ , and a system with many entanglements per chain will have a smaller  $N_e$ . In particular,  $N_e$  will be much less than  $N$  for very long chains in a dense solution or melt.

Entanglements are sometimes referred to as “physical crosslinks”, and are dominant in determining the rheological properties of uncrosslinked polymer solutions and melts. The reasons for this can be seen by considering the different solution densities shown in Figure 13. When  $\rho < \rho^*$ , the presence of polymer chains will tend to simply change the viscosity of the solution. At high concentrations ( $\rho \gg \rho^*$ ) the behavior is much different due to the presence of intermolecular entanglements. A melt of entangled polymer chains will behave somewhat like an elastic solid if stretched very quickly, since the entanglements temporarily provide a restoring force. However, chains with sufficient thermal energy will continually change their configurations to minimize the overall energy of the system, and therefore the restoring force provided by a collection of entangled chains will decrease with time.

This section has served to introduce the physical basis for some of the important properties of many chain polymer systems. We also introduced the concept of the primitive path and illustrated how the primitive path represents intermolecular entanglements in an uncrosslinked polymer. In Chapter 5 we will introduce primitive path analysis as a tool for quantifying

the entanglement characteristics of a simulated crosslinked polymer system. Primitive path analysis will be used extensively to interpret simulation results in Chapter 6.

## CHAPTER 3

### MODELING RUBBER ELASTICITY

---

In the last chapter we discussed the statistics of individual polymer chains as well as many-chain melts and solutions. When a sufficient number of crosslinks are added to a many-chain system, the chains join together and form a single macroscopic network polymer [4]. The resulting material behaves as a nonlinear elastic solid.<sup>1</sup> The objective of this chapter is to introduce a physics-based approach to modeling the elasticity of crosslinked polymers, and to review current models available in the literature. This information is presented to highlight deficiencies with current physics-based models, and introduce the statistical mechanics modeling approach which will be used to derive a new model in the following chapter.

At the molecular level an elastomer consists of crosslinked and entangled chains which form a network (Figure 16), and the material behaves as elastic because of the permanent network structure. Elastomers exhibit entropic elasticity; this means that individual chains in the network have the ability to undergo extensive microstructural rearrangement, and the conformations of chains are described statistically. The statistics of ideal chains were reviewed in the last chapter. The ability for microstructural rearrangement allows the material to undergo large, reversible deformations. At large deformations, the elastic response is nonlinear and exhibits a regime of strain softening followed by strain hardening. The natural rubber data of Treloar [1] in Figure 17 demonstrates this large deformation behavior, showing the characteristic S-shaped stress-stretch curve of rubber elastic materials. This curve contains three regions: A small initial linear region is followed by softening and then

---

<sup>1</sup> The term “elastic” is not used in a strict sense here: there is also a dependence on time and temperature.

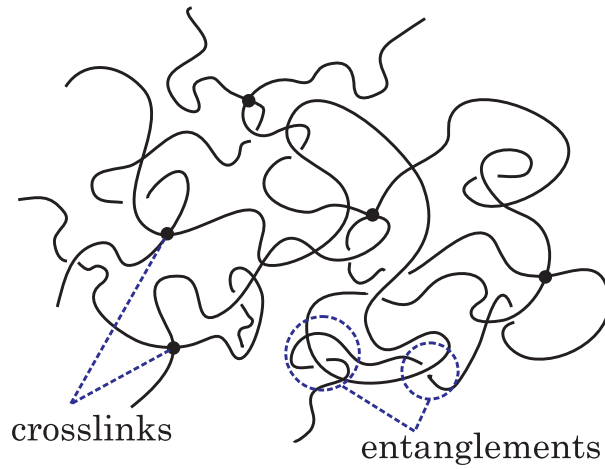


Figure 16: Schematic of an elastomer at the molecular level, showing crosslinks and entanglements between polymer chains.

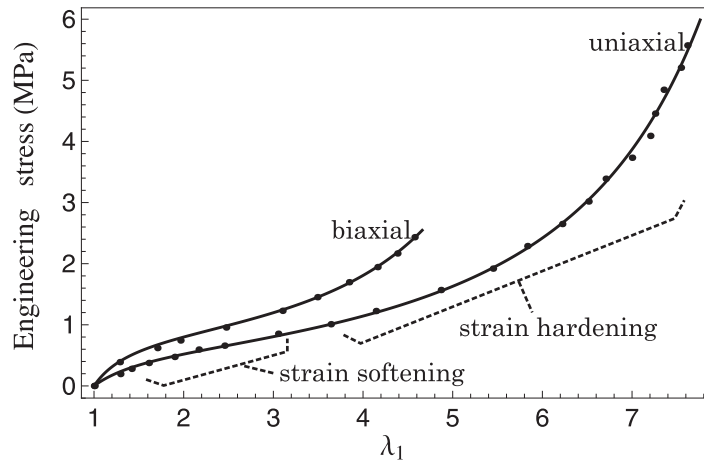


Figure 17: The characteristic stress-stretch response of vulcanized natural rubber, showing strain softening, hardening, and the difference between uniaxial and equi-biaxial deformation states for loadings applied in the 1 direction. The lines are drawn through the data of Treloar [1] to guide the eye.

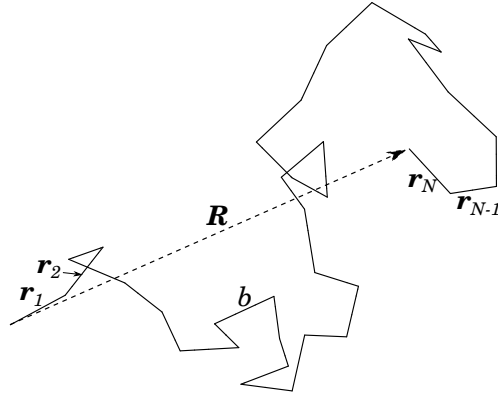


Figure 18: An ideal freely-jointed chain with  $N$  Kuhn monomers, each of length  $b$ . The chain follows random walk statistics and has end-to-end vector  $\mathbf{R}$ .

hardening regions. The large difference in stress for uniaxial vs. biaxial loadings is another characteristic of the mechanical response. These characteristics are universal features of a polymer that forms a crosslinked network, regardless of the detailed chemical makeup. It is important for a model to be able to capture these mechanical features.

Starting from the framework of statistical thermodynamics, the objective of a physics-based model of elasticity is to derive an expression for the Helmholtz free energy which can then be used to obtain equations of state. A statistical thermodynamics analysis typically begins by considering the number of molecular conformations available to a single, isolated polymer chain, where the end-to-end vector  $\mathbf{R}$  describes a given molecular conformation. In the following we use the notation  $\mathbf{R}$  for the end-to-end vector and  $R = |\mathbf{R}|$  for its magnitude. Consider an ideal freely-jointed chain with  $N$  Kuhn monomers, each of length  $b$ . This chain follows random-walk statistics; a schematic of the quantities involved is shown in Figure 18. It was discussed in the previous chapter how any chain can be mapped onto an equivalent freely-jointed chain by defining the Kuhn monomer length ( $b$ ) and the equivalent number of Kuhn monomer segments ( $N$ ). We therefore can consider the ideal freely-jointed chain model without loss of generality. This simplified theoretical treatment is sufficient for the description of many physical phenomena associated with polymers, and is the basis for nearly all theories of rubber elasticity.

As the chain is extended, the number of available conformations decreases and therefore the entropy decreases. For a single chain with the probability of

a given molecular conformation represented by  $\Psi$ , the entropy is determined via Boltzmann's equation:  $S = k \ln \Psi$ , where  $k$  is Boltzmann's constant. If there is no change in the internal energy of the system during deformation, the free energy density is calculated via an entropic contribution which follows from the individual chain probability distribution:

$$\begin{aligned} W &= -\frac{\rho_m}{N} T \Delta S \\ &= -\frac{\rho_m}{N} T \left( \overline{\langle k \ln \Psi \rangle} - \underbrace{\langle k \ln \Psi_0 \rangle}_{S_0} \right), \end{aligned} \quad (25)$$

where  $\rho_m$  is the monomer density,  $T$  is temperature,  $\langle \cdot \rangle$  is an average over thermal fluctuations, the overbar is an average over all chains in the network, and  $S_0$  is a constant. Eq. 25 is simply the number density of chains times the average free energy of a chain. The constant  $S_0$  is included in order to identify  $W$  as the elastically stored free energy per unit volume (the strain energy density). However, since we are interested in determining the stress, which depends on *changes* in free energy, in the following we will neglect the constant factor  $S_0$  for simplicity.

When the end-to-end distance of a chain is much less than its chain contour length ( $R \ll Nb$ ), the probability of a given molecular conformation can be approximated using Gaussian statistics (see Section 2.2). Gaussian statistics were discussed in the last chapter; the probability function is repeated here for clarity:

$$\begin{aligned} \Psi_G(R) &= C_G \exp \left[ -\frac{3R^2}{2Nb^2} \right] \\ &= C_G \exp \left[ -\frac{3R_1^2}{2Nb^2} \right] \exp \left[ -\frac{3R_2^2}{2Nb^2} \right] \exp \left[ -\frac{3R_3^2}{2Nb^2} \right], \end{aligned} \quad (26)$$

where  $C_G$  is a normalization constant and the indices 1, 2, 3, refer to three orthogonal directions. The mean square end-to-end distance of a chain in an undeformed network using  $\Psi_G$  is  $R_0^2 = Nb^2$ , where the subscript zero refers to

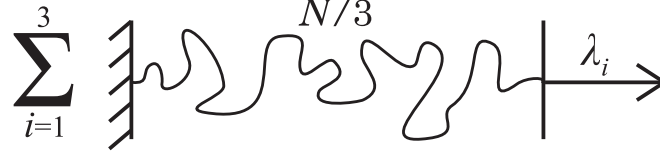


Figure 19: The affine network model. A chain is decomposed into 3 chains in orthogonal directions, and each chain deforms affinely with the applied deformation.

the undeformed configuration. The free energy density of a system of Gaussian chains is<sup>2</sup>

$$W = \frac{3\rho_m kT}{2N^2 b^2} \langle R^2 \rangle. \quad (27)$$

The simplest network model of microscopic chain deformation is the affine network model, shown in Figure 19. Because of the exponential form of  $\Psi_G$ , it is possible to decompose a Gaussian chain into 3 chains in orthogonal directions, each with length  $N/3$ . If these chains are aligned with the principal directions of the deformation, each chain deforms as  $R_i = \lambda_i R_0 / \sqrt{3}$ , where  $\lambda_i$  is the principal stretch in the  $i^{\text{th}}$  direction. This assumption of chain behavior is used with Eq. 25 to determine the free energy in the affine network model. In this model (originally proposed by Kuhn [52]), all chains have the same probability distribution so the network average is trivial. There are no fluctuations of the end-to-end length in the affine network model, so the thermal average is also trivial. The free energy is

$$\begin{aligned} W^{\text{affine}} &= -\frac{kT\rho_m}{N} \ln \Psi_G \\ &= \frac{kT\rho_m}{2N} (\lambda_1^2 + \lambda_2^2 + \lambda_3^2). \end{aligned} \quad (28)$$

<sup>2</sup> Note that Eqs. 25 and 27 have implicitly assumed that  $N$  and  $b$  are the same for all chains in the network; for a polydisperse network the averages in Eq. 27 should enclose the entire expression.



The Cauchy stress in the principal directions for an incompressible material<sup>3</sup> is calculated from the free energy as

$$\sigma_i = \lambda_i \frac{\partial W}{\partial \lambda_i} + p, \quad (29)$$

where  $i = 1, 2, 3$ , and  $p$  is a hydrostatic pressure due to incompressibility and is determined by the boundary conditions. For the affine network model, the Cauchy stress in the principal directions is

$$\sigma_i^{\text{affine}} = \underbrace{\frac{kT\rho_m}{N}}_G \lambda_i^2 + p, \quad (30)$$

where  $G$  is the shear modulus.

In an actual polymer network the chains do not deform affinely, i.e. the imposed stretch is not directly transmitted to each chain. The individual chains in the network will deform sub-affinely since the network connectivity allows for extensive rearrangement at the molecular level. We will use molecular dynamics simulations to perform a detailed analysis of this behavior in Chapter 6. The first (and still widely used) nonaffine network model is the phantom network model, first derived by James and Guth [53]. The physics behind this model is that chain end-to-end vectors deform nonaffinely because the number of chains connected to a crosslink ( $\phi$ ) is small. The value  $\phi$  is called the junction functionality. A value of  $\phi = 4$  is the most common; examples include natural rubber crosslinked with sulfur, polybutadiene crosslinked with dicumyl peroxide, and irradiated polyethylene. A functionality of 3 can be obtained via an endlinking reaction, such as vinyl-terminated polydimethylsiloxane chains crosslinked with trifunctional silanes [54, 55]. The phantom network model relates changes in length and the magnitude of fluctuations of chain end-to-end distance to  $\phi$ . The model is derived by considering only the constraints imposed on chains via the connections at crosslinks; all other intermolecular interactions, including entanglement constraints, are ignored (hence the name ‘phantom’).

---

<sup>3</sup> Crosslinked polymer materials may be treated as incompressible since the shear modulus is typically several orders of magnitude lower than the bulk modulus.

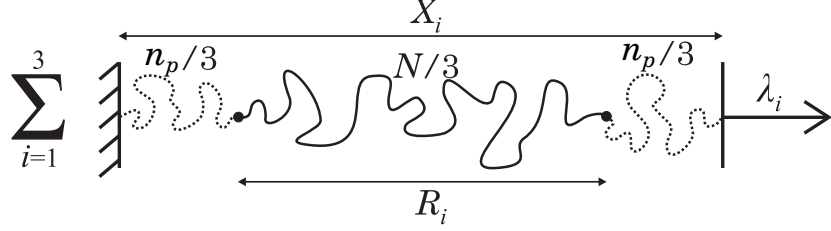


Figure 20: The single chain description of network connectivity proposed by Rubinstein and Panyukov [5]. A chain with  $N$  monomers is coupled to the applied deformation via 2 effective chains of length  $n_p$ . For Gaussian chains, this is decomposed into a sum over 3 chains aligned with the principal directions of stretch, each with length  $N/3$  and coupled to the applied deformation via 2 effective chains of length  $n_p/3$ .

Rubinstein and Panyukov [5, 6] presented a solution to the phantom network model by mapping it onto the single chain representation shown in Figure 20. The network structure is represented by a chain of length  $N$  coupled to the applied deformation via 2 effective chains of length  $n_p$  (the subscript  $p$  refers to phantom network). The effective chains represent the molecular structure and the network connectivity, and their length determines the magnitude of the applied stretch transferred to the test chain. The combined chain shown in Figure 20 follows Gaussian statistics and has a total of  $(N + 2n_p)$  monomers, or, equivalently,  $(N + 2n_p)/3$  monomers in each direction. The undeformed end-to-end length of the combined chain is

$$X_0^2 \equiv |\mathbf{X}_0|^2 = b^2 (N + 2n_p). \quad (31)$$

The ends of the combined chain deform affinely and undergo zero thermal fluctuations since they are coupled directly to the applied deformation. The affine deformation relation is

$$X_i = \lambda_i X_0 / \sqrt{3}. \quad (32)$$

Now consider the  $N$  monomers in the test chain. The end-to-end vector is  $\mathbf{R}$ , and the undeformed mean-square end-to-end distance is determined via Gaussian statistics<sup>4</sup> to be

$$\langle \mathbf{R}_0^2 \rangle = b^2 N, \quad (33)$$

where  $\mathbf{R}_0$  denotes the undeformed end-to-end vector. The brackets are an average over thermal fluctuations (i.e. an average over all possible configurations that the chain may assume). If the chain were not connected at each end, the thermal average of the end-to-end vector would be  $\langle \mathbf{R}_i \rangle = 0$ .<sup>5</sup> However, the test chain is not free here since it is connected by its ends as part of the combined chains. The vector average  $\langle \mathbf{R}_i \rangle$  is determined by a force balance instead of using  $\Psi_G$ . The *average* force acting on the ends to the test chain is the same as the force acting on the combined chain. The ends of the combined chain are “fixed” (i.e. non-fluctuating), and their deformation is equal to the applied deformation. The rest of the chain undergoes thermal fluctuations, so we therefore equate the *average* force acting on a segment of the chain with the force acting on the ends.

The free energy of the combined chain is

$$A(\mathbf{X}) = -kT \ln \Psi_G(\mathbf{X}) = \frac{3kT X^2}{2b^2(N + 2n_p)},$$

where the individual chain free energy has been denoted by  $A$ . The force acting on the ends of the combined chain is

$$f_i(\mathbf{X}) = -\frac{\partial A(\mathbf{X})}{\partial X_i} = -\frac{3kT}{b^2(N + 2n_p)} X_i. \quad (34)$$

<sup>4</sup> The overall dimensions of a chain that follows Gaussian statistics can be represented by a model where each monomer follows Gaussian statistics [33]. With this, it follows that the mean-square distance of any two beads separated by  $k$  monomers on the chain has a mean-square end-to-end distance of  $b^2 k$ . This result can be derived using the properties of the Gaussian integral (see, for example, Chapter 2 and Appendix 2.I of Doi and Edwards [33]). Therefore, although the test chain is connected at each end to the effective chains, the mean-square end-to-end distance is still given by Gaussian statistics.

<sup>5</sup> This can be seen by using  $\Psi_G(\mathbf{R})$  from Eq. 26 and performing the integral  $\langle \mathbf{R}_i \rangle = \int \int \int \mathbf{R}_i \Psi_G(\mathbf{R}) dR_1 dR_2 dR_3$ . Since  $\Psi_G$  is an even function and  $\mathbf{R}_i$  is an odd function, this evaluates to zero.

This is the applied force (i.e. the “macroscopic” force) which does not fluctuate. The average force acting on the test chain is determined in a similar manner to be

$$\langle f_i(\mathbf{R}) \rangle = \left\langle -\frac{\partial A(\mathbf{R})}{\partial R_i} \right\rangle = -\frac{3kT}{b^2(N + 2n_p)} \langle R_i \rangle. \quad (35)$$

Setting Eqs. 34 and 35 equal and rewriting yields

$$\langle R_i \rangle = \frac{N}{N + 2n_p} X_i. \quad (36)$$

The mean-square end-to-end length in each direction can be written as

$$\langle R_i^2 \rangle = \langle R_i \rangle^2 + \langle \Delta R_i^2 \rangle, \quad (37)$$

where  $\langle \Delta R_i^2 \rangle = \langle (R_i - \langle R_i \rangle)^2 \rangle$  is the mean-square magnitude of thermal fluctuations in direction  $i$ . The mean-square end-to-end length in the undeformed state follows Gaussian statistic ( $\langle R_i^2 \rangle = b^2 N / 3$ ). Using this, Eq. 32 with  $\lambda_i = 1$ , and Eq. 36 in Eq. 37 yields

$$\frac{b^2 N}{3} = \frac{b^2 N^2}{3(N + 2n_p)} + \langle \Delta R_i^2 \rangle.$$

Rearranging leads to the expression [5, 6]

$$\langle \Delta R_i^2 \rangle = \frac{b^2}{3} \left( \frac{1}{N} + \frac{1}{2n_p} \right)^{-1}. \quad (38)$$

In the phantom network model [53, 56, 57], the positions of the chain ends fluctuate about an average with a magnitude that depends on  $\phi$ , the number of chains connected at a crosslink. The magnitude of fluctuations of the end-to-end distance is [5, 56, 57]

$$\langle \Delta R^2 \rangle = \frac{2}{\phi} b^2 N. \quad (39)$$

Since the fluctuations of a Gaussian chain are not correlated, the magnitude of fluctuations in each direction is simply

$$\langle \Delta R_i^2 \rangle = \frac{2}{3\phi} b^2 N. \quad (40)$$

Equating Eq. 40 with Eq. 38 and solving for  $n_p$  yields the number of monomers in an effective chain in the single-chain representation [5, 6] of the phantom network model:

$$n_p = \frac{N}{\phi - 2}. \quad (41)$$

The number of monomers in the effective chains represents the magnitude of thermal fluctuations, and how the applied deformation is transferred to an individual chain. The phantom network model description does not assign a deformation dependence to the magnitude of end-to-end fluctuations. The mean-square length of the test chain in direction  $i$  is now expressed as

$$\langle R_i^2 \rangle = \frac{b^2 N}{3} \left[ \lambda_i^2 \left( 1 - \frac{2}{\phi} \right) + \frac{2}{\phi} \right]. \quad (42)$$

The overall mean-square end-to-end length is

$$\begin{aligned} \langle R^2 \rangle &= \sum_{i=1}^3 \langle R_i^2 \rangle \\ &= b^2 N \left[ \frac{\lambda_1^2 + \lambda_2^2 + \lambda_3^2}{3} \left( 1 - \frac{2}{\phi} \right) + \frac{2}{\phi} \right]. \end{aligned} \quad (43)$$

The free energy density of a system of Gaussian chains is given in Eq. 27. Recall that for the affine network model we did not include the ensemble and thermal averages (see Eq. 28) since the ends of a chain did not undergo fluctuations and all chains were represented by the same probability function. For the phantom network model it is important to consider the macroscopic free energy being related to the *average* free energy of a chain. In the single chain representation, all chains in the network are described by Eq. 43 so the

network average is trivial (i.e.  $\overline{\langle R^2 \rangle} = \langle R^2 \rangle$ ). Using Eq. 43 in Eq. 27 yields the free energy for the phantom network model:

$$W^{\text{phantom}} = \frac{3\rho_m kT}{2N} \left[ \frac{\lambda_1^2 + \lambda_2^2 + \lambda_3^2}{3} \left( 1 - \frac{2}{\phi} \right) + \frac{2}{\phi} \right]. \quad (44)$$

The last term in Eq. 44 is the free energy contribution due to fluctuations of the chain ends. Since the phantom network model does not assign a deformation dependence to the magnitude of fluctuations of end-to-end length, these thermal fluctuations do not contribute to the stress acting on the network. Applying Eq. 29 yields the principal components of stress:

$$\sigma_i^{\text{phantom}} = \frac{kT\rho_m}{N} \left( 1 - \frac{2}{\phi} \right) \lambda_i^2 + p. \quad (45)$$

Note that the stress in the affine model (Eq. 30) and phantom model (Eq. 45) only differ by the constant factor multiplying the stretch; the functional relationship between stress and stretch is the same. The difference in these two models is therefore in how the polymer network configuration leads to a certain modulus value.

The affine and phantom network models are concerned with changes in end-to-end chain length. In general, there are two mechanisms in a polymer network which lead to a decrease in entropy and the elastic stress of a polymer network when a deformation is applied. The first is changes in the average distances between monomers. End-to-end chain length is a measure of this (changes in average distances). Fewer configurations with large end-to-end length are possible, so entropy decreases when end-to-end length increases. The other mechanism is changes in the magnitude of thermal fluctuations with deformation. Although the phantom network considers the chain ends to fluctuate about a mean position, the magnitude of these fluctuations is taken to be constant with deformation and therefore the fluctuations do not contribute to the stress. Additionally, it is important to consider thermal fluctuations along the length of the chains (not just at the ends) because of the distributed nature of entanglements. In the following, the physical description

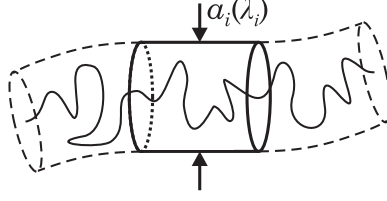


Figure 21: The magnitude of monomers fluctuations varies with stretch, and this is modeled by a deformation-dependent 'tube' potential.

of restricted fluctuations will be discussed, and the Rubinstein and Panyukov [5, 6] nonaffine tube model will be reviewed.

In a polymer network the position of the  $m^{\text{th}}$  bond between monomers,  $\mathbf{R}_m$ , will fluctuate about its mean according to  $\mathbf{R}_m = \langle \mathbf{R}_m \rangle + \Delta \mathbf{R}_m$ . The vector from the current monomer position to the average position is  $\Delta \mathbf{R}_m$  and satisfies  $\langle \Delta \mathbf{R}_m \rangle = 0$ . Interactions with neighboring chains will restrict the magnitude of these fluctuations, i.e. excursions of a bond from its mean position will not be entirely random. The mean-square magnitude of monomer fluctuations can be quantified using the tube concept of Edwards [30]. The magnitude of fluctuations in direction  $i$  is quantified by the 'tube' radius  $a_i$ :

$$\langle \Delta R_{m,i}^2 \rangle = a_i^2, \quad (46)$$

where  $R_{m,i}$  refers to the position of the  $m^{\text{th}}$  monomer in direction  $i$ . Figure 21 shows a schematic of a chain confined to a deformation-dependent tube. Note that Figure 21 is only a schematic; there are also fluctuations along the length of the tube which are not labeled in the figure. The ensemble averaged magnitude of fluctuations is the same in each direction for an undeformed material ( $a_1 = a_2 = a_3$ ).

Although the original Edwards [30] tube model treated the tube radius as a constant  $a_1 = a_2 = a_3 = \text{const.}$ , later theoretical and experimental work demonstrated that it should vary with deformation. Small-angle neutron scattering (SANS) studies [58, 59, 60] have shown that the variation of the form factor [61] with the applied stretch for labeled chains in uniaxially deformed polymer networks can be described well by using a tube radius which varies as  $a_i \propto \lambda_i^{1/2}$ . A comparison with models considering tube variations of  $a_i = \text{const}$

and  $\alpha_i \propto \lambda_i$  demonstrated that the tube variation exponent of 1/2 was the only choice that provided a good fit to the data [59, 60].

For a tube radius that varies as  $\alpha_i \propto \lambda_i^{1/2}$ , the mean-square magnitude of monomer fluctuations in a given direction varies as

$$\langle \Delta R_{m,i}^2 \rangle \propto \lambda_i. \quad (47)$$

This is equivalent to saying that the confining tube potential varies affinely with the applied deformation. This functional form was first proposed by Heinrich and Straube [62], and was also used by Heinrich et al. [63] in a model of rubber elasticity.

The functional form in Eq. 47 is used in the nonaffine tube model Rubinstein and Panyukov [5, 6]. The effective size of the deformation-dependent tube direction  $i$  is

$$\alpha_i = \alpha_0 \lambda_i^{1/2}, \quad (48)$$

where  $\alpha_0$  is the undeformed tube radius. The Rubinstein and Panyukov [5] model assigns

$$\alpha_0 = \frac{1}{2} b N_e^{1/2}, \quad (49)$$

where  $N_e$  is the number of monomers between entanglements in the undeformed state (i.e. the entanglement length - see Section 2.3). The factor of 1/2 in Eq. 49 is due to the nomenclature used here; Ref. [5] assigns a tube *diameter* of  $b N_e^{1/2}$ , so the radius is half of this. This assignment says that random walk statistics can be used to describe segments of a chain between entanglements, but that the entanglements add an additional length scale to the problem and cause the chain as a whole to not behave as a random walk.

The total stress acting on the network in the nonaffine tube model Rubinstein and Panyukov [5, 6] is obtained by considering a decomposition into crosslinked and entangled components. A schematic of this representation is shown in Figure 22. With this decomposition, two separate contributions to free energy are considered. The first is due to thermally averaged chain conformations and is represented by a phantom network component. The



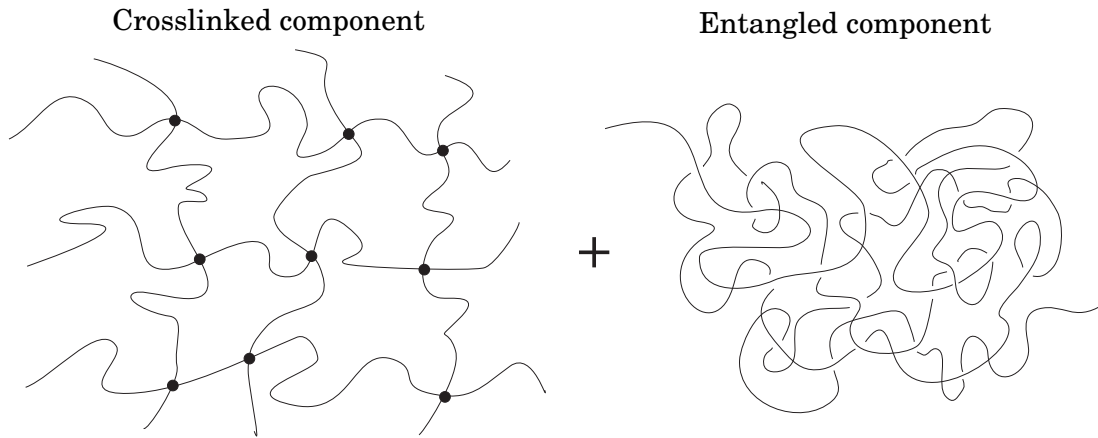


Figure 22: The free energy of a crosslinked, entangled network is determined by Rubinstein and Panyukov [5] by assuming a decomposition into crosslinked and entangled components.

second is due to the entangled component; this part represents changes in thermal fluctuations during deformation, and its contribution to free energy is determined by considering a chain confined to a tube with radius that varies according to  $a_i = bN_e^{1/2}\lambda_i^{1/2}/2$ .

Here, a brief overview of the solution method used to obtain the entangled contribution to stress will be presented. The discussion here will highlight some of the main parts of the derivation of the nonaffine tube model stress; it is not meant to give a full account. The original derivation is found in Refs. [5, 6]. A schematic of the representation used to derive the entangled component of stress is shown in Figure 23. Chains with  $q$  monomers are attached in series (i.e. a junction functionality of  $\phi = 2$ ), and a virtual chain of  $m_i$  monomers attaches each junction point to the nonfluctuating (and affinely deforming) elastic background. The overall representation is of a single, infinitely long chain with entanglements spaced on average  $q$  monomers apart. The entangled component stress will then be calculated in the limit  $q \rightarrow 0$  in order to represent a continuous confining potential. The “virtual chains” of  $m_i$  monomers act to restrict the fluctuations of the junctions. The representation in Figure 23 shows a single dimension; since Gaussian statistics are used, the chain can be decomposed into 3 chains in orthogonal directions, so this representation is sufficient.

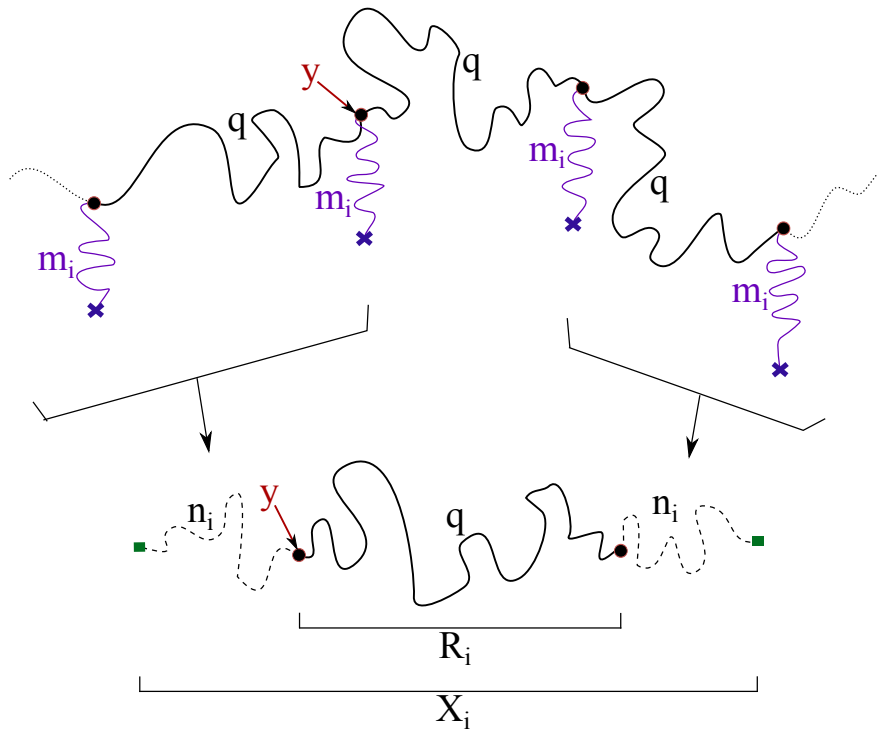


Figure 23: A schematic of the representation used in the solution of the nonaffine tube model [5]. Chains with  $q$  monomers are attached in series (i.e. a junction functionality of  $\phi = 2$ ), and a virtual chain of  $m_i$  monomers attaches each junction point to the nonfluctuating elastic background. This representation is mapped onto the combined chain picture where a chain of  $q$  monomers is attached to effective chains of  $n_i$  monomers at each end.

Recall the use of the “effective” chains shown previously in Figure 20 to derive the phantom network model chain behavior and stress. The effective chains were defined to represent the connective structure of the network. In contrast, the virtual chains of  $m_i$  monomers shown in Figure 23 represent topological constraints and other interactions which function to restrict the magnitude of fluctuations. Because virtual chains represent constraints instead of actual chains, they do not contribute directly to the stress; they act only to change the probability that a chain will assume a certain configuration. It was shown in Refs. [5, 6] that the assignment  $m_i \propto \lambda_i^2$  is consistent with this microscopic representation.<sup>6</sup> With the virtual chain representation, it was shown in the appendix of Ref. [6] that the fluctuations of a junction point  $y$  (e.g. the point labeled “ $y$ ” in Figure 23) are

$$\langle \Delta R_{y,i} \rangle = \frac{b^2}{2} \sqrt{m_i q}. \quad (50)$$

Since  $m_i \propto \lambda_i^2$ , this is in agreement with Eq. 47 for the change in the magnitude of fluctuations with deformation. Comparing this with Eqs. 46, 48, and 49, it is seen that

$$\sqrt{m_i q} = \frac{N_e \lambda_i}{2}. \quad (51)$$

The stress in the nonaffine tube model is calculated by an analogy with the phantom network model. Previously in this chapter, the stress for the phantom network model was calculated by writing  $\langle R^2 \rangle$  as a function of the applied stretch (Eq. 43), using this to determine the free energy (Eq. 44), and differentiating the free energy to obtain the stress (Eq. 45). Alternatively, the stress in the principal directions can be written as a function of the mean-square end-to-end length [5]:

$$\sigma_i = \frac{\rho_m kT}{N} \left( \frac{3 \langle R_i^2 \rangle}{b^2 N} - \frac{2}{\phi} \right) + p. \quad (52)$$

<sup>6</sup> A simple reasoning for why this choice is consistent can be given by demonstrating that it leads to zero stress contribution. Consider the affine network model stress is Eq. 30 and replace  $N$  with  $m_i$ , leading to  $\sigma_i \propto \lambda_i^2/m_i$ . If  $m_i \propto \lambda_i^2$ , then an affinely deforming virtual chain does not alter the stress-stretch relationship. A more rigorous derivation of this choice is in Refs. [5, 6].

Using the phantom network expression for  $\overline{\langle R_i^2 \rangle}$  from Eq. 42 in Eq. 52 leads to the same result obtained earlier in Eq. 45. Here, we will use Eq. 52 with  $\phi = 2$  and  $N \rightarrow q$  to calculate stress for the nonaffine tube model:

$$\sigma_i = \frac{\rho_m kT}{q} \left( \frac{3\overline{\langle R_i^2 \rangle}}{b^2 q} - 1 \right) + p. \quad (53)$$

The end-to-end length is determined using the combined chain representation shown in Figure 23 by relating  $R_i$  to  $X_i$ . In the phantom network model, the vector  $X_i$  deformed affinely. In the nonaffine tube model, the vector  $X_i$  is not coupled directly to the applied deformation: the deformation is applied to the ends of the virtual chains, and deformation of the vector  $X_i$  is determined self-consistently.

The relation of  $R_i$  to  $X_i$  is the same as in Eq. 36, but with  $N \rightarrow q$  and  $n_p \rightarrow n_i$ :

$$\langle R_i \rangle = \frac{q}{q + 2n_i} X_i. \quad (54)$$

The number of monomers in an effective chain,  $n_i$ , is defined by a recursive relation which follows from Figure 23: an effective chain is defined via the parallel connection of one virtual chain of length  $m_i$  with one combined chain of length  $q + n_i$  (the connections to the right of the chain of length  $q$  are also represented by an effective chain of length  $n_i$ ). Treating the chains as linear springs, this leads to

$$\frac{1}{n_i} = \frac{1}{m_i} + \frac{1}{q + n_i},$$

which is solved for  $n_i$  to yield

$$n_i = \frac{1}{2} \left( \sqrt{4m_i q + q^2} - q \right). \quad (55)$$

The mean-square end-to-end distance in direction  $i$  is written as

$$\overline{\langle R_i^2 \rangle} = \overline{\langle R_i \rangle^2} + \overline{\langle \Delta R_i^2 \rangle}. \quad (56)$$

To calculate this for the nonaffine tube model, the mean-square magnitude of fluctuations is determined using Eq. 38 with  $N \rightarrow q$  and  $n_p \rightarrow n_i$ :

$$\overline{\langle \Delta R_i^2 \rangle} = \langle \Delta R_i^2 \rangle = \frac{b^2}{3} \left( \frac{1}{q} + \frac{1}{2n_i} \right)^{-1}. \quad (57)$$

This, along with Eq. 54, is used to calculate mean-square end-to-end distance:

$$\overline{\langle R_i^2 \rangle} = \frac{q^2}{(q + 2n_i)} \overline{X_i^2} + \frac{b^2}{3} \left( \frac{1}{q} + \frac{1}{2n_i} \right)^{-1}. \quad (58)$$

The quantity  $\overline{X_i^2}$  must still be determined. In the phantom network model,  $X_i$  deformed affinely and was given by a simple expression (Eq. 32); this is not the case here, since the deformation is applied to the ends of the virtual chains. The calculation of  $\overline{X_i^2}$  is performed in the appendix of Ref. [5] using a recursion relation. For the case  $\phi = 2$ , the result is

$$\overline{X_i^2} = \frac{b^2 q}{3} \left[ \frac{\lambda_i^2 (1 + z_i^2) + 2z_i}{1 - z_i^2} \right], \quad (59)$$

where

$$z_i = \frac{n_i}{q + n_i}. \quad (60)$$

Using Eqs. 53, 58, 59, and 60, the stress is written as

$$\sigma_i = \frac{\rho_m kT}{q} \left( \lambda_i^2 - 1 \right) \frac{(1 - z_i)(1 + z_i^2)}{(1 + z_i)^3}. \quad (61)$$

The quantities  $n_i$  and  $z_i$  are rewritten using Eq. 51:

$$n_i = \frac{1}{2} \left( \sqrt{N_e^2 \lambda_i^2 + q^2} - q \right), \quad (62)$$

$$z_i = \frac{\sqrt{N_e^2 \lambda_i^2 + q^2} - q}{\sqrt{N_e^2 \lambda_i^2 + q^2} + q}. \quad (63)$$

With this, the stress in Eq. 61 is

$$\sigma_i = \rho_m kT \left( \lambda_i^2 - 1 \right) \frac{2q^2 + N_e^2 \lambda_i^2}{2 (q^2 + N_e^2 \lambda_i^2)^{3/2}}. \quad (64)$$

The limit  $q \rightarrow 0$  is considered to represent the limit of a continuous confining potential. This yields the expression for the entanglement contribution to stress in the nonaffine tube model [5]:

$$\sigma_i^{\text{tube}} = \frac{\rho_m kT}{2N_e} \left( \lambda_i - \frac{1}{\lambda_i} \right). \quad (65)$$

This is integrated to obtain the free energy density:

$$W^{\text{tube}} = \frac{kT \rho_m}{2N_e} \sum_{i=1}^3 \left( \lambda_i + \frac{1}{\lambda_i} \right) \quad (66)$$

The total free energy of the network in the nonaffine tube model is the sum of this “tube” contribution and a crosslinked component that is represented by a phantom network:

$$W^{\text{NA}} = \underbrace{\frac{kT \rho_m}{2N} (1 - 2/\phi) \sum_{i=1}^3 \lambda_i^2}_{\text{phantom network}} + \underbrace{\frac{kT \rho_m}{2N_e} \sum_{i=1}^3 \left( \lambda_i + \frac{1}{\lambda_i} \right)}_{\text{nonaffine tube}}. \quad (67)$$

The derivation here has served to highlight the physics behind the nonaffine tube model: topological constraints, which have an approximate spacing of  $N_e$  monomers, act to restrict the fluctuations of monomers along the chain, and these fluctuations vary sub-affinely with the applied deformation in a given direction.

Rubinstein and Panyukov [5] also derive the so-called slip-tube model which builds on the nonaffine tube model description to additionally include effects of redistribution of chain monomers along the confining tube. The number of monomers that are constrained by the confining tube potential in a given

direction increases for directions that are elongated and decreases for directions that are compressed. The result is the free energy function

$$W^{ST} = \frac{kT\rho_m}{2N} (1 - 2/\phi) \sum_{i=1}^3 \lambda_i^2 + \frac{kT\rho_m}{2N_e} \sum_{i=1}^3 \left( \frac{\lambda_i}{\sqrt{g_i}} + \frac{\sqrt{g_i}}{\lambda_i} \right) - \frac{kT\rho_m}{3N_e} \ln \left( N_e^3 \prod_{i=1}^3 g_i \right) \quad (68)$$

where the function  $g_i$  is determined via an energy minimization.

Because of its simplicity, we will focus on the nonaffine tube model (Eq. 67) instead of the slip-tube model. To demonstrate the capability of this model to describe stress-stretch data, first define the two modulus parameters:

$$G_c^{NA} = kT\rho_m \frac{1 - 2/\bar{\phi}}{N} \quad (69a)$$

$$G_e^{NA} = \frac{kT\rho_m}{2N_e} \quad (69b)$$

$G_c^{NA}$  is proportional to the density of chains, and  $G_e^{NA}$  is proportional to the density of entanglements. These parameter definitions are used to rewrite Eq. 67:

$$W^{NA} = \frac{1}{2} G_c^{NA} \sum_{i=1}^3 \lambda_i^2 + G_e \sum_{i=1}^3 \left( \lambda_i + \frac{1}{\lambda_i} \right) \quad (70)$$

Stress in the principal directions is calculated by using Eq. 70 in Eq. 29. This leads to

$$\sigma_i^{NA} = \underbrace{G_c^{NA} \lambda_i^2}_{\text{phantom network}} + \underbrace{G_e^{NA} \left( \lambda_i - \frac{1}{\lambda_i} \right)}_{\text{nonaffine tube}} + p, \quad (71)$$

For small deformations, Eq. 71 yields a shear modulus of  $G_c^{NA} + G_e^{NA}$ .<sup>7</sup> The ratio of the two parameters ( $G_e^{NA}/G_c^{NA}$ ) determines the extent of strain softening.

<sup>7</sup> The shear modulus can be calculated in a simple fashion by relating to the Young's modulus. The Young's modulus relates the stress to a uniaxial deformation of  $\lambda_1 = \lambda$ ,  $\lambda_2 = \lambda_3 = \lambda^{-1/2}$ . The 2 and 3-directions are free, so either can be used to calculate the value of  $p$ . Using these deformation conditions and expanding for  $\lambda \approx 1$  yields  $\sigma_1 \approx 3(G_c + G_e)(\lambda - 1)$ , i.e. a Young's

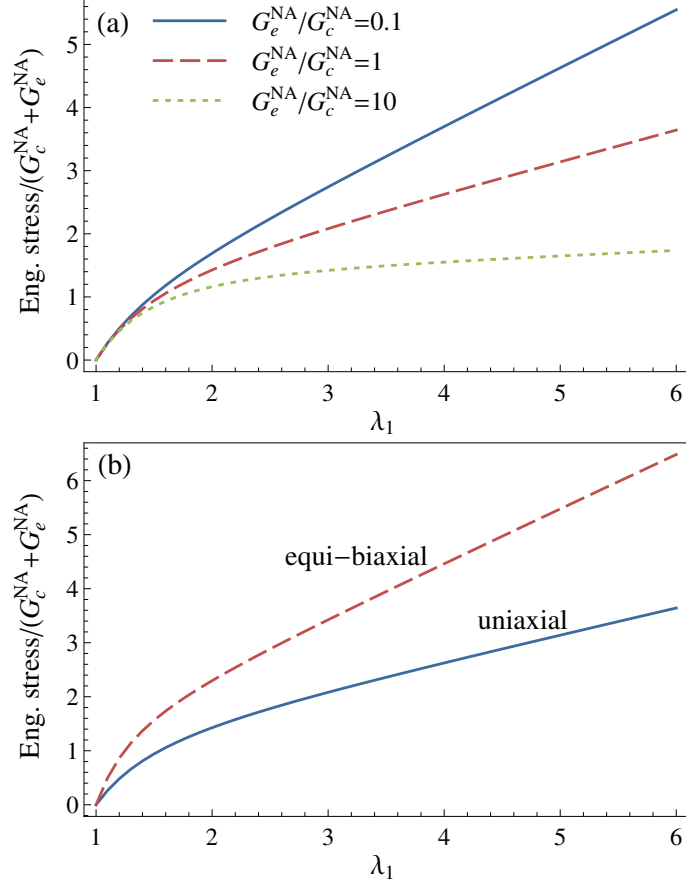


Figure 24: The stress-stretch modeling capabilities of the nonaffine tube model [5, 6] are demonstrated by (a) plotting stress with different values of the softening ratio  $G_e^{\text{NA}}/G_c^{\text{NA}}$ , and (b) showing the difference in stress-stretch behavior of uniaxial and biaxial deformation states for parameter values  $G_e^{\text{NA}} = G_c^{\text{NA}}$ . Stress is plotted for each by normalizing with respect to the shear modulus of  $G_c^{\text{NA}} + G_e^{\text{NA}}$

The effect of varying model parameters is demonstrated in Figure 24a. We refer to  $G_e^{\text{NA}}/G_c^{\text{NA}}$  as the softening ratio. Figure 24a shows model predictions for uniaxial (tension) stress-stretch behavior with different values of the softening ratio. A high value of  $G_e^{\text{NA}}/G_c^{\text{NA}}$  predicts extensive strain softening.

Figure 24b shows that the nonaffine tube model can differentiate between uniaxial and biaxial deformation states. This plot was made by setting  $G_e^{\text{NA}} = G_c^{\text{NA}}$ .

---

modulus of  $3(G_c + G_e)$ . For an incompressible, homogeneous, linear elastic solid the Young's modulus is 3 times the shear modulus [64] in the limit of small strain.



The nonaffine tube model (and other models reviewed thus far) do not contain a term representing strain hardening and limiting extensibility at large applied stretch. For the nonaffine tube model, this is because the crosslinked component is taken from the phantom network model, and the phantom network model uses Gaussian statistics. Any model of rubber elasticity using Gaussian statistics is limited to intermediate deformations where the individual chains have end-to-end distances that are still much less than their contour length (i.e.  $R \ll Nb$ ). Gaussian statistics cannot describe single chain behavior at large deformations where there is strain hardening, since here it becomes essential to capture limiting chain extensibility. The next section describes models which use Langevin statistics in order to capture limiting extensibility behavior of a polymer network.

### 3.1 MODELING LARGE DEFORMATION LIMITING EXTENSIBILITY

The models reviewed in the previous section do not capture the upturn in stress at large deformations of a polymer network. This section introduces how the Langevin probability function has been used to model the large deformation nonlinear elastic behavior of polymer networks. Figure 17 demonstrates the characteristic strain hardening behavior observed at large deformations of a crosslinked polymer. At the level of individual chains, this behavior arises when there is a sharp decrease in entropy as the length of a deformed chain nears its contour length. A chain cannot be stretched out farther than its contour length without breaking bonds; this is why we refer to the “limiting extensibility” of a polymer chain or a polymer network. For these large deformations, individual chains are best described by the Langevin probability function,  $\Psi_L$ , instead of the Gaussian function,  $\Psi_G$  (see Eq. 20 and the derivation in Section 2.2). As  $R \rightarrow Nb$ ,  $\Psi_L \rightarrow 0$ ; therefore, the use of the Langevin probability function enforces that chains cannot be extended beyond their contour length.

The Langevin probability function has been used in several physics-based models of large deformation elasticity. Placing  $\Psi_L$  into Eq. 25 leads to a free energy expression of

$$W = -\frac{\rho_m}{N} kT \langle \overline{\ln \Psi_L(R)} \rangle, \quad (72)$$

where, as before,  $\langle \cdot \rangle$  is an average over thermal fluctuations and the overbar is an average over all chains in the network. The difficulty in using Langevin statistics instead of Gaussian statistics to determine the free energy is that a chain can no longer be decomposed into 3 orthogonal directions.<sup>8</sup> This means that there is no simple or straightforward way to calculate the network and thermal averages in Eq. 72. Models of rubber elasticity which use the Langevin probability function have therefore proposed different ways to calculate these averages. Most neglect thermal fluctuations and focus on the network average. The 3-chain model, originally due to Wang and Guth [7], calculates the network average by considering chains placed on the three axes aligned with the principal directions of deformation. The chain in direction  $i$  deforms affinely according to  $R/R_0 = \lambda_i$ . Thermal fluctuations are not considered. Using Gaussian statistics for mean-square undeformed end-to-end length, this expression becomes  $R = b\sqrt{N}\lambda_i$ . The free energy is determined by averaging over the 3 chains oriented in the different directions:

$$W_{3\text{-chain}} = -\frac{\rho_m kT}{N} \left( \frac{1}{3} \sum_{i=1}^3 \ln \left[ \Psi_L \left( b\sqrt{N}\lambda_i \right) \right] \right). \quad (73)$$

The free energy for the 3-chain model (and the 4-chain [65] and 8-chain [8] models which are discussed next) can be simplified when  $R \ll Nb$  to yield the same result as the affine network model (Eq. 28). These models therefore have the same small deformation behavior. The affine network model result can be obtained using the same description as the 3-chain model (the network average

---

<sup>8</sup> This can be seen from the form of the probability function. Because of the simple exponential form, the Gaussian function can be decomposed into a product of the 3 directions (see Eq. 26). The free energy is therefore a sum over the behavior in each direction. An equivalent result for free energy is obtained if one-dimensional chains of length  $N/3$  are taken to be aligned along each axis. This same procedure cannot be done using the Langevin function (Eq. 20), since a multiplicative decomposition of the probability function into factors for three independent directions cannot be done.

calculated via chains aligned with each of the principal axes of deformation, each deforming affinely). The difference is that when using Gaussian statistics this description is theoretically rigorous, but when using Langevin statistics it is an approximation.

The 4-chain model of Flory and Rehner [65] calculates the network average by considering 4 chains joined together at the center of a regular tetrahedron; the tetrahedron is then deformed along with each chain. This model must be evaluated numerically for Langevin chains; there is no simple closed-form expression for the strain energy [49].

Although the 3-chain and 4-chain models capture large deformation limiting extensibility, they underpredict the difference between uniaxial and biaxial deformation states [8, 66]. This motivated the development of the 8-chain model by Arruda and Boyce [8]. This model considers 8 chains placed at the corners of a box, which deforms affinely with the applied stretch. Thermal fluctuations are not considered. In this configuration, each chain undergoes the same deformation, expressed by

$$R = b\sqrt{N}\sqrt{\frac{\lambda_1^2 + \lambda_2^2 + \lambda_3^2}{3}}. \quad (74)$$

The resulting free energy function is

$$W^{8\text{-chain}} = -\frac{\rho_m kT}{N} \ln \left[ \Psi_L \left( b\sqrt{N}\sqrt{\frac{\lambda_1^2 + \lambda_2^2 + \lambda_3^2}{3}} \right) \right]. \quad (75)$$

Ref. [49] contains more information on the 3- and 4-chain models, and Refs. [8, 66] contain more information on the 3-, 4-, and 8-chain models. Since these models assign affine chain deformation, the description they propose may be termed a representative volume element (RVE) instead of a true microscopic description which attempts to average over all internal degrees of freedom. This point is revisited in Chapter 4. Here, we will compare stress-stretch predictions from the 3-chain and 8-chain models in order to demonstrate their

modeling capability. First define the shear modulus parameter for both models as<sup>9</sup>

$$G = \frac{\rho_m kT}{N}, \quad (76)$$

and define a parameter related to the first stretch invariant to shorten the notation:

$$\Lambda = \sqrt{\frac{\lambda_1^2 + \lambda_2^2 + \lambda_3^2}{3}}. \quad (77)$$

The quantity  $\Lambda$  is referred to as the normalized first invariant in following chapters. An undeformed state has  $\Lambda = 1$ , and a deformed state has  $\Lambda > 1$ . The stress in the principal directions is determined using Eq. 29. For each model, this leads to

$$\begin{aligned} \sigma_i^{3\text{-chain}} &= \frac{G\lambda_i\sqrt{N}}{3} \beta\left(\frac{\lambda_i}{\sqrt{N}}\right) + p, \\ \sigma_i^{8\text{-chain}} &= \frac{G\lambda_i^2\sqrt{N}}{3\Lambda} \beta\left(\frac{\Lambda}{\sqrt{N}}\right) + p. \end{aligned}$$

These expressions contain the inverse Langevin function,  $\beta$ , which does not have a closed form. A simple way to evaluate is to use the Padé approximation [51] introduced in Eq. 21. Using this leads to

$$\sigma_i^{3\text{-chain}} = G\lambda_i^2 \frac{1}{3} \left( \frac{\lambda_i^2 - 3N}{\lambda_i^2 - N} \right) + p \quad (78)$$

$$\sigma_i^{8\text{-chain}} = G\lambda_i^2 \frac{1}{3} \left( \frac{\Lambda^2 - 3N}{\Lambda^2 - N} \right) + p. \quad (79)$$

These forms for stress are very similar, the only difference being that the 8-chain model contains the normalized first invariant instead of just the stretch in direction  $i$ . These are two parameters in each expression: the shear modulus is  $G$ , and limiting extensibility is set by  $N$ . For the 8-chain model, limiting

<sup>9</sup> Since both the 3-chain and 8-chain models are identical to the affine network model for  $R \ll Nb$ , the identification of  $G$  in Eq. 76 as the shear modulus can be seen by examining the affine network model stress in Eq. 30.

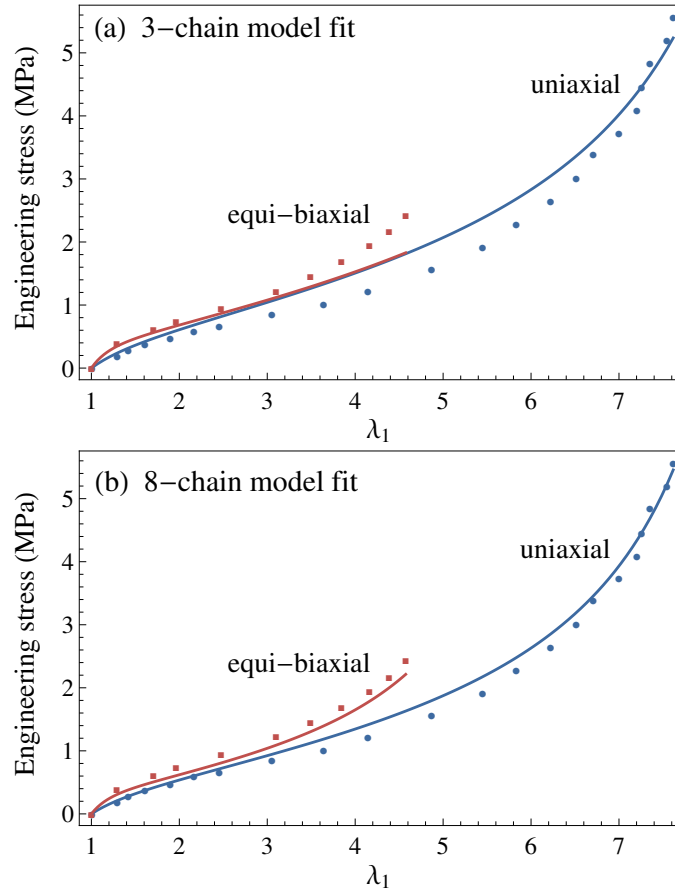


Figure 25: Model fits to uniaxial and biaxial deformations of the natural rubber data of Treloar [1]. (a) The 3-chain model [7] with best fit parameters  $G = 0.34$  MPa and  $N = 95$ , and (b) the 8-chain model [8] with best fit parameters  $G = 0.29$  MPa and  $N = 28$

extensibility occurs when  $\Lambda \rightarrow \sqrt{N}$ . For the 3-chain model,  $\lambda_i \rightarrow \sqrt{N}$  is the location of the stress-stretch asymptote.

Both the 3-chain and 8-chain models are shown fit to the natural rubber data of Treloar [1] in Figure 25. The best fit parameters were determined by optimizing parameters to both uniaxial and equi-biaxial deformation data using the least-squares Monte Carlo method described in Appendix A. Figure 25b shows that the 8-chain model provides a good fit to this data. However, Figure 25a shows the 3-chain model cannot sufficiently differentiate between the uniaxial and biaxial data. This result was also demonstrated by Arruda and Boyce [8].

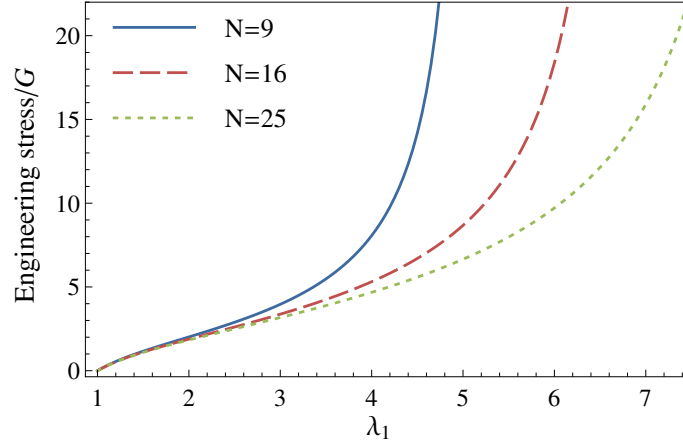


Figure 26: The effect of varying the finite extensibility parameter  $N$  in the 8-chain model [8].

The effect of varying the limiting extensibility parameter  $N$  in the 8-chain model is demonstrated in Figure 26. When  $N$  increases, limiting extensibility effects occur at a higher stretch value.

Although the 8-chain model [8] is a popular choice to represent large deformation material behavior, it does not fit data well for materials with extensive strain softening. This is demonstrated in Figure 27 by fitting the 8-chain model to data for VHB [9] (a polyacrylate rubber), and b186 rubber [10] (a carbon-black filled rubber). Fit parameters for the 8-chain model were determined by minimizing the residual over all the data points shown in Figure 27 using the least-square Monte Carlo method detailed in Appendix A. To compare, the nonaffine tube model is also fit to these data sets. The best fit of the nonaffine tube model was determined by optimizing parameters to only intermediate stretch data, at stretch values before hardening occurs. The data cutoff for fitting the nonaffine tube model was chosen as  $\lambda_1 < 3.5$  for VHB in Figure 27, and  $\lambda < 1.8$  for b186 rubber in Figure 27b. Only this data was included in the residual to be minimized in determining the best fit parameters.

It is seen that the 8-chain model captures the limiting extensibility behavior of VHB but that the model fit is not close to the data at small stretch values (Figure 27a). The nonaffine tube model can fit both the VHB and b186 rubber data well to intermediate deformations, but does not capture strain hardening for large applied stretch. The b186 rubber material has a sharp upturn in the stress-stretch curve for  $\lambda_1 > 1.8$  (Figure 27b). The parameters for the 8-

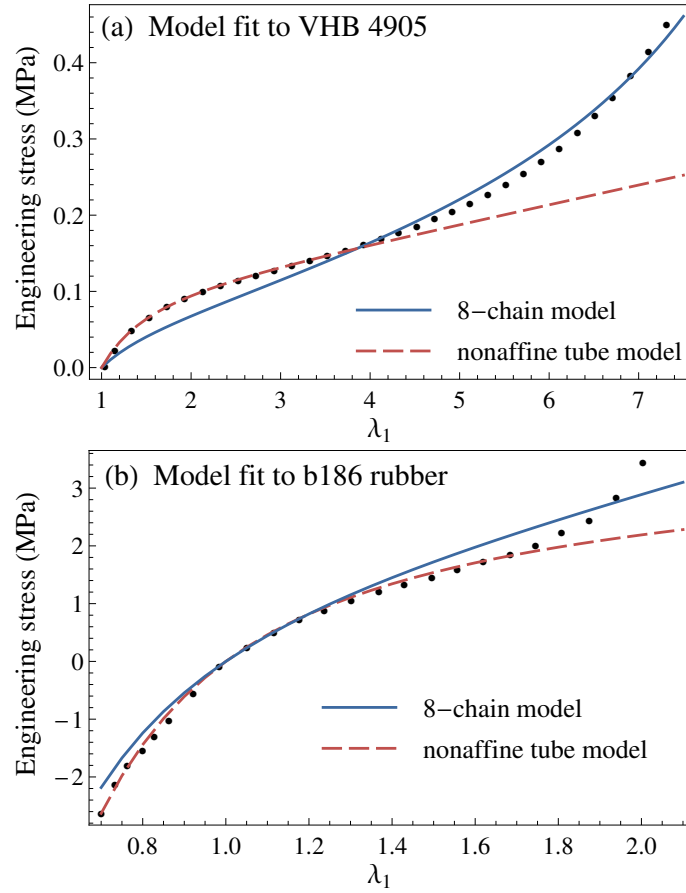


Figure 27: Fits of the Arruda and Boyce [8] 8-chain model and the Rubinstein and Panyukov [5, 6] nonaffine tube model to two data sets. (a) VHB 4905 data from Fox and Goulbourne [9] was fit by optimizing parameters of the 8-chain model to all of the data, and optimizing fit parameters for the nonaffine tube model to data with  $\lambda_1 < 3.5$ . Best fit parameters are  $G = 0.037$ ,  $N = 38$  for the 8-chain model, and  $G_c = 0.026$ ,  $G_e = 0.044$  for the nonaffine tube model. (b) b186 rubber data from Lulei and Miehe [10] was fit by optimizing parameters of the 8-chain model to all of the data, and optimizing fit parameters for the nonaffine tube model to data with  $\lambda_1 < 1.8$ . Best fit parameters are  $G = 1.59$ ,  $N = 29$  for the 8-chain model, and  $G_c = 0.40$ ,  $G_e = 1.35$  for the nonaffine tube model.

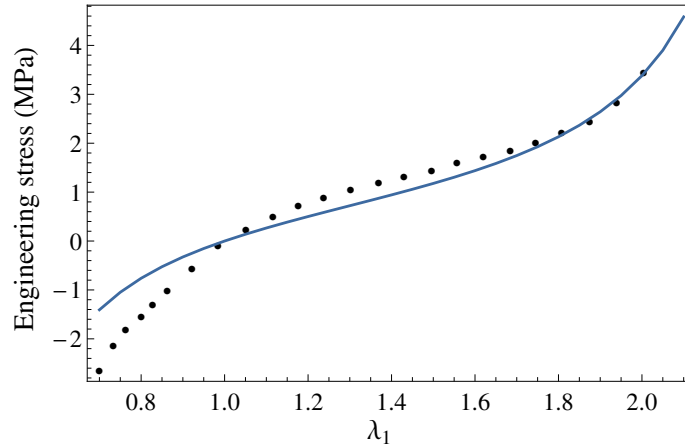


Figure 28: The result of fitting the 8-chain model [8] to b186 rubber [10] by optimizing parameters to data only with  $\lambda > 1.8$ . With this restriction, best fit parameters are  $G = 0.62$ ,  $N = 2.2$ , and the model captures limiting extensibility but not small deformation behavior.

chain model were optimized to all of the data points for b186 rubber for the result shown in Figure 27b; with this choice the residual is minimized if the model captures the initial behavior but not the upturn in stress. If the 8-chain parameters are optimized to fit only data with  $\lambda > 1.8$ , the model captures the upturn in stress but not the small-to-intermediate deformation behavior. The result of this alternative fitting procedure is shown in Figure 28.

This comparison demonstrates that each of these models has a clear range of applicability. The nonaffine tube model can fit data for different materials up to intermediate deformations, before strain hardening is observed. The 8-chain model can fit large deformation data for materials that do not display extensive strain softening; however, it cannot fit the full range of stress-stretch data for materials such as VHB [9] and b186 rubber [10], which display extensive strain softening behavior. In the next section we review physics-based models that can describe all aspects of the stress-stretch behavior for different rubber-like materials (i.e. softening, hardening, and deformation state dependence).

### 3.2 COMPREHENSIVE PHYSICS-BASED MODELS OF ELASTICITY

The elasticity models reviewed thus far in this chapter are limited in scope to either certain materials (e.g. the 8-chain model) or to intermediate deformations



(e.g. the nonaffine tube model). To fit data for large deformations of different materials, a model must be able to capture strain softening, finite extensibility effects, and deformation state dependence. Mathematically, a minimum of 3 adjustable parameters is needed in order to perform this function: one parameter is needed for the initial modulus, one for softening, and one for limiting extensibility. The deformation state dependence is a consequence of the incompressibility of rubbery-like materials and therefore can be embedded in a model.

In this section we review physics-based models that are able to capture large deformation stress-stretch behavior for many different materials. The models reviewed in this section include the Edwards and Vilgis slip-link [11], Kaliske and Heinrich extended tube [12], Meissner and Matejka ABGI [13], and Miehe micro-sphere [14] models. Note that other models exist in the literature which can capture general nonlinear elastic behavior (e.g. the Ogden model [67]); here we focus only on models with physically-motivated derivations. The slip-link, extended tube, and ABGI models have 4 parameters, and the micro-sphere model has 5. Although physics-based, these models are not in a form where the molecular contribution to macroscopic material response can be easily identified and systematically analyzed. The micro-sphere, extended tube, and ABGI models all contain empirical fit parameters, and the slip-link model contains the parameter  $\eta$ , which has a difficult interpretation in terms of molecular quantities. In addition, the slip-link model does not use the theoretically rigorous Langevin probability function. An overall goal of the work in this dissertation is to relate the microscopic properties and processes in crosslinked polymer materials to the macroscopic mechanical behavior. There are many reasons for forming models that make this connection; these include facilitating the development of new materials, being able to understand and optimize multi-physics phenomena (e.g. electroactive polymers), and constructing a robust modeling framework for the observed nonlinear rate, time and temperature dependent properties. These factors motivate the development of the nonaffine network model in the following chapter. Nonetheless, the four models reviewed in this section are able to fit stress-stretch data for many different rubber-like materials. This is demonstrated by applying these models

to stress-stretch data , including natural rubber [1], silicone rubber [8], VHB 4905 [9], and b186 rubber [10].

The following is a brief summary of each model:

- The **Edwards and Vilgis slip-link model** [11] derives a free energy function by considering the primitive path to be the relevant length scale for microscopic deformation. The primitive path length is assumed to increase affinely with the magnitude of the applied deformation. This model has 4 parameters:  $G_c^{SL}$ ,  $G_e^{SL}$ ,  $\alpha$ , and  $\eta$ . The free energy density is

$$\begin{aligned}
 W^{SL} = & \\
 & \frac{1}{2} G_c^{SL} \left[ \frac{(1 - \alpha^2) \sum_j \lambda_j^2}{1 - \alpha^2 \sum_j \lambda_j^2} + \ln \left[ 1 - \alpha^2 \sum_j \lambda_j^2 \right] \right] \\
 & + \frac{1}{2} G_e^{SL} \left[ \sum_i \left( \frac{\lambda_i^2 (1 + \eta) (1 - \alpha^2)}{(1 + \eta \lambda_i^2) (1 - \alpha^2 \sum_j \lambda_j^2)} + \ln \left[ 1 + \eta \lambda_i^2 \right] \right) \right. \\
 & \left. + \ln \left[ 1 - \alpha^2 \sum_j \lambda_j^2 \right] \right], \quad (80)
 \end{aligned}$$

where the first term is due to crosslinks and the second term is due to entanglements. The parameter  $\eta$  is a measure of entanglement slip, and may be given a theoretical estimate of  $\eta \approx 0.2$  [68]. The other parameters are defined in terms of molecular quantities according to

$$G_c^{SL} = \frac{kT\rho_m}{N}, \quad (81a)$$

$$G_e^{SL} = \frac{kT\rho_m}{N_e}, \quad (81b)$$

$$\alpha = \frac{L_{pp}}{Nb}. \quad (81c)$$

$G_c^{SL}$  and  $G_e^{SL}$  are modulus-like parameters,  $L_{pp}$  is the undeformed primitive path length, and  $\alpha$  is the finite extensibility parameter. With this definition of  $\alpha$  finite extensibility effects occur when the ‘slack’ inside each step of the primitive path is used up. This happens when the de-

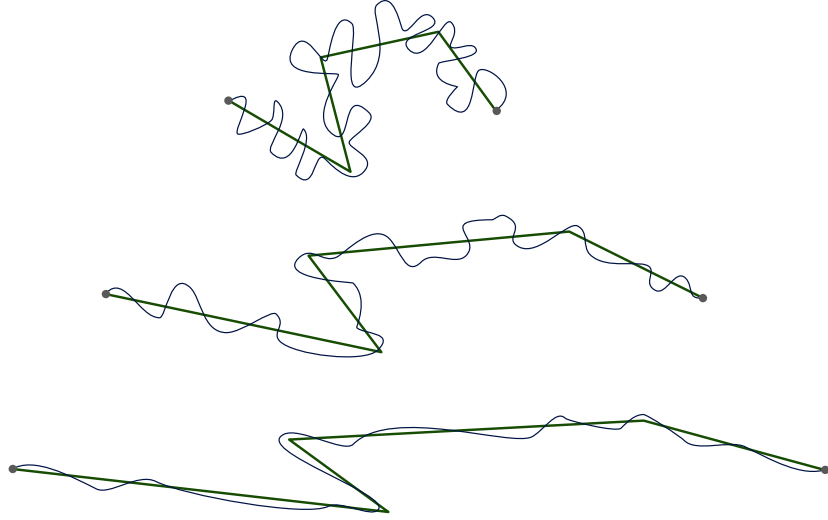


Figure 29: In the Edwards and Vilgis [11] slip-link model, deformation is transferred to an individual chain (curved lines) through a deformation of the primitive path (straight lines). Finite extensibility occurs when the primitive path length equals the contour length of the chain. This is a different physical mechanism for finite extensibility effects than the other models in this section, which consider limiting chain extensibility when the chain end-to-end distance equals the contour length. The slip-link model definition of  $\alpha$ , the limiting extensibility parameter, will be used in Chapter 7 to analyze trends in limiting extensibility for different simulated polymer networks.

formed length of the primitive path of the chain reaches the contour length of the chain. A schematic of this physical representation is shown in Figure 29. The slip-link model definition of  $\alpha$ , the limiting extensibility parameter, will be used in Chapter 7 to analyze trends in limiting extensibility for different simulated polymer networks.

- The **Kaliske and Heinrich extended tube model** [12] contains a similar network contribution to stress as the slip-link model but uses a simpler form for the intermolecular contribution. This model contains a scaling parameter,  $\gamma$ , relating deformation of the tube to the macro deformation.  $\gamma$  has a theoretically expected range of  $0 \leq \gamma \leq 1$ .  $\delta$ , the finite extensibility parameter, is related to  $\alpha$  in the slip-link model [11] and is motivated by the same physical description. In total, the model has 4 parameters:  $G_c^{ET}$ ,  $G_e^{ET}$ ,  $\delta$ , and  $\gamma$ . The two moduli parameters are given a detailed relation to

molecular quantities in Ref. [12]. The free energy density in the extended tube model is

$$W^{\text{ET}} = \frac{1}{2} G_c^{\text{ET}} \left( \frac{(1 - \delta^2) (\sum_j \lambda_j^2 - 3)}{1 - \delta^2 (\sum_j \lambda_j^2 - 3)} + \ln [1 - \delta^2 (\sum_j \lambda_j^2 - 3)] \right) + 2G_e^{\text{ET}} \frac{1}{\gamma^2} \sum_j \lambda_j^{-\gamma}. \quad (82)$$

- The **Meissner and Matejka ABGI model** [13] is a sum of the Arruda and Boyce 8-chain model [8] plus the “generalized invariant” of the extended tube model for the intermolecular contribution (hence the name ABGI). The 4 parameters of the ABGI model are  $G_c^{\text{ABGI}} = kT\rho_m/N$ ,  $N$ ,  $G_e^{\text{ABGI}}$ , and  $\gamma$ . This model was presented by defining the Cauchy stresses in the principal directions:

$$\sigma_i^{\text{ABGI}} = G_c^{\text{ABGI}} \lambda_i^2 \frac{1}{3} \left( \frac{\sum_j \lambda_j^2 - 9N}{\sum_j \lambda_j^2 - 3N} \right) - \frac{2G_e^{\text{ABGI}} \lambda_i^{-\gamma}}{\gamma} + p. \quad (83)$$

Meissner and Matejka [13] also introduce the ABGIL model; this model uses the concept of a strain-dependent finite extensibility and has a total of 7 parameters; however, the additional parameters do not have direct physical meaning so it is not discussed further here.

- The **Miehe micro-sphere model** [14] micro-sphere model is based on an average over chains with ends located on the surface of a unit sphere. This model does not have a closed analytical form. Conceptually, the free energy density is determined as

$$W^{\text{MS}} = -G_c^{\text{MS}} \ln \left[ \Psi_L \left( \left[ \frac{1}{4\pi} \int \left( \frac{|\mathbf{X}|}{|\mathbf{X}_0|} \right)^p dA \right]^{1/p} \right) \right] + G_c^{\text{MS}} N U \frac{1}{4\pi} \int \bar{v}^q(\mathbf{X}_0) dA, \quad (84)$$

where  $G_c^{\text{MS}} = kT\rho_m/N$  is a modulus-like parameter,  $N$  defines finite extensibility,  $U$  is the tube geometry parameter, and  $p$  and  $q$  are micro-macro averaging parameters (there are 5 parameters total). In this equa-

tion, the Langevin probability function is evaluated at a value of chain stretch determined by taking the  $p$ -root average of a deformed vector over all initial configurations.  $p = 2$  leads to an analytical result and gives a network contribution to stress mathematically equivalent to Eq. 105.  $\bar{v}(\mathbf{X}_0)$  is the affine area stretch of an element with initial vector  $\mathbf{X}_0$  in the undeformed configuration. The integration is performed over the surface area of a unit sphere and must be evaluated numerically. Therefore, calculating the stress involves several additional steps; these are detailed in Table 3 of Ref. [14].

The ability of the slip-link, extended tube, ABGI, and micro-sphere models to fit stress-stretch is demonstrated by fitting to the data sets for natural rubber [1],<sup>10</sup> VHB [9], and b186 rubber [10]. These fits are shown in Figure 30, and the best fit parameters are in Table 1. Best fit parameters were determined using the least-square Markov chain Monte Carlo method detailed in Appendix A. Each models is able to capture the stress-stretch behavior for these different materials, and therefore their best-fit curves are nearly indistinguishable. The only difference noticeable to the eye is for the slip-link model fit to b186 rubber in Figure 30d (the slip-link model fit is not quite as good as the others).

Although the models reviewed in this section can fit these data sets, they are not in a form where the molecular contribution to macroscopic material response can be systematically analyzed. The Meissner and Matejka [13] ABGI model adds an empirical term with two additional parameters to the strain energy density of the 8-chain model [8] in order to capture softening. This allows the model to capture the mechanical behavior of materials that display strain softening, but the added fit parameter is not related to molecular quantities. The softening term added to the ABGI model [13] was taken from the Kaliske and Heinrich [12] extended tube model; this model has 4 parameters and can also capture softening, hardening, and deformation state dependence, but contains the same fit parameter which does not have a molecular connection. The Edwards and Vilgis [11] slip-link model contains 4 parameters which can all be connected to molecular quantities; however,

<sup>10</sup> The Treloar [1] data also includes pure shear deformation; this data has been omitted in Figure 30 for clarity of presentation. The pure shear boundary condition leads to a stress-stretch curve close to the uniaxial curve, and all of the models here fit this additional part of the data as well.

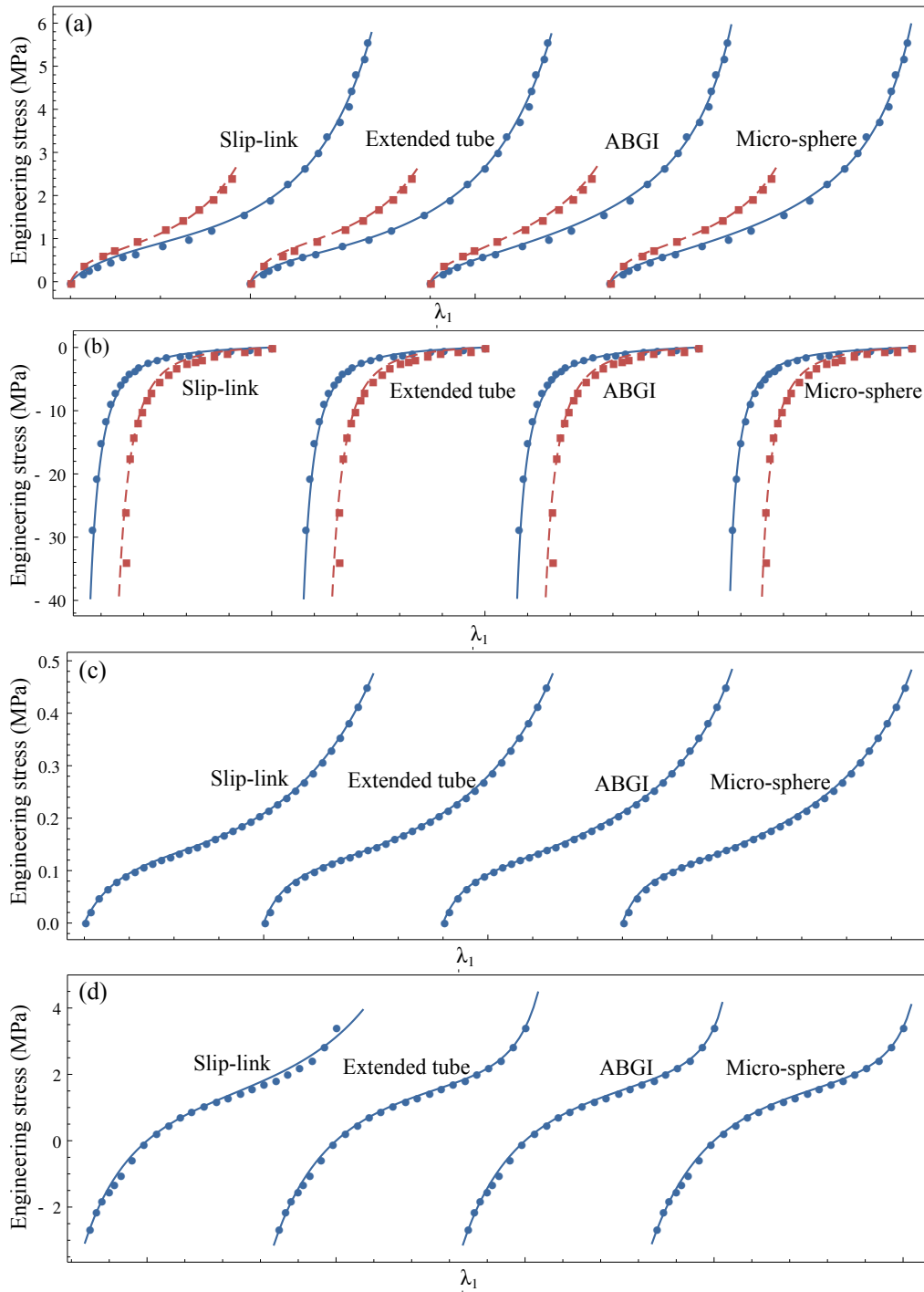


Figure 30: The slip-link [11], extended tube [12], ABGI [13], and micro-sphere [14] models applied to (a) vulcanized natural rubber [1], including uniaxial (blue circles) and biaxial (red squares) data, (b) silicone rubber [8], including uniaxial (blue circles) and pure shear (red squares) data, (c) VHB 4905 uniaxial data [9], and (d) b186 rubber uniaxial data [10]. The curves are shifted on the x-axis in order to display all on a single plot: the shift in (a) and (c) is a stretch of 4, and the shift in (b) and (d) is a stretch of 1 for each curve.

(a) Natural rubber fit parameters

Model	Parameters
Slip-link	$G_c^{SL} = 0.14, G_e^{SL} = 0.22, \alpha = 0.093, \eta = 0.045$
Extended tube	$G_c^{ET} = 0.20, G_e^{ET} = 0.17, \delta = 0.093, \gamma = 0.24$
ABGI	$G_c^{ABGI} = 0.26, G_e^{ABGI} = 0.046, N = 26, \gamma = -1.0$
Micro-sphere	$G_c^{MS} = 0.27, N = 24, U = 0.11, p = 1.7, q = 0.45$

(b) Silicone rubber fit parameters

Model	Parameters
Slip-link	$G_c^{SL} = 0.34, G_e^{SL} = 0.047, \alpha = 0.16, \eta = 0.0007$
Extended tube	$G_c^{ET} = 0.46, G_e^{ET} = 0.0016, \delta = 0.17, \gamma = 0.13$
ABGI	$G_c^{ABGI} = 0.43, G_e^{ABGI} = 0.0022, N = 7.1, \gamma = -0.17$
Micro-sphere	$G_c^{MS} = 0.32, N = 6.8, U = 0.011, p = 3.4, q = 0.12$

(c) VHB fit parameters

Model	Parameters
Slip-link	$G_c^{SL} = 0.021, G_e^{SL} = 0.046, \alpha = 0.081, \eta = 0.072$
Extended tube	$G_c^{ET} = 0.023, G_e^{ET} = 0.053, \delta = 0.084, \gamma = 0.059$
ABGI	$G_c^{ABGI} = 0.027, G_e^{ABGI} = 0.045, N = 29, \gamma = 0.51$
Micro-sphere	$G_c^{MS} = 0.022, N = 38, U = 0.19, p = 3.7, q = 1.1$

(d) b186 rubber fit parameters

Model	Parameters
Slip-link	$G_c^{SL} = 0.00079, G_e^{SL} = 2.5, \alpha = 0.30, \eta = 0.79$
Extended tube	$G_c^{ET} = 0.30, G_e^{ET} = 1.6, \delta = 0.54, \gamma = 0.12$
ABGI	$G_c^{ABGI} = 0.18, G_e^{ABGI} = 1.4, N = 1.9, \gamma = -0.39$
Micro-sphere	$G_c^{MS} = 0.18, N = 2.5, U = 49, p = 5.4, q = 0.27$

Table 1: Best fit parameters for the slip-link [11], extended tube [12], ABGI [13], and micro-sphere [14] models applied to (a) vulcanized natural rubber [1], (b) silicone rubber [8], (c) VHB 4905 uniaxial data [9], and (d) b186 rubber uniaxial data [10].

its form is more mathematically complicated than other approaches and it is often not included with other large deformation constitutive models (for example, it was not considered in the review and comparisons by Boyce and Arruda [66] and Marckmann and Verron [69]). The slip-link model parameter  $\eta$  also has a difficult interpretation in terms of molecular quantities. The Miehe et al. [14] micro-sphere model does not have an analytical form and contains two micro-macro averaging parameters  $p$  and  $q$  which do not have a direct physical connection.

One of the underlying goals of the work in this dissertation is to relate microscopic properties and processes in crosslinked polymers to the macroscopic elastic behavior. To do this requires a model that is not only sufficiently general so that it can capture all relevant macroscopic behavior (softening, hardening, deformation-state dependence, etc.), but also has parameters defined solely in terms of molecular parameters. The latter makes it possible to systematically evaluate modeling assumptions to determine microscopic mechanisms responsible for observed macroscopic behavior. To facilitate such a comparison, it is ideal to be able to describe a wide range of mechanical behavior with a minimum number of parameters. The models reviewed in this section contain 4 or more parameters; however, 3 is the minimum number of parameters required to describe generalized mechanical behavior of a rubber-like material. The model developed in the next chapter is able to describe general elastic behavior with only 3 parameters.



## CHAPTER 4

### A NONAFFINE NETWORK MODEL FOR THE LARGE DEFORMATION MECHANICAL RESPONSE OF ELASTOMERS

---

In this chapter we develop a new physics-based model of large deformation elasticity that has parameters related to micro-scale deformation mechanisms and the observable softening and hardening in the stress-stretch curve. This new model is able to capture the mechanical behavior of rubbery elastic materials with only 3 parameters; this is fewer than the other large-stretch constitutive models reviewed in Section 3.2, which contain at least 4 parameters. Additionally, since all of the parameters of the model are related to polymer network characteristics and chain behavior, the assumptions about chain behavior and the predictions of the model for material properties can be analyzed by testing polymer networks of known structure. In polymer physics, it is desired to make this micro-macro connection in order to form robust models for nonlinear materials properties, understand and optimize for multi-physics phenomena, and develop new materials. The coarse-grained molecular dynamics simulations of Chapters 5-7 will be used to test the description put forward by the model of this chapter, and the model will also be used to interpret simulation results for micro-macro deformation and mechanical properties.

The new model contains a factor representing general nonaffine deformation of chain end-to-end distances. Although nonaffine chain deformation has been suggested by small angle neutron scattering [58] and nuclear magnetic resonance spectroscopy [70], there is still no consensus on how this behavior changes for different materials. The model derived in this chapter will be used

to quantify nonaffine chain deformation for simulated polymer networks in Chapter 6.

In the last chapter, we reviewed the Rubinstein and Panyukov nonaffine tube model [5, 6]. This model includes considerations of both chain deformation and suppression of monomer fluctuations (via the ‘tube’ concept); however, since it uses Gaussian statistics, it cannot describe material response at large deformations where the material exhibits strain hardening and limiting extensibility effects (see Figure 27). In addition to the nonaffine tube [5, 6] and phantom network [53] models discussed in Chapter 3, other physics-based models have been derived from considerations of the structure and interactions of the chains in the polymer network, but cannot capture strain hardening at large extensions. These descriptions include the constrained-junction [71, 72], diffused constraint [73], and tube [30, 33] models in several different forms (constant tube dimensions [30], constant tube volume [74, 75], affine deformation of the mean-square magnitude of monomer fluctuations [6, 62], double tube [76], and slip-tube [5]), and more recently the phonon fluctuation model [77, 78].

Large deformation constitutive models with physically motivated derivations were reviewed in Sections 3.1-3.2. These included the Wang and Guth [7] 3-chain, Arruda and Boyce [8] 8-chain, Edwards and Vilgis slip-link [11], Kaliske and Heinrich extended tube [12], Meissner and Matejka ABGI [13], and Miehe micro-sphere [14] models. However, it was noted that these models are in general limited to certain classes of polymer materials (e.g. heavily crosslinked) or contain parameters that are difficult to identify with the mechanical response or the underlying physics. The micro-sphere, extended tube, and ABGI models all contain empirical fit parameters, and the slip-link model contains the parameter  $\eta$ , which has a difficult interpretation in terms of molecular quantities. In addition, the slip-link model does not use the theoretically rigorous Langevin probability function. The strain energy functions and parameter definitions of these models were presented and discussed in Sections 3.1-3.2.

The model derived in this chapter is a generalization of Rubinstein and Panyukov’s nonaffine tube model [5, 6] to include large deformation limiting extensibility of the polymer chains as well as general nonaffine microscopic

chain deformations. The model is derived in Section 4.1. Model fits to data for natural rubber, silicone rubber, VHB 4905 (polyacrylate rubber), and b186 rubber (a carbon black-filled rubber) are presented in Section 4.2. This experimental data analysis demonstrates the model's performance in describing rubber materials with a wide range of properties. A discussion of the model results is given in Section 4.3, and conclusions from this chapter are presented in Section 4.4.

#### 4.1 MODEL DEVELOPMENT

The derivation of the model in this section is driven by two insights. These are reflected in the underlying process of the derivation:

- The Rubinstein and Panyukov [5, 6] nonaffine tube model is able to capture strain softening, and the Arruda and Boyce [8] 8-chain model can capture strain hardening. Both of these models have simple mathematical forms and only two parameters. It was anticipated that combining aspects of these two models would lead to a simple 3-parameter model able to capture softening, hardening, and deformation state dependence.
- Although the deformation of individual chains in a network is expected to be nonaffine, this behavior may differ significantly from the phantom network model. Computer simulations may be used to directly measure the affineness of chain deformation and compare with model results. A model containing a formalism for general nonaffine chain deformation can therefore make testable predictions about chain behavior and how it affects mechanical properties. A descriptive representation of nonaffine chain deformation (i.e. one that does not predict a specific value for the affineness) will facilitate a comparison with simulations.

In this model the polymer network is represented as a sum of crosslinked and entangled components. The proposed microscopic model representation is shown in Figure 31. The decomposition into crosslinked and entangled components is done following Rubinstein and Panyukov [5, 6] (see Figure 22 of Chapter 3). The difference in the new model and the nonaffine tube model is the representation of chain behavior in the network component (Figure 31a).

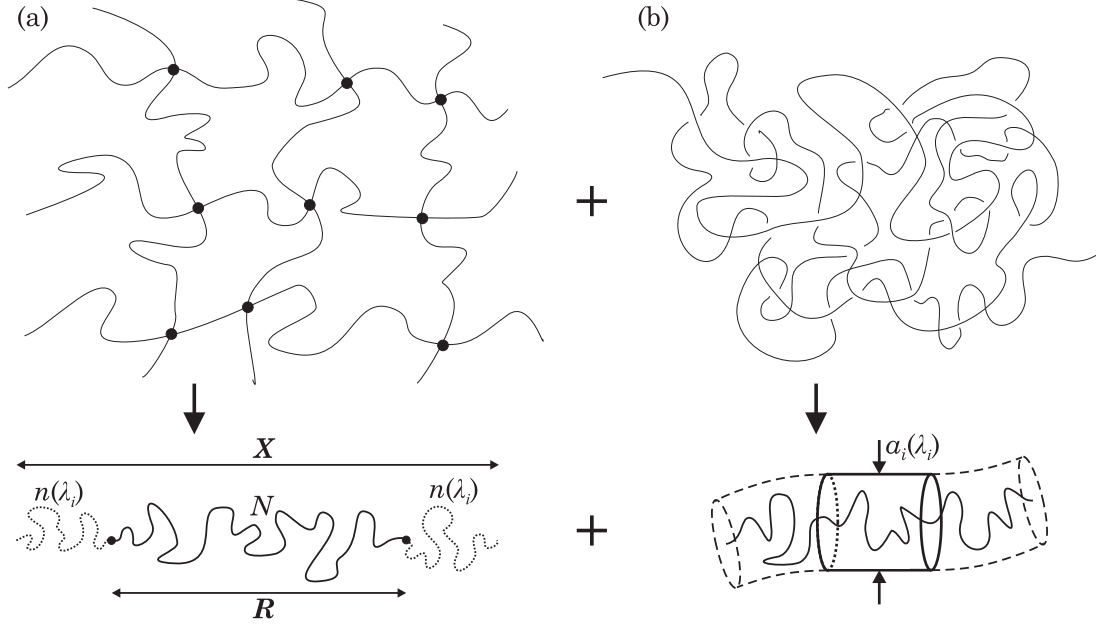


Figure 31: A schematic of the polymer network model, represented as a sum of (a) crosslinked and (b) entangled components. Each is then mapped onto a single chain description to determine the stress.

The nonaffine tube model assumed phantom network behavior with Gaussian chain statistics; here we will use Langevin statistics and include a factor which represents general nonaffine chain deformation. The free energy density of the new model consists of contributions from network and tube components:

$$W = W^{\text{net}} + W^{\text{tube}}. \quad (85)$$

$W^{\text{net}}$  is the free energy due to changes in the end-to-end distance of chains connected between crosslinks in the network and is modeled by an un-entangled crosslinked network (Figure 31a).<sup>1</sup>  $W^{\text{tube}}$  is the free energy due to changes in the magnitude of thermal monomer fluctuations and is modeled via the entangled network shown in Figure 31b.

For large deformations, we generalize the Rubinstein and Panyukov [5, 6] single chain description of the phantom network model that was previously shown in Figure 20. The new form, shown in Figure 31a, allows for deviations from phantom network behavior by defining the length of the effective chains

<sup>1</sup> The ends of the chains in the crosslinked component may still fluctuate, but the magnitude of the fluctuations of the chain ends is taken to be constant.

to be a function of the applied stretch. The two effective chains of length  $n(\lambda_i)$  represent network structure and connectivity, and their properties determine the magnitude of the applied stretch transferred to the test chain. With this, Eq. 36 is rewritten as

$$\langle R_i \rangle = \frac{N}{N + 2n(\lambda_i)} X_i. \quad (86)$$

For an isotropic material, the invariance of properties with respect to rotations of the coordinate system makes it reasonable to assume that the effective chains can be represented as having no directional dependence in the undeformed state. This assumption is then extended to deformed state, i.e. the number of monomers in the effective chains is the same in all directions when the system is deformed.<sup>2</sup> To formalize this, recall the definition of the normalized first invariant from Eq. 77:

$$\Lambda = \sqrt{\frac{\lambda_1^2 + \lambda_2^2 + \lambda_3^2}{3}}.$$

If there is no directional dependence, the number of monomers in the effective chains is written as only a function of the normalized first invariant:  $n = n(\Lambda)$ . In the undeformed state there are  $n(1)$  monomers in the effective chains. For phantom network behavior,  $n(\Lambda) = n(1) = n_p$ , where  $n_p$  the number of monomers in the effective chains for the phantom network model and is given in Eq. 41. However, in general,  $n(1)$  may differ from  $n_p$ .

In the combined chain representation, the vector  $\mathbf{X}$  shown in Figure 31a is coupled directly to the applied deformation and deforms affinely. The undeformed end-to-end length of this vector is

$$|\mathbf{X}_0| = b\sqrt{N + 2n(1)}. \quad (87)$$

---

<sup>2</sup> Strictly, macroscopic isotropy does not imply isotropy at the level of individual chains. An alternative wording would say that the *average* length of the effective chains, averaged over a suitably large ensemble of chains with end-to-end vectors in the same direction, does not have a directional dependence. The agreement of the angular dependence of end-to-end lengths in Section 6.3 with that of a deformed ellipsoid suggests that the description of the effective chains having no angular dependence is an accurate representation of chain end-to-end deformation.

By aligning the coordinate system with the principal axes of the applied deformation, the vector  $\mathbf{X}$  deforms affinely according to  $X_i = \lambda_i |\mathbf{X}_0| / \sqrt{3}$ . With this, the average chain deformation is

$$\begin{aligned}
\langle R_i \rangle &= \left( \frac{N \sqrt{N + 2n(1)}}{N + 2n(\Lambda)} \right) \frac{b}{\sqrt{3}} \lambda_i \\
&= \underbrace{\left( \frac{\sqrt{N + 2n_p} \sqrt{N + 2n(1)}}{N + 2n(\Lambda)} \right)}_{g(\Lambda)} \underbrace{\sqrt{\frac{N}{N + 2n_p}}}_{\sqrt{1-2/\phi}} \frac{b\sqrt{N}}{\sqrt{3}} \lambda_i \\
&= g(\Lambda) \sqrt{1 - 2/\phi} \frac{b\sqrt{N}}{\sqrt{3}} \lambda_i.
\end{aligned} \tag{88}$$

where the expression for  $n_p$  from Eq. 41 is used, and the non-phantom factor  $g(\Lambda)$  has been defined. Phantom network deformation ( $n(\Lambda) = n(1) = n_p$ ) is represented by  $g(\Lambda) = 1$ , and affine network deformation ( $n(\Lambda) = n(1) = 0$ ) by  $g(\Lambda) = (1 - 2/\phi)^{-1/2}$ . This function may therefore be used to interpolate between phantom and affine network behavior in the range  $1 \leq g(\Lambda) \leq (1 - 2/\phi)^{-1/2}$ . The mean-square end-to-end chain length is

$$\langle R_i^2 \rangle = \langle R_i \rangle^2 + \langle \Delta R_i^2 \rangle, \tag{89}$$

where  $\langle R_i \rangle$  is given in Eq. 88, and  $\langle \Delta R_i^2 \rangle$  is the mean-square magnitude of fluctuations of end-to-end length. In the phantom network model, the magnitude of fluctuations of end-to-end length is constant with deformation. Here, we retain this treatment of constant fluctuations of end-to-end length since deformation-dependent monomer fluctuations are treated in the tube component of stress. The mean-square magnitude of fluctuations in direction  $i$  is a constant that is chosen so that the mean-square undeformed end-to-end length in direction  $i$  follows Gaussian statistics (i.e.  $\langle R_i(1)^2 \rangle = b^2 N / 3$ ). This leads to

$$\begin{aligned}
\langle \Delta R_i^2 \rangle &= \underbrace{1 - g(1)^2 (1 - 2/\phi)}_K \frac{b^2 N}{3} \\
&= K \frac{b^2 N}{3},
\end{aligned} \tag{90}$$

where  $K$  is a constant. For phantom network behavior,  $g(1) = 1$  and  $K = 2/\phi$  (see Eq. 40). In the derivation here,  $K$  will be used for ease of notation. Using Eqs. 88 and 90, the mean-square end-to-end chain length is

$$\langle R_i^2 \rangle = g(\Lambda)^2(1 - 2/\phi)\frac{b^2N}{3}\lambda_i^2 + \frac{K}{3}b^2N, \quad (91)$$

Summing over the three principal directions and noting that all chains in the network have the same behavior in the single-chain representation, the mean-square end-to-end length is

$$\overline{\langle R^2 \rangle} = b^2N \left[ g(\Lambda)^2(1 - 2/\phi)\Lambda^2 + K \right] \quad (92)$$

The free energy density of the network component is determined using Langevin statistics:

$$W^{\text{net}} = -\frac{kT\rho_m}{N} \overline{\langle \ln \Psi_L(\mathbf{R}) \rangle}, \quad (93)$$

where the Langevin probability function  $\Psi_L(\mathbf{R})$  is given in Eq. 20. The thermal average  $\langle \cdot \rangle$  and the ensemble average (denoted by the overbar) in Eq. 93 must be addressed in order to determine the free energy. To proceed with this calculation, it is assumed that the average free energy of the chains can be well approximated by the free energy of a chain whose length is given by the mean-square calculation in Eq. 92. This assumption enables us to use Eq. 92 in a simple calculation of the free energy. To employ this treatment in the calculation, first let

$$R^* = \frac{\sqrt{\overline{\langle R^2 \rangle}}}{Nb}. \quad (94)$$

This represents the extension of a chain relative to its contour length, with the value of  $\overline{\langle R^2 \rangle}$  given in Eq. 92. The free energy is now written as

$$W^{\text{net}} = \rho_m kT \left[ R^* \beta(R^*) + \ln \frac{\beta(R^*)}{\sinh \beta(R^*)} \right]. \quad (95)$$

The stress is determined using Eq. 29:

$$\begin{aligned}\sigma_i^{\text{net}} &= \lambda_i \frac{\partial W^{\text{net}}}{\partial \lambda_i} + p^{\text{net}} \\ &= \lambda_i \frac{\partial W^{\text{net}}}{\partial R^*} \frac{\partial R^*}{\partial \lambda_i} + p^{\text{net}},\end{aligned}\quad (96)$$

where the derivatives are calculated to be

$$\begin{aligned}\frac{\partial W^{\text{net}}}{\partial R^*} &= \rho_m kT \beta(R^*) \\ \frac{\partial R^*}{\partial \lambda_i} &= \lambda_i \frac{g(\Lambda)^2 (1 - 2/\phi)}{3NR^*} \left( 1 + \frac{\Lambda}{g(\Lambda)} \frac{\partial g(\Lambda)}{\partial \Lambda} \right).\end{aligned}$$

To simplify, we assume that changes in mean-square end-to-end length are proportional to  $\Lambda^2$ , which leads to  $g(\Lambda) = g = \text{const.}$  We will test this assumption in Chapter 6 by tracking chain deformation in a simulated polymer network during a molecular dynamics simulation; these results show that it does indeed hold for different simulated networks. With this, the network stress is written as

$$\sigma_i^{\text{net}} = \frac{\rho_m kT}{N} g^2 (1 - 2/\phi) \lambda_i^2 \left( \frac{\beta(R^*)}{3R^*} \right) + p^{\text{net}}. \quad (97)$$

Using the Padé approximation to the inverse Langevin function [51] (Eq. 21),

$$\frac{\beta(R^*)}{3R^*} \approx \frac{1}{3} \left( \frac{(R^*)^2 - 3}{(R^*)^2 - 1} \right). \quad (98)$$

For  $R^* \ll 1$  (i.e. the root-mean-square end-to-end length is much smaller than the contour length  $Nb$ ), this can be simplified further to

$$\left( \frac{\beta(R^*)}{3R^*} \right)_{R^* \ll 1} \approx 1. \quad (99)$$

In this small deformation limit the network stress is

$$\sigma_i^{\text{net}} = \frac{\rho_m kT}{N} g^2 (1 - 2/\phi) \lambda_i^2 + p^{\text{net}}. \quad (100)$$



In analogy with Eq. 71, the network shear modulus parameter is identified to be

$$G_c = \frac{kT\rho_m}{N} g^2 (1 - 2/\phi). \quad (101)$$

Using this along with Eqs. 94 and 98 to rewrite Eq. 97 leads to

$$\sigma_i^{\text{net}} = G_c \lambda_i^2 \frac{1}{3} \left( \frac{g^2(1 - 2/\phi)\Lambda^2 + K - 3N}{g^2(1 - 2/\phi)\Lambda^2 + K - N} \right) + p^{\text{net}}. \quad (102)$$

From this, we define the limiting extensibility parameter  $\lambda_{\text{max}}$  as the value of  $\Lambda$  where  $\sigma_i^{\text{net}} \rightarrow \infty$ . This occurs when

$$g^2(1 - 2/\phi)\Lambda^2 + K - N = 0. \quad (103)$$

Setting  $\Lambda = \lambda_{\text{max}}$  in Eq. 103 and solving yields

$$\begin{aligned} \lambda_{\text{max}} &= \frac{1}{g} \sqrt{\frac{N - K}{1 - 2/\phi}} \\ &\approx \frac{1}{g} \sqrt{\frac{N}{1 - 2/\phi}}. \end{aligned} \quad (104)$$

The second line in Eq. 104 can be used to define  $\lambda_{\text{max}}$  since  $K < 1$ , and therefore  $N \gg K$  is expected, if the numbers of monomers per chain is known. With the parameter definitions in Eqs. 101 and 104 the network stress is expressed as

$$\sigma_i^{\text{net}} = G_c \lambda_i^2 \frac{1}{3} \left( \frac{\Lambda^2 - 3\lambda_{\text{max}}^2}{\Lambda^2 - \lambda_{\text{max}}^2} \right) + p^{\text{net}}, \quad (105)$$

The shear modulus is  $G_c$ , and  $\lambda_{\text{max}}$  sets the onset of limiting extensibility effects. Both of the parameter definitions contain the factor  $g$ : phantom deformation of chains is represented by  $g = 1$ , and affine deformation by  $g = (1 - 2/\phi)^{-1/2}$ . If the chain lengths as a function of deformation are known, Eq. 92 may be used to determine  $g$  and establish a rigorous evaluation of this theory. We perform this analysis in Chapters 6 and 7 using molecular dynamics simulation results. However, in practice, the molecular quantities  $N$ ,  $\phi$ , and  $\rho_m$  are not always known, and the determination of the molecular kinematics to calculate  $g$  is a

difficult experimental task. The parameters  $G_c$  and  $\lambda_{\max}$  are then determined by fitting to macroscopic stress-stretch data. This point is discussed further in Section 4.3.

Eq. 105 is identical in mathematical form to the Arruda and Boyce [8] 8-chain model but with the parameters modified to account for the nonaffine deformation of chains. This can be seen by comparing Eq. 105 with Eq. 78. The shear modulus for the 8-chain model was defined in Eq. 76 to be  $G = \rho_m kT/N$ . The network shear modulus in the new model differs from this by the inclusion of nonaffine deformation (the factor  $g^2(1 - 2/\phi)$  in Eq. 101). Similarly, limiting extensibility occurs in the 8-chain model when  $\Lambda^2 \rightarrow N$ , but in the new model,  $\lambda_{\max}$  defined in Eq. 104 predicts that limiting extensibility occurs when  $\Lambda^2 \rightarrow N/(g(1 - 2/\phi))$ . If simply curve-fitting to macroscopic stress-stretch data, these differences are not of interest. However, we wish to determine how individual chain behavior affects mechanical properties. The parameter definitions in Eqs. 101 and 104 provide a framework to test how nonaffine chain deformation affects mechanical properties. Nonaffine chain end-to-end deformation is tracked for different simulated polymer networks in Chapter 6, and significant differences are seen for networks of short, unentangled chains in comparison with networks of long, entangled chains. In Chapter 7 we demonstrate that nonaffine chain deformation is correlated with the shear modulus of simulated polymer networks.

We now turn to the entangled network shown in Figure 31b, which represents the stress due to changes in the magnitude of thermal fluctuations with the applied deformation. We refer to this as the ‘tube’ stress. Since the network stress in Eq. 105 captures limiting extensibility effects, we use Rubinstein and Panyukov’s [5] expression for the tube stress without further modification. This expression was given in Eq. 71 and is repeated here for clarity:

$$\sigma_i^{\text{tube}} = G_e \left( \lambda_i - \frac{1}{\lambda_i} \right) + p^{\text{tube}}. \quad (106)$$

The parameter  $G_e$  is proportional to the density of the entanglements,<sup>3</sup> and is defined to be [5]

$$G_e = \frac{kT\rho_m}{2N_e}, \quad (107)$$

where  $N_e$  is the entanglement length. The quantity  $N_e$  was introduced in Section 2.3; it is a measure of the average number of chain monomers that exist between entanglements. Because it is a measure of entanglements,  $N_e$  can be determined using the primitive path length [25]. The definition of  $N_e$  is discussed further in Chapter 7.

Combining Eqs. 105 and 106 we obtain the final model expression for the principal stresses:

$$\sigma_i = G_c \lambda_i^2 \frac{1}{3} \left( \frac{\sum_j \lambda_j^2 - 9\lambda_{\max}^2}{\sum_j \lambda_j^2 - 3\lambda_{\max}^2} \right) + G_e \left( \lambda_i - \frac{1}{\lambda_i} \right) + p. \quad (108)$$

The strain energy density function corresponding to Eq. 108 is

$$W = \underbrace{\frac{1}{6} G_c \sum_j \lambda_j^2 - G_c \lambda_{\max}^2 \ln \left( 3\lambda_{\max}^2 - \sum_j \lambda_j^2 \right)}_{W^{\text{net}}} + \underbrace{G_e \sum_j \left( \lambda_j + \frac{1}{\lambda_j} \right)}_{W^{\text{tube}}}. \quad (109)$$

In Eq. 109,  $W^{\text{net}}$  was obtained by searching for a free energy expression such that when Eq. 29 is applied, the stress in Eq. 108 is obtained; the mathematical form is therefore simpler than that obtained by simply evaluating Eq. 95.

<sup>3</sup>  $G_e$  is proportional to the density of entanglements and may be identified as the plateau modulus, which can be measured in the melt state before crosslinking. Although it is well accepted that the plateau modulus is proportional to the density of entanglements, the constant of proportionality has been given different values. The factor of 1/2 in the definition of  $G_e$  in Eq. 107 comes from the derivation of the nonaffine tube model in Ref. [5]. Ref. [6] contains a simpler derivation of the nonaffine tube model using scaling arguments, and the definition  $G_e = \rho_m kT/N_e$  is used (i.e. the constant of proportionality is set to 1). Doi and Edwards [33] provide a constant of proportionality of 4/5, and the Rubinstein and Panyukov [5] slip-tube model has a value of 2/7. In addition to this, the entanglement length  $N_e$  is not a well-defined quantify: recent work has defined measures which differentiate the rheological entanglement length and the topological entanglement length [25]. Here, we retain the factor of 1/2 in Eq. 107 for simplicity. In Chapter 7 we use the Hoy et al. [25] modified S-coil measure of rheological entanglement length to compare trends in predicted vs. measured modulus values for different simulated polymer networks.

Unique combinations of the 3 parameters in Eqs. 108 and 109 correspond to different parts of a characteristic macroscopic stress-stretch curve. The initial modulus is the sum of both moduli and therefore varies with both the density of crosslinks and the density of entanglements:  $G_c + G_e$ . The amount of softening is determined by the ratio  $G_e/G_c$ , which varies with the relative density of entanglements to crosslinks. The onset of strain hardening is determined by  $\lambda_{\max}$ , which is defined using the number of monomers in a chain between crosslinks (Eq. 104). The effect of varying  $G_e/G_c$  and  $\lambda_{\max}$ , which define the shape of the stress-stretch curve, is shown in Figure 32 for an applied uniaxial deformation in the 1 direction. Figure 32a shows different softening behaviors. For  $G_e/G_c = 0.1$ , softening effects are hardly noticeable. With  $G_e/G_c = 10$ , the tangent modulus becomes very small for a large region of the stress-stretch curve after the initial deformation. Figure 32b shows different strain hardening behaviors. The response is nearly identical up to  $\lambda_1 \approx 2$ ; after this the different cases start to quickly diverge. All of the example cases in Figure 32 have the same initial modulus but display much different stress-stretch behavior in the large deformation regime.

Figure 33 demonstrates the ability of Eq. 108 to differentiate between different applied deformation states. This is shown by plotting stress predictions under different loading configurations with the parameters set to  $G_e/G_c = 1$  and  $\lambda_{\max} = 4$ . Figures 32 and 33 demonstrate that the form for stress in the new model (Eq. 108) is able to capture the characteristic features of rubber elasticity (softening, hardening, and deformation state dependence) with only 3 parameters. These 3 parameters ( $G_c$ ,  $G_e$ , and  $\lambda_{\max}$ ) are defined in terms of independent combinations of molecular quantities and deformation mechanisms in Eqs. 101, 107, and 104.

## 4.2 EXPERIMENTAL DATA ANALYSIS

In this section we demonstrate that Eq. 108 can be used to fit a wide range of stress-stretch data by presenting fits to large deformation data for natural rubber from Treloar [1], silicone rubber from Arruda and Boyce [8], VHB 4905 (polyacrylate rubber) from Fox and Goulbourne [9], and b186 rubber (a carbon black-filled rubber) from Lulei and Miehe [10]. These data sets are chosen to

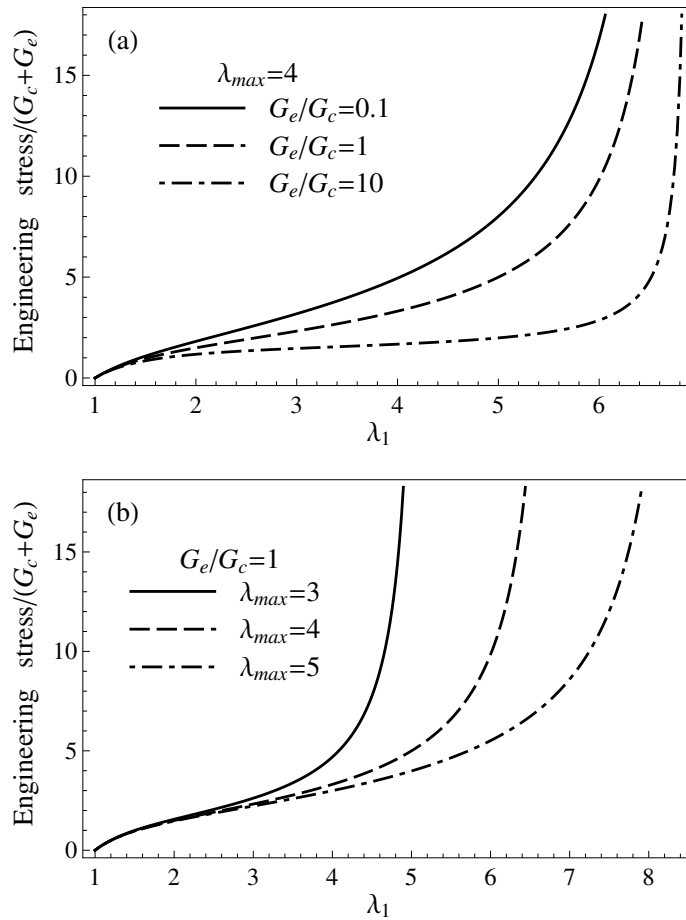


Figure 32: The effect of varying the model parameters on predictions for stress for an applied uniaxial deformation. (a) a range of strain softening behavior, shown by setting  $\lambda_{max} = 4$  and varying the softening ratio  $G_e/G_c$ , (b) different strain hardening behavior, shown by setting  $G_e/G_c = 1$  and varying the hardening parameter  $\lambda_{max}$ .

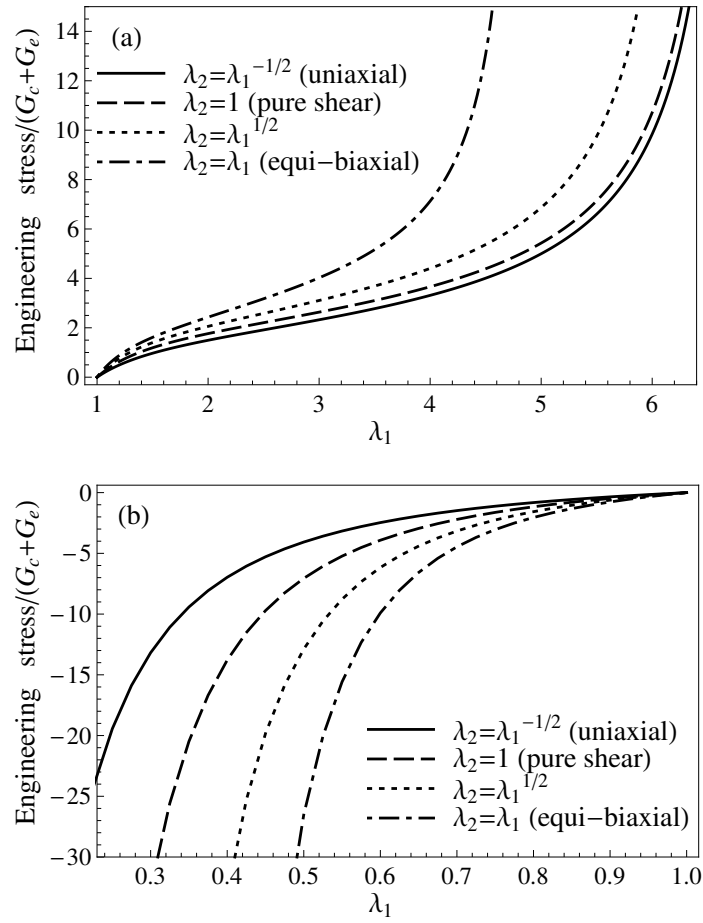


Figure 33: Model predictions for stress with  $G_e/G_c = 1$  and  $\lambda_{\max} = 4$  for different loading conditions in (a) tension, (b) compression.

represent different material loadings and properties. The Treloar [1] data is well accepted as representative of the mechanical properties of rubber and includes uniaxial, pure shear, and biaxial loadings.<sup>4</sup> The Arruda and Boyce [8] data is for the compressive stress of uniaxial and pure shear loadings. VHB 4905 is much softer than the other three rubber materials, and its response in uniaxial tension shows a significant strain softening region. The b186 rubber material is carbon black-filled, shows a large softening region, and has a very sharp upturn in the strain hardening region. Although filler particles were not considered in the model derivation in the previous section, we demonstrate that Eq. 108 may still be used to fit the quasistatic stress-stretch data for this material.

Eq. 108 was fit to the experimental data using a least-squares Markov chain Monte Carlo method, detailed in Appendix A. For the Treloar [1] data, the fit parameters were obtained by using the uniaxial and biaxial deformation states. The fit to the Arruda and Boyce [8] data was obtained using both uniaxial and shear states, and all available data was used for the VHB and b186 rubber fits since these were only uniaxial deformations. Simultaneous fitting to at least two deformation states is required in order to obtain accurate and precise parameter values; the reasons for this are discussed in the next section. By “simultaneous” fitting, it is meant that the residual to be minimized consists of a sum over multiple deformation states. Figure 34 shows the best fit to each large deformation data set. The model is able to accurately capture the strain softening, strain hardening, and difference between deformation states displayed by these different materials. Table 2 lists the best fit parameters for each of these data sets. VHB is the softest, with an initial modulus of only 67 kPa, while b186 rubber is the hardest with a modulus of 1.6 MPa. The softening ratio  $G_e/G_c$  also varies over a large range: silicone rubber has a ratio  $G_e/G_c \approx 0$  while b186 rubber has  $G_e/G_c = 12$ . From the molecular definitions of the model parameters it is reasonable to expect, for example, that the tested samples of natural rubber [1] or VHB 4905 [9] have proportionally

---

<sup>4</sup> The pure shear loading data from [1] was omitted in Chapter 3 for clarity of presentation; only the uniaxial and equi-biaxial deformation states were shown. Fitting uniaxial and equi-biaxial data is the best test of a model, since these states are the most different in terms of boundary conditions Urayama [79]. This is discussed further in the next section. The pure shear data of Treloar [1] is included here for completeness.

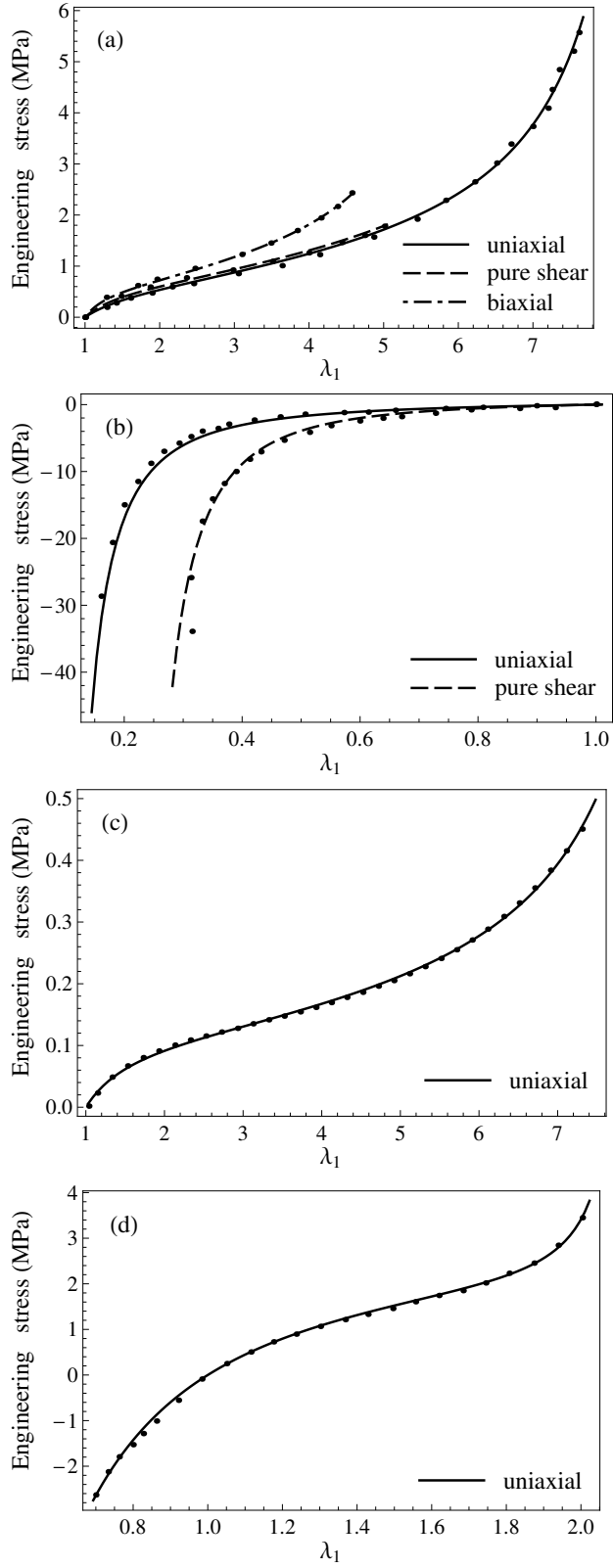


Figure 34: Eq. 108 with the best fit parameters from Table 2 applied to (a) natural rubber [1], (b) silicone rubber [8], (c) VHB 4905 [9], (d) b186 rubber [10].



Data set	$G_c + G_e$ (MPa)	$G_e/G_c$	$\lambda_{\max}$
Natural rubber	0.32	0.31	5.1
Silicone rubber	0.43	0.00089	2.7
VHB 4905	0.067	1.7	5.2
b186 rubber	1.6	12	1.3

Table 2: Best fit parameters for Eq. 108 applied to the different large deformation data sets.

more entanglements in comparison with the silicone rubber tested by Arruda and Boyce [8]. Since b186 rubber is filled with carbon black, a more detailed study would be needed to quantify softening for this material in relation to molecular parameters.

In Section 3.2 we reviewed other physics-based models which are able to fit data for rubber-like materials with different properties, including the experimental data sets considered in this section. These models included the Edwards and Vilgis [11] slip-link, Kaliske and Heinrich [12] extended tube, Meissner and Matejka [13] ABGI, and Miehe et al. [14] micro-sphere models. The slip-link, extended tube, and ABGI models have 4 parameters, and the micro-sphere model has 5 parameters. The data fits in this section demonstrate that the newly proposed model can provide a good fit to the materials shown in Figure 34 with fewer parameters than other physics-based models. Additionally, it is easy to identify all of the new model parameters with observable parts of the stress-stretch curve. To compare, the slip-link, extended tube, and ABGI models each have 2 parameters which influence the softening behavior. In the new model, the softening behavior is determined only the ratio  $G_e/G_c$ . Since the 3 parameters are directly connected to stress-stretch behavior (i.e.  $G_e + G_c$  is the shear modulus,  $G_e/G_c$  represents softening, and  $\lambda_{\max}$  represents limiting extensibility), fitting the new model will result in well-defined best fit parameters. This means that it is likely for only a single “best” combination of parameter values to exist. This is ideal for ease of fitting and for comparing different materials.

In summary, the new model has the following features which differentiate it from other models in the literature:

- Ability to capture large deformation behavior for materials with different properties with only 3 parameters; other models able to fit the same range of data sets have 4 or more parameters.
- The parameters are clearly connected to observable parts of a typical stress-stretch curve:  $G_e + G_c$  is the shear modulus,  $G_e/G_c$  represents softening, and  $\lambda_{\max}$  represents limiting extensibility.
- Each parameter is connected to polymer network characteristics and deformation behavior. In particular, a factor representing general nonaffine deformation of the end-to-end distances of polymer chains is included.

#### 4.3 DISCUSSION OF RESULTS

In the previous section we fit Eq. 108 to data sets for natural rubber [1], silicone rubber [8], VHB 4905 [9], and b186 rubber [10] by simultaneously optimizing best fit parameters to two deformation states (when available). Although some studies have attempted to describe, for example, biaxial data with fit parameters obtained from only a uniaxial test, this cannot be considered as a reliable procedure for all materials. Since elastomers are generally incompressible, only two dimensions of a sample under an applied loading can be varied independently. Using only a uniaxial test is insufficient to differentiate between different theories. For example, both the 3-chain [7] and 8-chain [8] models can fit the uniaxial data for natural rubber [1], but only the 8-chain model can reasonably differentiate between uniaxial and biaxial deformations. The fit of the 3-chain and 8-chain models to this data is shown in Figure 25 of Chapter 3, and is also presented by Arruda and Boyce [8]. Urayama [79] discussed further reasons that multiaxial testing is needed, showing that the full form of the strain energy function cannot be determined by a single uniaxial test. Other work by Kawamura et al. [80] has attempted to experimentally determine a functional form for the strain energy function in terms of the stretch invariants  $I_1$  and  $I_2$  through general biaxial deformations. These studies demonstrate the

need for a biaxial deformation test in order to uniquely determine material parameters. Uniaxial and equi-biaxial deformations are the most different in terms of possible deformation states when considering the relative variation of the stretch invariants  $I_1$  and  $I_2$  [79]. As a result, these two<sup>5</sup> tests may be used together to obtain reliable parameter fit values for Eq. 108. If it is not possible to perform both uniaxial and biaxial tests, then the three fit parameters of the model can still be determined from a single uniaxial test. This will, in general, result in parameter values that are slightly different than the values that are obtained by optimizing to both tests; because of this difference, the model predictions for deformation states other than uniaxial may not be as good. However, since the three parameter combinations  $G_c + G_e$ ,  $G_e/G_c$ , and  $\lambda_{\max}$  each define a certain portion of the stress-stretch curve ( $G_c + G_e$  is the initial modulus,  $G_e/G_c$  determines the extent of the softening region, and  $\lambda_{\max}$  defines the onset of strain hardening), this model performs better than other models with more parameters in terms of the uniqueness of the best fit parameter values.

In Section 4.1 we made several key assumptions in order to obtain a simple form for the stress. These include the decomposition of the network shown in Figure 31, and setting the function representing deviations from phantom behavior to  $g(\Lambda) = \text{const}$ . Using this approach we were able to derive a simple model that captures all the relevant characteristics of elastomeric stress-stretch behavior. Since an individual chain will experience both crosslinked and entangled interactions, a distinct separation of the network into crosslinked and entangled components is an idealization. As previously mentioned, the ‘network’ component of Figure 31 is better described as stress due to changes in thermally averaged chain conformations, and the ‘entangled’ component is better described as stress due to changes in the magnitude of thermal fluctuations with the applied deformation. Therefore, both crosslinks and entanglements will affect each component of the model in some manner. This was discussed by Grest et al. [82] in reference to using the Rubinstein and Panyukov [5, 6] nonaffine tube model to describe results of molecular

---

<sup>5</sup> The requirement of two tests to determine material behavior only applies to isotropic materials, and all of the materials considered in this dissertation are isotropic. For anisotropic materials, an additional test is needed [81].

dynamics simulations, and by Daoulas et al. [83] in using the similar slip-tube model [5] applied to experimental results. Edwards and Vilgis [11] discussed how both crosslinks and entanglements contribute to determining the strain hardening parameter in the derivation of the slip-link model. Because of these factors, the network and entangled components are best described as together forming an “equivalent” representation of a polymer network.

Regardless of whether the microscopic description is correct, we have here shown that the mechanics works. Determining and testing the precise relationship of the microscopic physics to the mechanics is the missing link. The model developed in this work is well suited for comparing chain behavior to macroscopic properties since all its parameters are defined in terms of molecular quantities. Because the network stress in the nonaffine network model derived in this chapter has the same mathematical form as the 8-chain model [8], we note the conceptual differences in the derivations of these two models. Here, the network stress was derived by considering the mean-square end-to-end length of nonaffinely deforming chains in a polymer network. If the chains did not interact, this would lead to an exact form for the stress. However, we noted in this discussion reasons why this treatment is a definite simplification of the real situation. The network chains are therefore best labeled as “equivalent network chains”. Nonetheless, since the model considers the mechanism of nonaffine chain deformation, it provides a framework to test how nonaffine deformation affects mechanical properties. The Arruda and Boyce [8] 8-chain model derives a stress by considering the free energy as an average from the contributions of 8 chains attached at the corners of an affinely-deforming cube. The affine deformations suggest that the model is better described as defining a representative volume element, instead of attempting to average over all microscopic degrees of freedom. The 8-chain model replaces the real network of interacting, nonaffinely deforming chains with an equivalent network of 8 non-interacting, affinely deforming chains. The 8-chain model and the nonaffine network model derived in this chapter therefore differ in their microscopic representation, and in their connection to the mechanisms of chain deformation. The nonaffine network model contains the factor  $g$ , which interpolates between phantom and affine network behavior. The value of  $g$  may be determined by tracking chain movement during a simu-

lation. We determine the value of  $g$  for different simulated polymer networks in Chapter 6, and demonstrate how entanglement and crosslink density affect the affineness of chain deformation.

Experimentally, the relation of the molecular network structure with macroscopic mechanical properties may be analyzed by testing polymer networks with known chemical structure [55]. To determine the expected values of the parameters in the new model, the value of  $g$  may be determined by tracking (via light scattering) the displacements of tagged polymer chains in a sample during deformation.

Finally, we note that the model may be applied to filled rubber materials even though filler particles were not considered in its derivation. This was demonstrated by fitting to the b186 rubber data [10] in Section 4.2. The model parameters will, of course, not have a physical relation to the size and density of filler particles for these materials; however, since Eq. 108 has a simple and general mathematical form it may be used to capture the stress-stretch response.

#### 4.4 CONCLUSIONS

In this chapter, we constructed a 3 parameter physics-based model for the large deformation mechanical behavior of elastomers. This model can be used within a general continuum mechanics framework to describe rubbery behavior. The derivation was motivated by the need for a simple model able to capture strain softening, hardening, and the difference between deformation states characteristic to elastomers. We used the Rubinstein and Panyukov [5, 6] single-chain description of polymer network behavior in order to construct a model where the parameters define the stress-stretch curve as follows:  $G_c + G_e$  is the initial modulus,  $G_e/G_c$  determines the extent of the softening region, and  $\lambda_{\max}$  defines the onset of strain hardening. We demonstrated that this model is able to provide an excellent fit to the stress-stretch response of rubber materials with a wide range in properties by applying it to natural rubber [1], silicone rubber [8], VHB 4905 [9], and b186 rubber [10]. We will use this model in Chapters 6 and 7 to interpret simulation results. Specifically, Chapter 6 contains an analysis of nonaffine deformation using the relation for non-

phantom microscopic deformation presented in Eq. 92. The simulation results demonstrate that the assumption  $g(\Lambda) = g = \text{const}$  holds even for very large deformations, and the value of  $g$  is tabulated for simulated polymer networks with different chain lengths and entanglement densities.

## CHAPTER 5

### MOLECULAR DYNAMICS SIMULATIONS OF POLYMERS: INTRODUCTION AND SIMULATION METHODS

---

The last two chapters were concerned with physics-based modeling of elasticity. The models contained in these chapters were constructed by making assumptions about chain behavior. In the absence of detailed experimental characterization, we fit models to macroscopic stress-stretch data. Computer simulations can be used to analyze polymer elasticity in a different manner: By simulating a representative polymer material, we can view and analyze the behavior of individual chains when a material is deformed. Molecular dynamics (MD) simulations, as the “computer approach to statistical mechanics” [84], can be used to calculate quantities that are difficult or impossible to measure experimentally. The MD simulation method is therefore invaluable as a tool to test and develop microscopic theories of polymer mechanics. The underlying goal in the simulation work in this dissertation is to determine how the arrangement and deformation behavior of chains in a crosslinked polymer network contribute to the mechanical properties of the material. We use coarse-grained MD simulations to analyze nonaffine micro-macro deformation relationships for polymer networks with different microscopic structures. Both chain and primitive path deformation are tracked, and we introduce concepts that form a consistent picture of microscopic chain deformation for polymer networks with different structures and properties. With both characterization and deformation results, we discuss how entanglements, the number of monomers per chain, nonaffine deformation, and thermal fluctuations affect the behavior of individual chains and the macroscopic elastic properties of the material.

This chapter first introduces the molecular dynamics simulation method in Section 5.1. Coarse-grained simulations of polymer materials are discussed in Section 5.2. This is followed in Section 5.3 by the methods used in the MD simulations in this dissertation. We review primitive path analysis of polymer simulations and describe how it is applied to the simulations in this dissertation in Section 5.4.

## 5.1 MOLECULAR DYNAMICS: BASICS

The molecular dynamics (MD) simulation method was first used in the 1950s and 60s, following the development of the Monte Carlo simulation method in the 30s and 40s. Some of the first MD simulation work was done by Alder and Wainwright [85] and Rahman [86]. The development of the MD simulation method was foreshadowed by the advent of the computer coupled with early discoveries and advances in classical mechanics by Newton, Laplace, Lagrange, Hamilton, and others. The majority of molecular dynamics simulations use classical (not quantum) interactions; indeed, classes of problems where classical physics is dominant are where the MD method can be most effectively used.

Classical molecular dynamics simply uses Newton's laws in the form

$$m \frac{\partial^2 \mathbf{r}}{\partial t^2} = -\nabla U(\mathbf{r}), \quad (110)$$

where  $m$  is particle mass,  $\mathbf{r}$  is particle position,  $t$  is time, and  $U$  is a potential function that is defined to represent the system. The physics here is basic; the utility of using the simulation approach is that one can investigate the behavior of large groups of particles. The most popular form for  $U$  is the Lennard-Jones 12-6 pair potential,

$$U_{\text{LJ}}(r_{ij}) = \begin{cases} 4\epsilon \left[ \left( \frac{\sigma}{r_{ij}} \right)^{12} - \left( \frac{\sigma}{r_{ij}} \right)^6 \right], & r_{ij} < r_c \\ 0, & r_{ij} \geq r_c \end{cases} \quad (111)$$

where  $\epsilon$  is the energy scale,  $\sigma$  is the length scale,  $r_{ij}$  is the distance between particles  $i$  and  $j$ , and  $r_c$  is the potential cutoff. Figure 35 shows a plot of



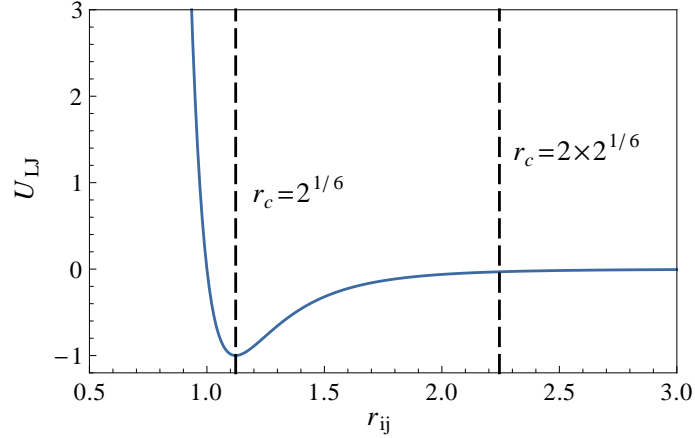


Figure 35: The Lennard-Jones 12-6 pair potential (Eq. 111) plotted with the parameter values  $\epsilon = \sigma = 1$ . The cutoff of  $r_c = 2^{1/6}$  includes only the repulsive part of the potential, while  $r_c = 2 \times 2^{1/6}$  includes repulsive and attractive parts.

this potential function with lines corresponding to  $r_c = 2^{1/6}$  (includes only the repulsive part of the potential) and  $r_c = 2 \times 2^{1/6}$  (includes repulsive and attractive parts). The Lennard-Jones potential is empirical: it represents hard-core repulsion at close distances due to electron orbital overlap, and long-range attraction at further separation distances due to van der Waals interactions. An MD simulation using Eqs. 110 and 111 can reproduce the general behavior of matter in gas, liquid, and solid forms. At high temperature, the particles have high kinetic energy and the system behaves as a gas, with the hard-core repulsive interactions dominating. When the attractive part of the potential is included, a system of Lennard-Jones particles will behave as a liquid when the temperature is lowered; the cohesive forces keep the particles close together and cause the system to exhibit viscous flow. When the temperature is lowered further the system behaves as a solid, with a hexagonal close-packed structure being energetically favorable at low temperatures due to the spherical shape of the particles [87].

The particles are placed together in a simulation box to perform an MD simulation. Since the simulation box size and the number of particles will always be finite, periodic boundary conditions are often used to approximate the behavior of an ‘infinite’ medium. An example of particles placed in a simulation box with periodic boundary conditions is shown in Figure 36. To begin the simulation, the particles are given some distribution of initial

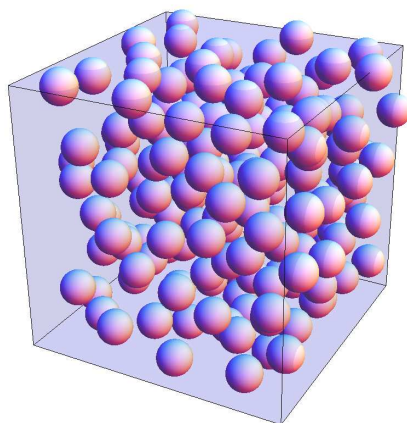


Figure 36: An example of particles placed in a simulation box with periodic boundaries; particles that go out one side come back in the other side.

velocities. The simulation behavior at long times is not dependent on the initial distribution of velocities, since the system as a whole is able to sample a sufficiently large area of phase space. If this were not true, the method would not be useful in performing calculations. An MD simulation is performed using a specified ensemble; these include NVT, NVE, NPT, NPH, and  $\mu$ VT. The ensemble name refers to the quantities held constant. For example, with the NVT ensemble the number of particles (N), volume (V) and temperature (T) are held constant during a simulation. Other quantities that can be controlled are energy (E), pressure (P), enthalpy (H), and chemical potential ( $\mu$ ). Although these ensembles are the most common, this list is not exhaustive in regards to the possible ensembles and quantities which can be controlled during a simulation.

Any thermodynamic quantity that can be expressed in terms of the positions and momenta of the particles can be calculated during a simulation. Using equipartition of energy, each particle (in a 3-dimensional simulation) has its kinetic energy related to temperature via

$$\frac{1}{2}m|\mathbf{v}|^2 = \frac{3}{2}kT, \quad (112)$$

where  $k$  is Boltzmann's constant. The magnitude of the pressure is calculated as

$$P = \frac{NkT}{V} + \frac{1}{3V} \sum_{k=1}^N \mathbf{r}^{(k)} \cdot \mathbf{f}^{(k)}, \quad (113)$$

where  $V$  is volume, and  $\mathbf{r}^{(k)}$  and  $\mathbf{f}^{(k)}$  are the position and force acting on particle  $k$ . The pressure acting in the  $j$  direction on the simulation box face with surface normal in the  $i$  direction is calculated as

$$P_{ij} = \frac{1}{V} \sum_{k=1}^N m v_i^{(k)} v_j^{(k)} + \frac{1}{V} \sum_{k=1}^N m r_i^{(k)} f_j^{(k)}. \quad (114)$$

By convention, stress is defined as negative pressure, so the Cauchy (true) stress is simply

$$\sigma_{ij} = -P_{ij}. \quad (115)$$

## 5.2 COARSE-GRAINED SIMULATIONS OF POLYMER MATERIALS

Recently, coarse-grained simulations of simplified polymer models [15] have contributed to rapid theoretical progress in polymer physics (see, for example, Refs. [88, 89]). Although coarse-grained models often represent a highly simplified situation, they are amenable to systematic study and analysis and can be used to identify patterns and yield insights on length and time scales inaccessible to all-atomistic simulations [84]. In this section we discuss the basic concept of coarse-graining applied to polymer materials and review how coarse-grained simulations have been used to examine the properties of crosslinked polymer materials.

An example of coarse-graining is in Figure 37, first showing an all-atomistic representation of a chain of polyethylene. In an all-atomistic simulation, appropriate potentials are used to represent each atom and its interactions. Some potentials that have been used in atomistic simulations of polymers include DREIDING [90], PCFF [91], AMBER [92], OPLS [93], COMPASS [94], and CHARMM [95]. Ref. [96] gives a list of which potentials have been used in the

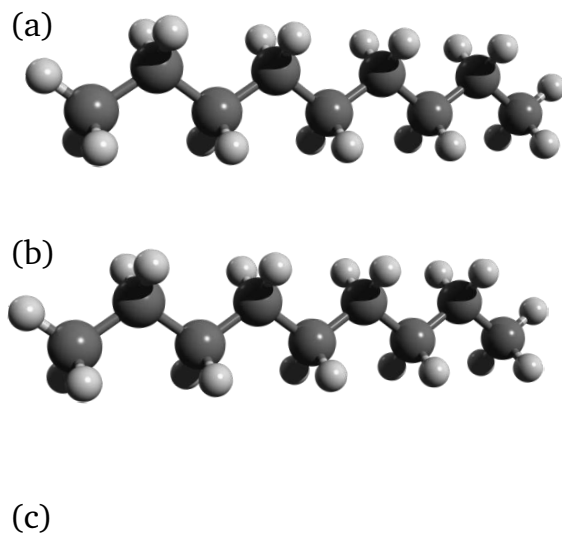


Figure 37: (a) An all-atomistic representation of a polyethylene (PE) chain. (b) Atoms in the PE chain grouped together to form a united-atom model. (c) The bead-spring model of Kremer and Grest [15].

literature for atomistic simulations of various polymers. Due to computational cost, all-atomistic simulations are limited in the length and time scales they are able to probe. One method of coarse-graining is the so-called “united-atom” method illustrated in Figure 37b. Here, several atoms are grouped together and an appropriate potential is used to represent the group of atoms. The example in Figure 37b shows hydrogen atoms being grouped with the carbon atoms to which they are attached. Various levels of coarse-graining detail are possible with the united-atom approach. Currently, multiscale simulations and the development of united-atom or other coarse-grained descriptions of specific polymer materials is an active area of research [97].

All-atomistic or united-atom simulations are set up to represent a specific material, e.g. polyethylene as shown in Figures 37a-b. A different class of simulation models seeks to capture generic features of polymer behavior without including atomistic detail specific to any single polymer. Figure 37c

shows the bead-spring polymer model of Kremer and Grest [15]. We will use this model in the subsequent chapters. The bead-spring model does not represent any specific polymer; it neglects chemical details and only includes a limited set of interactions between particles. It has been shown that this model captures the most essential features of a polymer material: chains of a finite length are joined together from basic repeat units, and a system of chains becomes entangled since individual chains cannot cross each other [15].

The generic bead-spring polymer model discards many of the degrees of freedom in comparison with a full molecular representation; these include the atoms branching off of the backbone connections, bond angle bending, torsional energy states, and others. It is therefore not of use to address certain classes of questions (e.g. high frequency molecular rotations and vibrations). However, the bead-spring model is well suited to study problems that depend on the interactions between large numbers of molecules; problems in this class include polymer melt rheology and rubber elasticity. Since the behavior of the system as a whole depends on many interactions it is more important to simulate a large, interacting system of polymer chains than to capture the molecular details of any specific interaction. This allows one to address problems at larger length and time scales than possible with all-atomistic simulations, and to develop a conceptual scheme suitable for understanding the collective behavior. In this mindset, the overall approach is hierarchical or multi-scale. The bead-spring simulation model provides a level of detail somewhere between atomistic and continuum.

Polymers are simulated with MD using the Langevin equation of motion,

$$m \frac{d^2 \mathbf{r}}{dt^2} = -\nabla U(\mathbf{r}) - \frac{m}{\Gamma} \frac{d\mathbf{r}}{dt} + \boldsymbol{\eta}(t), \quad (116)$$

where  $\Gamma$  is a damping factor and  $\boldsymbol{\eta}(t)$  is a random force associated with thermal motion. To perform a simulation, this equation is discretized in time and integrated in steps of  $\Delta t$ . Using the discretization in time, the magnitude of the random force is,

$$\langle \boldsymbol{\eta}(t)^2 \rangle = \frac{2mkT}{\Gamma \Delta t}, \quad (117)$$

where  $\langle \cdot \rangle$  represents an average over all thermal fluctuations.<sup>1</sup> This magnitude of the random force comes from the fluctuation-dissipation theorem. Eq. 116 can be thought of as Newton's equation (Eq. 110) coupled to a heat bath. A system of particles using the Langevin equation of motion can dissipate kinetic energy due to the inclusion of the viscous term. The Langevin equation acts as a thermostat and is used to set the temperature in the simulation. A simulation using Eq. 116 is termed Langevin dynamics; Brownian motion refers to the specific case where inertial effects are small in comparison to viscous effects, and the LHS of Eq. 116 can be set to zero [84]. Since Eq. 116 includes viscous forces and a random force term it can represent solvent effects without explicitly including solvent molecules in the simulation. Eq. 116 can also be used to represent a dense polymer system. The random force contributes less than inter-particle forces in a dense polymer system since long-time diffusion depends mainly on inter-particle interactions. The viscous and random forces serve as a method to thermostat a dense system. They also represent some of the effective randomness in behavior (due to many inter-atomic collisions) that is not explicitly included in a coarse-grained simulation. The simulations in this dissertation are all performed using Langevin dynamics.

Previous coarse-grained simulation work with crosslinked polymers has been used to investigate various macroscopic properties in relation to microscopic quantities. On a basic level, it was demonstrated that modulus increases with crosslink density, entanglement density, and crosslink functionality [82, 98, 99]. Dubrovskii and Vasilev found that the shear modulus increases with crosslink functionality because of both decreased junction fluctuations and increased chain coupling (chains are more coupled since they are chemically bonded together in a crosslinked network) [100]. Other work used coarse-grained MD to show that monomers become increasingly localized and their relaxation is slowed due to crosslinking [17, 101]. Svaneborg et al. [17, 102] found that variations in monomer fluctuations with deformation can be reasonably described by the double-tube model [76]. Heine et al. saw that, depending on the simulation model used, crosslinking may alter equilibrium chain end-to-end distances [103]. Grest et al. [82] and Svaneborg et

---

<sup>1</sup> This average can also be thought of as an average in time (i.e. an average over many timesteps).

al. [104] found that stress due to crosslinks is in reasonable agreement with the phantom network model at small deformations, but noted deviations at large stretch values. Several studies have suggested that the onset of network strain hardening behavior depends on both crosslinks and entanglements [104, 105, 106, 107]. None of these analyses have considered nonlinear elasticity at large deformations, and all have considered simple uniaxial elongation.

### 5.3 SIMULATION METHODS

The bead-spring model of Kremer and Grest [15] captures the most essential elements of a many-chain polymer system: chains consist of many monomers joined together, and become entangled in a melt since chain-chain crossing is prohibited. We use this model and perform Langevin dynamics simulations to represent a crosslinked polymer via MD. Polymer networks are formed with different chain lengths and entanglement densities, and simulated large deformation uniaxial, pure shear, and equi-biaxial tests are performed. This section details the methods used for the simulations in Chapters 6 and 7. In Chapter 8 we modify these methods to represent shape memory polymer behavior and describe the different parameters and procedures therein. LAMMPS is used for all simulations [108, 109].

The Kremer and Grest [15] model has been previously used in the literature to simulate crosslinked polymers [17, 82, 98, 99, 101, 102, 104, 110]. The results of these and other simulations of crosslinked polymers were reviewed in the previous section. We use the Kremer and Grest [15] model because of its simplicity, proven track record, and reasonable equilibration times. All beads interact via a Lennard-Jones (LJ) 12-6 potential (Eq. 111), with  $\epsilon = 1$  as the energy scale,  $\sigma = 1$  as the length scale, and  $r_c = 2^{1/6}$  as the cutoff radius.<sup>2</sup> This cutoff radius truncates the potential so that only repulsive Lennard-Jones interactions are included, and the force between two particles separated by a distance of  $r_c$  is

---

<sup>2</sup> With  $r_c = 2^{1/6}$ , the LJ force between particles is zero at the cutoff but the LJ potential is nonzero. It is possible to shift the potential to zero at the cutoff. However, whether or not the LJ potential is zero at the cutoff does not affect simulation results since it changes the energy by a constant. We therefore retain Eq. 111 as-is. In Chapter 8 we use a shifted LJ potential since several calculations involving energy values are performed. In this and the following two chapters no direct calculations of energy values are considered.

Parameter	Description	Value (LJ units)
$\sigma$	LJ length scale	1
$\epsilon$	LJ energy scale	1
$r_c$	LJ cutoff distance	$2^{1/6}$
$K$	FENE elastic constant	30
$R_0$	FENE maximum bond elongation	1.5
$\Gamma$	Damping factor for Langevin dynamics	0.5
$m$	Mass of particles	1

Table 3: Parameters used in the simulations of Chapters 6-7.

zero (see Figure 35). With this choice of  $r_c$  the system is nearly athermal [15]. We will discuss this choice further in Chapter 8, where we modify it in order to simulate temperature-dependent behavior. The analysis in Chapters 6 and 7 is concerned with only constant temperature behavior above  $T_g$ . The choice of  $r_c = 2^{1/6}$  is appropriate to study the above- $T_g$  mechanical properties where enthalpic effects are not considered important [82]. All bonds along a chain are connected using the finite extensible nonlinear elastic (FENE) potential,

$$u_{\text{FENE}}(r_{ij}) = \begin{cases} -0.5KR_0^2 \ln \left[ 1 - \left( \frac{r}{R_0} \right)^2 \right], & r_{ij} \leq R_0 \\ \infty, & r_{ij} > R_0 \end{cases} \quad (118)$$

where  $R_0 = 1.5$  is the maximum bond length and  $K = 30$  is the bond stiffness [15]. Table 3 lists all of the parameters used in the simulations. Note that the LJ timescale is defined using other quantities as  $\tau = (m\sigma^2/\epsilon)^{1/2}$ .

Langevin dynamics simulations are performed using the NVT ensemble with the temperature set to  $T = 1$ . In LAMMPS, this is done by using `fix nve` along with `fix langevin`. The temperature of  $T = 1$  is known to yield rubbery-like behavior [15, 98]. The NVT ensemble has a constant number of particles, volume, and temperature. Since the volume is constant, Poisson's ratio during deformation is 0.5, representing an incompressible material. This is used since it is known from experimental results that rubbery materials are nearly incompressible at temperatures above the glass transition.



The simulation model used here (Lennard-Jones potential with  $r_c = 2^{1/6}$ , FENE bonds, NVT ensemble) has been previously used in the literature to study crosslinked polymer networks [17, 82, 98, 99, 101, 102, 104, 110]. The early studies with this model (e.g. Refs. [98, 110]) demonstrated that this model is valid to use as a simplified representation of a polymer network, which can be simulated using standard molecular dynamics methods.

The chains are first generated as random walks with a backfolding restriction [82] (i.e. each added monomer is prevented from folding back on the previous one), and are then placed randomly in the simulation box and equilibrated. A Mathematica code was used to generate the initial simulation setups; this code is included in Appendix B.1. Because the chains are placed randomly in the simulation box, there will be some beads that end up very close together. The Lennard-Jones potential becomes very large at short distances (see Figure 35), and therefore beads that are very close will lead to numerical instabilities. The soft-pushoff method of Ref. [15] is one way to solve this problem. This method involves replacing the Lennard-Jones pair potential with a soft cosine potential,

$$u_{\text{soft}}(r_{ij}) = \begin{cases} A \left[ 1 + \cos \left( \frac{\pi r_{ij}}{r_c} \right) \right], & r_{ij} \leq r_c \\ 0, & r_{ij} > r_c \end{cases} \quad (119)$$

and increasing the value of  $A$  from 4 to 100 during a short simulation run of 4000 timesteps using  $\Delta t = 0.006$ . During this run, the velocity of each atom is set to zero every 50 timesteps in order to keep the system under control. The timestep of  $\Delta t = 0.006$  was only used for the soft push-off step; a timestep of  $\Delta t = 0.012$  was used for all subsequent steps. The LAMMPS input code used for the soft push-off step is included in Appendix B.2. After this step, the regular Lennard-Jones potential is used for all subsequent simulation steps.

The simulated chain lengths ( $N$ ) and number of chains in the system ( $M$ ) were chosen to be the same as Refs. [15, 17, 82, 98] so that a direct comparison of results could be made:  $(N, M) = (20, 5000)$ ,  $(35, 1000)$ ,  $(100, 2500)$ , and  $(200, 3000)$ . All of the simulations in Refs. [15, 17, 82, 98] were done at a monomer density of  $\rho_m = 0.85$ . In this work, we consider test cases with different initial simulation box sizes to correspond to different initial monomer densities. Three cases

for each chain length are considered, corresponding to monomer number densities per unit volume of  $\rho_{cl} = (0.45, 0.65, 0.85)$ . The notation  $\rho_{cl}$  designates that this is the density that the crosslinking reaction was performed at for the different cases. A lower density roughly corresponds to a polymer solution, although we do not include any additional interactions to represent solvent molecules. Even the lowest density is still well above the estimated overlap density for each system. Using Eq. 23 yields an estimate of 0.10 for the critical monomer density for overlap for the  $N = 20$  system, and an estimate of 0.03 for the  $N = 200$  system. Performing the crosslinking reaction at these different densities is anticipated to produce network topologies with different amounts of chain entanglements for a given chain length. This is confirmed in Section 6.1.

After the soft push-off and before crosslinking, each system is equilibrated by monitoring the mean-square distance between beads separated by  $m$  steps,  $\overline{R^2[m]}$ , where the overline represents an ensemble average, in comparison to that obtained Auhl et al. [16]. Auhl et al. [16] performed an extensive set of simulations to determine optimal methods and criteria for preparing well-equilibrated polymer melts in MD simulations. It was found that the quantity  $\overline{R^2[m]}$  is a sensitive measure of whether or not a system is fully equilibrated. We therefore use this to judge initial equilibration before crosslinking. The systems crosslinked at  $\rho_{cl} = 0.85$  can be directly compared to the results in Ref. [16] to determine if equilibrium had been reached. An example of the  $\overline{R^2[m]}$  comparison for the  $N = 100$ ,  $\rho_{cl} = 0.85$  system is shown in Figure 38a as a function of time. After sufficient time has elapsed, the curve of  $\overline{R^2[m]}$  fluctuates about a mean value - this signifies that the initial equilibrated state has been reached. For the  $\rho_{cl} = 0.45$  and  $\rho_{cl} = 0.65$  cases, equilibration takes noticeably less time because of the lower density. The initial equilibration of a lower density system ( $N = 100$ ,  $\rho_{cl} = 0.45$ ) is shown in Figure 38b. These systems were deemed as fully equilibrated once  $\overline{R^2[m]}$  reached steady state (a direct comparison with Ref. [16] cannot be made due to the lower density). The LAMMPS input code for the initial equilibration step is included in Appendix B.3.

Once steady-state conditions were reached, a stoichiometric number of chain ends were designated as crosslinkers with functionality  $\phi = 4$ . A functionality

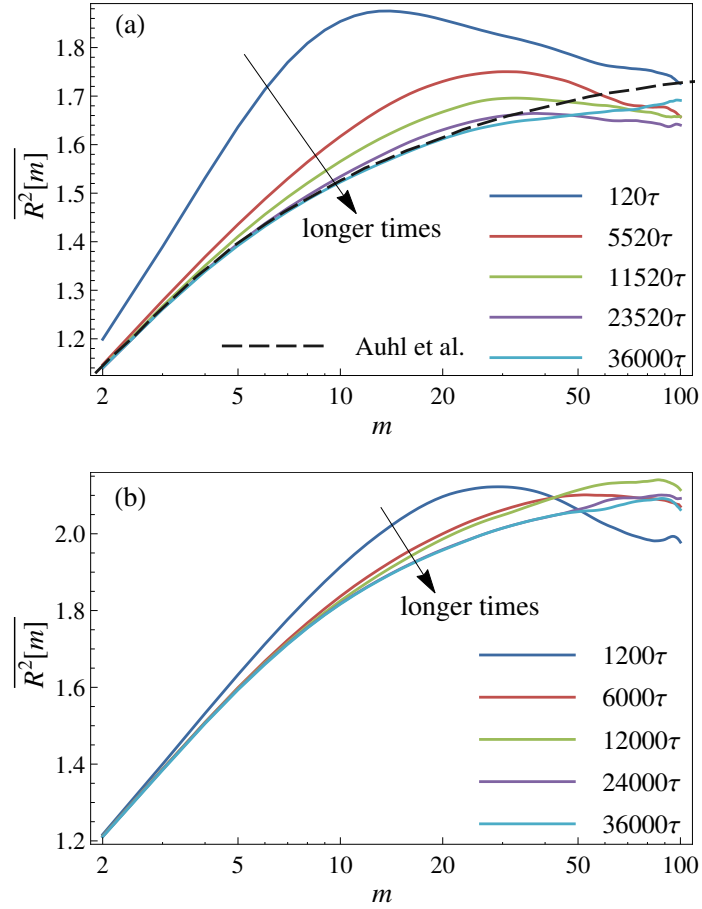


Figure 38: The mean-square distance between beads separated by  $m$  steps,  $\overline{R^2[m]}$ , plotted as a function of  $m$  at different times during equilibration for two different systems: (a)  $N = 100$ ,  $\rho_{cl} = 0.85$ , shown in comparison to the reference equilibrium curve for long chains obtained by Auhl et al. [16], (b)  $N = 100$ ,  $\rho_{cl} = 0.45$ .

of 4 means that each crosslink can connect up to 4 chain ends. By designating a “stoichiometric number” of crosslinkers, one crosslink bond site is available per chain end. An endlinking reaction was simulated by designating a distance criteria by which a crosslinker molecule forms a bond with another chain end [98]. The end-linking reaction produces an ideal network structure which features the exact same number of monomers in chains connected between crosslink junctions. These ideal structures facilitate the comparison of how network structure affects chain deformation mechanisms. The LAMMPS input code for the crosslinking reaction is included in Appendix B.4. The LAMMPS fix used to simulate crosslinking is

```
fix <name> all bond/create 20 1 2 1.3 1 &
    prob 1 <rand> iparam 2 1 jparam 4 2
```

Reading from left to right, this command says define the fix with specified name, apply to all atoms, this fix being bond/create; every 20  $\Delta t$ , bond atom type 1 to atom type 2 if within a reaction radius 1.3 to form a new bond of type 1 with probability 1, (random seed number), with regular atoms (iparam=type 1) having a max 2 bonds and staying as type 1 after bonding, and crosslinker atoms (jparam=type 2) having a maximum of 4 bonds and staying as type 2 after bonding. As more bonds are formed the rate of the reaction slows down exponentially; it is not possible for all bonds to form even after very long times. The crosslinking reaction was therefore simulated until it was deemed sufficiently close to completion.

The crosslinked systems at densities  $\rho_{cl} = (0.45, 0.65)$  were then compressed to a monomer number density of  $\rho_m = 0.85$ , so that all the samples for a given chain length had the same undeformed volume. A true strain rate of  $-8.333 \times 10^{-4} \tau^{-1}$  was used to compress the  $N = 20$  and  $N = 35$  samples, and a true strain rate of  $-8.333 \times 10^{-6} \tau^{-1}$  for the  $N = 100$  and  $N = 200$  samples.<sup>3</sup> An example LAMMPS code used to compress the samples is included in

<sup>3</sup> In LAMMPS, a true strain rate is specified with “trate”, and an engineering strain rate with “erate”. We specified a true strain rate for the compression step, but specified an engineering strain rate for the deformation step. Either specification could be used for the compression step, since an equilibration is performed afterwards. For the deformation step, the simulation runs would become excessively long if a true strain rate was specified since the applied deformations are very large; therefore, an engineering strain rate is best to use with the deformation step.

Test case		Equilibration and crosslinking timesteps and statistics			
N	$\rho_{cl}$	Initial equil.	Crosslinking	Reaction %	2 <sup>nd</sup> equil.
20	0.45	$2 \times 10^6$	$2 \times 10^6$	98.5	$2 \times 10^6$
20	0.65	$2 \times 10^6$	$2 \times 10^6$	98.0	$2 \times 10^6$
20	0.85	$1 \times 10^6$	$2 \times 10^6$	98.0	-
35	0.45	$2 \times 10^6$	$3 \times 10^6$	99.0	$10 \times 10^6$
35	0.65	$2 \times 10^6$	$5 \times 10^6$	98.9	$2 \times 10^6$
35	0.85	$1 \times 10^6$	$3 \times 10^6$	97.5	-
100	0.45	$5 \times 10^6$	$8 \times 10^6$	97.1	$5 \times 10^6$
100	0.65	$5 \times 10^6$	$8 \times 10^6$	97.6	$5 \times 10^6$
100	0.85	$3 \times 10^6$	$5 \times 10^6$	96.5	-
200	0.45	$5.3 \times 10^6$	$10 \times 10^6$	96.7	$8 \times 10^6$
200	0.65	$9.3 \times 10^6$	$10 \times 10^6$	97.0	$8 \times 10^6$
200	0.85	$17.4 \times 10^6$	$10 \times 10^6$	95.5	-

Table 4: The number of simulation timesteps used in equilibrating and crosslinking the networks along with the percentage completion of the crosslinking reaction. A second equilibration was performed on the samples with  $\rho_{cl} = 0.45$  and  $\rho_{cl} = 0.65$  after compressing to the test density of 0.85. A timestep of  $\Delta t = 0.012$  was used in all simulation steps shown here; the simulation time for  $n$  timesteps is simply  $n \times 0.012\tau$ .

Appendix B.5. As mentioned previously, only a density of 0.85 was considered in Refs. [15, 17, 82, 98]; this density was chosen since it is high enough to represent a polymer melt but not so high as to cause equilibration times to become excessively long [15]. We therefore test all samples at this density. After compressing the  $\rho_{cl} = (0.45, 0.65)$  samples, equilibration was again monitored by checking if the distribution of  $\overline{R^2[m]}$  had reached steady state [16]. Table 4 lists the number of simulation timesteps used in each step of the system setup along with the percentage completion of the crosslinking reaction. The soft push-off step is not included in Table 4 since it was performed for the same duration for each test case, and the compression step is not included since its duration is well defined by the strain rates. Note that the  $\rho_{cl} = 0.85$  simulations were performed in an initial investigation, and the  $\rho_{cl} = 0.45$  and  $\rho_{cl} = 0.65$  simulations were performed together at a later time, so there are differences in the times used for these cases. These differences in setup times

do not affect results, since equilibration was ensured by monitoring  $R^2[m]$  for all systems. The  $N = 35$ ,  $\rho_{cl} = 0.45$  system was equilibrated for a long time after compressing as an initial test to determine approximately how long would be needed to equilibrate the other samples.

A constant engineering strain rate deformation was applied to each sample by imposing the deformed dimensions of the simulation box. A sufficiently slow strain rate was chosen so that the size of the hysteresis loop was small; this procedure was chosen in analogy to typical experimental methods for testing soft viscoelastic materials. The rate of  $8.333 \times 10^{-5} \tau^{-1}$  was found to yield good results for uniaxial and pure shear deformation, and  $2.778 \times 10^{-5} \tau^{-1}$  for equi-biaxial deformation. Snapshots of the positions of all the beads in a simulation were outputted at specified intervals for use in the calculations of micro-macro chain deformation in the next chapter. A LAMMPS code used for uniaxial deformation is included in Appendix B.6 as an example. The viability of the constant strain rate method was verified by comparing stress-stretch results with those of Svaneborg [17], where the same simulation model and chain lengths were used (all simulations in Ref. [17] were done at a density of 0.85, so we can compare with test cases crosslinked at  $\rho_{cl} = 0.85$ ). To make this comparison, the equilibrium stress-stretch curve in each simulation was obtained by averaging the stress during both loading and unloading. An example of actual stress-stretch results and the calculated average for uniaxial extension is shown in Figure 39a. Previous MD simulations on crosslinked polymers have obtained stress results by applying a step deformation, stopping and equilibrating, then repeating this procedure until a desired strain was reached. By instead deforming at a slow constant strain rate we are able to reach much larger strains than previous work [17, 102, 104] due to the greatly decreased computational cost. The comparison with the stress-stretch results of Svaneborg [17] is shown in Figure 39b. The excellent agreement demonstrates that the constant strain-rate approach yields a reliable estimate of the equilibrium results. In Chapter 6 both the loading and unloading curves for micro-macro chain deformation are shown when displaying results, and in Chapter 7 the average between loading and unloading is used to display the stress-stretch curves.

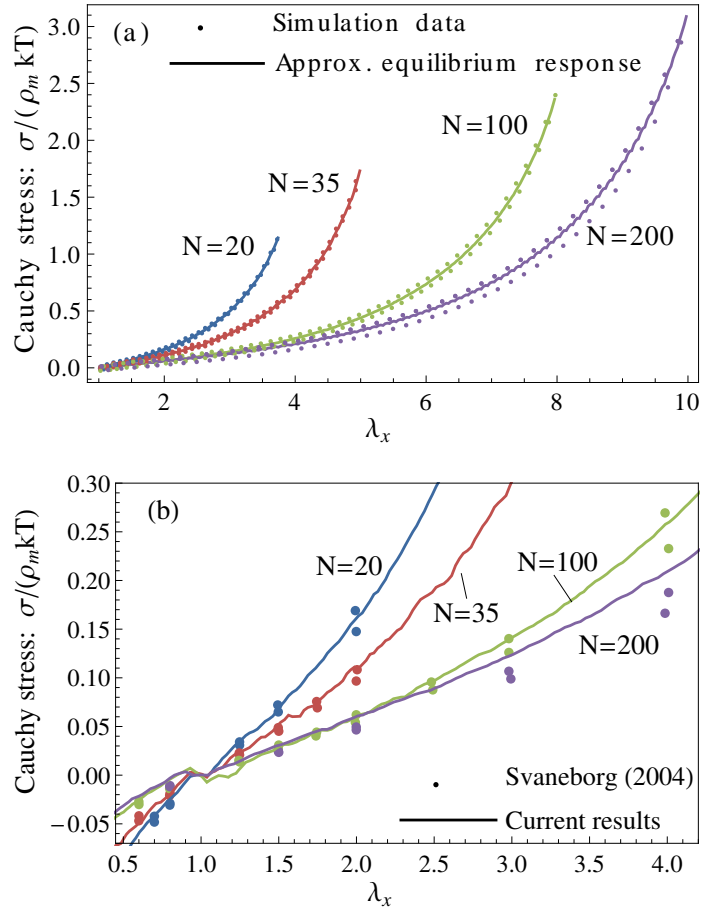


Figure 39: Uniaxial stress-stretch results for simulated tests cases crosslinked at  $\rho_{cl} = 0.85$  with different chain lengths: (a) The averaging process used to estimate equilibrium stress-stretch results for the simulations, (b) A comparison of stress-stretch results for uniaxial tension and compression obtained via averaging with those from Svaneborg [17].

The following list summarizes the simulation procedure. Example codes for generating a simulation setup and running each step of the simulation in LAMMPS are included in Appendix B.

1. Generate chains as random walks with a backfolding restriction [82] and place randomly in simulation box.
2. Soft push-off step using cosine potential in Eq. 119.
3. Equilibrate using Lennard-Jones potential (Eq. 111), checking on  $\overline{R^2[m]}$  to monitor progress towards equilibration.
4. Simulate a crosslinking reaction by designating a distance criteria for the reaction to occur.
5. Compress the samples crosslinked at monomer densities of  $\rho_{cl} = 0.45$  and  $\rho_{cl} = 0.65$  to a density of  $\rho_m = 0.85$ .
6. Additional equilibration for compressed samples, again monitoring  $\overline{R^2[m]}$  as a function of time.
7. Apply uniaxial, biaxial, and pure shear loadings by specifying a constant engineering strain rate deformation on the simulation box.

#### 5.4 PRIMITIVE PATH ANALYSIS

There are two sets of microscopic constraints which determine the micro-macro deformation relationship and properties of crosslinked polymer materials. First, the chains are connected to one another via chemical crosslinks. Since the chains are long, and the number of chain ends at a crosslink is small (4 is typical), the crosslinks rearrange so that the stretch of an individual chain is less than the macroscopic applied stretch. The second microscopic constraint is due to interchain entanglements imposed as a consequence of the chains not being able to cross each other (interchain entanglements are sometimes referred to as physical crosslinks). Primitive path analysis is used to quantify entanglement interactions in a polymer system. The primitive path is most commonly defined as the shortest path between chain ends



which still retains intermolecular entanglements; this path length is directly related to the number of entanglements a chain experiences. The output of a simulation can be processed to obtain the set of primitive paths representing the network. In this section we review methods to determine the primitive paths of a polymer simulation, and ways in which primitive path analysis has been used to investigate the behavior of polymeric systems. We also describe the primitive path analysis methods used in later chapters of this dissertation.

The first primitive path algorithm was introduced by Everaers et al. [111]; this approach used simulated annealing to minimize the path length of the chains in a simulated polymer system. Sukumaran et al. [112] elaborated on the method, and Hoy and Grest [113] introduced an update that was able to pull chains “tighter” by reducing their effective diameter. Hoy and Robbins [114] studied whether or not fully equilibrating a melt at a certain temperature affects primitive path statistics when using the annealing method. By using both the “soft push-off” and “double-bridging” methods of equilibrating melts [16], it was demonstrated that the primitive path statistics change significantly for melts that are not fully equilibrated [114]. Zhou and Larson [115] found differences in the annealing method results depending on which bonded potential was used as input to the minimization.

Kröger [18] introduced a different algorithm based on geometrical operations that reduces a network of chains to a network of primitive paths in much less computational time. The first version of this code was called Z, and a later update, which is available online, is called Z1 [19]. Tzoumanekas and Theodorou [116] introduced a separate algorithm called CReTa that is also based on geometrical operations. These different methods were reviewed in depth by Shanbhag and Kröger [117], and also summarized by Baig and Mavrantzas [89]. Other related reviews and summaries are found in Refs. [20, 118, 119]. In this work we use Kröger’s Z1 code <sup>4</sup> [18, 19, 20] due to its computational efficiency to extract the primitive paths from the simulated polymer networks. An example of a chain reduced to its primitive path using the Z1 code is shown in Figure 40. The Z1 algorithm determines primitive paths from simulation output by first fixing the positions of all the chain ends. Next, the path length from one end of a chain to the other is decreased, under

---

<sup>4</sup> Private communication with Martin Kröger.

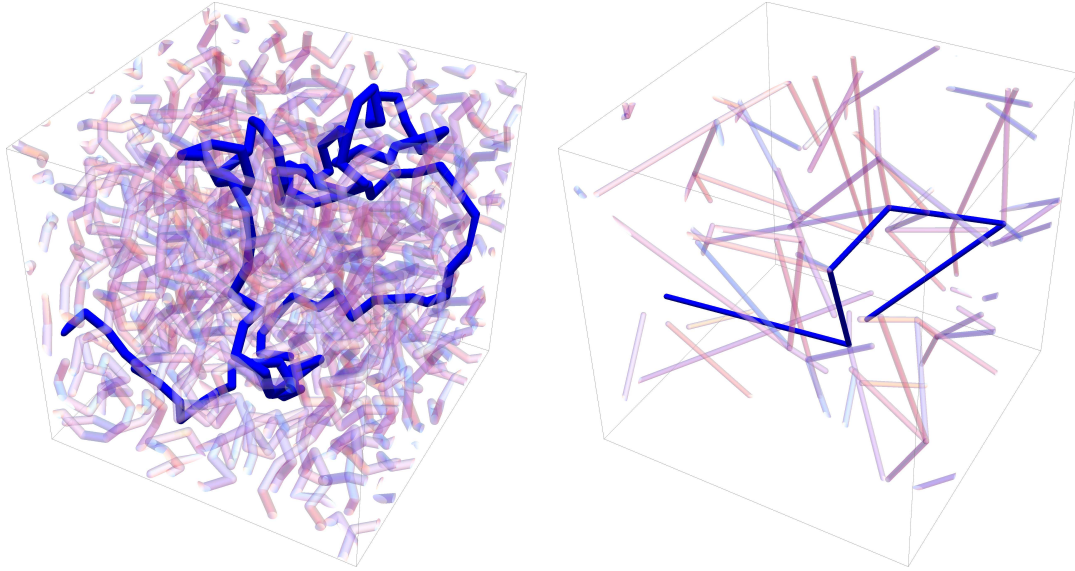


Figure 40: An example of a chain in a polymer network reduced to its primitive path using the Z1 code [18, 19, 20].

the condition that topological constraints with neighboring chains are retained. The procedure continues until the path lengths between all the chain ends have been simultaneously minimized. The primitive path length of a chain is directly related to the number of entanglements the chain experiences. For example, a chain with zero entanglements will be reduced to a primitive path that is a straight line between the two ends. A chain with several entanglements will have a primitive path that retains the entangled topological state, and therefore has several “kinks” that increase its contour length. The number of kinks per chain is denoted  $Z$ , and the contour length of each primitive path is denoted  $L_{pp}$ . The example chain in Figure 40 has  $Z = 4$ .

In this dissertation, primitive path analysis is a critical tool used to characterize the properties and deformation behavior of the simulated polymer networks. The entanglement properties of the undeformed simulated test cases are quantified using primitive path analysis. We then track primitive path length changes during deformation and analyze the statistics of deformed primitive path lengths. This study is the first to apply primitive path analysis to deformed polymer networks. The primitive path is used as a metric to characterize chain deformation, and to understand how entanglement constraints affect the conformational space available to individual chains.

Recent work on non-crosslinked systems has seen the concepts of the primitive path and the restraining ‘tube’ proposed by Doi and Edwards [33] evolve from theoretical abstractions into well-defined and measurable quantities able to describe the extent of intermolecular interactions in polymer systems [88]. Primitive path analysis [89, 117] has become an essential tool in polymer melt rheology [20, 118, 119] since intermolecular entanglements are important in determining the flow properties of uncrosslinked polymer melts. The general characteristics of entanglement and primitive path statistics have been studied for different systems. It has been shown that the entanglement length ( $N_e$ ) increases with chain length ( $N$ ), then reaches a constant value and becomes independent of chain length for chains that are sufficiently long and entangled [19, 25, 112, 120]. The number of entanglements per chain follows a Poisson distribution [19]; this was predicted theoretically by Khaliulin and Schieber [121]. In contrast to the original description by Doi and Edwards [33], simulation results showed that the primitive path is not completely a random walk, since the step sizes are not constant for typical chain sizes [19, 122, 123]. However, if the chains are *very* long, the random walk approximation becomes reasonable [123].

Hoy et al. [25] used primitive path analysis and an extensive set of simulations to create new metrics for topological and rheological entanglement length that obey the correct limits for both short and long chains. The difference between topological and rheological entanglement length was further discussed by Everaers [124]. Section 7.2 contains more information on these differences; in this section we use the the modified S-coil measure of rheological entanglement length [25] to compare theoretical predictions of modulus values with measured results from the simulations.

Foteinopoulou et al. [125] analyzed the effect of temperature on primitive path statistics, showing the number of entanglements per chain decreases at high temperatures. Foteinopoulou et al. [126] and Laso et al. [127] analyzed the effect of chain volume fraction on primitive path statistics. In Ref. [126] a comparison of the entanglement length distribution as a function of volume fraction was made with predictions from the model by Khaliulin and Schieber [121], showing a good agreement.

Other work has applied primitive path analysis to examine specific entanglement effects and micro-macro relationships. Several studies have used primitive path analysis to determine the persistence length, which was then used to analyze scaling of the plateau modulus determined via simulations and from experiments [111, 112, 123, 128, 129]. Hou et al. [130] obtained the plateau modulus using primitive path analysis and then compared the dynamic response with model predictions. Hoy et al. [131] analyzed nonaffine displacements in polymer glasses with different applied strain rates. Other studies have examined primitive path deformation and chain end-to-end deformation for different applied strain rates [132, 133, 134]; these simulations were for uniaxial compression [131], shear and uniaxial elongation [132], shear [133], and uniaxial tension [134]. Leonforte [134] and Mahajan & Sumit [135] examined how entanglements change after deformation. The entanglement statistics of polymer melts with embedded nanoparticles were analyzed in Refs. [136, 137, 138, 139, 140]. Qin et al. [141] determined primitive path length versus stretch for entangled ring polymers; in this study the primitive path was defined as the average over chain conformations. Recent work has focused on using simulations to form multiscale models by mapping simulation results onto the tube model [89, 142, 143]. This is done by defining  $\Phi(s, t)$ , which is the probability that a monomer at position  $s$  along the chain is still inside the original “tube” at time  $t$  [89, 142, 143].

#### 5.4.1 Primitive path analysis in crosslinked polymer networks

In a crosslinked polymer, the entanglements are “trapped” by the permanent network structure and the individual chains undergo zero net diffusion. Although the number of entanglements stays constant for an ideal crosslinked network, the chain primitive path lengths will change when the network is deformed. Despite the importance of using primitive path analysis to study polymeric systems, there appears to only be one study to date that considers the primitive path in a crosslinked polymer system: Li et al. [144] varied crosslink density to show how it affects tube diameter and primitive path step length in polyisoprene, and compared with corresponding results for uncrosslinked systems. This was a characterization of *undeformed* primitive

path characteristics in a crosslinked polymer network. In Chapter 6 we track *deformed* primitive path length by applying the Z1 algorithm of Kröger et al. [18, 19, 20]. Figure 41 shows the deformed configuration and the corresponding primitive path for the test chain shown previously undeformed in Figure 40. This chain is selected as representative of a chain in an entangled system. Snapshots of the simulated systems at various levels of deformation are used as input to the Z1 code to obtain primitive paths as a function of the applied stretch; the primitive path (thick green line) in Figure 41b corresponds to the chain (thick blue line) in Figure 41a. The end-to-end vector of a primitive path is the same as the end-to-end vector of the corresponding chain at the time of the snapshot used for input to the Z1 code. Note that although all kinks are due to topological entanglements, an entanglement may exist that does not cause a kink in the path of one or both chains. Similarly, more than two chains may share the same kink. These features are due to algorithmic details [20]. Indeed, the chain in Figure 41 has an additional kink in the two deformed configurations. Regardless of the precise definitions of kink and entanglement, the average number of kinks is always proportional to the average number of entanglements [25]. The contour length of each primitive path,  $L_{pp}$ , is larger for long, entangled chains and can also be used to determine the number of entanglements a chain feels [25]. Figure 41 shows how  $L_{pp}$  can increase with deformation. In the following chapter we quantify this behavior for the different simulated polymer networks.

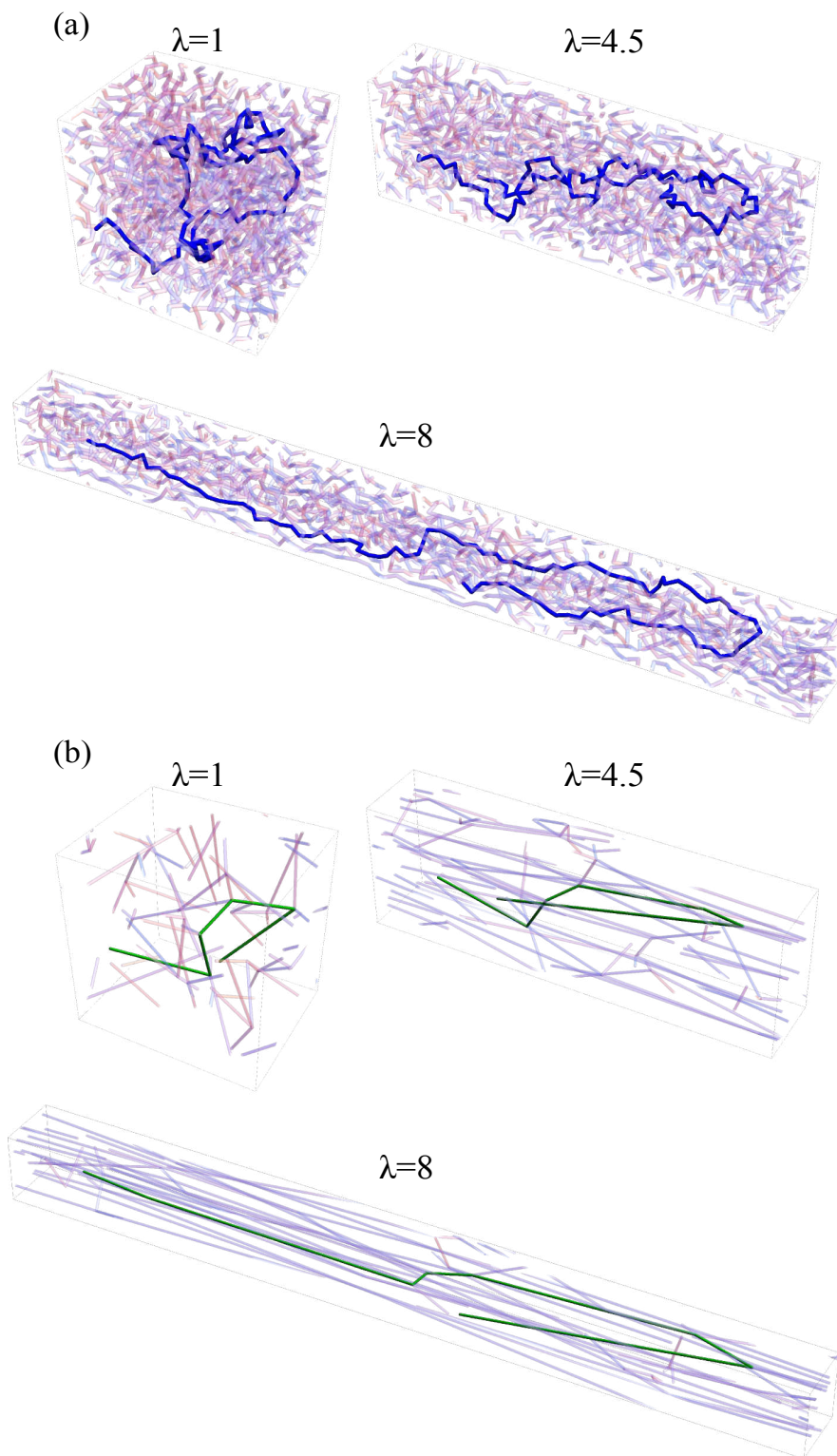


Figure 41: (a) A selection around a test chain in the  $N = 100$ ,  $\rho_{cl} = 0.85$  system is shown here at various levels of uniaxial deformation. (b) Snapshots of the system are used as input to the Z1 code [18, 19, 20] to extract the primitive paths at a given level of the applied deformation.

## CHAPTER 6

### MICRO-MACRO CHAIN AND PRIMITIVE PATH DEFORMATION IN CROSSLINKED POLYMER NETWORKS

---

Chains in a polymer network deform nonaffinely at small length scales due to the ability for extensive microscopic rearrangement. In this chapter we use coarse-grained MD simulations to perform a detailed analysis of nonaffine chain deformation for polymers with different network topologies. Changes in chain end-to-end length and primitive path length are tracked for simulated networks in response to applied uniaxial, biaxial, and pure shear deformations. The simulations encompass a wide range of network topologies, ranging from short, unentangled chains to long, entangled chains. Although chain end-to-end length deformation approaches an affine value for long chain systems, our simulations suggest that primitive path deformation is always nonaffine under quasistatic deformation, even for very long, entangled chains.

In Section 5.4, we introduced primitive path analysis and discussed how it has been used to analyze polymers simulations. The primitive path is defined as the shortest path from one end of a chain to the other which preserves the topological state of the network (i.e. retaining all inter-chain entanglements). The output of a simulation can be processed to obtain the set of primitive paths representing the network. Primitive path analysis [89, 117] has become an essential tool in polymer melt rheology [20, 118, 119] since intermolecular entanglements are important in determining the flow properties of uncrosslinked polymer melts. Hoy et al. [131] analyzed nonaffine displacements in polymer glasses with different applied strain rates. Other studies have examined primitive path deformation and chain end-to-end deformation for uncrosslinked polymer melts in response to different applied strain rates [132, 133, 134]. However, there appears to only be one study to

date that considers the primitive path in a crosslinked polymer system: Li et al. [144] varied crosslink density to show how it affects tube diameter and primitive path step length in polyisoprene, and compared with corresponding results for uncrosslinked systems. This was a characterization of *undeformed* primitive path characteristics in a crosslinked polymer network.

In this chapter we track *deformed* primitive path length in response to applied deformation. These results address fundamental assumptions regarding the behavior of soft elastic materials, since a basic element of any statistical mechanics theory of elasticity is how an applied deformation is transferred to individual chains in the network. Physics-based modeling of rubber elasticity was reviewed in Chapter 3. Many physics-based models of elasticity exist in the literature; these include the phantom network [53], nonaffine tube [5, 6], extended tube [12], double-tube [76], micro-sphere [14], and maximal advance path constraint [145] models, the field-theory approach of Goldbart and others [146, 147], and the nonaffine network model derived in Chapter 4. The phantom network model [53] was the first (and still widely used) model of nonaffine deformation of chain ends. The physics behind this model is that chain end-to-end vectors deform nonaffinely because the number of chain ends connected to a crosslink ( $\phi$ ) is small. The nonaffine network model derived in Chapter 4 generalizes this description, and in this chapter we tabulate the nonaffine chain end-to-end deformation factor  $g$  from Chapter 4 for different simulated networks. Other models have also considered nonaffine deformation of chain ends [12, 14, 145] in addition to nonaffine changes in the magnitude of monomer fluctuations [5, 6, 12, 14, 76], or a general nonaffine deformation field [146, 147]. Although nonaffine chain deformation has been suggested by small angle neutron scattering [58] and nuclear magnetic resonance spectroscopy [70], there is still no consensus on how this behavior changes for different materials.

In this chapter, different networks are used to systematically study the influence of both chain length and entanglement density on nonaffine deformations. The networks are formed by performing simulated crosslinking reactions at different system densities for each chain length; this procedure was described in Section 5.3. This results in different networks with constant chain length but different entanglement density. The simulated networks are deformed in dif-



ferent loading configurations (uniaxial, equi-biaxial, and pure shear), and the statistics of both chain end-to-end deformation and primitive path deformation are compared for the different systems. Full details on the simulation methods are contained in Chapter 5. Here, we first characterize the undeformed network properties of the different simulation test cases in Section 6.1 with the average undeformed end-to-end and primitive path lengths. In Section 6.2, we introduce theoretical considerations of micro-macro deformation and then present simulation results. It is found that primitive path deformation is always nonaffine, even for long, entangled chains. Both chain end-to-end length and primitive path length can be quantified as linear functions of the applied deformation, and the level of affineness increases when chains are longer and/or more entangled. The simulation results are presented to highlight differences in behavior for networks of short, unentangled chains in comparison with long, entangled chains. In Section 6.3, we take a more detailed look at chain deformation by looking at the distribution of chain lengths after a deformation is applied. Individual chains are tracked in time in Section 6.4 to visualize the available conformational space (the restraining “tube”) at various levels of deformation. These results are used to discuss the observed mechanisms and their relation to multiscale modeling in Section 6.5, and the chapter is concluded in Section 6.6.

## 6.1 UNDEFORMED NETWORK PROPERTIES

The 12 simulation test cases include chain lengths of  $N = (20, 35, 100, 200)$  crosslinked at monomer densities of  $\rho_{cl} = 0.45, 0.65, 0.85$ . These were chosen to assess the influence of both chain length and entanglement density on micro-macro deformation relationships. We first examine network properties in the undeformed state in terms of chain end-to-end statistics and primitive path statistics for each test case. Consider a set of rectangular Cartesian basis vectors in 3D space:  $\hat{\mathbf{e}}_i(\hat{\mathbf{e}}_1, \hat{\mathbf{e}}_2, \hat{\mathbf{e}}_3)$ . The corresponding principal stretches are given by  $\lambda_i$ . The chain end-to-end vector is  $\mathbf{R}$  with magnitude  $R = (R_1^2 + R_2^2 + R_3^2)^{1/2}$ . In general, both the end-to-end chain length and primitive path length depend on the stretch:  $R = R(\lambda_i)$  and  $L_{pp} = L_{pp}(\lambda_i)$ . The undeformed configuration is represented by a stretch of 1, i.e.  $R(1)$  or  $L_{pp}(1)$ . The values of mean-square

Test case		Chain end statistics		Primitive path statistics		
$\rho_{cl}$	N	$\bar{\phi}$	$\overline{R(1)^2}$	$\bar{Z}$	$\overline{L_{pp}(1)}$	$\overline{L_{pp}(1)^2}$
0.45	20	3.83	28.5	0.09	5.18	30.9
	35	3.88	51.1	0.38	7.37	63.1
	100	3.68	155.1	1.48	15.31	263.5
	200	3.64	305.0	2.94	26.08	747.6
0.65	20	3.77	31.8	0.14	5.50	35.0
	35	3.87	57.9	0.46	7.89	72.0
	100	3.73	168.5	1.82	16.87	315.0
	200	3.67	336.2	3.58	29.54	942.2
0.85	20	3.77	33.5	0.18	5.74	37.6
	35	3.72	61.1	0.62	8.46	81.1
	100	3.62	175.9	2.19	18.33	370.5
	200	3.53	347.5	4.27	32.63	1145.5

Table 5: Tabulated data on undeformed chain end-to-end and primitive path statistics for the different simulation test cases.

end-to-end chain length and other undeformed network characteristics are listed in Table 5. The mean-square end-to-end length of the simulation test cases crosslinked at the lower monomer densities (0.45 and 0.65) and then compressed are less the cases crosslinked at 0.85 and kept at this density. We attribute this difference to the  $\rho_{cl} = 0.45$  and  $\rho_{cl} = 0.65$  systems having fewer entanglements at the testing density of 0.85 in comparison to the number of entanglements that would naturally develop for chains in a melt at that density. With fewer entanglements the chains tend to coil, leading to a reduction in the end-to-end distances. For an ideal random walk of N monomers with bond length  $l$ , the mean-square end-to-end length is  $l^2N$ . The average bond length for the Kremer-Grest model is  $l = 0.97$  [15, 16]; since this depends on interactions along the length of the chain, it does not depend on the density. The mean square end-to-end length of all of the systems is greater than  $l^2N$  due to excluded volume effects.

Although the systems crosslinked at densities of 0.45 and 0.65 and then compressed have different undeformed end-to-end chain dimensions, the pressure on the simulation box for each system depends only on N after each

N	$\rho_{cl}$	$P_{iso}$
20	0.45	6.01
	0.65	6.00
	0.85	5.99
35	0.45	5.50
	0.65	5.49
	0.85	5.49
100	0.45	5.09
	0.65	5.09
	0.85	5.09
200	0.45	4.99
	0.65	4.98
	0.85	4.98

Table 6: The average isotropic pressure on each simulation box in the undeformed configuration. The values were calculated by averaging pressure values over time after equilibrating each system at the test density of 0.85.

has been compressed to the same density. Table 6 lists the average isotropic pressure on each simulation box in the undeformed configuration.<sup>1</sup> For a given value of  $N$ , the isotropic pressure shows no significant change with  $\rho_{cl}$ . This shows that after crosslinking at  $\rho_{cl} = 0.45$  or  $0.65$  and compressing to  $0.85$ , an “artificial” force is not required to maintain the density of  $0.85$ . If the pressure values were dependent on  $\rho_{cl}$ , this would suggest that the materials compressed to  $0.85$  may be unstable at this density. Since no correlation is seen, this provides an additional confirmation that the simulation procedure is valid. The procedure of crosslinking at a lower density and then compressing is analogous to crosslinking in a solution and then removing the solvent. An alternative simulation procedure is to crosslink at the different densities and then deform without compressing the  $\rho_{cl} = 0.45$  and  $\rho_{cl} = 0.65$  systems (i.e. keep them at densities of  $0.45$  and  $0.65$  during deformation). This procedure

<sup>1</sup> There is a nonzero isotropic pressure on the simulation box because a constraint of constant volume is imposed.

was done for the  $N = 35$  and  $N = 100$  systems at the density of 0.45 in order to compare, and these results are in the next section.

The average crosslink functionality ( $\bar{\phi}$ ) is included in Table 5 for each test case. Since the crosslinking reaction does not reach 100% (see Table 4),  $\bar{\phi}$  is less than 4 for each test case.

Table 5 lists the average number of kinks per chain ( $\bar{Z}$ ) along with the average undeformed primitive path length ( $\overline{L_{pp}(1)}$ ) and the mean-square primitive path length ( $\overline{L_{pp}(1)^2}$ ) for each test case. As expected, the number of kinks per chain and the primitive path length increase with both the number of monomers in the chain ( $N$ ) and the density at which the crosslinking reaction was performed ( $\rho_{cl}$ ). This verifies the expected results of the simulation procedure of crosslinking at different densities: the systems with the same  $N$  but different  $\rho_{cl}$  have the same chain length but different numbers of entanglements per chain. The  $N = 20$ ,  $\rho_{cl} = 0.45$  system has the fewest number of entanglements per chain ( $\bar{Z} = 0.09$ ), and the  $N = 200$ ,  $\rho_{cl} = 0.85$  system has the most ( $\bar{Z} = 4.27$ ). This section presented the properties of the simulation cases in the undeformed state. In the following sections we characterize how these systems deform.

## 6.2 AVERAGE CHAIN AND PRIMITIVE PATH DEFORMATION

The chains in a polymer network deform nonaffinely due to the ability for extensive rearrangement at the micro-scale. We wish to determine how both crosslinks and entanglements affect the affineness of chain deformation. The simulation test set includes networks with different chain lengths, and different entanglement densities for each chain length, and can therefore be used to systematically analyze this behavior. To characterize nonaffine deformation we examine both the deformation of chain end-to-end vectors and primitive path lengths. A brief theoretical background is given before presenting simulation results. Some of the questions we address here include: Are chain deformations always nonaffine? How do chain length and entanglement density affect nonaffine deformation? Do deformations become more affine at large stretch? And how do chain stretch and primitive path deformation differ?

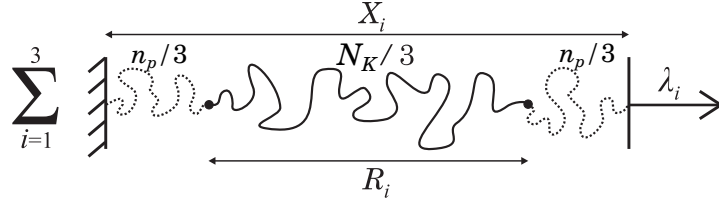


Figure 42: The single chain description of network connectivity proposed by Rubinstein and Panyukov [5, 6]. A chain with  $N_K$  monomers is coupled to the applied deformation via 2 effective chains of length  $n_p$ . For Gaussian chains, this is decomposed into a sum over 3 chains aligned with the principal directions of stretch, each with length  $N_K/3$  and coupled to the applied deformation via 2 effective chains of length  $n_p/3$ .

### 6.2.1 Theoretical background

The phantom network model [53] was the first (and still widely used) model of nonaffine deformation of chain ends. We reviewed this and other models in Chapter 3. A brief discussion is given here for clarity, and the mathematical preliminaries for quantifying simulation behavior are presented. The physics behind phantom network behavior says that since the chains are long, and the number of chain ends at a crosslink ( $\phi$ ) is small, the crosslinks rearrange so that the stretch of an individual chain is less than the macroscopic applied stretch. The junction functionality,  $\phi$ , is typically 3 or 4; for example, natural rubber crosslinked with sulfur has a functionality of 4. Rubinstein and Panyukov [5, 6] formulated a single-chain solution to the phantom network model to relate the deformation of a chain to the applied stretch. This model was reviewed in Chapter 3. A schematic of this model is shown in Figure 42. The test chain of length  $N_K$  (the subscript K is used here to denote the number of Kuhn monomers) is coupled to the applied deformation via two effective chains of length  $n_p$ . The effective chains represent the network structure and connectivity. The number of monomers in the effective chains is

$$n_p = \frac{N_K}{\phi - 2}. \quad (120)$$

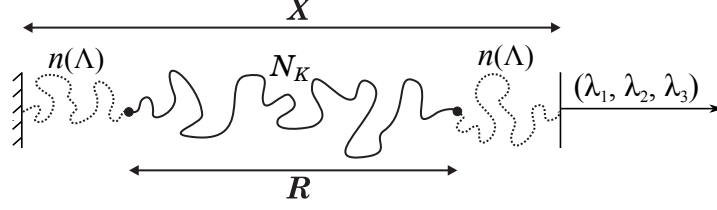


Figure 43: The generalized single-chain description of polymer network deformation [21]. The two effective chains which couple the test chain to the applied deformation may be functions of the applied stretch. The chains are no longer Gaussian so they cannot be simply decomposed into three orthogonal directions.

The value of  $n_p$  determines the magnitude of the applied deformation transferred to the test chain. The mean-square end-to-end length of the chains in the network is

$$\overline{\langle R(\Lambda)^2 \rangle} = b_K^2 N_K \left[ \Lambda^2 \left( 1 - \frac{2}{\phi} \right) + \frac{2}{\phi} \right], \quad (121)$$

where  $b_K$  is the Kuhn monomer length,  $\langle \cdot \rangle$  is an average over thermal fluctuations and the overbar is an average over all chains in the network.

In Chapter 4, we extended the Rubinstein and Panyukov [5, 6] solution of the phantom network model to allow for non-phantom chain deformation. A schematic of this generalized representation is shown in Figure 43. The effective chains are now defined to have a length that may vary with the applied deformation. This is expressed as  $n = n(\Lambda)$ , where  $\Lambda$  is the normalized first invariant previously defined in Eq. 77. To simplify the notation, a non-phantom factor  $g(\Lambda)$  was defined in Chapter 4 with the anticipated range  $1 \leq g(\Lambda) \leq (1 - 2/\phi)^{-1/2}$ . The lower limit represents phantom behavior and the upper limit affine network behavior. The mean-square chain end-to-end length is related to the applied deformation according to

$$\langle R(\Lambda)^2 \rangle = b_K^2 N_K g(\Lambda)^2 (1 - 2/\phi) \Lambda^2 + \text{const}, \quad (122)$$

In Chapter 4 we assumed that  $g(\Lambda)$  was constant. In the next section we show that  $g(\Lambda) = g = \text{const}$  is a good description of end-to-end chain deformation.

With the simulation results, only the ensemble average will be used since it is more accessible. End-to-end length changes are quantified by plotting

changes in mean-square end-to-end length as a function of  $\Lambda^2$ , and fitting a straight line with slope  $\beta_{ee}$  and y-intercept  $C_{ee}$ :

$$\frac{\overline{R(\Lambda)^2}}{\overline{R(1)^2}} = \beta_{ee}\Lambda^2 + C_{ee}. \quad (123)$$

The subscript “ee” stands for “end-to-end”. The results of the next section show that mean-square end-to-end length is indeed a linear function of  $\Lambda^2$  and therefore the coefficient  $\beta_{ee}$  is a valid metric to quantify end-to-end length changes. A value of  $\beta_{ee} = 1$  is affine and  $\beta_{ee} < 1$  is nonaffine.

Comparing Eqs. 123 and 122, the value of the non-phantom factor  $g$  that was introduced in Chapter 4 can be calculated. Note that in the theoretical treatment shown in Eq. 122,  $b_K$  refers to the Kuhn monomer length and  $N_K$  to the number of Kuhn monomers.<sup>2</sup> These quantities are defined to satisfy  $\overline{R(1)^2} = b_K N_K^2$ , where the subscript  $K$  has been added to denote the Kuhn length and number of Kuhn monomers in the theoretical treatment. Using this and Eqs. 123 and 122, the value of the non-phantom factor can be calculated:

$$g^2 = \frac{\beta_{ee}}{1 - 2/\overline{\phi}}, \quad (124)$$

where  $\overline{\phi}$  is the average junction functionality and is tabulated in Table 5. Phantom network behavior is represented by  $g = 1$ , i.e. a value of  $\beta_{ee} = (1 - 2/\overline{\phi}) \approx 1/2$  for a network with 4-functional crosslinkers. Since  $\overline{\phi}$  is slightly less 4, the actual calculation leads to a value of  $\beta_{ee}$  slightly less than  $1/2$ .

The majority of rubber elasticity modeling work has considered chain end-to-end deformation. However, Edwards and Vilgis considered primitive path deformation in the derivation of the slip-link model [11]. An affine deformation assumption of primitive path length was used to derive model results. Since primitive path length is a scalar quantity, affine deformation is expressed by relating primitive path length to  $\Lambda$ , a scalar measure of deformation:

$$L_{pp}(\Lambda) = L_{pp}(1) \Lambda. \quad (125)$$

<sup>2</sup> Since the chains do not follow ideal random walk statistics, the number of Kuhn monomers is not equal to the number of monomer segments in a simulated chain.

This expression was used in Ref. [11]. Here, to quantify nonaffine primitive path length changes for the different simulated networks we consider mean-square primitive path length changes as a function of  $\Lambda^2$  in the same fashion as was done for end-to-end length changes in Eq. 123. Here, we define  $\beta_{pp}$  as a nonaffine primitive path deformation parameter:

$$\frac{\overline{L_{pp}(\Lambda)^2}}{\overline{L_{pp}(1)^2}} = \beta_{pp}\Lambda^2 + C_{pp}, \quad (126)$$

where  $C_{pp}$  is the associated y-intercept of the line. The simulation results show that changes in mean-square primitive path length are indeed proportional to  $\Lambda^2$ , and therefore the slope  $\beta_{pp}$  can be used as a measure of the affineness of primitive path deformation.  $\beta_{ee} = 1$  is affine deformation and  $\beta_{ee} < 1$  is nonaffine. The parameters  $\beta_{ee}$  and  $\beta_{pp}$  will be used in the following section to quantify and compare nonaffine deformation for the different simulated networks.

### 6.2.2 Simulation results: average deformation

We first examine changes in the magnitude of mean-square end-to-end chain length and primitive path length with respect to the magnitude of the applied deformation. Figure 44 shows mean-square end-to-end length changes,  $\overline{R(\Lambda)^2}/\overline{R(1)^2}$ , and mean-square primitive path length changes,  $\overline{L_{pp}(\Lambda)^2}/\overline{L_{pp}(1)^2}$ , plotted as functions of  $\Lambda^2$  for two simulation cases: short, unentangled chains ( $N = 20$ ,  $\rho_{cl} = 0.45$ ) and long, entangled chains ( $N = 200$ ,  $\rho_{cl} = 0.85$ ). In this and the following sections we highlight the  $N = 20$ ,  $\rho_{cl} = 0.45$  and  $N = 200$ ,  $\rho_{cl} = 0.85$  systems in several comparisons since they are the most different in terms of network structure; these cases represent bounds on the spectrum of microscopic chain behavior for the different simulation systems. The  $N = 20$ ,  $\rho_{cl} = 0.45$  system has the shortest chains with the fewest number of entanglements, and the  $N = 200$ ,  $\rho_{cl} = 0.85$  system the longest chains with the largest number of entanglements of the different test cases. Each plot in Figure 44 contains data for uniaxial, pure shear, and equi-biaxial deformation states. The first observation is that both mean-square chain length and primitive path



length vary linearly with  $\Lambda^2$  for both of the different systems. Additionally, the same linear relationship applies to uniaxial, pure shear, and equi-biaxial deformation states, and to very large applied deformations of each of these states. Microscopic deformations of a network can therefore be described with a single linear expression that is defined solely by the network topology. For a given material, no additional theoretical consideration is needed to describe micro-macro deformation for large applied stretches and arbitrary boundary conditions. There is a small change in the uniaxial vs. equi-biaxial data for the long chain system shown in Figure 44a; however, this difference is small and does not warrant a new conceptual description. We therefore retain the assumption of linearity used in Section 6.2.1 to define  $\beta_{ee}$  and  $\beta_{pp}$  in Eqs. 123 and 126, and use these to quantify and compare nonaffine deformation of the different simulation test cases.

The  $N = 20$ ,  $\rho_{cl} = 0.45$  system has  $\beta_{ee} = 0.44$  for mean-square chain stretch (the slope of the line in Figure 44a). Using Eq. 124 and the value of  $\bar{\phi}$  from Table 5, this leads to  $g^2 = 0.93$  for the non-phantom factor. This is close to, although slightly less than, the lower limit of the theoretically expected range of  $1 \leq g(\Lambda) \leq (1 - 2/\bar{\phi})^{-1/2}$ . Phantom network behavior is represented by  $g = 1$ . This result suggests that chain deformation is phantom-like for this network of short, unentangled chains. The network of long, entangled chains ( $N = 200$ ,  $\rho_{cl} = 0.85$ ) shown in Figure 44c has  $\beta_{ee} = 0.81$ . This represents chain deformation that is closer to affine ( $\beta_{ee} = 1$  represents affine deformation).

Although end-to-end length changes are more affine for the network of long, entangled chains, the slope of the line representing primitive path deformation is nearly the same for both cases. In Figure 44, the short chain system has  $\beta_{pp} = 0.42$  and the long chain system has  $\beta_{pp} = 0.43$ . Table 7 lists values of  $g^2$ ,  $\beta_{ee}$ , and  $\beta_{pp}$  tabulated for all of the different simulation test cases. For very long chains  $\beta_{ee}$  is expected to reach a value of 1, representing affine deformation. However, it appears that primitive path deformation is always nonaffine. All of the values of  $\beta_{ee}$  are between 0.42 and 0.48 for all of the simulation test cases. From Table 7 it is seen that  $g^2$  and  $\beta_{ee}$  generally increase with  $N$  for a given value of  $\rho_{cl}$ , and increase with  $\rho_{cl}$  for a given value of  $N$ . The only exception to this trend is  $\beta_{ee}$  for the  $N = 100$  systems with  $\rho_{cl} = 0.65$  and  $\rho_{cl} = 0.85$ . However, these differences are small and may be

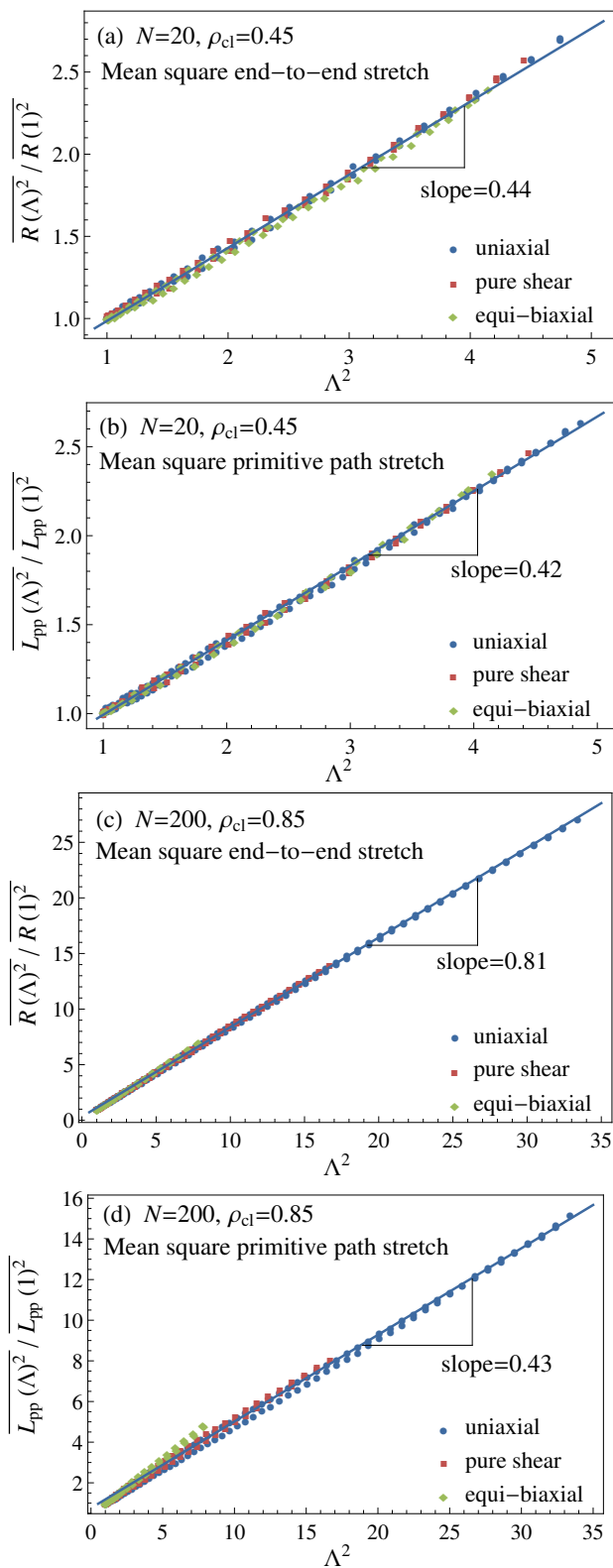


Figure 44: Changes in mean-square end-to-end chain length and primitive path length for uniaxial, biaxial, and pure shear deformations. (a)-(b) Short, unentangled chains:  $N = 20, \rho_{cl} = 0.45$ . (c)-(d) Long, entangled chains:  $N = 200, \rho_{cl} = 0.85$ .

Test case		Nonaffine deformation		
$\rho_{cl}$	N	$g^2$	$\beta_{ee}$	$\beta_{pp}$
0.45	20	0.93	0.44	0.42
	35	1.03	0.50	0.42
	100	1.40	0.64	0.44
	200	1.65	0.74	0.42
0.65	20	1.02	0.48	0.44
	35	1.16	0.56	0.48
	100	1.53	0.71	0.47
	200	1.71	0.78	0.43
0.85	20	1.09	0.51	0.47
	35	1.26	0.58	0.48
	100	1.50	0.67	0.44
	200	1.86	0.81	0.43

Table 7: Non-phantom and nonaffine parameters for the different simulation test cases.

due to differences in the extent of the crosslinking reaction (see Table 5 for the relevant crosslinking statistics). It is generally expected that  $\beta_{ee}$  increases with chain length and entanglement density, and will reach a value of 1 for very long chains. However, the results in Table 7 do not show any clear trends with respect to the nonaffine primitive path deformation parameter  $\beta_{pp}$ .

The preparation procedure of crosslinking at a lower density (0.45 or 0.65) and then compressing to the test density of 0.85 caused the chains to have a different mean-square end-to-end length in comparison with a case kept at a density of 0.85 during the entire procedure. An alternative procedure is to crosslink at the different densities and then deform without compressing the  $\rho_{cl} = 0.45$  and  $\rho_{cl} = 0.65$  cases (i.e. keep them at densities of 0.45 and 0.65 during deformation). To compare results, the  $N = 35$  and  $N = 100$  systems with  $\rho_{cl} = 0.45$  were deformed at a density of 0.45. At this density, the undeformed mean-square end-to-end length of the chains of the  $N = 35$  and  $N = 100$  systems are 72.8 and 231.3, respectively. These values are larger than the cases kept at or compressed to the density of 0.85. The undeformed mean-square primitive path length is 84.5 for the  $N = 35$  system and 372.1 for the  $N = 100$  system. Although these systems are at the density of 0.45,

these values of undeformed mean-square primitive path length are close to the mean-square primitive path length values for the systems of the same value of  $N$  crosslinked at  $\rho_{cl} = 0.85$ . The value of  $\beta_{ee}$  determined using Eq. 123 is 0.55 for the  $N = 35$  system and 0.66 for the  $N = 100$  system, and the value of  $\beta_{pp}$  determined using Eq. 126 is 0.50 for the  $N = 35$  system and 0.49 for the  $N = 100$  system. These values of the nonaffine deformation coefficients are numerically different than the results obtained by compressing and deforming at the density of 0.85. However, the values of  $\beta_{ee}$  and  $\beta_{pp}$  obtained by deforming these systems at the density of 0.45 suggest that a full analysis will yield the same trends: end-to-end deformation is more affine for chains that are longer and/or more entangled, and primitive path deformation is always nonaffine. A complete analysis of systems deformed at different densities could be a topic of future work.

### 6.3 DISTRIBUTION OF CHAIN LENGTHS

In the previous section, we examined changes in *average* chain end-to-end length and primitive path length and quantified this behavior for the different simulation test cases. Due to the network connectivity and the random nature of intermolecular interactions, each individual chain will not undergo the same stretch when a sample is deformed. Although a simple linear trend can be used to describe average chain and primitive path length, the actual chains in a network will have various lengths distributed about this average. To analyze this behavior we plot the distribution of chain and primitive path lengths at different levels of deformation. This is shown for undeformed and uniaxially deformed configurations of the  $N = 20$ ,  $\rho_{cl} = 0.45$  and  $N = 200$ ,  $\rho_{cl} = 0.85$  systems in Figures 45 and 46, respectively. Normal distributions defined by the mean and standard deviation of each chain or primitive path length distribution are overlaid to demonstrate the trends in the data. (For mean  $\mu$  and standard deviation  $s$ , the normal distribution is  $P(x) = (s\sqrt{2\pi})^{-1} \exp(-(x - \mu)^2/2s^2)$ ). The results are shown normalized by the contour length<sup>3</sup> of the chains ( $L$ ). First consider the short chain system in

<sup>3</sup> For the simulations, the contour length of the chains is calculated as  $L = Nl$ , where  $N$  is the number of monomer segments in the chain and  $l = 0.97$  is the average bond length.

Figure 45 ( $N = 20$ ,  $\rho_{cl} = 0.45$ ). The chain length and primitive path length distributions look very similar at the different levels of deformation and do not deviate much from the normal distribution curve. The standard deviation increases with deformation in nearly the same manner for both chain and primitive path distributions (Figure 45c).

The chain and primitive path length distributions for the long chain,  $N = 200$ ,  $\rho_{cl} = 0.85$  system are shown in Figure 46. This system was deformed to a very large stretch ( $\lambda_x = 10$  for the uniaxial deformation), and it is seen that the standard deviations of both the chain and primitive path lengths increase greatly at large stretch values. However, in contrast to the short chain system, the chain end-to-end and primitive path length distributions for this long chain system are significantly different. The primitive path lengths follow a normal distribution until very large deformations, where the distribution becomes left-skewed. In contrast, the chain lengths only follow a normal distribution in the undeformed configuration. After deformation there remains a considerable number of chains with short end-to-end length, but nearly zero chains with short primitive path length. Figure 46c shows that the standard deviation of chain end-to-end lengths increases more quickly than the standard deviation of primitive path lengths for a system of long, entangled chains.

Figures 47 and 48 contain 3D plots of the locations of the chain end-to-end vectors in undeformed and uniaxially deformed configurations. The  $N = 20$ ,  $\rho_{cl} = 0.45$  system is shown in Figure 47, and the  $N = 200$ ,  $\rho_{cl} = 0.85$  system in Figure 48. These plots are obtained by shifting one end of each chain to the origin and plotting the location of the other end with a color defined by its vector length. A half-ellipsoid with axes defined by the RMS chain stretch in each direction is overlaid for reference. Due to symmetry in the boundary conditions only a single quadrant in 3-dimensional space needs to be considered; the half-ellipsoid form is shown for ease of viewing. The undeformed configuration for each system shows spherical symmetry as expected. After a uniaxial deformation in the  $x$ -direction is applied, chains tend to align and elongate in the direction of deformation. Chains with end-to-end vectors remaining in the transverse directions tend to contract.

The short and long chain systems display different behavior after the uniaxial deformation. The long chain system in Figures 46 and 48 has a very large

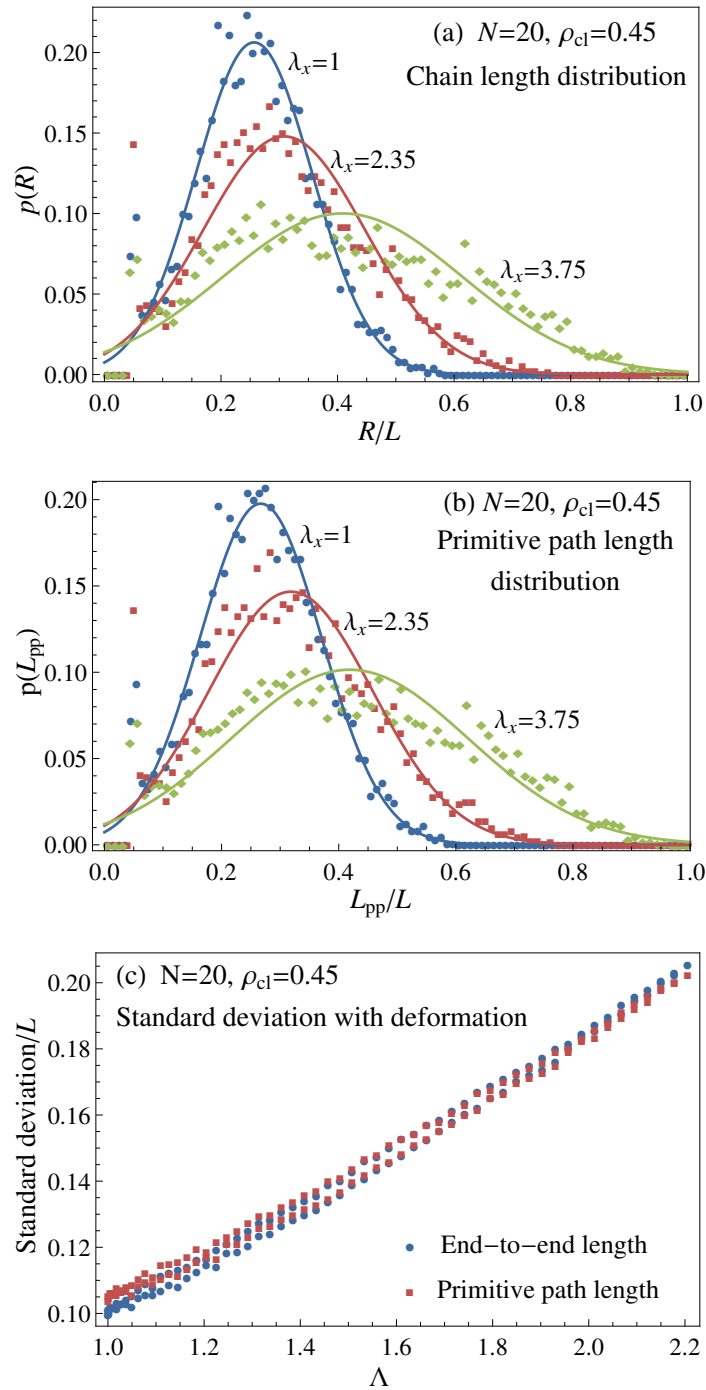


Figure 45: The probability distribution of chain lengths (a) and primitive path lengths (b) for the  $N = 20$ ,  $\rho_{cl} = 0.45$  system with an applied uniaxial stretch. A normal distribution defined by the mean and standard deviation of each distribution (lines) is shown with the data (points) in order to visualize the trends. The standard deviation of each distribution as a function of deformation is shown in (c).

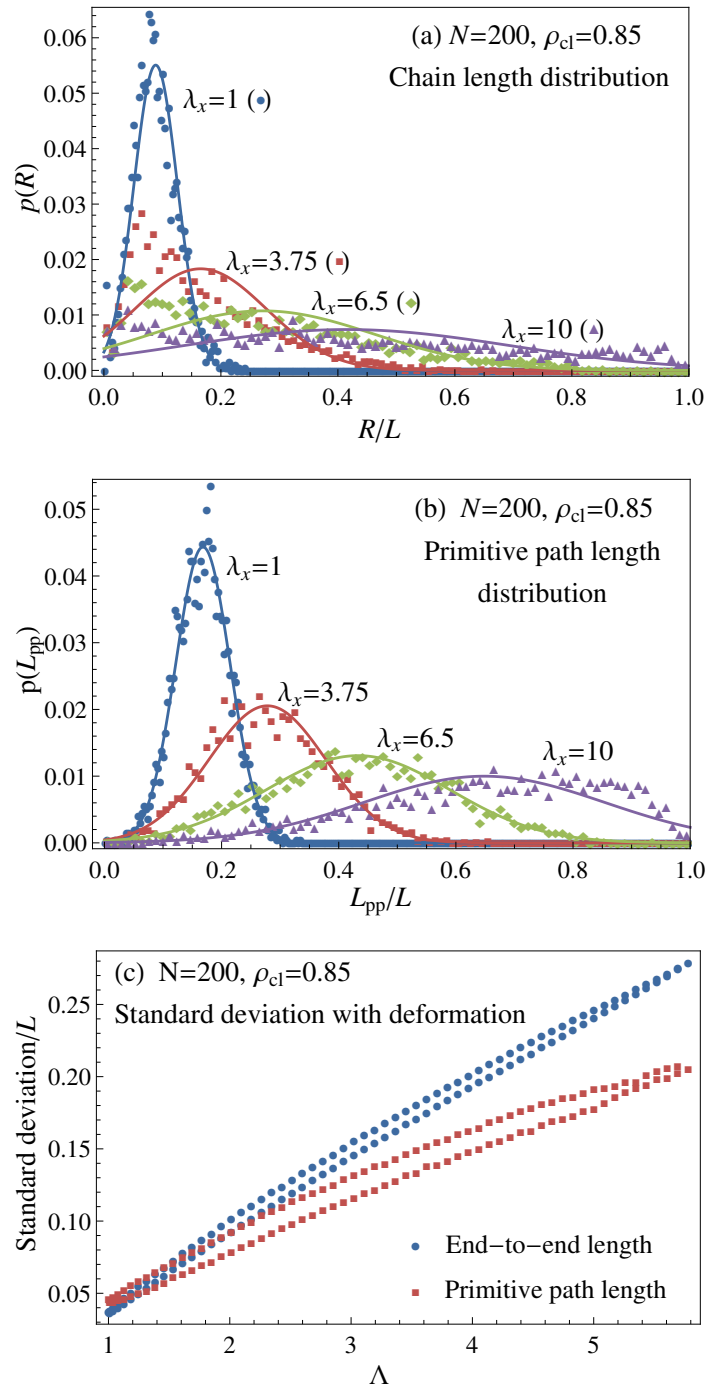


Figure 46: The probability distribution of chain lengths (a) and primitive path lengths (b) for the  $N = 200$ ,  $\rho_{cl} = 0.85$  system with an applied uniaxial stretch. A normal distribution defined by the mean and standard deviation of each distribution (lines) is shown with the data (points) in order to visualize the trends. The standard deviation of each distribution as a function of deformation is shown in (c).

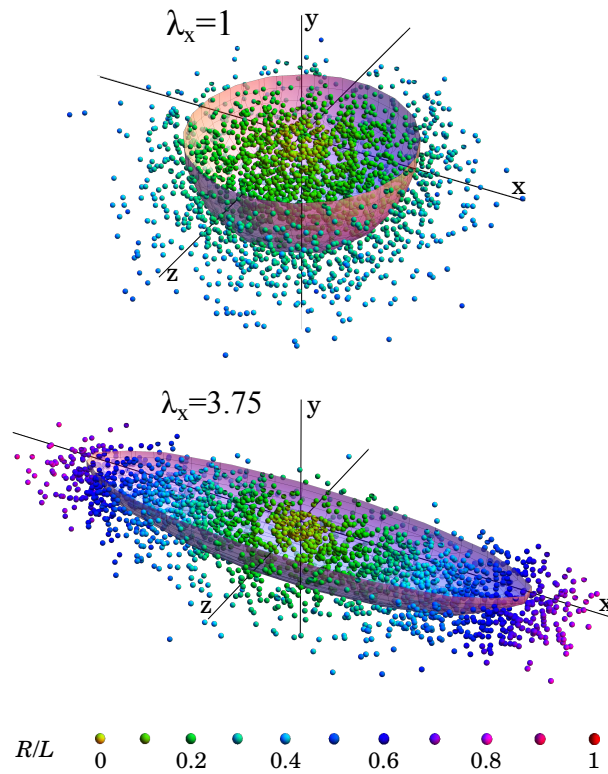


Figure 47: 3D plots of the distribution of chain end-to-end vectors in undeformed and uniaxially deformed states of the  $N = 20$ ,  $\rho_{cl} = 0.45$  system. The half-ellipsoid has axes defined by the RMS chain stretch in each direction and is overlaid for reference. The colors of each point are defined by the end-to-end length of a chain ( $R$ ) divided by its contour length ( $L$ ).



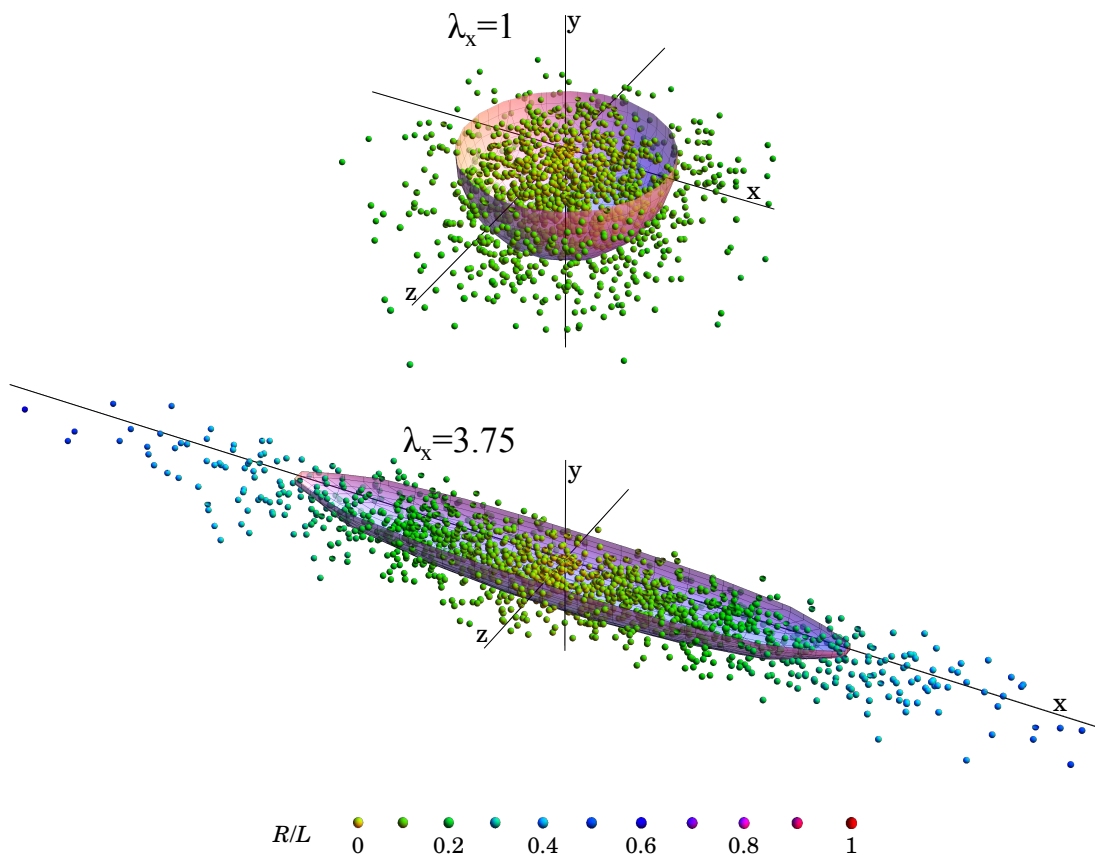


Figure 48: 3D plots of the distribution of chain end-to-end vectors in undeformed and uniaxially deformed states of the  $N = 200$ ,  $\rho_{cl} = 0.85$  system. The half-ellipsoid has axes defined by the RMS chain stretch in each direction and is overlaid for reference. The colors of each point are defined by the end-to-end length of a chain ( $R$ ) divided by its contour length ( $L$ ).

spread in end-to-end lengths after the uniaxial deformation. This spread in end-to-end lengths is most noticeable in the direction of elongation. The next section will take a closer look at this behavior by looking at mean-square end-to-end lengths with respect to the angle of orientation with the axis of elongation for a uniaxial deformation. The end-to-end vectors in the deformed short chain system (Figures 45 and 47) are overall clustered closer to the average in comparison with the long chain system.

### 6.3.1 Angular dependence of end-to-end length distribution

We take a closer look at the distribution of end-to-end chain vectors for the short and long chain systems by analyzing the dependence of end-to-end lengths on the direction of alignment. This is done by comparing the distribution of end-to-end vectors to the surface of a deformed ellipsoid in 3-dimensional space. In Figures 47 and 48 we overlaid a half-ellipsoid over the 3D vector distribution of chain lengths. However, this was done just to visualize the trends. Looking closer, we wish to determine, does the distribution of deformed end-to-end vectors actually conform to the surface of an ellipsoid? In this section we show that an average of the end-to-end chain vectors does form the surface of an ellipsoid, and this ellipsoid is related to the macroscopic stretch via the nonaffine end-to-end deformation parameter  $\beta_{ee}$ . The parameter  $\beta_{ee}$  is determined by an *average* over all chains in the system; the comparison here demonstrates that this average value is sufficient to describe the angular dependence of chain deformation (i.e. a more detailed direction-dependent characterization measure is not needed). This analysis also quantifies the behavior suggested in Figures 47 and 48, that the long chain system has a very large spread in chain lengths in the direction of elongation.

To compare an end-to-end chain vector distribution to the shape of an ellipsoid, some background is first needed. All macroscopic (continuum) deformations conform to the strain ellipsoid in the principal frame. In continuum mechanics, a spherical shape deforms into an ellipsoid. Consider the deformation of a unit sphere shown in Figure 49. The vectors defining each axis of

the undeformed sphere are  $\mathbf{v}_i = \hat{\mathbf{e}}_i$ , where  $i = 1, 2, 3$ . The surface of the unit sphere is defined by the equation

$$x^2 + y^2 + z^2 = 1. \quad (127)$$

Now consider an applied stretch defined by the deformation gradient  $\mathbf{F}$ , whose components are given by the matrix

$$[\mathbf{F}] = \begin{bmatrix} \alpha_1 & 0 & 0 \\ 0 & \alpha_2 & 0 \\ 0 & 0 & \alpha_3 \end{bmatrix}, \quad (128)$$

where the stretches in each direction are  $\alpha_i$ , and only diagonal terms are included because we only consider principal stretches. Consider a point  $\mathbf{p} = (x, y, z)$  on the undeformed surface of the sphere. Using Eq. 128, this point deforms according to

$$\mathbf{p}' = (x', y', z') = \mathbf{F}\mathbf{p} = (\alpha_1 x, \alpha_2 y, \alpha_3 z). \quad (129)$$

Solving for the initial coordinates yields

$$x = \frac{x'}{\alpha_1}, \quad y = \frac{y'}{\alpha_2}, \quad z = \frac{z'}{\alpha_3}.$$

Plugging these values into Eq. 127 yields the equation for an ellipsoid:

$$\left(\frac{x'}{\alpha_1}\right)^2 + \left(\frac{y'}{\alpha_2}\right)^2 + \left(\frac{z'}{\alpha_3}\right)^2 = 1. \quad (130)$$

The axes of the ellipsoid have lengths  $\alpha_i$ , and the vectors that define each axis are  $\mathbf{v}'_i = \mathbf{F}\mathbf{v}_i = \alpha_i \hat{\mathbf{e}}_i$ . A deformed ellipsoid with the axes labeled is shown in Figure 49b. Following the results of Section 6.2, we can define a chain end-to-end stretch ellipsoid with principal stretches ( $\alpha_i$ ) that are related to the macroscopic stretches ( $\lambda_i$ ) via

$$\alpha_i = \sqrt{1 + \beta_{ee} (\lambda_i^2 - 1)}, \quad (131)$$

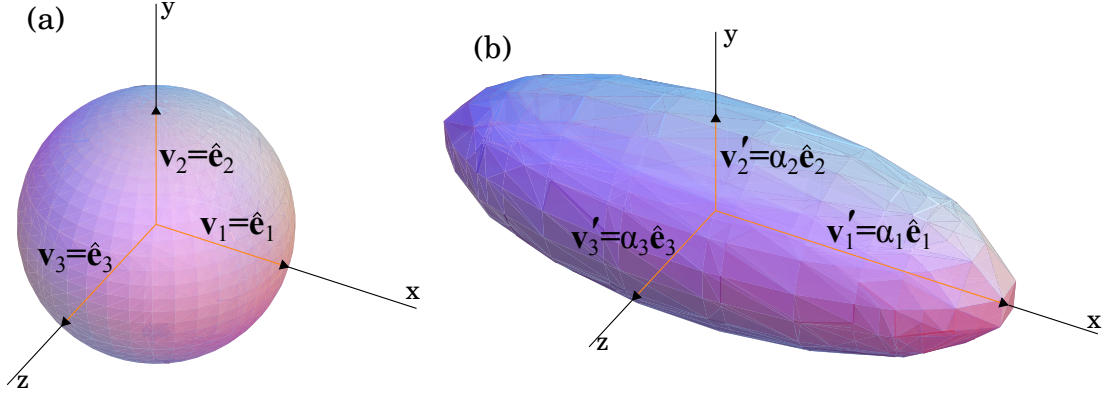


Figure 49: A unit sphere (a) deforms into an ellipsoid (b), with axes defined by the principal stretches.

where the values of  $\beta_{ee}$  are given in Table 7 for the different simulation test cases. With this, the equation of the deformed chain stretch ellipsoid is

$$\frac{(x')^2}{1 + \beta_{ee}(\lambda_1^2 - 1)} + \frac{(y')^2}{1 + \beta_{ee}(\lambda_2^2 - 1)} + \frac{(z')^2}{1 + \beta_{ee}(\lambda_3^2 - 1)} = 1. \quad (132)$$

This expression for the distribution of end-to-end chain lengths depends only on the applied deformation and the nonaffine end-to-end deformation factor  $\beta_{ee}$ . Note that  $\beta_{ee}$  is determined using an average over all chains in the system, regardless of their orientation (see Eq. 123). Comparing the angular dependence of end-to-end lengths with the distribution in Eq. 132 will assess whether the average deformation measure  $\beta_{ee}$  is sufficient to represent the microscopic mechanisms of chain deformation.

We wish to determine if the distribution of end-to-end vectors actually conforms to the surface of an ellipsoid. To formalize this comparison we begin by placing 1001 points on the surface of a unit sphere as shown in Figure 50a.<sup>4</sup> The points on the surface of the sphere will be used to discretize and bin the collection of end-to-end vectors for performing an average. The points are placed quasi-uniformly on the surface of the sphere using the algorithm of Saff and Kuijlaars [148]. Each point on the surface of the sphere deforms according to Eq. 129 with the values of  $\alpha_i$  from Eq. 131. Figure 50b shows points distributed on an ellipsoidal surface after a uniaxial deformation. To

<sup>4</sup> The number 1001 was chosen since it was found to lead to consistent results.

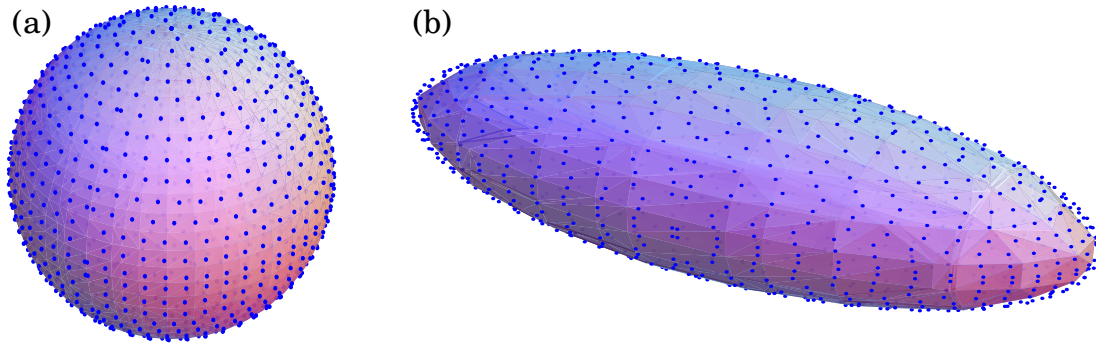


Figure 50: 1001 points placed quasi-uniformly on the surface of (a) a unit sphere, and (b) an ellipsoid.

quantify the mean-square end-to-end length in each direction, the data for end-to-end vectors are placed into different “bins” based on their orientation; the distributed points on the surface of an ellipsoid make up the different bins. The binning procedure is described as follows. We consider only a uniaxial deformation for this calculation. First, one end of each end-to-end vector is placed at the origin (this was also done to make Figures 47-48). The other end of each end-to-end vector is then moved so that it exists in the first quadrant (i.e. all positive coordinates:  $(x, y, z) \rightarrow (|x|, |y|, |z|)$ ). This is done due to the symmetry of the uniaxial deformation.<sup>5</sup> After moving to the first quadrant, an end-to-end vector  $\mathbf{R}$  is placed into the bin for the point  $\mathbf{p}'$  that is closest in terms of the angle between the two vectors. This is repeated until all of the end-to-end vectors are placed into bins. Note that all of the points  $\mathbf{p}'$  used for binning exist in the first quadrant as well. The average and standard deviation of the end-to-end lengths in each bin is then calculated. This entire procedure is repeated for different levels of the applied uniaxial stretch.<sup>6</sup>

We wish to compare the angular dependence of the calculated mean-square end-to-end vector lengths from the simulation results with the surface of the ellipsoid defined in Eq. 132. This can be done by considering end-to-end vector lengths as a function of the angle of orientation with respect to the

<sup>5</sup> Considering the principal directions of deformations, a uniaxial deformation has symmetry about reflections about the  $x$ ,  $y$ , and  $z$  axes. A point at  $-x$ ,  $-y$ , or  $-z$  has the same expected behavior as a point at  $x$ ,  $y$ , or  $z$ , respectively.

<sup>6</sup> An alternative way to calculate the mean-square lengths and standard deviations as a function of the angle of orientation is to sort the end-to-end vectors by angle with respect to the  $x$ -axis, and then define an angular bin size for grouping. The method used here was chosen since the data analysis code for this method was already available.

axis of elongation. The uniaxial deformation is applied in the  $x$ -direction, so a point that lies directly on the  $x$ -axis is assigned an angle of  $0^\circ$ . Points that lie either on the  $y$ -axis or  $z$ -axis have an angle of  $90^\circ$ , and points that lie between this and the  $x$ -axis are assigned appropriate values. With this, the calculated average vector lengths can be plotted as a function of the angle of orientation with the  $x$ -axis. This can then be compared with the surface of the nonaffinely-deforming ellipsoid defined using the parameter  $\beta_{ee}$  in Eq. 132.

Figure 51 shows the result of this calculation for the  $N = 20$ ,  $\rho_{cl} = 0.45$  system, and Figure 52 for the  $N = 200$ ,  $\rho_{cl} = 0.85$  system. Each plot shows the calculated average of end-to-end lengths versus angle of orientation in comparison with the nonaffine ellipsoid defined in Eq. 132. The value of  $\beta_{ee}$  from Table 7 is used to plot Eq. 132 for each system. The standard deviation of end-to-end chain lengths in each bin is included on the plots.

The average end-to-end lengths calculated from the simulation results match Eq. 132 well for both the short and long chain systems. The line for the deformed ellipsoid of Eq. 132 is slightly above the simulation data at the largest deformation of both systems; this is because the root-mean-square value is used to represent the simulation, and also to define the stretches in Eq. 131, instead of the mean. Overall, this shows that the average deformation end-to-end chain vectors do indeed conform to the surface of an ellipsoid. Moreover, the surface of this ellipsoid is defined solely by macroscopic applied stretch and the nonaffine chain end-to-end deformation factor  $\beta_{ee}$

In Figures 45 and 46 we saw that the standard deviation of end-to-end chain lengths increases with deformation for both short and long chain systems. The results in this section provide more detail with respect to this behavior. The short chain system in Figure 51 has a modest increase in the spread of chain end-to-end lengths after deformation. The results look different for the long chain system in Figure 52: a very large increase is seen in the standard deviation of chain end-to-end lengths after deformation. The direction of elongation has the largest spread of chain end-to-end lengths. This result gives more detail on chain deformation mechanisms for systems of long, entangled chains. Although the chains tend to stretch and align with the axis of elongation, there is a wide range of behavior at the microscopic level. Some chains are stretched very far, while others retain short end-to-end distances.

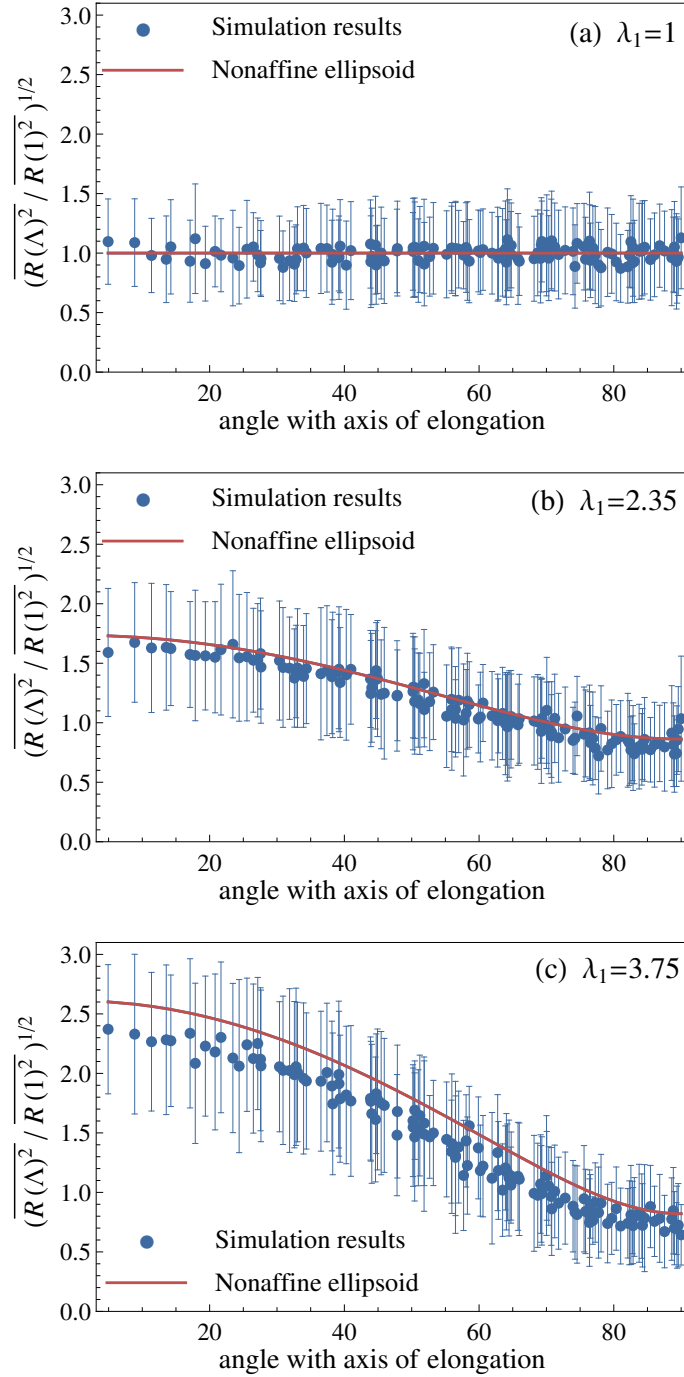


Figure 51: RMS end-to-end chain lengths for the  $N = 20$ ,  $\rho_{cl} = 0.45$  system as a function of the angle of orientation with respect to the axis of elongation. The standard deviation of end-to-end chain lengths in a given “bin” is shown on each plot, and calculated results from the simulations (points) are compared with the nonaffine ellipsoid defined Eq. 132 (lines). The plots are for different levels of a uniaxial applied stretch: (a)  $\lambda_1 = 1$ , (b)  $\lambda_1 = 2.35$ , and (c)  $\lambda_1 = 3.75$ .

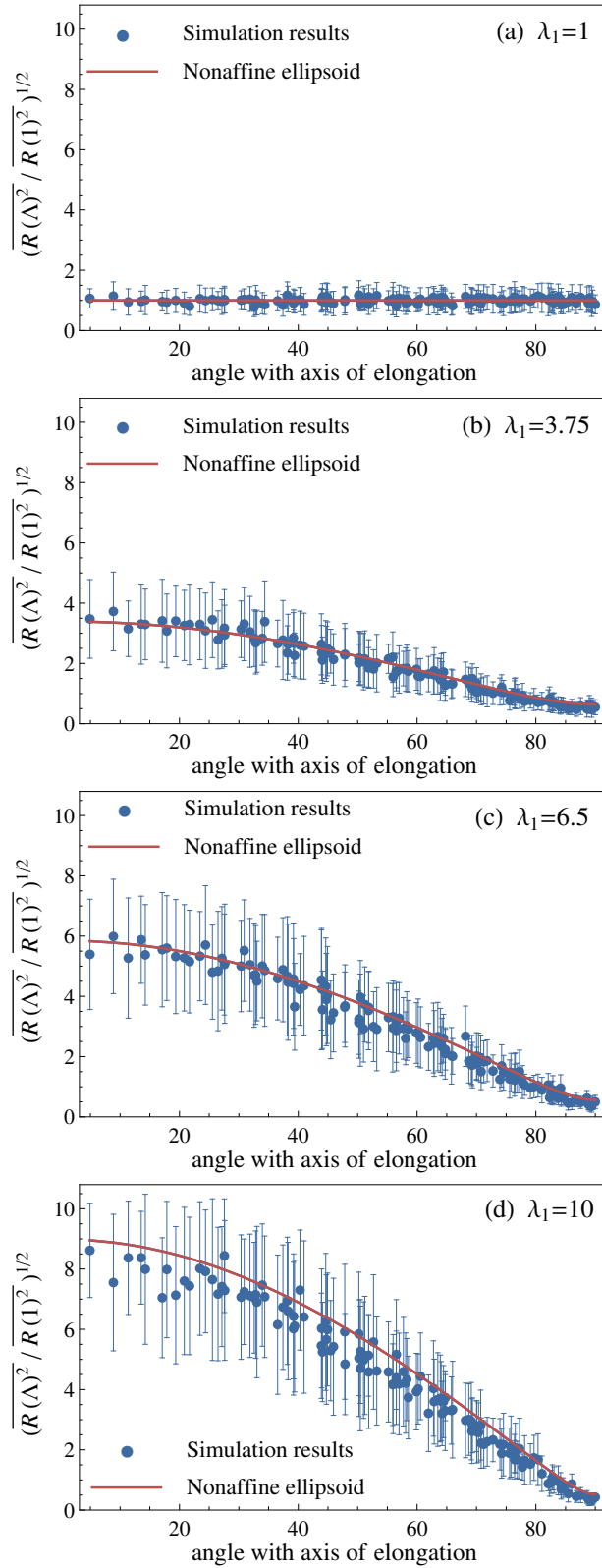


Figure 52: Results for the  $N = 200$ ,  $\rho_{c1} = 0.85$  system in the same manner as Figure 51. The different levels of the uniaxial applied stretch are (a)  $\lambda_1 = 1$ , (b)  $\lambda_1 = 3.75$ , (c)  $\lambda_1 = 6.5$ , and (d)  $\lambda_1 = 10$ .



This behavior is due to entanglements. The next section takes a closer look at this behavior by examining individual chains after deformation.

#### 6.4 PHASE SPACE AND TIME-DEPENDENT CONFORMATIONS

To further examine chain behavior and the difference between chain end-to-end deformation and primitive path deformation we track the conformations of individual chains over time. Figure 53 shows two representative chains in the  $N = 20$ ,  $\rho_{cl} = 0.45$  system. This system has an average of approximately 0.09 entanglements per chain. Note that there is no net diffusion of individual chains over time due to the crosslinks. The time-averaged conformation and primitive path determined by applying the Z1 code [18, 19, 20] to a snapshot at  $t = 0$  are shown in Figure 53 along with the time-dependent conformations over a duration of  $720\tau$  (this is 15.3 times the Rouse relaxation time [33] for these chains). After uniaxial deformation, the primitive path length of each chain increases and the magnitude of monomer fluctuations around the mean path decreases. The time dependent conformations constitute the so-called phase space and show the effective restraining “tube”. For this relatively unentangled system it is seen that the chains tend to undergo simple elongation and align in the direction of the applied deformation. Since the primitive paths of these short, unentangled chains are nearly straight lines, either the primitive path or the chain end-to-end length can be used to accurately represent microscopic deformation. The similarity of chain and primitive path deformation for this short chain system is also reflected in the similarity of the length distributions shown in Figure 45.

The behavior of longer, more entangled chains in a network looks different from the behavior of short chains. Figure 54 shows the time-averaged conformation, time-dependent conformations over a duration of  $16800\tau$ , and primitive path determined from a snapshot at  $t = 0$  for two chains in the  $N = 100$ ,  $\rho_{cl} = 0.85$  system. These chains were tracked for 14.3 times their Rouse relaxation time [33]; since the Rouse time scale as  $N^2$ , the  $N = 100$  system was tracked due to the decreased computational cost in comparison with the  $N = 200$  system. The  $N = 100$ ,  $\rho_{cl} = 0.85$  system has an average of 2.19 kinks per chain. The individual chains in this system no longer undergo

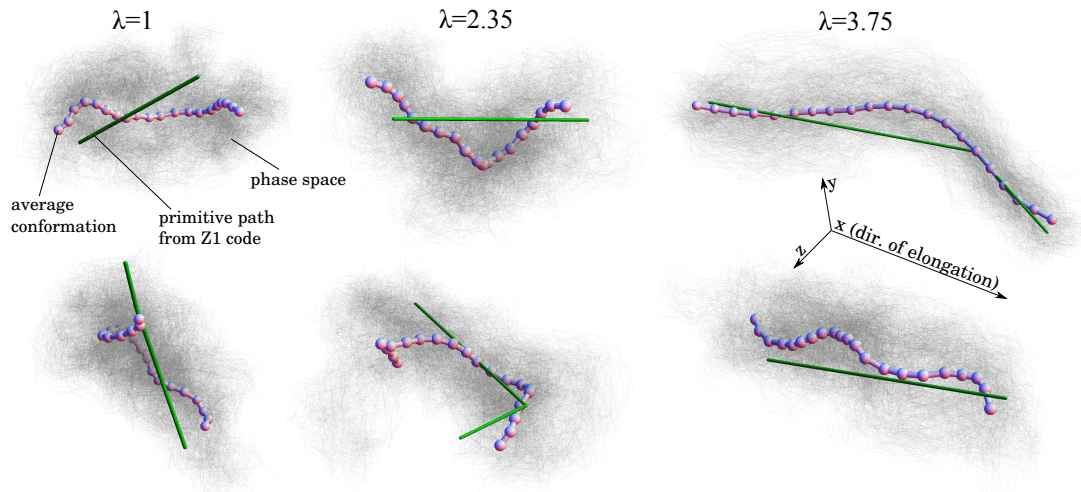


Figure 53: The time averaged chain conformations, primitive paths determined using the Z1 algorithm [18, 20], and phase space of 2 representative chains in the  $N = 20$ ,  $\rho_{cl} = 0.45$  system at various levels of uniaxial deformation:  $\lambda_x = 1$ ,  $\lambda_x = 2.35$ , and  $\lambda_x = 3.75$ . The dark shading (shadow) represents the phase space of each chain, i.e. the region in space the chain explores over time.

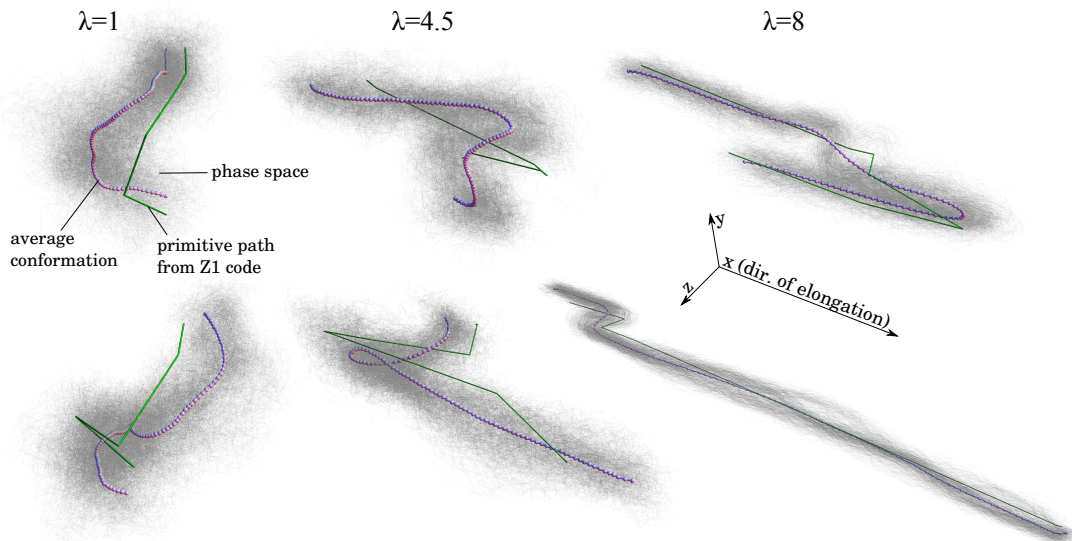


Figure 54: (Color online) The time averaged chain conformations, primitive paths determined using the Z1 algorithm [18, 20], and phase space of 2 representative chains in the  $N = 100$ ,  $\rho_{cl} = 0.85$  system at various levels of uniaxial deformation:  $\lambda_x = 1$ ,  $\lambda_x = 4.5$ , and  $\lambda_x = 8$ . The dark shading (shadow) represents the phase space of each chain, i.e. the region in space the chain explores over time.

simple reorientation and elongation when a uniaxial deformation is applied. It is clear that this behavior is due to the presence of intermolecular entanglements. Figure 54 shows that the chain end-to-end length may be small if the entanglements make the chain coil around, but the primitive path length in such a case will be large. This is the reason for the difference in the chain and primitive path length distributions shown in Figure 46. For a system of long chains with many entanglements, primitive path length is a more accurate description of the available conformational space of individual chains than end-to-end length. Primitive path length also applies equally well as a measure of microscopic deformation in a network of short, unentangled chains, since in the limit of zero entanglements the primitive paths become straight lines which coincide with the chain end-to-end vectors. These results can be combined with the results of nonaffine primitive path deformation from Section 6.2.2 to form a universal description of micro-macro chain deformation in polymer networks.

The results of this chapter bring together several important points about how individual chains deform in both short chain and long chain networks. This discussion is facilitated using the “deformation map” shown in Figure 55. In a network of short, unentangled chains, the end-to-end vectors tend to extend and align with the direction of elongation. Since there are minimal entanglements, most of the primitive paths in a short chain network are straight lines. Considering either primitive path or end-to-end chain length deformation therefore yields virtually identical results.

For a network of long chains, entanglements play an important role in determining the behavior of an individual chain. Although end-to-end chain lengths tend to be extended, there is a very large spread in the end-to-end lengths. This spread is particularly large for chains that are aligned with the axis of elongation. The deformed chains of the  $N = 100$ ,  $\rho_{cl} = 0.85$  system shown in Figures 54 and 55 clearly demonstrate how entanglements lead to a large spread in end-to-end lengths. If a chain has several entanglements it may be highly deformed but retain a short end-to-end length. Depending on how the entanglement constraints are arranged, the chain may also have a long end-to-end length. In either case, the primitive path length will increase. This is why primitive path length is more descriptive of the local deformed behavior

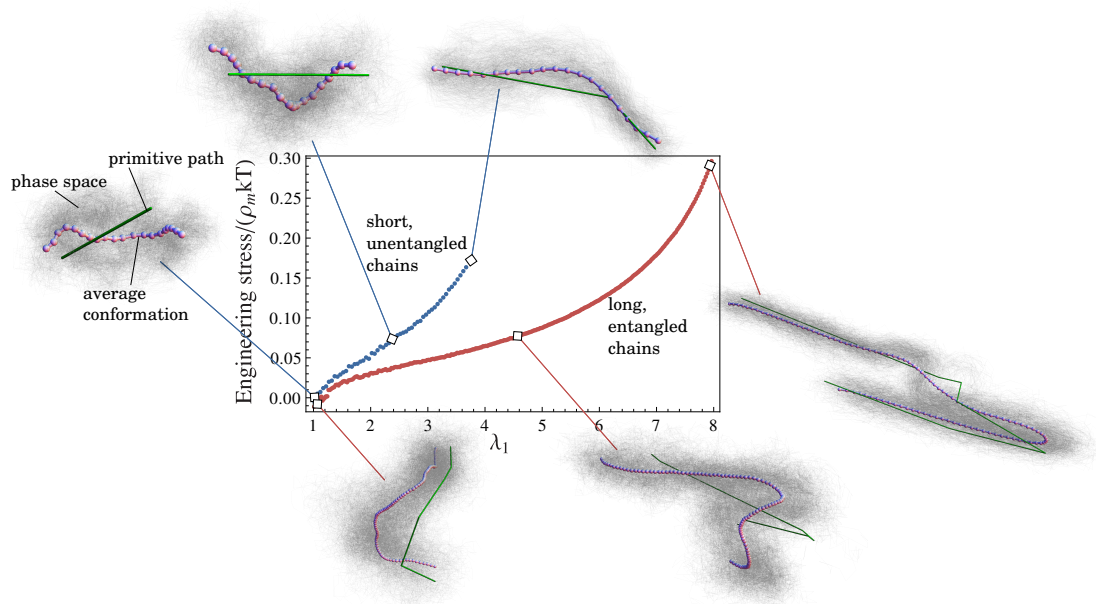


Figure 55: A “deformation map” for the short vs. long chain systems. The uniaxial stress-stretch curve is shown for the short system  $N = 20$ ,  $\rho_{cl} = 0.45$ , and the long chain system  $N = 100$ ,  $\rho_{cl} = 0.85$ . A representative chain is shown at different stretch levels for each system; the chain images are taken from Figures 53 and 54.

of long, entangled chains. At large deformations, such as shown in Figure 55, entanglements play an important role in determining the conformational space available to long chains.

Both chemical crosslinks and physical chain entanglements affect the conformational space available to individual polymer chains; however, they do so in different ways. The chemical crosslinks are fixed, whereas the entanglements do not have a definite location along the length of a chain. The visualization results of Figures 53-55 suggest that entanglements have a role similar to chemical crosslinks in determining the average configuration of a chain. This is also supported by the nonaffine deformation coefficients: the value of  $\beta_{ee}$  for the relatively un-entangled  $N = 20$  systems (especially the  $\rho_{cl} = 0.45$  and  $\rho_{cl} = 0.65$  cases - see Table 7) is about the same as the values of  $\beta_{pp}$  for all the systems. This suggests that the deformation of a section of a chain between kinks is analogous to the deformation of a chain with zero entanglements that is connected to chemical crosslinks at each end. However, although it is easy to count the number of monomers between two chemical crosslinks, it is only possible to assign a representative value to the number of monomers separating entanglements. The fact that entanglements do not have a well-defined location along the length of a chain means that they also affect changes in the magnitude of monomer thermal fluctuations in a different manner than crosslinks. Entanglements make a different overall contribution to the free energy of the system in comparison with crosslinks.

The differences in chain behavior for short and long chain systems lead to different stress-stretch behavior; this is shown in in Figure 55. Short chain systems have few entanglements and display only a small region of strain softening before strain hardening. Long chain systems have many entanglements and can be stretched very far; there is a large region of strain softening in the stress-stretch curve that comes before strain hardening behavior. Although there are many, many chains in a polymer material, the selected chains shown in Figure 55 are representative of the behavior that differentiates short and long chain systems at different locations on the stress-stretch curve.

For an isolated polymer chain, the number of available conformations and the average chain conformation only depends on end-to-end length. Both end-to-end length changes and primitive path length changes are a measure

of chain deformation. The results here show that entanglements significantly influence the average conformations of individual chains in long chain systems. However, changes in primitive path length accurately describe the average conformations of chains in entangled systems. This observation is important since, in a physics-based model of elasticity, a suitable average over microscopic degrees of freedom is used to determine macroscopic mechanical properties. The results here suggest that averaging over end-to-end length changes to calculate macroscopic properties is likely to be insufficient to relate chain behavior to properties, since the average conformation of a chain is influenced by both end-to-end length and entanglements. How this observation relates to multiscale modeling is discussed further in the next section and in Chapter 7.

## 6.5 DISCUSSION

We used MD simulations to perform a systematic analysis of how the number of monomers in a chain and the entanglement density affect the affineness of chain deformation. Both mean-square chain end-to-end length and primitive path length were used to measure microscopic deformation. The average change in these quantities is a linear function of the applied deformation. A more in-depth look showed that the primitive path defines the most accurate length scale in describing micro-macro deformation since it captures effects of entanglements. The affineness of chain end-to-end length deformation was found to increase with both the number of monomers per chain and the entanglement density. However, the simulation results suggest that primitive path deformation is always nonaffine, and shows no trend for networks with different topologies.

The affineness of chain end-to-end deformation appears to depend on three factors: chain length, entanglement density, and crosslink functionality. The phantom network model considers only the effects of crosslink functionality ( $\phi$ ), which was not varied in our simulation test set. Other simulation work has formed networks with different values of  $\phi$ . For example, Dubrovskii and Vasilev [100] used Monte Carlo simulations with the bond fluctuation model to study the effect of junction functionality on elasticity of polymer networks formed via radical polymerization, and found that shear modulus

increases with  $\phi$ . Since we did not vary  $\phi$  in the present work, we cannot comment on whether the phantom network model accurately predicts changes in micro-macro deformation for networks with different  $\phi$ . However, we have shown that it is an incomplete theoretical description since the affineness of end-to-end chain deformation also depends on chain length and entanglement density.

An underlying goal in this and related simulation work is to identify a minimal set of microscopic mechanisms along with a suitable conceptual representation which together can be used to form multiscale models of polymer properties of interest. For crosslinked polymers, these are the nonlinear, rate- and time-dependent mechanical properties. From the results in Sections 6.2-6.4 we can draw several conclusions about an appropriate simplified microscopic description. First, it was seen that both average chain end-to-end and primitive path length deformation follow a simple linear trend for a given network. This suggests that there exists a definite relationship between *undeformed* network topology and how a network *deforms*. To explore this concept we plot the nonaffine deformation parameters  $\beta_{ee}$  and  $\beta_{pp}$  versus the average number of kinks per chain ( $\bar{Z}$ ) for each simulation test case in Figure 56. For very long chains, affine deformation is expected:  $\lim_{\bar{Z} \rightarrow \infty} \beta_{ee}(\bar{Z}) = 1$ . However, as previously noted, it appears that primitive path deformation does not become affine for very long, entangled chains, and does not vary for networks with different microscopic structures.

In Sections 6.3-6.4 we noted that entanglements will cause some of the chain end-to-end distances in a system of long, entangled chains to remain small after deformation. However, primitive path length will always increase with deformation, reflecting the decrease in entropy and decrease in conformational space available to deformed chains. Additionally, it was seen that the nonaffine primitive path deformation parameter  $\beta_{pp}$  is nearly the same for polymer networks with very different microscopic structures. These results together suggest that the primitive path is the most relevant length scale for nonaffine deformation. Using primitive path deformation may be a promising route to link chain conformations with elastic and viscoelastic properties of crosslinked polymers in a multiscale modeling framework. Stephanau et al. [142, 143] have formulated a simulation-informed multiscale model of uncrosslinked

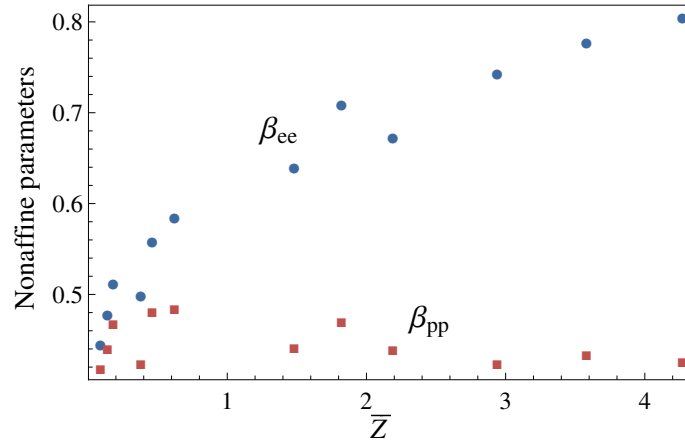


Figure 56: Nonaffine deformation parameters  $\beta_{ee}$  (for chain end-to-end length changes) and  $\beta_{pp}$  (for primitive path length changes) determined from each simulation plotted versus the average number of kinks per chain ( $\bar{Z}$ ).

polymer rheology; the same concept of linking simulation results with systems of equations based on the primitive path concept may be useful for future modeling work on the viscoelastic response of crosslinked polymers. The time-dependent relaxation of primitive path length in crosslinked polymers is one possible mechanism to explore in this regard. Even for very long chains, our simulations suggest that quasistatic primitive path length deformation is not affine. Since nonaffine deformation is due to extensive rearrangement, deformations at high strain rates will be more affine if the rate is fast enough to not allow molecular rearrangement to occur. Molecular rearrangement of the primitive path occurs via chain reptation [33, 149] which has been well-studied with respect to the rheology of uncrosslinked polymer melts [34, 119]. The difference for the crosslinked systems studied here is that average primitive path length will relax to a deformation-dependent equilibrium value; for an uncrosslinked system the primitive path lengths will change until the original, undeformed primitive path statistics are recovered. After, say, a high-rate step deformation, average primitive path length will change via reptation from a more affine value to the “equilibrium affineness” values reported in Section 6.2.2. The investigation of this or related mechanisms will be useful for future efforts in multiscale modeling.

The analysis in this chapter considered changes in end-to-end distance and primitive path length. Another important quantity to describe chain



deformation is the effective “tube” diameter. The tube diameter quantifies the magnitude of monomer fluctuations (see Chapter 3). The effective tube diameter can be estimated using the primitive path length or entanglement length (see, for example, Ref. [25]), or calculated directly by tracking monomer displacements [89, 150, 151]. We note that looking at changes in effective tube diameter along with primitive path length in different deformed networks could be a topic of future work.

## 6.6 CONCLUSIONS

In this work, we performed the first analysis of primitive path deformation in crosslinked polymers. It was shown that both average primitive path length and chain end-to-end length are linear functions of an applied deformation, and that the same linear relationship applies to different deformation states (uniaxial, pure shear, and equi-biaxial deformations). The affineness of microscopic deformation depends on the network topology and was quantified via the nonaffine deformation parameters  $\beta_{ee}$  and  $\beta_{pp}$  for end-to-end length and primitive path length, respectively. We demonstrated a relationship between network topology and microscopic deformation by plotting the nonaffine deformation parameters versus  $\bar{Z}$ , the average number of kinks per chain, for each simulated system. For short chains, it was found that both chain end-to-end and primitive path deformation are nonaffine and follow similar statistics. For long, entangled chains, these measures of deformation differ. Chain end-to-end length deformation approaches an affine value for long chain systems. However, our simulations suggest that primitive path deformation is always nonaffine under quasistatic deformation, even for very long, entangled chains. The statistical analysis and visualization of chain deformation suggests that the primitive path is the correct length scale to quantify microscopic deformation in crosslinked polymers. Although nearly all existing theories of elasticity consider end-to-end chain deformation, the simulations suggest that a model based on primitive path deformation is the most promising route to link microscopic deformations with macroscopic elastic and viscoelastic properties of crosslinked polymers. The simulation results in this work form the basis for such a description.

In this chapter we focused on microscopic deformations for the different simulated systems, and quantified how the affineness of microscopic deformations is affected by chain length and the number of entanglements. In the next chapter we will use these results to look at how the macroscopic elastic stress acting on these networks is affected by network topology and nonaffine deformation.

## CHAPTER 7

### CONNECTING CHAIN BEHAVIOR AND MECHANICAL PROPERTIES

---

In this chapter, we analyze how nonaffine chain deformation and network topology affect the mechanical properties of the different simulated polymer networks. The different simulated networks described in Section 6.1 have a range of molecular network structures; these include networks ranging from short, relatively unentangled chains to long chains with an average of several entanglements per chain. The number of monomers per chain and the average number of entanglements per chain are the two defining characteristics of a given network configuration. In addition to these, we expect nonaffine deformation to play a role in determining the mechanical properties.

In Chapter 6 we performed a detailed analysis of nonaffine chain end-to-end and primitive path deformation for the different simulated networks. It was shown that deformation is generally more affine for chains that are longer and/or more entangled, and primitive path length is a proper descriptive measure of chain deformation in entangled systems. However, nearly all models of rubber elasticity consider end-to-end chain deformation (including the nonaffine network model derived in Chapter 4). The Edwards and Vilgis [11] slip-link model is the only model we are aware of that is based on primitive path deformation.

In this chapter we address two key unanswered questions. First, it is expected that networks with different chain lengths and entanglement densities have different elastic properties, but it is not clear whether nonaffine deformation also has a significant effect on elastic properties. Second, although we noted in the last chapter that primitive path deformation is more descriptive of chain conformations than end-to-end deformation, it is not clear whether the

macroscopic elastic properties can still be accounted for in terms of end-to-end deformation. To answer these questions we first quantify the properties of the different simulated networks in Section 7.1. We then analyze modulus values and compare with model predictions in Section 7.2. The large deformation limiting extensibility behavior of the different networks is analyzed in Section 7.3 by comparing predictions from several different models. Section 7.4 discusses these results in the context of multiscale modeling, and the overall conclusions are summarized in Section 7.5.

## 7.1 SIMULATED MECHANICAL TEST RESULTS

Uniaxial, biaxial, and pure shear tension and compression tests were performed on the simulated test cases via the procedure described in Section 5.3. The samples were deformed to stretch values large enough to exhibit limiting extensibility effects. This section presents stress-stretch data for the different simulated networks and quantifies the differences in mechanical properties by fitting the data.

In Figure 57 we demonstrate the effects of varying chain length ( $N$ ) and density at crosslinking ( $\rho_{cl}$ ). The complete set of stress-stretch data for all the simulated networks is in Appendix C. Figure 57a shows how short vs. long chains affect the large deformation uniaxial response. The modulus increases for the shorter chain systems. Shorter chains also lead to finite extensibility effects at a relatively lower stretch. The samples in Figure 57a were all crosslinked at the same density of  $\rho_{cl} = 0.65$ . The same trend is seen for the systems with different chain lengths crosslinked at either  $\rho_{cl} = 0.45$  or  $\rho_{cl} = 0.85$ . Figure 57b shows uniaxial and biaxial extension test results for systems with a chain length of  $N = 100$  crosslinked at the 3 different densities. In Section 6.1 we quantified how crosslinking at a higher density leads to more entanglements per chain (Table 5). Figure 57b demonstrates how this affects the mechanical response. An increase in the density of entanglements translates into an increase in the initial modulus as well as limiting extensibility occurring at a lower stretch. This shows that large deformation hardening is affected by both crosslinks and entanglements.

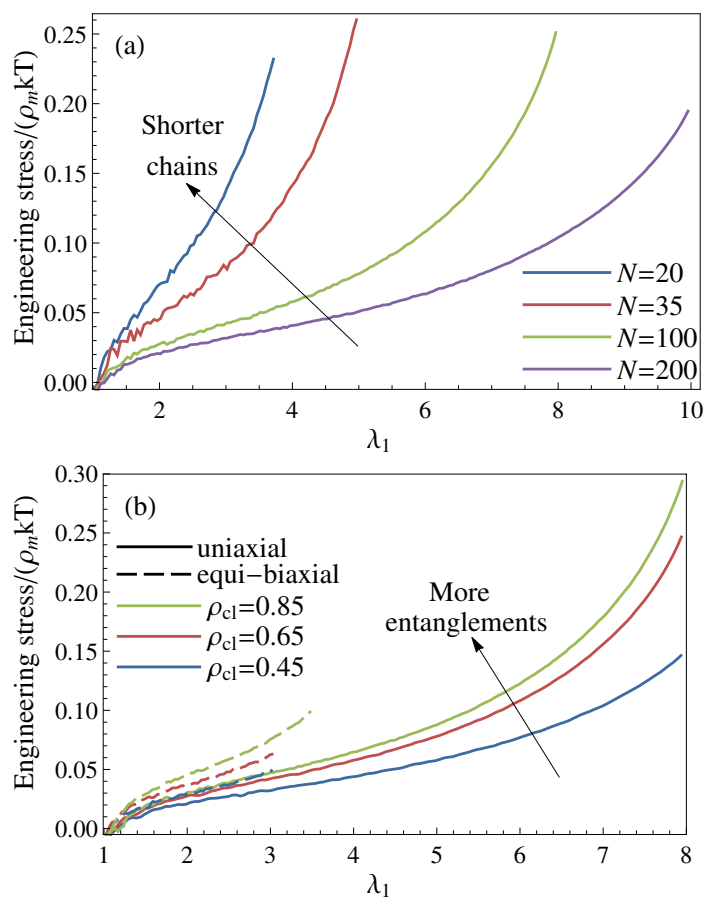


Figure 57: Large deformation stress-stretch results obtained via MD, showing (a) uniaxial deformation of samples with different chain lengths crosslinked at the same density of  $\rho_{cl} = 0.65$ , (b) uniaxial and biaxial deformations of samples with the same chain length ( $N = 100$ ) crosslinked at different densities.

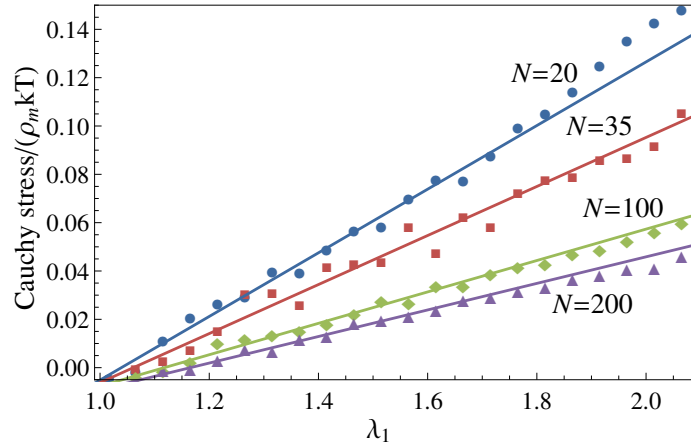


Figure 58: The Young’s modulus was determined by fitting a straight line to the initial linear part of the curve for Cauchy (true) stress versus stretch for a uniaxial deformation. This shows the best fit line for samples with different chain lengths, each case crosslinked at  $\rho_{cl} = 0.65$ .

To quantify the mechanical properties of the different simulation test cases, the modulus was determined by fitting to the initial linear region of the uniaxial stress-stretch curve. A straight line was fit to the Cauchy (true) stress as a function of stretch. An example of the result of this procedure is shown in Figure 58; systems with different  $N$  crosslinked at  $\rho_{cl} = 0.65$  are included in this plot. The slope of the line is the Young’s modulus for each case; the shear modulus ( $G$ ) is this slope divided by 3.<sup>1</sup> The shear modulus is non-dimensionalized as  $\tilde{G} = G/kt\rho_m$  and the values determined by fitting are tabulated for the different networks in Table 8.<sup>2</sup>

We also wish to compare the large deformation limiting stretch behavior. Stress-stretch is nonlinear in this regime and therefore a simple metric to compare different systems does not exist. One method to quantify limiting extensibility is to estimate the location of a stress-stretch asymptote by inspection [152]. This method, however, suffers from a lack of precision and repeatability. Here we use the model from Chapter 4 to quantify limiting extensibility since it is able to fit the data for all of the simulation test cases. This leads to a well-

- 1 This relationship between the Young’s modulus and the shear modulus holds for an isotropic, incompressible, linear elastic material. Since we are fitting to the initial linear region of the stress-stretch curve, these assumptions hold for the stretch ranges shown in Figure 58
- 2 Either the Young’s modulus or the shear modulus could be used to compare properties of the different networks; the shear modulus was chosen here because of the simplicity in comparing with model parameter definitions.

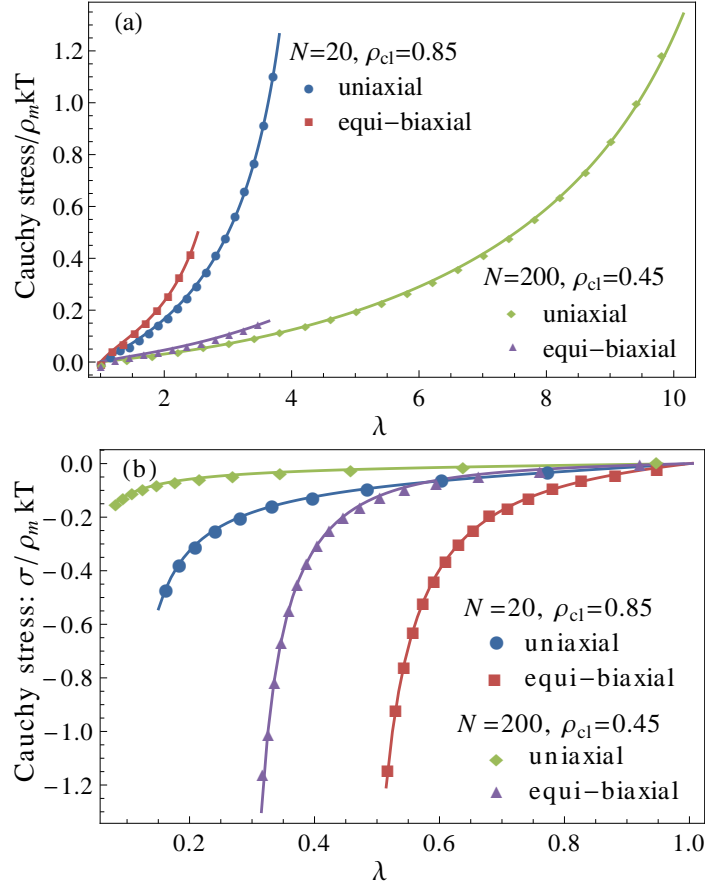


Figure 59: Stress-stretch data with the nonaffine network model fit to two simulated systems with very different mechanical properties. The model parameters are optimized to simultaneously fit uniaxial and biaxial extension and compression data. Fit results are shown for extension (a) and compression (b).

defined measure of the limiting stretch. Using the strain energy function in Eq. 109, the parameters  $G_c$ ,  $G_e$ , and  $\lambda_{max}$  were determined by simultaneously fitting to both uniaxial and biaxial tension and compression stress-stretch results. Fits were performed using the Monte Carlo fitting procedure described in Appendix A.

Figure 59 shows an example of the nonaffine network model fit to two simulated systems with very different mechanical properties. The  $N = 20, \rho_{cl} = 0.85$  system has the highest modulus of the simulated systems ( $\tilde{G} = 0.0433$ ), and the  $N = 200, \rho_{cl} = 0.45$  system has the lowest modulus ( $\tilde{G} = 0.0101$ ). Figure 59 demonstrates the ability of the nonaffine network model to fit data

Test case		Linear fit	Model fit		
$\rho_{cl}$	N	$\tilde{G}$	$\tilde{G}_c + \tilde{G}_e$	$\tilde{G}_e/\tilde{G}_c$	$\lambda_{max}$
0.45	20	0.035	0.029	0.20	2.91
	35	0.025	0.021	0.29	3.84
	100	0.019	0.013	0.51	5.89
	200	0.015	0.010	0.66	7.49
0.65	20	0.044	0.038	0.28	2.78
	35	0.034	0.029	0.34	3.52
	100	0.022	0.017	0.44	5.47
	200	0.018	0.013	0.62	7.04
0.85	20	0.052	0.043	0.22	2.71
	35	0.036	0.034	0.30	3.45
	100	0.025	0.020	0.56	5.39
	200	0.022	0.016	0.55	6.70

Table 8: Tabulated properties for the different systems. The modulus  $\tilde{G}$  was determined by fitting to the linear region of uniaxial stress-stretch, and the model parameters were determined via a fit to uniaxial and biaxial stress-stretch curves.

for the different deformation states of these systems. Appendix C contains plots of stress-stretch data with the fit of the nonaffine network model for all of the different test cases.

The parameters of the nonaffine network model are non-dimensionalized with  $\tilde{G}_c = G_c/kt\rho_m$  and  $\tilde{G}_e = G_e/kt\rho_m$ , and the shear modulus can be calculated using these fit values as  $\tilde{G}_c + \tilde{G}_e$ . These values are tabulated in Table 8 along with the softening ratio ( $\tilde{G}_e/\tilde{G}_c$ ) and  $\lambda_{max}$  for each simulated network.

Although the values of  $\tilde{G}_c + \tilde{G}_e$  are close to  $\tilde{G}$ , these values are not equal due to the fitting procedure that was used. The model fit parameters are optimized to fit the entire uniaxial and biaxial stress-stretch curves for both tension and compression, and the shear modulus  $\tilde{G}$  was determined by fitting to only the small deformation uniaxial tension response. Either determination of the shear modulus shows the same trend: modulus decreases with N for a given  $\rho_{cl}$ , and increases with  $\rho_{cl}$  for constant N. We will use the definition of the shear



modulus from the linear fit to small deformation data when comparing the modulus values of the different networks in the next section.

The influence of the softening ratio ( $\tilde{G}_e/\tilde{G}_c$ ) on stress-stretch was previously discussed in Section 4.1 and demonstrated in Figure 32. A material with a higher softening ratio will have a larger decrease in the tangent modulus at intermediate deformations. The softening ratio generally increases with N for chains crosslinked at a given  $\rho_{cl}$ .

Finite extensibility is quantified by the best fit value of  $\lambda_{max}$ . The fit values of  $\lambda_{max}$  in Table 8 increase with chain length (N), and decrease with the density at crosslinking ( $\rho_{cl}$ ). We saw in Section 6.1 that the number of entanglements per chain is larger for systems crosslinked at higher  $\rho_{cl}$ . A simple description of the trends for finite extensibility is that  $\lambda_{max}$  decreases for networks of chains that are shorter and/or more entangled. In Section 7.3 we will test the ability of several models to capture this trend for the changes in  $\lambda_{max}$ .

## 7.2 MODULUS DEPENDS ON NONAFFINE DEFORMATION

In this section we demonstrate how nonaffine chain end-to-end deformation affects the modulus of the different simulated polymer networks. The Rubinstein and Panyukov [5, 6] nonaffine tube model and the nonaffine network model (Chapter 4) are used to analyze trends in the data. Although this comparison shows some promising results, we note several difficulties that surround the approach.

Different models of rubber elasticity were reviewed in Chapter 3. The simplest of these is the affine network model, which predicts a shear modulus of  $\tilde{G}^{affine} = 1/N$  (the non-dimensionalization here is the same used for other modulus values). This result is derived by considering affine deformation of non-interacting chains and is found in Eq. 30 of Chapter 3. We refer to this as the classical prediction for the modulus. The simulation results do not follow this prediction because of intermolecular interactions and nonaffine deformation. The trend of increasing modulus with increasing affineness of deformation is demonstrated by plotting the ratio of measured modulus to the classical prediction ( $\tilde{G}/\tilde{G}^{affine}$ ) as a function of the nonaffine deformation

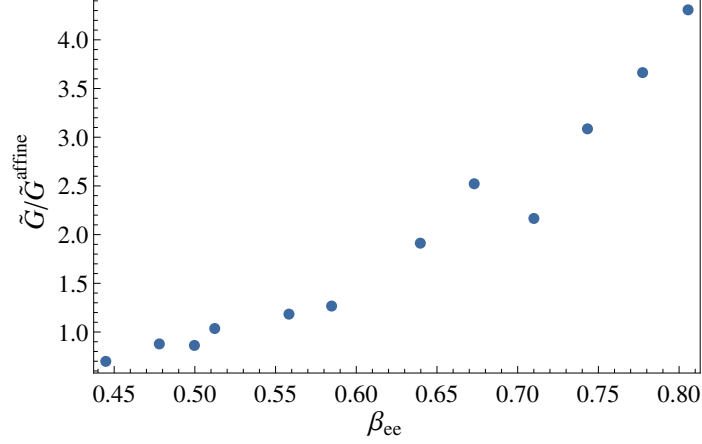


Figure 60: The departure of the measured modulus values from the classical prediction shows a correlation with the affinity of deformation of chain end-to-end distance.

parameter  $\beta_{ee}$ . This parameter was defined in Eq. 123 of the previous chapter via the relation

$$\frac{\overline{R^2(\Lambda)}}{\overline{R^2(1)}} = \beta_{ee}\Lambda^2 + C_{ee},$$

where  $\overline{R(\Lambda)^2}$  is deformed mean-square end-to-end chain length,  $\overline{R(1)^2}$  is undeformed mean-square end-to-end chain length,  $C_{ee}$  is a constant, and  $\Lambda$  is the normalized first invariant defined in Eq. 77. The values of  $\beta_{ee}$  determined for each simulation test case are contained in Table 7 of Chapter 6. Figure 60 shows a clear trend of increasing deviations from the classical prediction for modulus with increasing affinity of end-to-end chain deformation.

To further analyze the influence of nonaffine deformation on modulus we compare the measured modulus values to predictions from two different models:

- **The Rubinstein and Panyukov nonaffine tube model** [5, 6] is used since it has parameters defined solely in terms of network characteristics and has previously been applied to interpret simulation results [17, 82, 100, 104]. This model contains two terms: a phantom-network term plus a contribution from a chain confined to a nonaffine tube. The stress-stretch behavior for this model is in Eq. 71, with parameter definitions in Eq. 69. The shear modulus is the sum of the two moduli parameters

$G_c^{\text{NA}}$  and  $G_e^{\text{NA}}$  defined in Eq. 69; this can be shown by considering small deformations in Eq. 71. This leads to a prediction for the non-dimensionalized shear modulus of [5, 6]

$$\tilde{G}^{\text{NA}} = \frac{1 - 2/\bar{\phi}}{N} + \frac{1}{2N_e},$$

where the superscript “NA” is used to denote the nonaffine tube model.

- **The nonaffine network model** [21] of Chapter 4 generalizes the non-affine tube model to describe large deformation hardening and general nonaffine chain end-to-end deformation. All of the parameters can be defined using simulation results, and it was shown in the previous section that the model can be used to fit all of the data for the different simulation test cases. The shear modulus for this model can be obtained by assuming small deformations in Eq. 108. This yields a shear modulus that is the sum of the two parameters  $G_c$  and  $G_e$ , which are defined in Eqs. 101 and 107, respectively. The factor  $G_e$  is the same as in the nonaffine tube model (i.e.  $G_e = G_c^{\text{NA}}$ ). With this, the prediction for the non-dimensionalized shear modulus is

$$\tilde{G}^{\text{NAN}} = \frac{g^2 (1 - 2/\bar{\phi})}{N} + \frac{1}{2N_e},$$

where the superscript “NAN” is used to denote the nonaffine network model.

The only difference between these two model predictions is the non-phantom parameter  $g$ . In the previous chapter we showed that the simulations do not follow phantom network predictions for micro-macro deformation behavior. The value of  $g$  was measured for the different test cases (Table 7). Comparing the measured vs. predicted modulus values for these two models serves to assess whether non-phantom chain end-to-end deformation is a significant factor in determining the modulus.

The values of  $N$  and  $\bar{\phi}$  are listed in Table 5 for each system and values of  $g$  are in Table 7. To calculate the predicted value of the modulus we need to determine values of the entanglement length,  $N_e$ . The difficulty with this lies

in the fact that entanglement length is not a well-defined parameter. There is no current consensus on how it can be determined from the output of an MD simulation. Theoretically,  $N_e$  is a measure of the average number of monomers between entanglements. A simple estimate for  $N_e$  was given in Eq. 24 of Chapter 2. However, this equation is not suitable for use with short chain systems [25]. For a short chain system with an average of less than one entanglement per chain the entanglement length should become greater than the number of monomers per chain (i.e.  $N_e$  should become greater than  $N$ ); Eq. 24 does not satisfy this requirement. Hoy et al. [25] addressed this issue and came up with new estimators for entanglement length that follow the expected behavior for short chain systems. These include the modified S-coil ( $N_e^{\text{S-coil}}$ ) and the modified S-kink ( $N_e^{\text{S-kink}}$ ) measures of entanglement length. There is a well-known difference between these quantities in the limiting case of long, entangled chains (see, example, Refs. [25, 124]).  $N_e^{\text{S-coil}}$  is called the rheological entanglement length since it is the measure that has been shown to correlate with rheological trends [25, 111]. For long chain systems, the rheological entanglement length is approximately a factor of two higher than  $N_e^{\text{S-kink}}$ , which is called the topological entanglement length since it is defined by direct enumeration of the topological entanglements. These measures are calculated in relation to molecular quantities using

$$N_e^{\text{S-coil}} = (N - 1) \left( \frac{\overline{L_{pp}^2}}{\overline{R^2}} - 1 \right)^{-1}, \quad (133)$$

$$N_e^{\text{S-kink}} = \frac{N}{\overline{Z}}, \quad (134)$$

where the overline is an ensemble average,  $Z$  is the number of kinks per chain, and  $L_{pp}$  and  $R$  refer to the undeformed primitive path length and end-to-end chain length, respectively. The “coil” nomenclature in  $N_e^{\text{S-coil}}$  is used since this measure of entanglement length is determined by relating to  $\overline{R^2}$ , which is a measure of the tendency of the chains to coil (a lower  $\overline{R^2}$  value for a given value of  $N$  represents chains that are more coiled). Likewise, the “kink” in  $N_e^{\text{S-kink}}$  is used since this measure is related to the average number of kinks per chain. The values of  $N_e^{\text{S-coil}}$  and  $N_e^{\text{S-kink}}$  for each simulation test case are listed in Table 9. Since rheological entanglement length is related to the plateau

Test case		N <sub>e</sub> calculation	
$\rho_{cl}$	N	N <sub>e</sub> <sup>S-kink</sup>	N <sub>e</sub> <sup>S-coil</sup>
0.45	20	236.5	245.2
	35	95.0	156.7
	100	68.3	145.8
	200	68.4	137.0
0.65	20	144.4	192.3
	35	77.9	135.0
	100	55.5	117.9
	200	56.1	111.4
0.85	20	115.4	162.3
	35	58.3	107.0
	100	46.1	90.3
	200	47.1	87.1

Table 9: The values of rheological entanglement length,  $N_e^{S-coil}$ , and topological entanglement length,  $N_e^{S-kink}$ , for each simulation test case. The S-coil and S-kink measures of entanglement length were proposed by Hoy et al. [25].

modulus of an uncrosslinked melt [25, 124], we choose to use  $N_e = N_e^{S-coil}$  to determine model predictions for modulus. (Recall that  $G_e$  may be identified as the plateau modulus of an uncrosslinked polymer melt - see note 3 in Chapter 4). This choice of  $N_e$  and other considerations with respect to the plateau modulus are discussed at the end of this section.

We now have all values required to calculate model predictions and proceed with the comparison. Figure 61 shows the fit modulus values plotted versus the predicted values for these two models. The different symbols in Figure 61 denote the systems with different chain lengths, and the symbols are filled in according to the monomer density at crosslinking. For a given chain length the modulus increases for the systems crosslinked at a higher density. A straight line is shown on each plot in Figure 61 in order to demonstrate scaling behavior. We judge the predictions of a given model to be successful if the data points for predicted vs. fit parameters collapse onto a single linear trend line. With this metric, a model is deemed successful if it captures *changes* in parameter values for the different systems; a quantitative agreement between

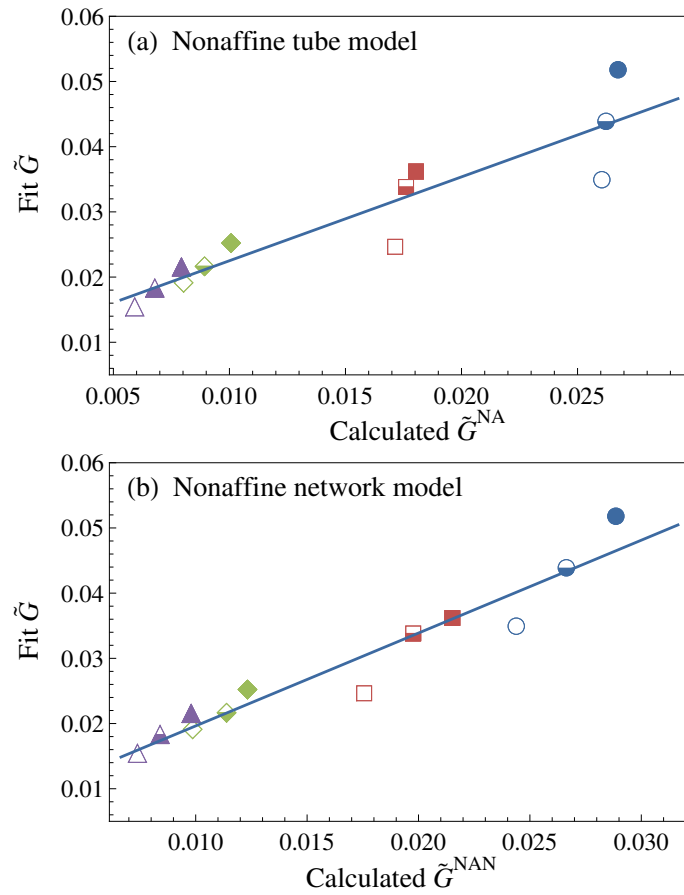


Figure 61: A comparison of the measured to the predicted modulus values for the nonaffine tube and nonaffine network models. A linear fit is shown on each to highlight the predicted trend. The simulation data points are shown for chain lengths of 20 (blue circles), 35 (red squares), 100 (green diamonds), and 200 (purple triangles), each crosslinked at the different densities:  $\rho_{cl} = 0.45$  (open symbols), 0.65 (half-filled), and 0.85 (filled symbols).

fit and calculated parameters is not required. This approach is essentially an analysis of scaling behavior. Since each model necessarily contains a set of simplifying assumptions, we seek to identify scaling parameters or laws for each model of micro-macro deformation. The requirement of a quantitative modulus prediction can obfuscate the reasons a given model prediction may be insufficient. Indeed, both of the models do not quantitatively predict the measured modulus values.<sup>3</sup> The concept of scaling behavior in polymers has, of course, a long history [32]. Current work on coarse-grained simulations of uncrosslinked polymers has looked at the scaling behavior of the plateau modulus for different systems [111, 112, 123, 128, 129]. Although the elastic modulus<sup>4</sup> of a crosslinked polymer depends on more microscopic factors (i.e. both crosslinks and entanglements) than the plateau modulus of a melt (which depends only on entanglements), we are able to perform a quantitative assessment since the simulation test set includes cases with both different chain lengths and entanglement densities.

In the analysis shown here, the nonaffine network model is able to most closely collapse the predicted vs. measured modulus values to a linear trend. For a given chain length, the modulus increases for a system crosslinked at a higher density since this leads to an increased number of entanglements. The affineness of chain end-to-end deformation also increases when chains are longer and/or more entangled.

Although these results suggest that nonaffine deformation of chain ends is an important factor in determining the modulus, several limitations must be noted with respect to the methods of analysis used in this section. In particular, we consider the definition of the modulus parameter  $G_e$ . This parameter is identified as the plateau modulus, which can be measured in the melt state

---

<sup>3</sup> This is true of all of the models reviewed in Chapter 3 as well: none are able to quantitatively predict the measured modulus values of all of the simulation test cases.

<sup>4</sup> By elastic modulus, we mean a coefficient that measures the ability of a material to resist a change in shape. This can take the form of the Young's modulus (uniaxial deformation), shear modulus (shear deformation), or other similar measures. Here, we used the shear modulus to analyze results. However, since the simulated materials are isotropic and incompressible and only linear stress-stretch behavior is considered, any measure of the modulus would have led to identical results. The term "elastic modulus" is used here instead of "shear modulus" to refer to this generality.

before crosslinking. The nonaffine tube and nonaffine network models both have

$$G_e = \frac{1}{2} \frac{\rho_m kT}{N_e},$$

and we used the modified S-coil measure of rheological entanglement length [25] to determine  $N_e$  in both models. Although it is accepted that  $G_e \propto 1/N_e$ , different factors of proportionality have been used (see note 3 in Chapter 4). The models in this section have a factor of 1/2 in the definition of  $G_e$ . The choice of prefactor in  $G_e$  affects results, since it affects the ratio of the two modulus terms. An alternative method of data analysis would determine the plateau modulus before crosslinking, and then use this value to compare modulus trends. This would fix the problem about the numerical prefactor; however, it is not clear whether such a study would yield any additional insights. The real difficulty is on the theoretical side, since it is desired to capture the effects of both crosslinks and entanglements in a consistent manner. For example, it would be interesting to perform the same analysis of modulus trends to test the predictions of a model based on nonaffine primitive path deformation, if such a model existed. Here, we saw that the nonaffine network model can reasonably describe the trends in modulus values when the nonaffine end-to-end deformation factor  $g$  is known and the modified S-coil measure of  $N_e$  is used. Although this comparison is promising, it remains an open question as to what is the best way to relate network topology and chain deformation to macroscopic modulus.

### 7.3 LIMITING EXTENSIBILITY: SIMULATION RESULTS VS. MODEL PREDICTIONS

In this section, we investigate the measured vs. predicted trends for limiting extensibility of the different simulated networks. This is done in a similar fashion to the comparison of modulus trends contained in the previous section. The limiting stretch value for each simulation test case is quantified by the fit



parameter  $\lambda_{\max}$ , and the best fit values are contained in Table 8. First recall the definition of the normalized first invariant from Eq. 77:

$$\Lambda = \sqrt{\frac{\lambda_1^2 + \lambda_2^2 + \lambda_3^2}{3}}.$$

Limiting extensibility occurs in the nonaffine network model when  $\Lambda \rightarrow \lambda_{\max}$ . For this model,  $\lambda_{\max}$  is defined in terms of molecular parameters and nonaffine deformation in Eq. 104. A comparison with other models is made as follows. We determine the value of  $\Lambda$  which causes a given model to have an unbounded increase in the free energy function. This value is assigned to be the predicted value of the limiting extensibility parameter for that model. The predicted value is calculated using known network properties and deformation behavior. These predicted values are compared with fit values of  $\lambda_{\max}$  for the different models. The models considered for comparison in this section include:

- **The Arruda and Boyce 8-chain model** [8] is considered since it is a popular choice for modeling the large deformation behavior of rubber-like materials. This model was reviewed in Section 3.1; it is derived by considering 8 chains placed at the corners of a box which deforms affinely with the applied stretch. Each chain follows Langevin statistics (Eq. 20) and deforms according to Eq. 74. The strain energy function for this model is in Eq. 75. It is predicted that finite extensibility occurs when

$$\Lambda \rightarrow \sqrt{N},$$

so the predicted parameter value is set to

$$\lambda_{\max}^{8C} = \sqrt{N},$$

where the superscript “8C” denotes the 8-chain model.

- **The nonaffine network model** [21] of Chapter 4 is derived by considering two parts: a network component represented by Langevin chains that deform nonaffinely with the applied stretch, and a tube component represented by a chain with its fluctuations restricted by a nonaffine tube. Only the network component contributes to limiting extensibility. This

model predicts a finite extensibility value that differs from the 8-chain model by the inclusion of nonaffine deformation. The free energy function is in Eq. 109 with parameters in Eqs. 101, 104, and 107. It is predicted that finite extensibility occurs when

$$\Lambda \rightarrow \frac{1}{g} \sqrt{\frac{N}{1-2/\phi'}}$$

so the predicted parameter value is set to

$$\lambda_{\max}^{\text{NAN}} = \frac{1}{g} \sqrt{\frac{N}{1-2/\phi'}}$$

where the superscript “NAN” denotes the nonaffine network model.

- **The Edwards and Vilgis slip-link model [11]** is used since it can capture large deformation limiting extensibility, and has previously been used to analyze micro-macro property relationships [55, 153]. This model is derived by considering an affine deformation of the primitive path length. Entanglements are treated as “slip-links” which are free to move (slip) a distance equal to the primitive path step length, and crosslinks are accounted for by considering the limit of zero slip. In the slip-link model derivation, the primitive path is considered to be a random walk of constant step length. In a real system, simulations have shown that the primitive path is not completely a random walk, since the step sizes are not constant for typical chain sizes [19, 122, 123]. However, if the chains are *very* long, the random walk approximation becomes reasonable [123]. We therefore may expect a better agreement between model and simulation results for long chain systems. The slip-link model was introduced and fit to several experimental data sets in Section 3.2. The free energy function is in Eq. 80 with parameter definitions in Eq. 81. It is predicted that finite extensibility occurs when

$$\Lambda \rightarrow \frac{L}{L_{\text{pp}}(1)\sqrt{3}}$$

so the predicted parameter value is set to

$$\lambda_{\max}^{\text{SL}} = \frac{L}{L_{\text{pp}}(1)\sqrt{3}},$$

where the superscript “SL” denotes the slip-link model, and  $L$  is the contour length of the chains in the simulation. With this description, finite extensibility effects occur when the primitive path length nears the contour length of the chains.

The nonaffine tube model is not included here since it does not capture large deformation limiting extensibility behavior. The scaling predictions of the 8-chain and nonaffine network models differ only by the inclusion of nonaffine deformation. The slip-link model presents a different description of limiting extensibility, which is based on the primitive path. We compare the measured vs. predicted values of limiting extensibility for each model.<sup>5</sup> All of the values needed to calculate the predicted value of  $\lambda_{\max}$  for the 8-chain, nonaffine network, and slip-link models are listed in Tables 5 and 7, and the fit  $\lambda_{\max}$  values are listed in Table 8.

Figure 62 shows the measured (fit) value of  $\lambda_{\max}$  plotted versus the predicted value for the three different models. For a given chain length,  $\lambda_{\max}$  decreases for a system crosslinked at a higher density. Since the 8-chain model prediction for  $\lambda_{\max}$  only depends on chain length, this model does not differentiate between systems with the same chain length but different entanglement densities. This is shown by the vertical groupings of points in Figure 62a; the fit values (y-axis) change for these different systems, but the calculated values (x-axis) do not. The nonaffine network model changes the prediction by including nonaffine deformation and the non-phantom deformation factor  $g$ . From Chapter 6 we know that nonaffine deformation depends on both chain

---

<sup>5</sup> The measured value refers to the value of  $\lambda_{\max}$  determined in Section 7.1 by fitting the nonaffine network model to the simulation data. Note that any model that can capture the full range of stress-stretch behavior could have been used to quantify limiting extensibility. Such models include (among others), the slip-link [11], extended tube [12], ABGI [13], and micro-sphere [14] models that were reviewed and discussed in Chapters 3-4. Although fitting a different model leads to slightly different values for limiting extensibility, the differences are not large and the trends will be the same as long as the model is able to properly fit all of the stress-stretch data. The nonaffine network model is used for simplicity because it has the fewest parameters of these different models.

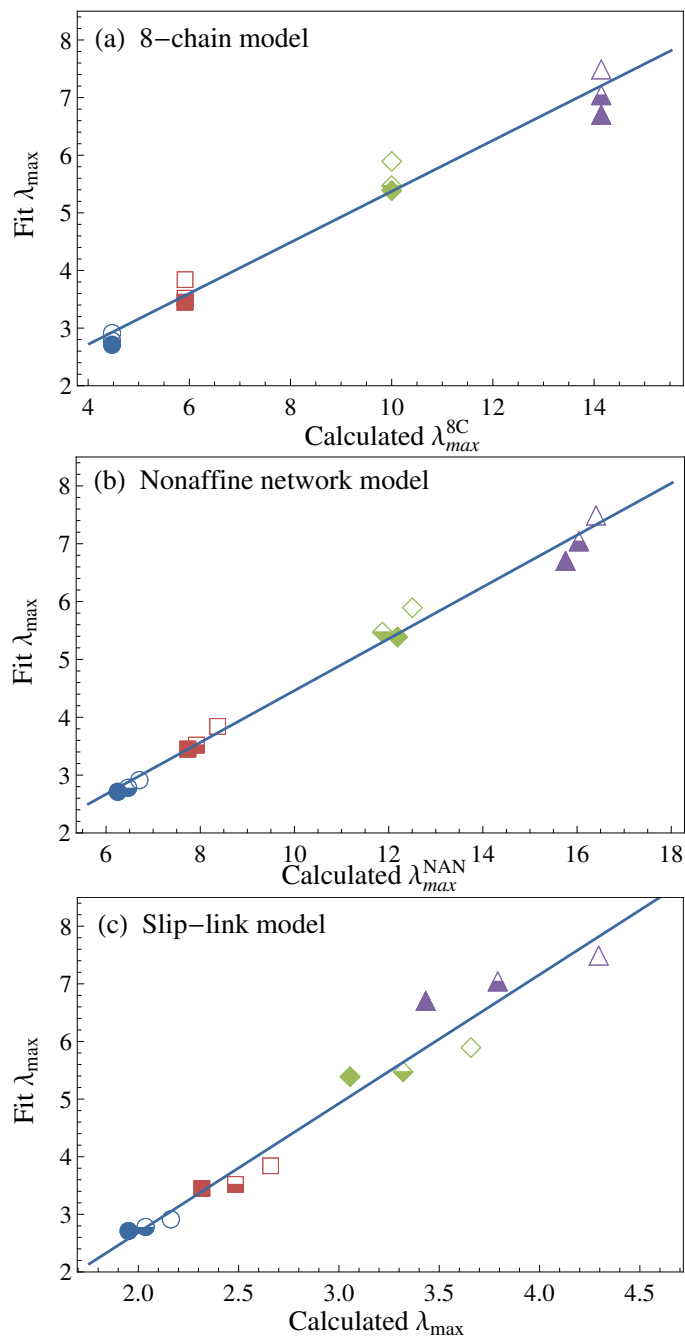


Figure 62: A comparison of the limiting extensibility parameter value  $\lambda_{max}$  obtained by curve fitting to the predicted value for (a) the 8-chain model [8], (b) the nonaffine network model [21], and (c) the slip-link model [11]. A linear fit is shown on each to highlight the predicted trend. The simulation data points are shown for chain lengths of 20 (blue circles), 35 (red squares), 100 (green diamonds), and 200 (purple triangles), each crosslinked at the different densities:  $\rho_{cl} = 0.45$  (open symbols), 0.65 (half-filled), and 0.85 (filled symbols).

length and entanglement density. With this change the model predictions nearly follow a linear trend. The slip-link model also does a fairly good job of collapsing the data to a linear trend (Figure 62c), although some deviation is noted here for the long chain systems (high values of  $\lambda_{\max}$ ).

The variation of fit limiting extensibility parameter values for systems with constant  $N$  and different  $\rho_{cl}$  is proportionally smaller than the corresponding change in modulus. For example, the  $N = 200$  systems with  $\rho_{cl} = 0.45$  and  $\rho_{cl} = 0.85$  have modulus values of 0.015 and 0.022, respectively (these values are in Table 8. This is a percent difference<sup>6</sup> of 38%. These systems have fit  $\lambda_{\max}$  values of 7.49 and 6.70, which is a percent different of only 11%. For the  $N = 20$  systems, the percent difference in modulus values for systems with  $\rho_{cl} = 0.45$  and  $\rho_{cl} = 0.85$  is 39%, and the percent difference for these systems in terms of fit  $\lambda_{\max}$  values is only 7%. The dominant trend in the  $\lambda_{\max}$  values is a variation with  $N$  (the number of monomers per chain).

In this section the value of  $N$  was set equal to the number of monomers in the chains of a simulated system. Since the simulated chains do not follow ideal random walk statistics, to make a strict comparison with theory we could have defined the equivalent number of Kuhn monomers per chain and used this to calculate the finite extensibility parameters for each model. Although this slightly changes the calculated values for the 8-chain and nonaffine network models, the same dominant trend of a variation of  $\lambda_{\max}$  with the number of monomers in the simulated chains is seen. This distinction does not affect the comparison of modulus trends.

## 7.4 DISCUSSION

By using a coarse-grained description we can access large length and time scales, but cannot quantitatively predict the modulus of a specific material. We can, however, consider higher-level mechanisms like nonaffine chain and primitive path deformation. These mechanisms are expected to be present in all crosslinked polymers, regardless of chemical detail. Most modeling work on crosslinked polymers has considered deformation of chain end-to-end length; this includes the nonaffine network model derived in Chapter 4. However, we

---

<sup>6</sup> The percent difference of two numbers  $x$  and  $y$  was calculated as  $|x - y| / ((x + y) / 2)$ .

noted in Section 6.3 that primitive path length is more representative than end-to-end length with respect to describing microscopic deformations of systems with many entanglements. It was discussed how changes in primitive path length can be used to form an accurate description of microscopic chain conformations for both un-entangled and entangled chain systems.

Because there is not a quantitative agreement between model predictions and simulation results, all of the models reviewed in this chapter (as well as all the models reviewed in Chapter 3) are best described as forming an “equivalent” representation of a polymer network. There is not a one-to-one connection between the equivalent network of the model representation and the actual polymer network. However, we demonstrated in this chapter that certain models still have explanatory power in terms of interpreting the microscopic mechanisms responsible for different mechanical properties. For example, although we demonstrated in Chapter 6 that end-to-end deformation is not a very descriptive measure of local chain deformation in entangled systems, it was shown in Figure 62 that a model based on end-to-end deformation can explain *changes* in limiting extensibility for different systems.

These results at first seem somewhat contradictory: how can a model accurately predict changes in modulus values if the microscopic picture it represents is known to be an over-simplification? To answer this, we note that our analysis only considered the *elastic* behavior of the different simulated networks; no attempts were made to analyze any micro-macro relationships related to the time-dependent *viscoelastic* response. The primitive path and tube concepts were originally introduced to describe the viscous behavior of uncrosslinked polymers [33]; the description has evolved into forms that can accurately predict the time and temperature dependent rheological properties of polymer melts [20, 118, 119]. Current simulation work on polymer melts is directed towards multiscale modeling: the simulation is used to calculate the primitive paths, the tube, and the “tube survival” function, and these quantities are used as input into a rheological model [142, 143]. The success of this approach suggests that a similar treatment using the primitive path and tube concepts may exist with regards to crosslinked polymer elasticity and viscoelasticity. This treatment would necessarily consider primitive path deformation.

Whether or not a given model description is justified depends highly on the scope of the model. For example, the results of this chapter suggest that the nonaffine network model includes important features which determine the elastic properties of a polymer material (crosslinks, entanglements, and non-affine deformation). However, this model is based on a single chain probability function and end-to-end chain length, and it was shown in Chapter 6 that end-to-end length is not a very descriptive measure of local chain deformation in entangled systems. Additionally, we noted difficulties in the interpretation of modulus results at the end of Section 7.2. We therefore anticipate problems if the same microscopic representation is used as a basis for a model of viscoelasticity. Since end-to-end deformation is not a descriptive measure of local chain deformation in entangled systems, a model based on end-to-end deformation is best described as forming an “equivalent” representation of a real network. This was also discussed in Chapter 4 with respect to the non-affine network model. Conversely, the primitive path actually does describe deformed chain conformations well, and therefore a model based on primitive path deformation may yield a representation that can be defined by taking an average over the actual chains in the network. Using primitive path concepts to form a consistent micro-macro model of polymer elasticity and viscoelasticity could be a topic for future work.

## 7.5 SUMMARY AND CONCLUSIONS

In this chapter, we analyzed the mechanical properties of the different simulated polymer networks. The modulus was quantified by fitting a line to the linear part of the stress-stretch curve, and limiting extensibility was quantified by fitting the nonaffine network model of Chapter 4. These values were compared to predictions from several different models. It was shown that modulus is correlated with nonaffine deformation, and that the nonaffine network model can explain the trends for the different test cases. These results were discussed in the context of multiscale modeling and connecting microscopic chain behavior with macroscopic properties. The results of this chapter demonstrate that nonaffine chain end-to-end deformation is correlated with the mechanical properties of different polymer networks. However,

the results bring up additional questions regarding how to best represent a polymer network in a model description that applies in different contexts. We noted several of these difficulties after comparing the modulus values at the end of Section 7.2. In Section 7.4 it was suggested that although a model representation based on end-to-end chain deformation can reasonably describe elastic property changes, a more descriptive picture based on primitive path statistics is needed to capture other properties (such as viscoelasticity).



## CHAPTER 8

### THE SHAPE MEMORY EFFECT

---

This chapter presents the first coarse-grained simulation of shape memory polymer behavior. The shape memory effect in a polymeric material refers to the ability of a sample to hold a deformed shape and then subsequently recover its initial shape when subject to some external stimulus. We consider thermal shape memory polymers (SMPs), where heating and cooling above and below the glass transition temperature is the stimulus behind shape changing. A thermal SMP will retain a deformed shape when cooled below  $T_g$  and will recover its original shape when heated above  $T_g$ . Figure 63 shows a schematic of the shape memory cycling procedure with stress-free shape recovery. In this chapter we seek to answer, can we simulate this behavior?

The coarse-grained model used in Chapters 5-7 represents the most basic molecular features of a polymer material [15]: chains of a finite length are joined together from basic repeat units, and a system of chains becomes entangled since the chains cannot cross each other. However, using the parameters and simulation setup detailed in Section 5.3, it is known that this model behaves athermally [15]. At the other end of the spectrum, we expect that a detailed all-atomistic simulation of a shape memory polymer material will certainly display temperature-dependent behavior. To date, the only molecular dynamics (MD) simulation of a shape memory polymer was done by Diani and Gall [154], who performed an all-atomistic simulation consisting of 5 chains of polyisoprene. These authors found evidence of shape-memory behavior by examining chain mobility in the above  $T_g$  versus below  $T_g$  states. In an intermediate level of detail between the basic bead-spring model and an all-atomistic representation, we expect to see behavior that represents the characteristic temperature-dependent mechanical properties and cycling response of a shape

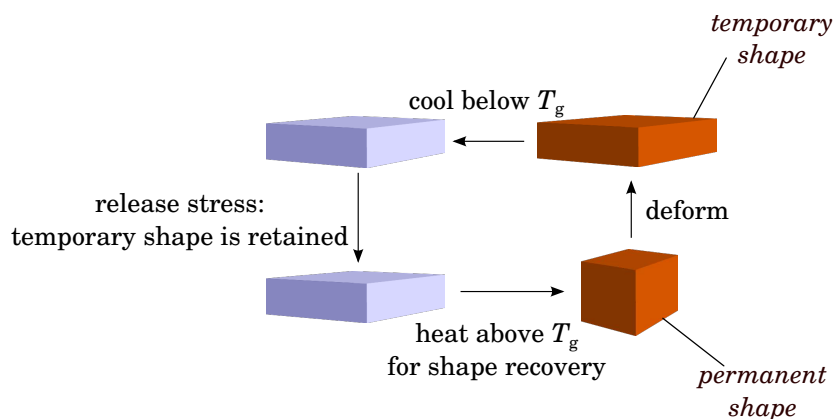


Figure 63: The typical shape memory cycling procedure, with stress-free heating to recover the initial shape.

memory polymer material. In this chapter we consider different simulation setups to determine what this required level of detail is. The question *what simulation setup is required to reproduce SMP-like behavior?* is synonymous with *what are the most important molecular mechanisms that contribute to the shape memory effect?* Coarse-grained simulations are an ideal tool to answer this question since they exist at a level of detail between atomistic and continuum. In the context of multiscale modeling, the goal is to understand the molecular mechanisms of shape memory polymer behavior; this will facilitate in closing the “gap” between synthesis, processing, structure, and morphology at the micro-scale, and material and device performance at the macro-scale.

SMP materials have recently received increased attention due to a large number of potential applications, particularly in the aerospace and biomedical fields. Some examples include deployable space structures [155, 156, 157], self-healing materials [39, 158, 159, 160], passively deployed solar arrays [161, 162], various applications to textiles [163], SMP stents [164], bio-compatible micro-scale neuronal probes [44], and other biomedical applications [36, 37]. At the device level, the main concerns are shape memory recovery rate, the stress generated in the material during temperature cycling, the modulus ratio between low- and high-temperature states, cyclability (i.e. retention/loss of SMP behavior), and aging (shape holding and/or change of properties after long times). Several continuum and mesoscale models have been proposed to represent these phenomena. Nguyen et al. [22] formulated a model based on

temperature-dependent chain mobility; this approach was later adopted and used in other work [165, 166]. Kafka [167] proposed a model with internal variables to represent elastic and elastic-plastic-viscous components. Other models [3, 24, 168, 169] have represented an SMP as separate frozen (glassy) and active (rubbery) phases, and used this treatment to derive a set of constitutive equations; this modeling approach arises by analogy with the modeling of shape memory alloys.

At the other end of the spectrum of shape memory polymer research, work has been done to develop, test, and optimize the performance of new materials. Some examples of thermal SMP materials are tert-butyl acrylate (tBA) with diethylene glycol diacrylate (DEGDA) crosslinker [164, 170, 171] or poly(ethylene glycol) dimethacrylate (PEGDMA) crosslinker [3, 22, 43, 170, 171, 172], Methyl methacrylate (MMA) with PEGDMA crosslinker [173], DP5.1 epoxy [23, 24, 174], Veriflex<sup>®</sup> SMP epoxy [144, 175], and many others [176]. Material development work is done by changing synthesis parameters based on experimental trends. It is desired to know how different polymer structures leads to specific temperature-dependent mechanical properties and optimized shape memory behavior.

By constructing a suitable coarse-grained representation of an SMP we can determine which parameters affect relevant shape memory behavior, and examine the molecular mechanisms at the level of individual chains during temperature cycling. In particular, we note the importance of attractive monomer attractions in the SMP simulation model. The molecular configurations which make shape memory behavior possible are first discussed in Section 8.1, followed by a summary of SMP test protocols and performance metrics Section 8.2. Section 8.3 reviews temperature-dependent MD simulations of polymers. The simulation model used in the previous chapters is modified in order to capture the temperature-dependent behavior of a shape memory polymer; these modified methods are described in Section 8.4. Different choices for the ensemble and pairwise potential cutoff are compared in Section 8.5 in order to demonstrate that the NPT ensemble with attractive Lennard-Jones (LJ) interactions is the most appropriate simulation setup to represent an SMP. The molecular properties of simulated systems corresponding to three different chain models are analyzed in Section 8.6; these different systems approxi-

mately represent the freely jointed chain (FJC), freely-rotating chain (FRC), and rotational isomeric state (RIS) chain models that were reviewed in Chapter 2. The modulus as a function of temperature for each system is measured in Section 8.7, and simulated shape memory cycling results are presented and compared with experimental trends in Section 8.8. This is followed by a visualization of temperature-dependent chain conformations for each chain model, and a discussion of the current results in Section 8.10. We conclude the present study in Section 8.11 and present an outlook for future work.

## 8.1 THERMAL SMP'S AND THE GLASS TRANSITION

At the molecular level a polymer chain can take on many different configurations. We visualized this behavior for crosslinked polymers in Section 6.3, showing the phase space available to individual chains after deformation. For chains crosslinked into a network or existing in a melt, cooling below a certain temperature causes conformational fluctuations to decrease and then nearly stop. The temperature at which this switch in the molecular behavior occurs is known as the glass transition temperature ( $T_g$ ). Above  $T_g$  chains can take on many different conformations, and below  $T_g$  the individual monomers are “caged” and conformational fluctuations cease. This description is, of course, ideal, since a real material will gradually change its behavior as it is cooled. Understanding the precise nature of the glass transition in polymeric materials remains an important problem in polymer physics, despite many years of study [177, 178].

Experimentally, the glass transition temperature can be determined several different ways; one of this is using dynamic mechanical analysis (DMA). Figure 64 shows a representative schematic of the storage modulus ( $G'$ ) and the loss tangent ( $\tan \delta = G''/G'$ , where  $G''$  is the loss modulus) determined as functions of temperature for a crosslinked polymer using DMA. The peak in the  $\tan \delta$  plot is one way to define  $T_g$ . This peak also approximately coincides with the steepest part of the storage modulus vs. temperature curve. For an uncrosslinked polymer melt, the material undergoes viscous flow at temperatures above  $T_g$  and does not display the rubbery plateau show in Figure 64.

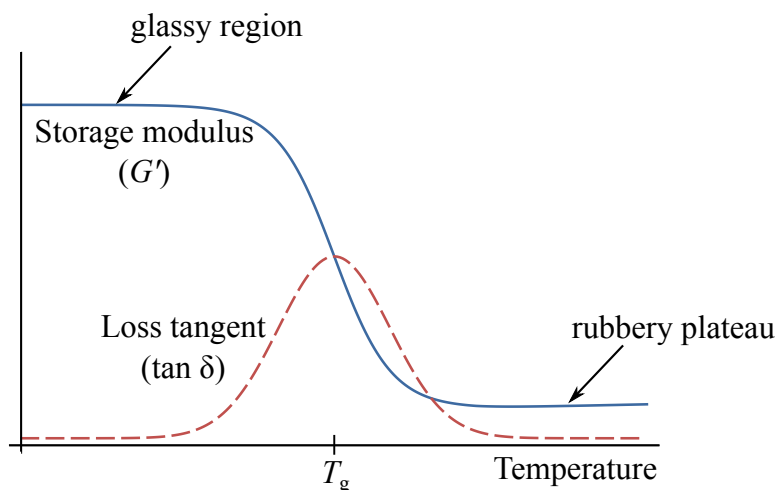


Figure 64: A schematic of the temperature-dependent storage modulus ( $G'$ ) and loss tangent ( $\tan \delta$ ) of a crosslinked polymer, showing the glass transition temperature ( $T_g$ ) and the glassy and rubbery regions

Thermal SMPs exploit the large change in the modulus of a polymer material across  $T_g$ . A thermal SMP is simply a crosslinked polymer; the designation of a material as a “shape memory polymer” is one of degree, not of kind [179]. The term “shape memory polymer” is reserved for materials that display desirable shape holding and recovery properties; all crosslinked polymers display the shape memory effect to some degree.<sup>1</sup> A shape memory polymer can be made by incorporating a permanent network structure (via the addition of crosslinks) into a good glass-forming polymer [180, 181]. Below  $T_g$ , monomer fluctuations are localized and the material has a high modulus. Above  $T_g$ , the material exhibits rubbery behavior and the permanent network structure provides the driving force for shape recovery.

<sup>1</sup> An uncrosslinked polymer can also exhibit the shape memory effect if there are a sufficient number of entanglements. However, the shape memory properties of an uncrosslinked material are very time-dependent. Since there are no covalent crosslinks between chains, uncrosslinked materials only display shape holding and recovery on timescales short enough so that thermal fluctuations have not caused chains to lose their original intermolecular entanglements. We only consider the shape memory effect in crosslinked polymers in this dissertation.

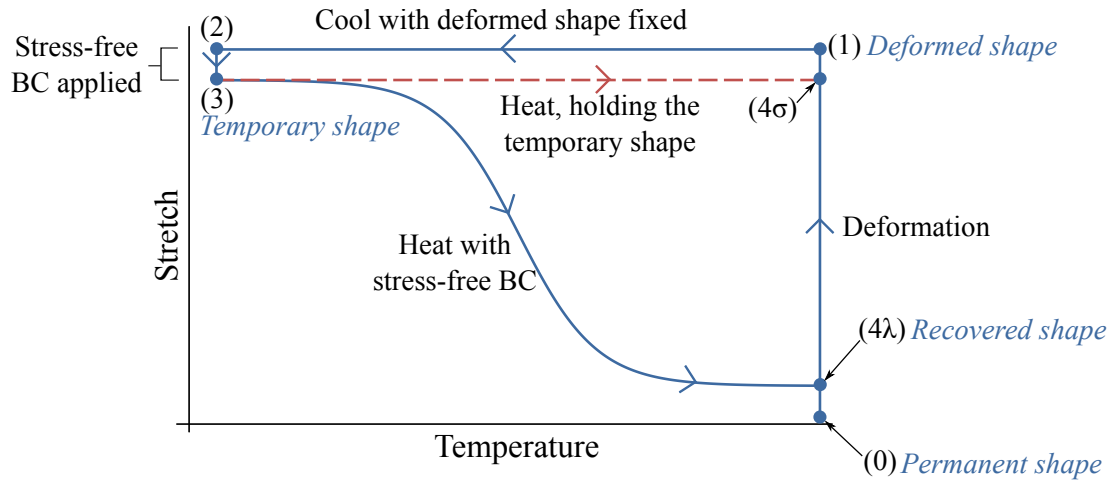


Figure 65: A schematic of the temperature-dependent deformation of a material during shape memory cycling, showing both fixed and stress-free heating boundary conditions.

## 8.2 SMP CYCLING PROCEDURE

Figure 63 shows the typical procedure for thermal shape memory cycling with stress-free shape recovery. First the material is deformed above  $T_g$ , then cooled to below  $T_g$  with the deformed shape held. The applied force is then released, and the material will retain the deformation. Upon stress-free heating to a temperature above  $T_g$ , the material will regain its permanent shape. This is called a stress-free recovery cycle. The other method for shape memory cycling is a constant strain recovery cycle, where the fixed deformation is held while the material is heated above  $T_g$ . With the deformation held, the stress generated in the sample can be measured as a function of temperature.

Figure 65 shows a schematic of the temperature-dependent deformation of a sample during shape memory cycling. This plot can be used to quantify the behavior represented in Figure 63. The sample initially has its permanent shape in an undeformed configuration above  $T_g$  at the point labeled (0), and an applied deformation brings the sample to point (1). Point (1) is labeled the deformed shape. The material is then cooled below  $T_g$  (2), and any applied tractions are released to allow the material to hold the deformation (3). The stretch value at point (3) is called the temporary shape. After this, the boundary conditions are either set to fix the temporary shape while heating and measure

stress generation in the sample ( $4\sigma$ ), or stress-free to measure the stretch recovered upon heating ( $4\lambda$ ). Several measures of SMP performance can be defined using the results of a shape memory cycling test. The first is related to the temporary shape. This can be quantified as the deformation retained divided by the deformation applied,

$$D_H = \frac{\lambda_{(3)} - 1}{\lambda_{(2)} - 1}, \quad (135)$$

where  $\lambda_{(2)}$  and  $\lambda_{(3)}$  are the stretch values at points (2) and (3) in Figure 65, and  $D_H$  refers to fraction of deformation held. This is a measure of shape fixity.  $D_H = 1$  is ideal SMP behavior, and  $D_H < 1$  corresponds to some change in shape occurring from step (2) to step (3). After stress-free heating, one way to quantify recovery is the percentage of the temporary shape that is recovered:

$$D_R = \frac{\lambda_{(3)} - \lambda_{(4\lambda)}}{\lambda_{(3)} - 1}. \quad (136)$$

This is a measure of shape recovery. With this definition  $D_R = 1$  represents complete recovery of the undeformed shape, regardless of how much of the applied deformation is held. Liu et al. [176] defined a similar measure of shape recovery,  $R_R = D_R D_H$ , which is deformation recovered upon heating divided by the applied deformation. These authors suggested using  $D_H$  and  $D_R$  (or, equivalently,  $D_H$  and  $R_R$ ) to classify SMPs based on their shape holding and recovery ability. A good SMP has both  $D_H$  and  $D_R$  close to 1, an SMP with only good shape fixing abilities has  $D_H \sim 1$  but  $D_R < 1$ , an SMP with only good shape recovery abilities has  $D_R \sim 1$  but  $D_H < 1$ , and a poor SMP has both  $D_H$  and  $D_R$  significantly less than 1.

The cycling procedure described in this section will be applied to the different simulation test cases in Section 8.8. We compare the shape holding and recovery abilities of the different simulated materials, and compare trends during cycling with experimental results.

### 8.3 TEMPERATURE-DEPENDENT SIMULATION OF POLYMERS

The SMP system is crosslinked and we are interested in its mechanical properties above, below, and across the glass transition, since this spans the operating regime for the shape memory cycle. Current coarse-grained MD simulation studies to date have not covered the scope of temperature, mechanical properties, and material configuration relevant to address the fundamental mechanisms of SMP operation. We build on previous work in order to construct a coarse-grained molecular dynamics model which is representative of a shape memory polymer and study the effect of the attractive monomer interactions and chain stiffness on shape memory behavior.

The original Kremer-Grest model used in Chapters 5, 6, and 7 included only repulsive interactions and behaved athermally. To simulate a shape memory polymer we need to modify this model so that it can capture temperature-dependent behavior. Wolfgardt et al. [182, 183] used Monte Carlo simulations with the bond fluctuation model to demonstrate that the bead-spring model displayed temperature-dependent behavior if attractive interactions were included. Subsequent work has employed this simple model (the bead-spring model with attractive Lennard-Jones interactions included) to study the glass transition via MD [101, 150, 151, 184, 185, 186, 187]. Topics covered by these studies include interfacial effects of adhesion [184], fracture (by changing the potential to allow for bond rupture) [187], the comparison of microscopic displacements with theoretical Rouse model predictions across  $T_g$  [150, 151, 185], and the effect of crosslinking on microscopic chain dynamics and the glass transition [101]. The glass transition temperature is typically identified via molecular dynamics by examining volume-temperature curves [188, 189] or the structure factor [150, 185]. The bead-spring model, which represents a freely-joined chain (FJC), has also been augmented to include bond angle bending [16, 190, 191], (the so-called freely-rotating chain (FRC) model) and an energy landscape for the restricted rotation of dihedral angles [192, 193] (the rotational isomeric state (RIS) model). In simulations that did not include attractive interaction between monomers, Bulacu et al. [192, 193] found that the FRC and RIS models displayed glass transition-like behavior while the FJC model did not.



Other simulation results have examined mechanical properties below and above  $T_g$ . Lyulin et al. [194] performed uniaxial tests below  $T_g$  using united atoms models and concluded that polystyrene shows more softening than polycarbonate due to the increased mobility of polystyrene segments in the deformed direction after yielding. Röttler and Robbins [195, 196, 197, 198] studied the large deformation strain hardening of glassy polymers below  $T_g$  and concluded that this hardening is due to a thermally activated process and is not consistent with rubber elasticity models of below  $T_g$  hardening. Barrat et al. [34] reviewed other mechanical studies of polymers below  $T_g$ . Above  $T_g$ , a number of studies have examined the microscopic mechanisms of polymer rheology for uncrosslinked systems [111, 128, 129, 130, 138, 199, 200, 201, 202, 203, 204, 205] as well as rubber elasticity for crosslinked systems [17, 82, 100, 101, 102, 103, 104, 105, 107, 206, 207, 208, 209]. Most work has focused on mechanical behavior either above  $T_g$  or below  $T_g$ ; fewer studies have examined these properties across the glass transition. Gao and Weiner [210, 211] saw a transition to rubbery-like behavior by looking at the shear relaxation modulus as a function of time for simulated systems at different temperatures. Liu et al. [212] determined stress-strain behavior for simulated crosslinked polymer networks with simple Lennard-Jones filler particles above and below  $T_g$ .

In this chapter we perform the first investigation to identify a suitable coarse-grained simulation model for SMPs. We begin by including attractive interactions. Since the glass transition reflects a change in the molecular mobility of chain segments, we include other interactions that are known to restrict molecular mobility. These include bond angle and torsional bending restrictions. The simulation methods are detailed in the next section.

#### 8.4 SMP SIMULATION METHODS

We employ the Kremer and Grest [15] bead-spring model that was previously described in Section 5.3, and extend this to include bond angle bending and an energy landscape for dihedral rotation following Bulacu and van der Giessen [192, 193]. The work in Refs. [192, 193] focused on the effect of chain stiffness on the glass transition; the characteristic ratio, chain self-diffusion

behavior, and decay in the torsional angle autocorrelation function with time were analyzed at different temperatures. The different simulation cases in Refs. [192, 193] included potentials and parameters sets which correspond approximately to the FJC, FRC, and RIS models. Using this setup will allow us to increase chain stiffness (i.e. to include additional restrictions on microscopic chain motion), and investigate how this affects shape memory behavior and material properties.

Each bead in the simulation interacts through a Lennard-Jones potential:

$$u_{\text{LJ}}(r_{ij}) = \begin{cases} 4\epsilon \left[ \left( \frac{\sigma}{r_{ij}} \right)^{12} - \left( \frac{\sigma}{r_{ij}} \right)^6 \right] + C, & r_{ij} < r_c \\ 0, & r_{ij} \geq r_c \end{cases} \quad (137)$$

In contrast with Eq. 111, the constant  $C$  is included here in order to shift the potential to zero at the cutoff. This does not affect the forces in the system; it simply tidies the bookkeeping in calculations of the total energy. In this chapter we will use the cutoff values of  $r_c = 2^{1/6}$  and  $r_c = 2 \times 2^{1/6}$ . The former includes only repulsive LJ interactions while the latter includes both repulsive and attractive interactions - see Figure 35. Using  $r_c = 2 \times 2^{1/6}$ , the force between two LJ particles at the cutoff is nonzero. Alternatively, one could use a smoothed potential function which leads to a nonzero force at the cutoff. However, since the force at  $r_c = 2 \times 2^{1/6}$  is small, this would lead to essential identical results. We therefore retain Eq. 137 for simplicity. The value of  $r_c = 2 \times 2^{1/6}$  was previously used in Refs. [150, 151, 185, 186] to simulate temperature-dependent behavior of polymer systems. All bonds use the finite extensible nonlinear elastic (FENE) potential:

$$u_{\text{FENE}}(r_{ij}) = \begin{cases} -0.5KR_0^2 \ln \left[ 1 - \left( \frac{r}{R_0} \right)^2 \right], & r_{ij} \leq R_0 \\ \infty, & r_{ij} > R_0 \end{cases} \quad (138)$$

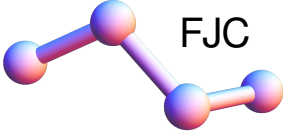
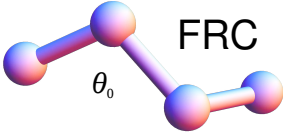
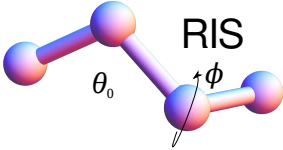
Chain model	Potentials used
 <p>FJC</p>	$U_{LJ}, U_{FENE}$
 <p>FRC</p> <p><math>\theta_0</math></p>	$U_{LJ}, U_{FENE}, U_B(\theta)$
 <p>RIS</p> <p><math>\theta_0</math></p> <p><math>\phi</math></p>	$U_{LJ}, U_{FENE}, U_B(\theta), U_T(\phi)$

Figure 66: A schematic of the angular potentials included for each chain model.

The bond angle and torsional bending potentials are [193]

$$U_B(\theta) = k_\theta (\cos \theta - \cos \theta_0)^2, \quad (139)$$

$$U_T(\phi) = k_\phi \sum_{n=0}^3 a_n \cos^n \phi. \quad (140)$$

The simulated system is the rotational isomeric state (RIS) model when all of the potentials are present. Technically this setup could be called the hindered rotation chain (HRC) model since it defines an energy landscape for torsional bending [4]. However, the energy wells are deep enough that monomer segments will assume discrete torsional states at low temperatures. Successive torsional angles are also not independent. We therefore retain the RIS nomenclature as used in Refs. [192, 193]. Omitting  $U_T$  reduces the system to the freely-rotating chain (FRC) model, and omitting both  $U_T$  and  $U_B$  is the freely-jointed chain (FJC) model. Figure 66 shows a schematic of the different simulation models and a table of which potentials are included for each.

Parameter values were chosen following Bulacu et al. [192, 193] and are listed in Table 10. Note that  $k_\theta = 25$  was used, which is twice the value of Ref. [193]. This was chosen to enhance numerical stability. In Ref. [193], the

Parameter	Description	Value (LJ units)
$\sigma$	LJ length scale	1
$\epsilon$	LJ energy scale	1
$r_c$	LJ cutoff distance	$2^{1/6}$ or $2 \times 2^{1/6}$
K	FENE elastic constant	30
$R_0$	FENE maximum bond elongation	1.5
$k_\theta$	Bond angle bending stiffness	25
$\theta_0$	Equilibrium bond angle	$109.45^\circ$
$k_\phi$	Torsional constant	$\sin^6 \theta_0$
Torsional polynomial coefficients in Eq. 140		
	$\alpha_0$	3
	$\alpha_1$	-5.9
	$\alpha_2$	2.06
	$\alpha_3$	10.9

Table 10: Parameters used in the SMP simulations.

torsional potential was made to be a function of both of the angles  $\theta$  of the bonds contributing to the torsional angle, since this was found to decrease numerical instabilities due to the alignment of successive bonds. Here we use the torsional potential in Eq. 140 for simplicity, and choose a higher  $k_\theta$  to aid with numerical stability. In comparison with Ref. [193], the parameter  $k_\phi$  was also modified by using the equilibrium value of the bond angle since the torsional potential does not depend on bond angles. With these parameter choices the simulated system has stiffer bond bending than the system in Ref. [193], but the rest of the behavior is very similar so that a comparison can be made. Figure 67 shows a plot of the torsional potential  $U_T(\phi)$  for possible values of the torsion angle ( $\phi$ ). There are three energy minima, corresponding to *gauche*<sup>-</sup>, *trans*, and *gauche*<sup>+</sup> states at  $68.5^\circ$ ,  $180^\circ$ , and  $291.5^\circ$ , respectively.

The general simulation procedure is similar to what was previously described in Section 5.3. However, there are differences in the choices of potential functions used in each step. Specifically, we crosslink a system with all the potentials included ( $U_{LJ}$ ,  $U_{FENE}$ ,  $U_B$ ,  $U_T$ ), and then turn the relevant potentials off in order to represent the different chain models. This yields systems with identical network topology but different properties due to the different chain

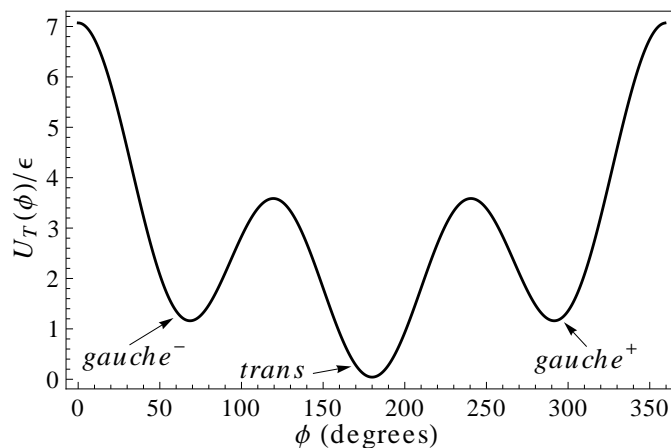


Figure 67: A plot of the torsional angle potential  $U_T(\phi)$  from Eq. 140 with the parameters listed in Table 10.

interactions. This removes network structure as a major variable in determining properties, since it is known from Chapters 5-7 that different network structures leads to different properties. Here, we focus on how bond bending, dihedral torsion, and monomer interactions affect material properties.

First, chains of length  $N = 20$  are generated as random walks with fixed bond angles of  $\theta_0 = 109.45^\circ$  and random dihedral angles. The Mathematica code used to generate these configurations is included in Appendix B.7. Next, 1000 chains are placed randomly in a simulation box with size chosen so that the monomer density is  $\rho_0 = 0.85$ . After an initial soft push-off using the cosine potential from Eq. 119, the regular LJ potential with  $r_c = 2^{1/6}$  is applied and the system is equilibrated [15]. Since the chains are short, equilibration can be achieved without the use of the double-bridging moves which alter chain connectivity [16]. The equilibration run was performed at a temperature of  $T = 1.75$  for  $25 \times 10^6$  timesteps using  $\Delta t = 0.003$ . At this point there is only one simulated system, and this system has all the potentials included. Note that  $T = 1.75$  is significantly higher than the temperature  $T = 1$  used in of Chapters 5-7. This temperature was chosen for equilibration and crosslinking since it was found to be above  $T_g$  for the potentials and parameters used in these steps (i.e. for the RIS chain model with  $r_c = 2^{1/6}$ ). As in Section 5.3, the ensemble-averaged mean-square distance between monomers separated by  $m$  bonds,  $\overline{R^2[m]}$ , was monitored to ensure equilibrium. After sufficient time

this curve appeared to fluctuate about a mean, so the system was deemed as equilibrated.

The system was then crosslinked using the procedure of Duering et al. [98] described in Section 5.3. The NVT ensemble with an LJ potential cutoff of  $r_c = 2^{1/6}$  was used for the initial equilibration and crosslinking steps. The crosslinking reaction was performed for a time of  $75000\tau$ , after which the extent of the reaction was 97.9%. After crosslinking, the simulated material was divided into different cases for each chain model: FJC, FRC, and RIS. The NPT ensemble with  $P = 0$  and an LJ potential cutoff of  $r_c = 2 \times 2^{1/6}$  was used to simulate temperature-dependent behavior of each chain model. In addition to these simulations, different ensembles and LJ potential cutoffs were used with the FJC system to demonstrate that the NPT ensemble with  $r_c = 2 \times 2^{1/6}$  is the most appropriate choice to represent a thermal SMP. Previous work has used  $r_c = 2 \times 2^{1/6}$  along with the NPT ensemble to simulate temperature-dependent behavior of polymers [150, 151, 185, 186]. Refs. [150, 151, 185] used a value of  $P = 1$  for the constant pressure boundary condition. Here, we use  $P = 0$  since this value was found to lead to a monomer density of approximately 0.85 for the FJC system at a temperature of  $T = 1$ .

After dividing the single crosslinked system into different systems, each case was equilibrated for a time of  $12000\tau$  at a temperature of  $T = 1.75$ . A timestep of 0.006 was used for all cases except RIS, where  $\Delta t = 0.003$  was used to ensure numerical stability. Each system was then cooled from  $T = 1.75$  to  $T = 0.05$  at a rate of  $dT/dt = 8.333 \times 10^{-5}\epsilon/k\tau$  ( $k$  is Boltzmann's constant; for the Lennard-Jones potential the temperature is expressed in units of  $\epsilon/k$ ). This rate was determined to be sufficiently slow so that rate effects in cooling were minimized. A timestep of  $\Delta t = 0.003$  was used for  $T > 1$ , and  $\Delta t = 0.006$  was used for  $T < 1$ . Snapshots of the system during cooling were outputted every  $\Delta T = 0.05$ . The snapshots were used to determine the temperature-dependent modulus via a procedure described in Section 8.5. Simulation runs were used to determine the temperature-dependent  $C_\infty$ , primitive path length, cohesive energy density, and number of kinks per chain for each chain model in Section 8.6, and the additional procedures are described therein. The additional simulation procedures required for SMP thermomechanical cycling

(Section 8.8) and the visualization of chain conformations (Section 8.9) are described in these sections.

## 8.5 ENSEMBLE AND PAIRWISE POTENTIAL COMPARISON

The Kremer and Grest [15] bead-spring model used in Chapters 5-7 is known to yield approximately athermal behavior. To represent a shape memory polymer we must choose an appropriate simulation model, ensemble, and pairwise potential cutoff, so that the simulated material displays temperature-dependent behavior that is characteristic of an SMP. In this section we compare the volume-temperature and modulus-temperature behavior of the FJC model simulated with different ensembles and LJ potential cutoff values in order to identify the most appropriate choice to represent an SMP. Both NPT and NVT ensembles are used with LJ potential cutoff values of  $r_c = 2^{1/6}$  and  $r_c = 2 \times 2^{1/6}$ . Table 11 is a list of the different systems considered in this section. These systems were prepared using the method described in the previous section. The ensemble and pairwise potential combinations include:

- (A-NPT): Attractive LJ interactions included ( $r_c = 2 \times 2^{1/6}$ ), simulation performed with the NPT ensemble with a constant pressure of  $P = 0$ .
- (R-NPT): Only repulsive LJ interactions ( $r_c = 2^{1/6}$ ), simulation performed with the NPT ensemble with  $P = 5.5$ . A nonzero value of the isotropic pressure was used to keep the volume of the system from continually increasing; the value  $P = 5.5$  was found to lead to a monomer density of approximately 0.85 at  $T = 1$ .
- (A-NVT): Attractive LJ interactions included ( $r_c = 2 \times 2^{1/6}$ ), simulation performed with the NVT ensemble at a constant density of 0.85.
- (R-NVT): Only repulsive LJ interactions ( $r_c = 2^{1/6}$ ), simulation performed with the NVT ensemble at a constant density of 0.85.

Before analyzing the properties of the different systems, we note that the NPT ensemble will facilitate applying stress-free boundary conditions during shape memory cycling. Therefore, it may be expected *a priori* that using NPT is

Chain model	Network struct.	Ensemble	LJ cutoff	Abbrev.
FJC	Crosslinked	NPT, $P = 0$	$2 \times 2^{1/6}$	A-NPT
		NPT, $P = 5.5$	$2^{1/6}$	R-NPT
		NVT	$2 \times 2^{1/6}$	A-NVT
		NVT	$2^{1/6}$	R-NVT

Table 11: A list of the different ensemble and pairwise potential simulations considered in this section.

more suitable than NVT for simulating SMPs. However, since both choices have been used to investigate temperature-dependent properties in other molecular dynamics, we include both and analyze the effect of these different boundary conditions on simulated material properties.

The modulus was determined at temperature intervals of  $\Delta T = 0.05$  using the following procedure. First, a snapshot outputted at a specified temperature during cooling was briefly equilibrated for  $300\tau$ . A uniaxial strain of 0.1 was then applied by prescribing a constant engineering strain rate of  $8.33 \times 10^{-6}\tau^{-1}$  to the  $x$ -dimension of the simulation box. The  $y$  and  $z$  dimensions continued to have boundary conditions of zero pressure for the NPT cases, and were deformed to enforce the constant volume condition for the NVT cases. A straight line was fit to the initial linear region of the stress-strain curve to obtain the modulus. Note that the stress-strain curve for the systems below  $T_g$  is only linear to strains around 0.02, whereas the above  $T_g$  systems behave linearly to much larger strains. The result of this procedure is shown in Figure 68 for the FJC-A-NPT system at temperature values above and below  $T_g$ . The modulus at each temperature is determined as the slope of the fitted line as shown in Figure 68.

Figure 69 shows the modulus-temperature behavior of the four different FJC systems with the different ensemble and pairwise potential cutoff values. All of the cases show transition-like behavior as the temperature is lowered with the exception of R-NVT. Note that even the R-NPT case shows transition-like behavior in the modulus values. This demonstrates that a system with only repulsive interactions can exhibit a glass transition if the NPT ensemble with a positive, nonzero isotropic pressure is used. However, the chosen value of the pressure will affect this behavior.  $P_{\text{iso}} = 5.5$  was chosen as a reasonable



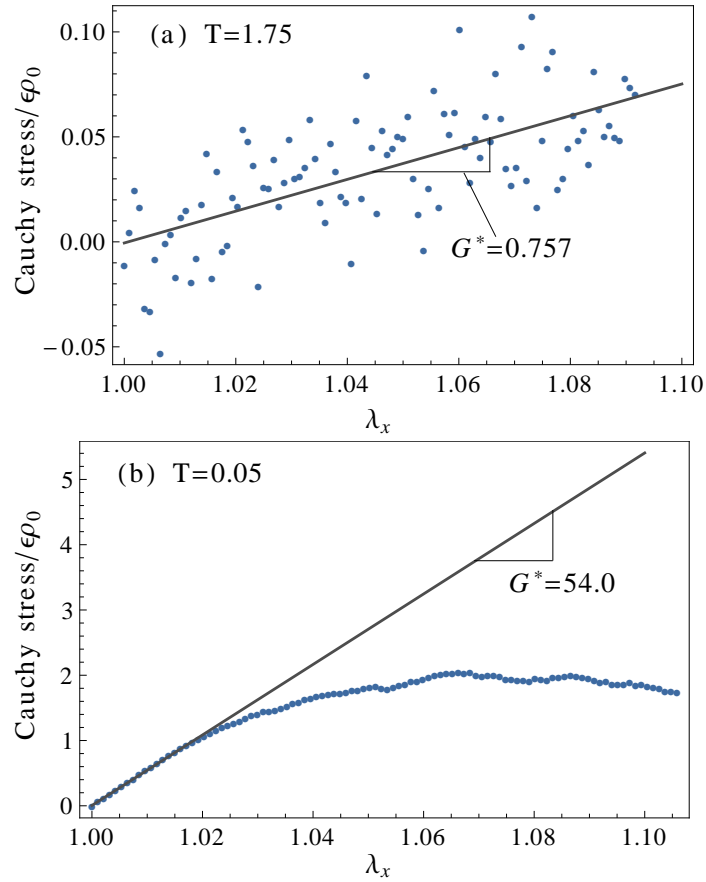


Figure 68: The modulus is determined as the slope of a line fit to the linear region of the stress-stretch curve. The result of this procedure is shown here for the FJC system (a) above  $T_g$ , and (b) below  $T_g$ .

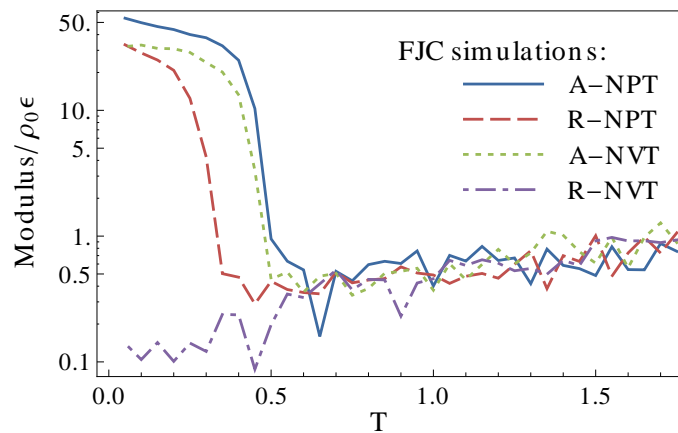


Figure 69: The modulus-temperature results for the FJC system simulated with the different ensembles and pairwise potential cutoff values.

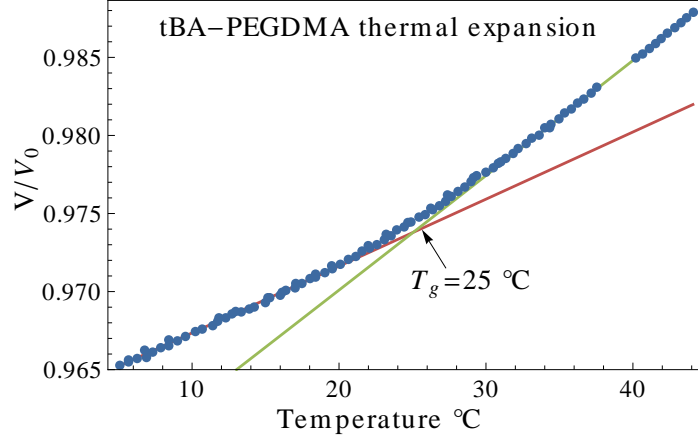


Figure 70: Volumetric thermal expansion data of the shape memory polymer tBA-PEGDMA from Nguyen et al. [22]. Lines are fit to the glassy and rubbery regions to determine thermal expansion coefficients. In Ref. [22],  $T_g$  was determined by the intersection of these lines.

value for the R-NPT systems in order to keep the density at  $T = 1$  close to the initial value of  $\rho_0 = 0.85$ .<sup>2</sup> Without this isotropic pressure, the simulation box for the R-NPT systems will expand and become very large. The modulus values of each system are nearly identical at temperatures above  $T_g$ . At these temperatures, the thermal energy is high enough to cause the beads in the system to move around rapidly and continually collide. Repulsive interactions are therefore the main factor that determines the response of the system at temperatures above  $T_g$ . The increase in the modulus with temperature above  $T_g$  is a signature of entropic elasticity. All systems display the same trend for these above  $T_g$  temperature values.

Next we examine volume-temperature behavior for the NPT systems in comparison with experimental trends. The volume-temperature curve for the shape memory polymer tBA-PEGDMA from Nguyen et al. [22] is plotted in Figure 70. The temperature-dependent volume curve shows a characteristic change in slope near  $T_g$ . The volumetric coefficient of thermal expansion (CTE) is defined as

$$\alpha_V = \frac{1}{V} dVdT. \quad (141)$$

<sup>2</sup> This value was determined by looking at the isotropic pressure acting on the simulation box for the NVT simulations.

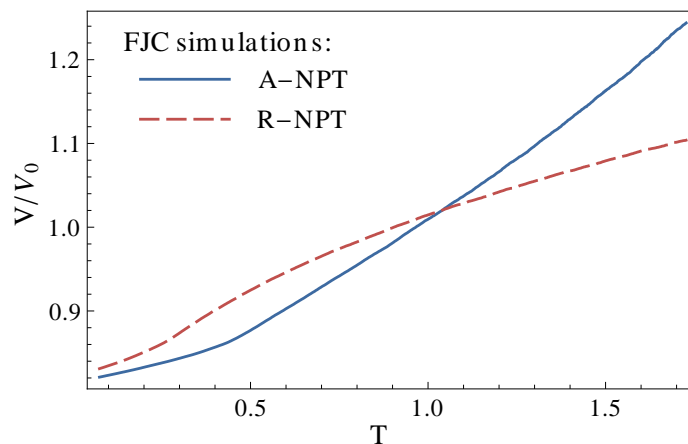


Figure 71: The volume-temperature curves of the FJC system using both A-NPT and R-NPT. Volume is normalized by the initial volume of the simulation box during equilibration and crosslinking.

Calculating the intersection of the lines fit to the glassy and rubbery phase behaviors is one method of several which can be used to determine  $T_g$ ; this is shown in Figure 70.<sup>3</sup> The coefficient of thermal expansion is different in the glassy and rubbery phases, and the different values are denoted  $\alpha_g$  and  $\alpha_r$ , respectively. For the meth(acrylate)-based SMP shown in Figure 70 the CTE's are  $\alpha_g = 3.85 \times 10^{-4} (\text{°C})^{-1}$  and  $\alpha_r = 7.67 \times 10^{-4} (\text{°C})^{-1}$  [22]. The Veriflex SMP tested by Li and Xu [165] has measured CTE's of  $\alpha_g = 5.46 \times 10^{-4} (\text{°C})^{-1}$  and  $\alpha_r = 8.44 \times 10^{-4} (\text{°C})^{-1}$ . Nearly all polymeric materials display this sort of temperature-volume behavior: the V-T curve is approximately linear both above and below  $T_g$ , with the slope being higher above  $T_g$ . We therefore compare the simulated A-NPT and R-NPT systems to test if they show realistic changes in volume-temperature behavior. This is plotted in Figure 71. With attractive interactions (A-NPT), the volume-temperature curve shows bi-linear behavior similar to Figure 70 and a transition can be clearly seen around  $T = 0.45$ . Without attractive interactions (R-NPT), the shape of the volume-temperature curve does not resemble the typical bi-linear trend seen in experimental results. The volumetric thermal expansion of both of the systems in Figure 71 is much larger than what is observed experimentally. This very large volume change

<sup>3</sup> Note that  $T_g$  values will vary for a given material depending on which method is used (e.g. DMA versus volume-temperature behavior). Since  $T_g$  itself is not a well-defined quantity, these differences are only a matter of convention.

can be considered an artifact of the simplified coarse-grained model. For the A-NPT system, the coefficient of thermal expansion is  $\alpha_g \approx 0.109k/\epsilon$  below  $T_g$  and  $\alpha_r \approx 0.296k/\epsilon$  above  $T_g$ , and the overall volume change from the lowest to highest temperatures is over 30% of the volume at  $T = 1$ . Although the overall volume change in the simulation is large, the ratio of CTE's for the A-NPT system is reasonable in comparison to experiments:  $\alpha_r/\alpha_g = 2.7$  for the A-NPT simulation,  $\alpha_r/\alpha_g = 2.0$  for the meth(acrylate) CMP shown in Figure 70, and  $\alpha_r/\alpha_g = 1.5$  for the Veriflex SMP material Li and Xu [165].

In comparing the A-NPT and R-NPT simulations as candidates for representing shape memory polymer behavior, the volume-temperature behavior solidifies the choice of A-NPT as the most appropriate to represent a thermal SMP. Although the R-NPT system displays transition-like behavior, this behavior depends on the arbitrary choice of the isotropic pressure, and the shape of the volume-temperature curve does not resemble experimental results. Due to the need to apply stress boundary conditions during simulated cycling, the NVT systems may be similarly discarded. In the remainder of this chapter we use the NPT ensemble with  $P = 0$  and  $r_c = 2 \times 2^{1/6}$  to investigate the temperature-dependent behavior of the different chain models.

## 8.6 MOLECULAR PROPERTIES OF THE DIFFERENT CHAIN MODELS

In this section, we examine the molecular properties of the different chain models in terms of equilibrium chain dimensions, nearest-neighbor packing, and cohesive energy density. We consider both crosslinked and uncrosslinked systems of the FJC, FRC, and RIS chain models, and following the results of the last section, use the NPT ensemble with  $P = 0$  and attractive interactions included in the LJ potential function. Table 12 lists the systems considered in this section. The crosslinked networks were prepared using the procedure describe in Section 8.4. For the uncrosslinked networks, a snapshot of the system was taken before the crosslinking step and divided into the 3 cases for the different chain models. The appropriate potentials were then set for each system and an equilibration run was carried out for a time of  $12000\tau$ . Uncrosslinked systems were considered in order to assess the influence of the crosslinking procedure on the temperature-dependent chain dimensions.

Network structure	Chain model
Crosslinked	FJC
	FRC
	RIS
Uncrosslinked	FJC
	FRC
	RIS

Table 12: Each chain model is considered in both crosslinked and uncrosslinked form for the comparison of molecular properties in Section 8.6. Each is simulated using the NPT ensemble with  $r_c = 2 \times 2^{1/6}$ , i.e. attractive LJ interactions enabled (A-NPT).

We first examine the temperature-dependent chain end-to-end distances for each system. In Chapter 2 we discussed the quantity  $C_\infty$ , which is defined according to

$$\overline{R^2} = C_\infty n l^2, \quad (142)$$

where  $\overline{R^2}$  is the mean-square ensemble average of chain end-to-end lengths,  $n$  is the number of monomers in the chain and  $l$  is the bond length. Note that in general the number of monomers ( $n$ ) and the bond length ( $l$ ) may not be equal to the number of Kuhn monomers ( $N$ ) and the Kuhn monomer length ( $b$ ) - see Chapter 2.  $C_\infty$  is a measure of the tendency of a chain to coil. A low  $C_\infty$  value represents a chain that tends to coil, and a high  $C_\infty$  value a chain that tends to be more extended. The ideal FJC model has  $C_\infty = 1$ . Using an angle of  $\theta_0 = 109.45^\circ$  in Eq. 9, the ideal FRC chain has  $C_\infty \approx 2$  (note that the ideal FRC does not have a temperature dependence). Although it is difficult to perform an exact calculation for the RIS model since each sequence of dihedral angles does not have the same probability [4], an estimate can be obtained by neglecting correlations between successive dihedral angles (the hindered rotation chain (HRC) model). The  $C_\infty$  value for the HRC model with energy landscape  $U_T(\phi)$  is calculated using Eq. 10. Using Eq. 140 for  $U_T(\phi)$  with the parameters from Table 10, this yields an estimate of  $C_\infty = 3.78$  at  $T = 1.75$ .

We calculate  $C_\infty$  for each simulated system using the mean-square end-to-end distances outputted at temperature intervals of  $\Delta T = 0.05$  during cooling.

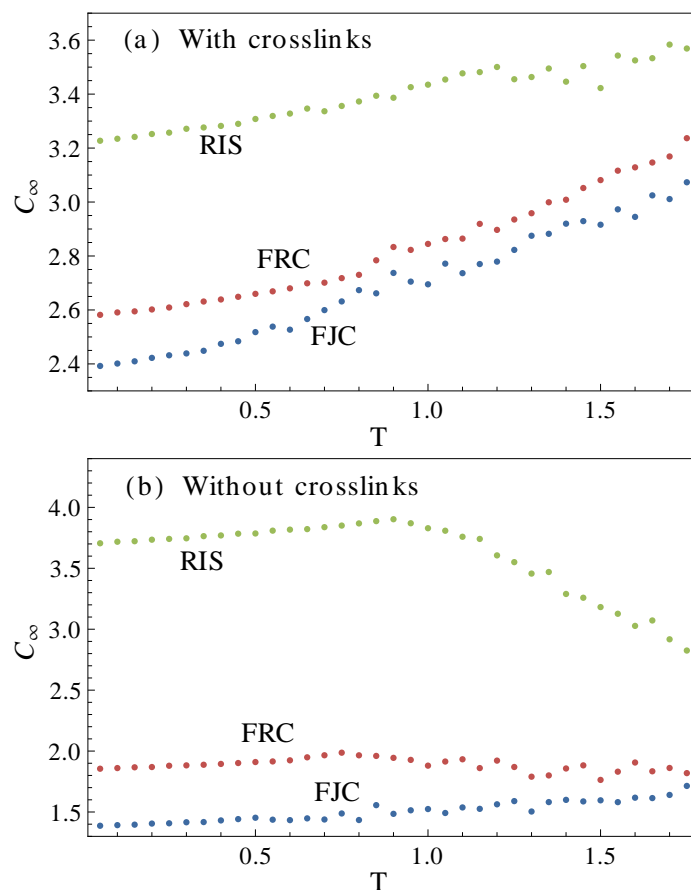


Figure 72: The  $C_\infty$  values as a function of temperature for each chain model in (a) crosslinked, and (b) uncrosslinked forms.

The result of this calculation is shown in Figure 72 for both the crosslinked and uncrosslinked systems of each chain model. The chain models follow  $C_\infty(\text{RIS}) > C_\infty(\text{FRC}) > C_\infty(\text{FJC})$  as expected in both crosslinked and uncrosslinked forms. The crosslinked systems have a smaller range of  $C_\infty$  values in comparison with the uncrosslinked systems. This is because the crosslinking procedure was performed with both the bending and torsional potentials enabled; these results would be different if the crosslinking procedure was performed specific to each chain model. With the current procedure, only the uncrosslinked and crosslinked RIS systems can be compared to assess the influence of crosslinking on chain dimensions. It is seen that the crosslinking causes a slight increase in  $C_\infty$  at the temperature where it was performed ( $T = 1.75$ ). However, the difference between the crosslinked and uncrosslinked

systems is most seen when the temperature is changed.  $C_\infty$  decreases for all of the crosslinked systems when the temperature is lowered, and increases or stays about the same for the uncrosslinked systems. The uncrosslinked RIS system has a fairly large increase in  $C_\infty$  when cooled. This is due to the effective increase in stiffness of the chains with a decrease in temperature: as the thermal energy decreases, transitions between torsional states become less frequent, and the chains are effectively stiffer. There is no such mechanism for the uncrosslinked FRC and FJC systems, so the  $C_\infty$  values of these do not change much with respect to temperature. The uncrosslinked systems represent a better comparison of how the potentials affect chain dimensions, since they do not have crosslinks to restrict the motion and diffusion of the chain ends.

We also compare the  $C_\infty$  values from the simulations to the ideal theoretical calculations, which neglect excluded volume interactions. Only the uncrosslinked systems can be compared with the theoretical result. Although the ideal theoretical FJC calculation gives  $C_\infty = 1$ , the simulated uncrosslinked FJC system has  $C_\infty > 1$  for all temperature values. This is attributed to excluded volume interactions between beads in the simulated chains (i.e. the beads have a finite spherical size that is effectively set by the LJ potential). Although it was initially expected that the uncrosslinked FRC system would also have a  $C_\infty$  value greater than the theoretical estimate of  $C_\infty \approx 2$ , the simulation results show a  $C_\infty$  value of less than 2 for all temperature values. There are two possible reasons for this behavior. First, the theory assumes a fixed angle between monomers, while the actual chains are more flexible since they follow Eq. 139. The theory additionally assumes infinitely long chains, while the chains here are only of length 20. For these reasons we cannot comment on how excluded volume interactions affect chain dimensions of the FRC system. The same applies for the RIS system, which has an above  $T_g$   $C_\infty$  value from the simulations that is less than the ideal theoretical calculation.

In Chapters 5-6 we used the Z1 code [18, 19, 20] to obtain primitive path and entanglement properties of the different networks. Here, we perform these calculations at different temperatures for each chain model in both crosslinked and uncrosslinked forms. The average primitive path length ( $\overline{L_{pp}}$ ) is plotted as a function of temperature for each case in Figure 73. The trends for the

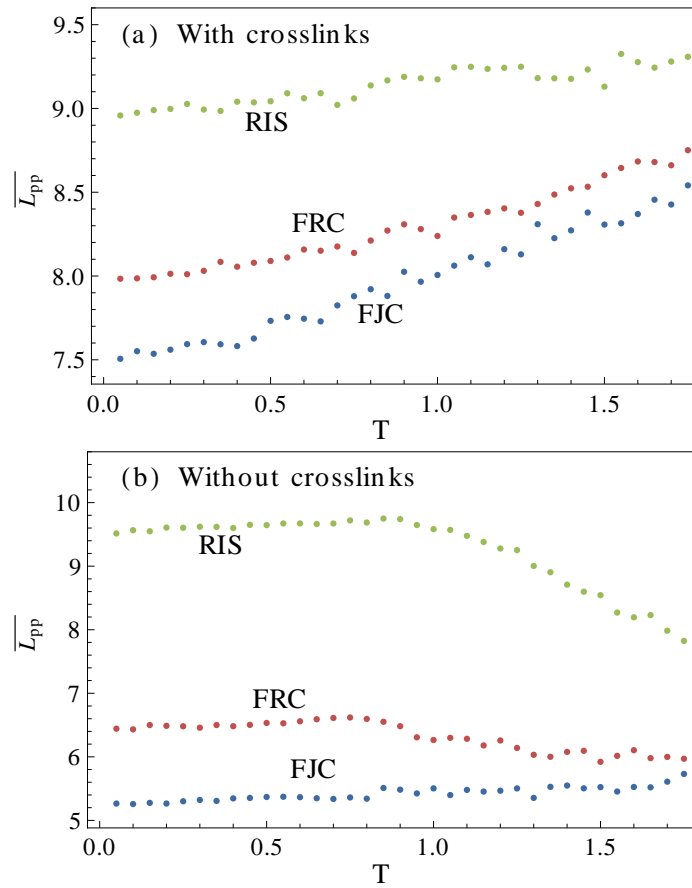


Figure 73: The average primitive path length ( $\overline{L_{pp}}$ ) as a function of temperature for each chain model in (a) crosslinked, and (b) uncrosslinked forms.



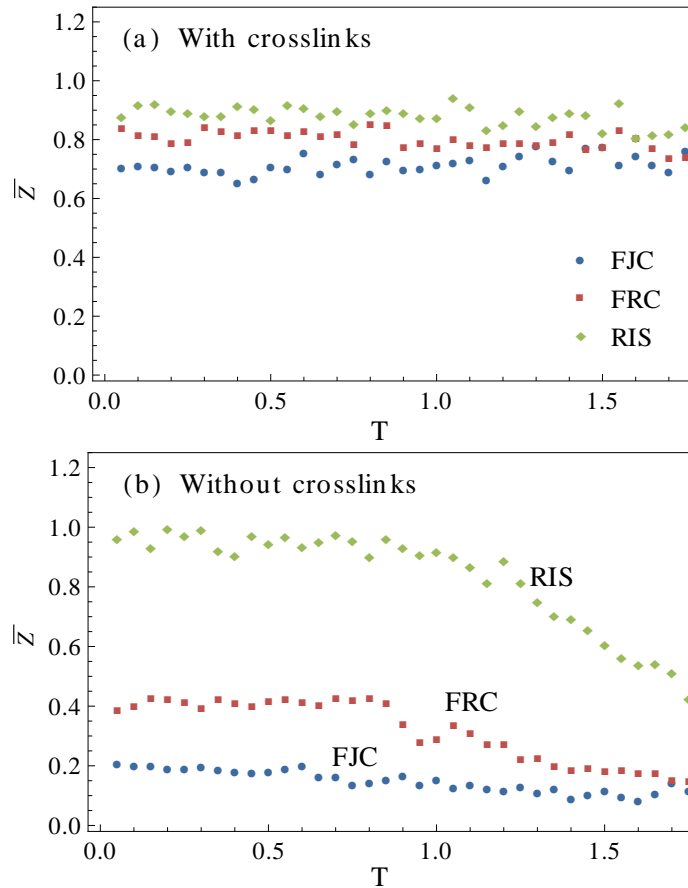


Figure 74: The average number of kinks per chain ( $\bar{Z}$ ) as a function of temperature for each chain model in (a) crosslinked, and (b) uncrosslinked forms.

different chain models, and for the uncrosslinked vs. crosslinked systems, follow the same behavior as the  $C_\infty$  values shown in Figure 72. This is because  $C_\infty$  and  $\overline{L_{pp}}$  both depend on the end-to-end distance. The average number of kinks per chain,  $\bar{Z}$ , displays different behavior. The results for  $\bar{Z}$  versus temperature are plotted in Figure 74 for each chain model in both crosslinked and uncrosslinked forms. The crosslinked systems all have approximately the same number of kinks per chain, and this value does not depend on the temperature. Since the crosslinking reaction was performed with the torsional and bending potentials enabled, and these potentials were then selectively turned off to represent the RIS and FJC systems, it is expected that each system have the same number of entanglements. The small differences seen in Figure 74a may be due to dangling chain ends (the extent of a the crosslinking

reaction was 97.9%, so there are still a few dangling ends). This result verifies the simulation procedure, which was intended to isolate the effects of bending and torsional potentials on simulated material properties. The  $\overline{Z(\overline{T})}$  trends for the uncrosslinked systems in Figure 74b are the same as for  $\overline{L_{pp}(\overline{T})}$  and  $C_{\infty}(T)$  for these systems. This shows that as more restrictions to chain motion are added, the average number of entanglements per chain increases with the average end-to-end distance.

The cohesive energy density (CED) is a measure of the extent of monomer-monomer interactions. It is defined as the sum of interaction energies over all interacting pairs in the system, divided by the total volume:

$$E_{CED} = \frac{1}{\text{volume}} \sum_i \sum_{j>i} U(r_{ij}). \quad (143)$$

This is a sum over *pair* interactions, and therefore the angular potentials are not included ( $U_B$  is a 3-body potential, and  $U_T$  is a 4-body potential). For the simulation results, we perform a simplified calculation of the CED using

$$E_{CED} = \rho_m \int_0^{r_c} 4\pi r^2 g(r) U_{LJ}(r) dr, \quad (144)$$

where  $g(r)$  is the radial pair-distance correlation function. Note that the FENE bond potential was not included in the calculation of the CED in Eq. 144; since all of the systems have the same bonded structure, including bonded pair interactions is expected to only shift the result by a constant. From Eq. 143 or 144 it can be seen that  $E_{CED} < 0$  represents an average attraction between monomer pairs, and  $E_{CED} > 0$  represents an average repulsion. A system of nonbonded particles with  $E_{CED} < 0$  is stable, but  $E_{CED} > 0$  means that the system will tend to continually expand. The cohesive energy density was calculated at each temperature interval using  $g(r)$  output from LAMMPS and Eq. 144. The result of this calculation is shown in Figure 75 for each chain model in both crosslinked and uncrosslinked forms. The energy is normalized by  $\epsilon$  (the LJ energy scale) times  $\rho_0 = 0.85$  (the initial monomer density of the system during equilibration and crosslinking). For the different chain models, the cohesive energy density follows  $E_{CED}(\text{FJC}) < E_{CED}(\text{FRC}) < E_{CED}(\text{RIS})$  at low temperatures, i.e. the monomers in the FJC system feel (on average) more

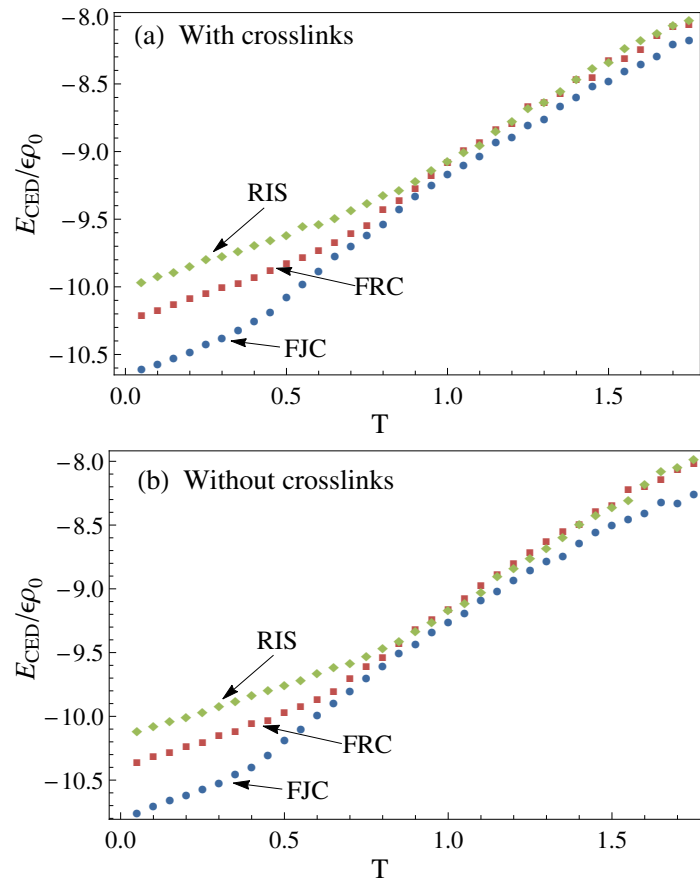


Figure 75: The cohesive energy density,  $E_{CED}$ , calculated as a function of temperature for each chain model in (a) crosslinked, and (b) uncrosslinked forms.

Network structure	Chain model
Uncrosslinked	FJC
Crosslinked	FJC
Crosslinked	FRC
Crosslinked	RIS

Table 13: Simulation cases considered for the modulus comparison of Section 8.7. Each is simulated using the NPT ensemble with  $r_c = 2 \times 2^{1/6}$ , i.e. attractive LJ interactions enabled (A-NPT).

attractive interactions than the other systems. At temperatures above  $T_g$ , the different systems have nearly the same  $E_{CED}$  values, with the FJC being slightly lower. Comparing the uncrosslinked and crosslinked systems, the  $E_{CED}$  values are nearly identical at temperatures above  $T_g$ . The uncrosslinked systems have slightly lower  $E_{CED}$  values at low temperatures, however. At  $T = 0.05$  each uncrosslinked system has an  $E_{CED}$  value that is lower than the corresponding crosslinked system by approximately 0.01 to  $0.015\epsilon\rho_0$ .

## 8.7 TEMPERATURE-DEPENDENT MODULUS

In this section, we examine the temperature-dependent modulus of the three crosslinked systems corresponding to the different chain models. The FJC model is also considered in an uncrosslinked form for comparison. The different systems considered in this section are listed in Table 13. We use the temperature-dependent modulus to determine  $T_g$  and define high and low temperatures for simulated shape memory cycling. Molecular reasons for the different modulus-temperature behavior of the three chain models is also examined through a comparison of the radial pair-distance correlation function.

Figure 76 shows the modulus-temperature behavior of the different systems. The modulus is normalized by  $\epsilon$  (the LJ energy scale) times  $\rho_0 = 0.85$  (the initial monomer density of the system during equilibration and crosslinking). The modulus was determined at temperature intervals of  $\Delta T = 0.05$  using the procedure described in Section 8.5. All of the different chain models display glassy-like behavior at low temperatures and each has a different glass transition temperature. The crosslinked materials display the expected rubbery

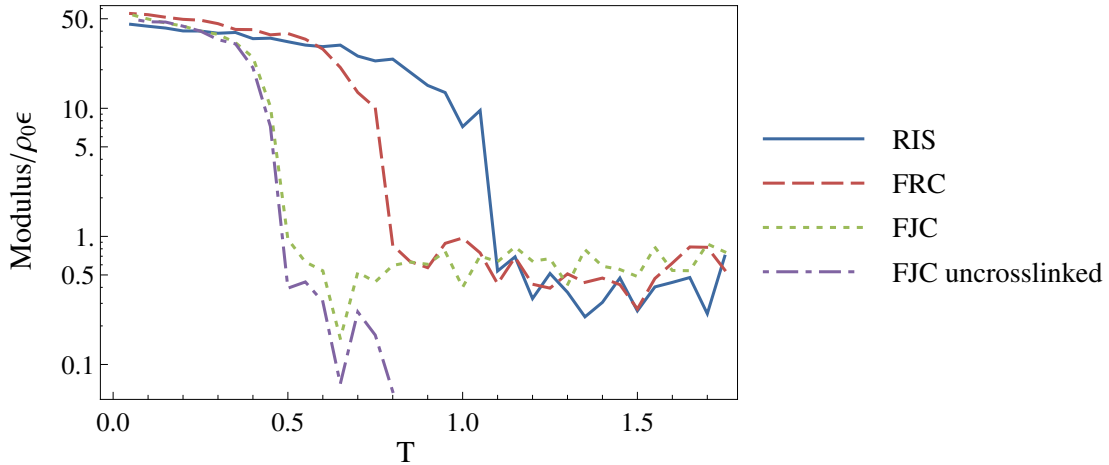


Figure 76: The modulus-temperature results for the different chain models in crosslinked form, along with the uncrosslinked FJC system. All are simulated with the NPT ensemble with  $P = 0$  and  $r_c = 2 \times 2^{1/6}$ .

plateau in the modulus-temperature behavior above  $T_g$ . The uncrosslinked FJC system displays viscous flow above  $T_g$  (i.e. the elastic modulus is zero), so therefore the curve does not extend to high temperatures. Figure 76 shows that the glass transition temperature increases when more restrictions on microscopic chain motion are included:  $T_g(\text{FJC}) < T_g(\text{FRC}) < T_g(\text{RIS})$ . This behavior is in agreement with Bulacu and van der Giessen [193], who examined monomer localization for the FJC, FRC, and RIS systems using the NVT ensemble and a pairwise potential cutoff of  $r_c = 2^{1/6}$  (this is designated R-NVT using the nomenclature in Section 8.5). With these simulation parameters and setup choices, evidence was seen in Ref. [193] for a glass transition in the FRC and RIS systems but not in the FJC system. Our results in Section 8.5 are also consistent with this. However, as discussed in Section 8.5, the NPT ensemble with  $r_c = 2 \times 2^{1/6}$  (attractive interactions enabled) is the most appropriate choice to simulate temperature-dependent polymer behavior, and therefore we only consider simulated systems with this choice in this section.

The glass transition temperature was determined for each system as the steepest part of the modulus-temperature curve. Figure 77 shows the modulus-temperature curve of each system shifted by  $T_g$ . The high and low temperatures for simulated shape memory cycling are marked in Figure 77. These temperatures were chosen relative to the  $T_g$  of each system so that a well-defined com-

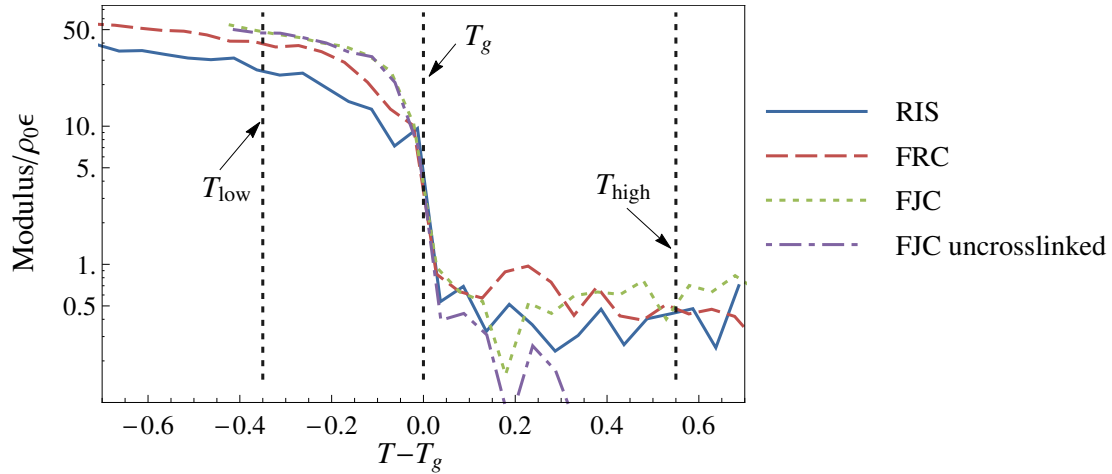


Figure 77: The glass transition temperature ( $T_g$ ) was determined as the steepest part of the modulus-temperature curve. High (above  $T_g$ ) and low (below  $T_g$ ) reference temperatures for simulated cycling and a comparison of properties were chosen relative to  $T_g$ .

Simulated system	$T_{low}$	$T_g$	$T_{high}$	$G^*(T_{low})$	$G^*(T_{high})$	$\frac{G^*(T_{low})}{G^*(T_{high})}$
FJC uncrosslinked	0.1	0.45	1.0	47.4	-	-
FJC	0.1	0.45	1.0	49.8	0.401	124
FRC	0.4	0.75	1.3	41.1	0.510	80.7
RIS	0.7	1.05	1.6	25.6	0.437	58.4

Table 14: Tabulated values for the approximate glass transition temperature, high and low reference temperatures, and the modulus values at the reference temperatures for each system.

parison of the modulus and shape memory cycling behavior of the different chain models could be made. Table 14 shows the glass transition temperature for each system, the temperatures designated  $T_{high}$  and  $T_{low}$ , and the corresponding modulus values at these temperatures. The non-dimensionalized modulus is calculated here as  $G^* = G/\epsilon\rho_0$ . The last column in Table 14 shows the modulus ratio from  $T_{high}$  to  $T_{low}$ . The magnitude of this modulus change is slightly smaller for the simulated systems than for a typical SMP material. Experimental work has demonstrated a modulus increase that varied in the range 200-2000 for the meth(acrylate) polymer tBA-DEGDA synthesized with different network structures [172]. However, since the modulus above  $T_g$  depends on the structure of the molecular network, it can be changed by

altering the crosslink density or the preparation procedure. This was demonstrated in Chapter 7 for simulated networks with different chain lengths and entanglement densities. In Chapter 7 the  $N = 200$ ,  $\rho_{cl} = 0.45$  system was the softest, with a modulus of  $G^* = .015$ .<sup>4</sup> Since the below  $T_g$  properties only depend weakly on the network structure, this system is likely to have a similar modulus below  $T_g$  as the FJC systems in Table 14. A below- $T_g$  modulus of 50 for this system would correspond to a modulus increase of over 3000 from below to above  $T_g$ . Note this is an estimate, since the above  $T_g$  modulus will also depend on the ensemble and pairwise potential cutoff used (NVT with  $r_c = 2^{1/6}$  was used in Chapter 7, and NPT with  $r_c = 2 \times 2^{1/6}$  is used in this section). This estimated range of modulus change values for the simulations compare well with this experimental range. This is another “check” that the simulation model is a reasonable representation of an SMP.

It is desirable for an SMP to have a large increase in modulus when cooled below  $T_g$ . Of the different chain models, the FJC system has the largest change in modulus from the rubbery to the glassy state. The trend shown in Table 14 is that the glassy modulus *decreases* when more restrictions to microscopic motion are included:  $G(\text{FJC}) > G(\text{FRC}) > G(\text{RIS})$ . This trend may be explained as follows. The spherical beads in the system experience a mutual attraction and can seek a state of minimum potential energy when the temperature is decreased. For the freely-jointed chains, the monomer units have no restrictions on rotation and can arrange in a way that maximizes attractive interactions in order to lower the free energy of the system. However, when restrictions to bond angle bending are imposed, the added constraint makes maximal close-packing more difficult to achieve. The addition of restricted dihedral rotations furthers this. Therefore, the FRC and RIS systems will have interactions on average that are less “deep” in the potential energy well since they are not packed as tight, and it will take less energy to make a shift in microscopic positions. This behavior is supported by the pair-distance correlation function shown in Figure 78 for each system at a temperature of  $T = 0.1$ , the volume-temperature behavior shown in Figure 79, and by the cohesive energy density

---

<sup>4</sup> In Chapter 7 the non-dimensionalization  $\tilde{G} = G/\rho_m kT$  was used, and here we use  $G^* = G/\epsilon\rho_0$ . Since  $k = 1$  using LJ units, and the temperature was set to  $T = 1$  for the simulations in Chapter 7, these non-dimensionalized modulus values are equal.

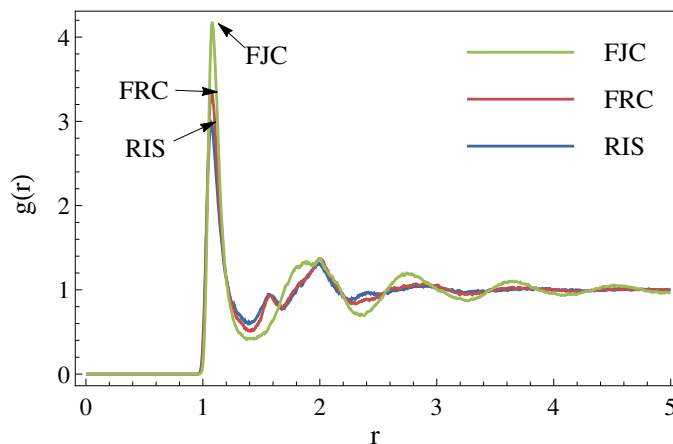


Figure 78: The pair-distance correlation function at  $T = 0.1$  for the FJC, FRC, and RIS models simulated using A-NPT.

shown earlier in Figure 75. At low temperatures, the addition of barriers to chain motion causes a frustration in the packing, and therefore the volume at low temperature follows  $V(\text{FJC}) < V(\text{FRC}) < V(\text{RIS})$  (Figure 79). The first peak in the pair-distance correlation function shown in Figure 78 consists of both bonded beads and beads in the first LJ coordination shell. This peak shifts down for the FRC and RIS systems since not as many monomers are able to enter this inner coordination shell. Additionally, the FJC system has more pronounced secondary peaks, suggesting a more regular structure. The cohesive energy density (Figure 75) is the lowest for the FJC system because of the high first peak in  $g(r)$ .

In Figure 77 and Table 14, the modulus results were presented by non-dimensionalizing with respect to the Lennard-Jones energy scale ( $\epsilon$ ) times the density of the system during initial equilibration and crosslinking ( $\rho_0$ ). Alternatively, we can use the temperature-dependent monomer density  $\rho_m(T)$  to non-dimensionalize the modulus results. The result of this calculation is shown in Figure 80 and the modulus values are tabulated in Table 15. This method of non-dimensionalizing yields the same trends for the different systems as obtained using the constant density  $\rho_0$ .

Below  $T_g$ , the energy of the system changes with deformation. Above  $T_g$ , energy stays constant and mechanical stresses are due to changes in entropy. This behavior is demonstrated in Figure 81 by plotting the potential energy of the FJC system as a function of an applied uniaxial deformation at  $T_{\text{high}} = 1$



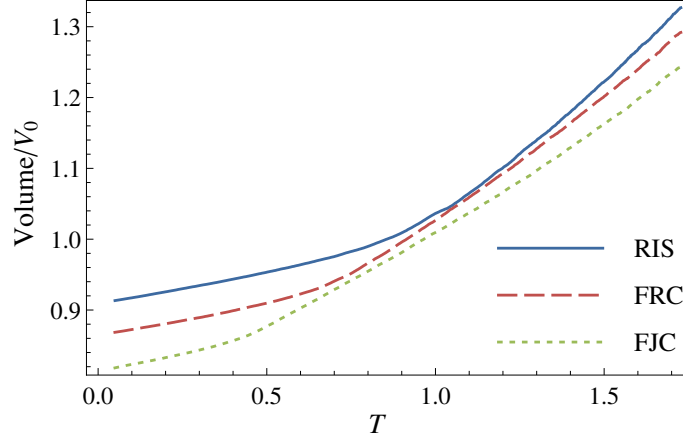


Figure 79: Volume as a function of temperature for the FJC, FRC, and RIS models simulated using A-NPT.

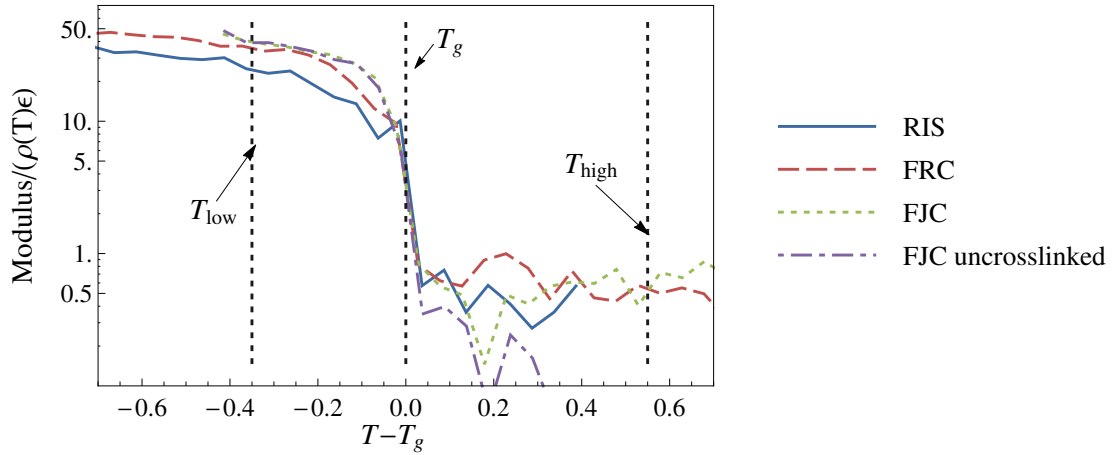


Figure 80: The modulus-temperature behavior of the different systems, plotted by non-dimensionalizing the modulus as  $G(T)/(\rho_m(T)\epsilon)$ . Figure 77 shows the same result using the non-dimensionalization  $G(T)/(\rho_0\epsilon)$ .

Simulated system	$\frac{G(T_{low})}{\rho_m(T_{low})\epsilon}$	$\frac{G(T_{high})}{\rho_m(T_{high})\epsilon}$	$\frac{G(T_{low})/\rho_m(T_{low})}{G(T_{high})/\rho_m(T_{high})}$
FJC uncrosslinked	39.2	-	-
FJC	41.0	0.405	101.2
FRC	37.0	0.575	64.3
RIS	24.9	0.554	45.0

Table 15: Tabulated values of the modulus non-dimensionalized using the temperature-dependent density  $\rho_m(T)$  at the reference temperatures for each system. These values show the same trends as those in Table 14, where modulus was non-dimensionalized using the constant density of  $\rho_0$ .

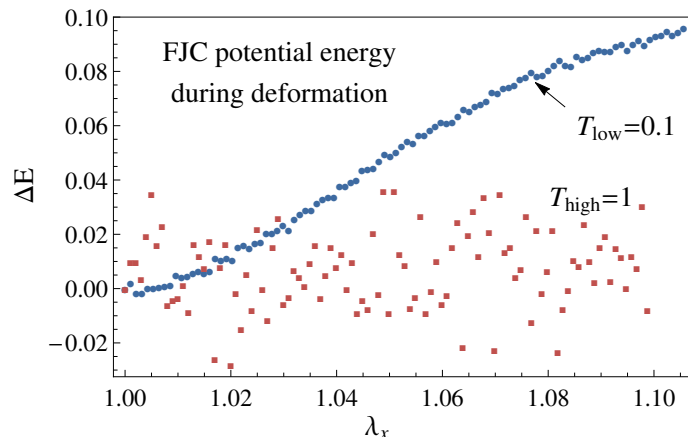


Figure 81: Potential energy as a function of deformation for the crosslinked FJC system at two different temperatures, simulated using A-NPT. At  $T_{\text{high}}$  the potential energy fluctuates about a mean, and the system displays entropic elasticity. At  $T_{\text{low}}$  the potential energy changes with deformation, and the system displays energetic elasticity.

and  $T_{\text{low}} = 0.1$ . Potential energy changes with stretch at the lower temperature but only fluctuates around a mean value at the higher temperature. Since energetic interactions determine the behavior below  $T_g$ , using a potential function other than Lennard-Jones may greatly change the behavior below  $T_g$ , but is expected to have less of an effect on the behavior above  $T_g$ .

## 8.8 SIMULATED SHAPE MEMORY CYCLING

After examining the modulus changes in Section 8.7 we look to see if the coarse-grained simulation models can reproduce experimentally observed trends for shape memory cycling behavior. In addition, we wish to determine which chain model shows the best shape holding and recovery abilities. Figure 63 shows the typical procedure for thermal shape memory cycling with stress-free shape recovery. In this section we perform simulated shape memory cycling for the different crosslinked chain model systems (the cases are the same as listed in Table 13, and also include the uncrosslinked FJC system). A uniaxial strain of  $\sim 100\%$  was first applied to the simulation box in the  $x$ -direction. Each system was then cooled from  $T_{\text{high}}$  to  $T_{\text{low}}$  with the deformation held constant. The high and low cycling temperatures for each system are listed in Table 14.

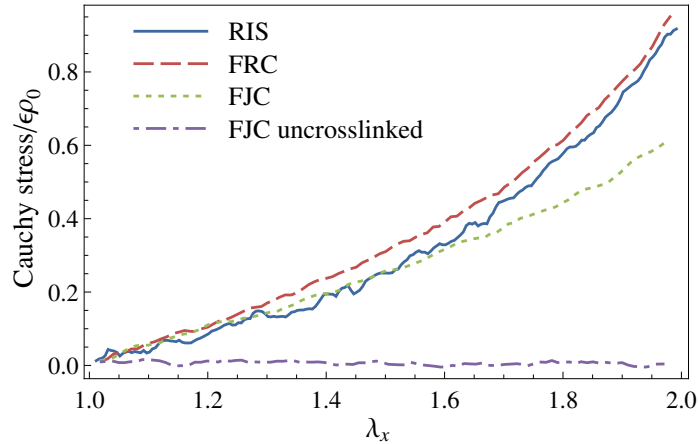


Figure 82: Uniaxial tension mechanical behavior (the first step of the simulated shape memory cycling procedure) for the different chain models. The uncrosslinked system undergoes viscous flow, with a stress that remained near zero for the deformation rate that was used.

The strain rate and cooling rate for simulated cycling are the same that were used to obtain modulus as a function of temperature. After cooling, the stress was released by specifying the isotropic pressure of  $P = 0$  on the simulation box (zero traction) and allowing the system to relax for a time of  $1.2 \times 10^5 \tau$ . The stretch value after this relaxation step is referred to as the temporary shape. The samples were then heated either with temporary shape fixed in order to measure temperature-dependent recovery stress, or with stress-free boundary conditions to measure recovery strain as a function of temperature.

Figure 82 shows the initial deformation of different systems at  $T_{\text{high}}$ . For the different chain models it is seen that the inclusion of bond bending in the FRC and RIS models makes the simulated material noticeably stiffer at the intermediate stretch levels shown in Figure 82. The uncrosslinked FJC system is also shown for comparison; this system undergoes viscous flow above  $T_g$ , and the stress at this deformation rate remained near zero. Since the systems in this section were deformed using constant pressure (as opposed to constant volume) boundary conditions, we can measure the Poisson ratio to see if volume is still approximately constant with deformation. The Poisson ratio ( $\nu$ ) of each system can be calculated using  $\lambda_y = \lambda_z = \lambda_x^{-\nu}$ .<sup>5</sup> This yields the values

<sup>5</sup> To apply this to data, rewrite as  $\ln \lambda_y = -\nu \ln \lambda_x$  (the y or z direction are coupled in the simulation and deform identically). The value of  $\nu$  is then found as the slope of the line fit to a data plot of  $\ln \lambda_y$  as a function of  $\ln \lambda_x$ .

Simulated system	Poisson ratio ( $\nu$ )
FJC uncrosslinked	0.4978
FJC	0.4959
FRC	0.4984
RIS	0.4943

Table 16: The Poisson ratio ( $\nu$ ) of each system, calculated using the uniaxial deformation result.

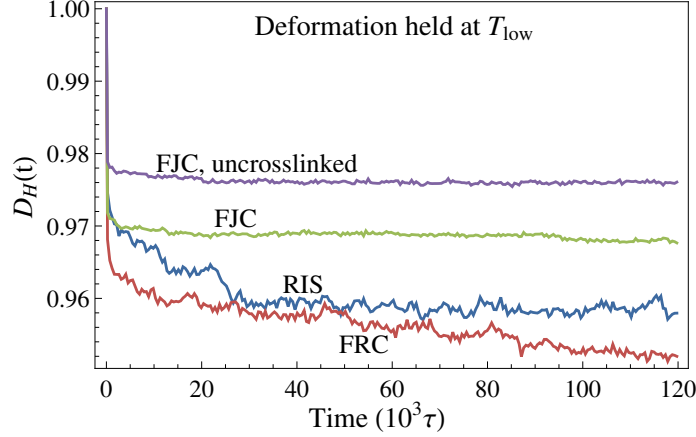


Figure 83: Stretch relaxation at  $T_{low}$  after cooling for the different systems.

of  $\nu$  given in Table 16. It is seen that these are close to the incompressible value of 0.5.

After cooling to  $T_{low}$ , the stress was released in order to test the ability of the simulated systems to hold the applied deformation. Figure 83 shows stretch relaxation as a function of time for each chain model. Referring to the initial deformation as  $\lambda_0$ , Stretch relaxation is quantified by plotting

$$D_H(t) = \frac{\lambda(t) - 1}{\lambda_0 - 1}, \quad (145)$$

as a function of time. This quantity was introduced in Eq. 135 as a measure of the deformation held. Both the crosslinked and uncrosslinked FJC systems appear to reach a steady state in the time given for relaxation. However, both the FRC and RIS systems appear to still be changing shape after  $1.2 \times 10^5 \tau$ . Although the changes in strain for these systems during relaxation are relatively small, the equivalent relaxation time examined during the simulation

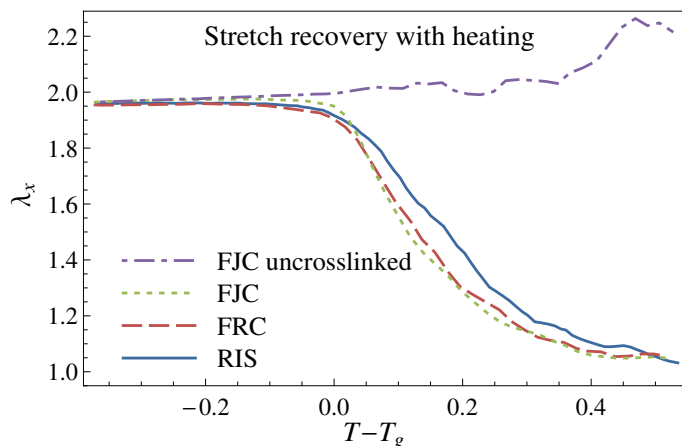


Figure 84: Stretch recovery upon stress-free heating to  $T_{\text{high}}$  for the different systems.

is also small compared to relevant experimental timescales for SMPs. The FRC and RIS chain systems may be classified as shape memory polymers if the relevant times required to hold a deformation are on the order of the time simulated in Figure 83. However, this designation is not practically useful since by any measure the simulation times are short compared to relevant experimental times for SMPs. We can reasonably conclude that the FRC and RIS systems at  $T_{\text{low}}$  do not hold their shape well enough to be considered shape memory polymers, and that the FJC system does. An alternative description is that the FJC system is the best shape holder. The reason for this is essentially the same as discussed in Section 8.7 with respect to the temperature-dependent modulus data: the FJC system is able to pack tighter to maximize favorable interactions at low temperatures because there are no restrictions on bond angle configurations.

After the relaxation step, the systems were heated back to  $T_{\text{high}}$  in order to obtain stretch recovery as a function of temperature (i.e. stress-free recovery). These results are in Figure 84. All of the crosslinked systems display recovery to a state near the undeformed configuration. To proceed, we again note that the designation of a crosslinked polymer as a “shape memory polymer” is one of degree, not of kind [179]. This means that any crosslinked polymer shows shape memory behavior on some length and time scale. The uncrosslinked system does not display shape recovery since it does not have a permanent network structure, and the chains in this system are not sufficiently entangled

to demonstrate shape holding over the time that was simulated. The FJC system has the steepest recovery curve and the RIS system the most gradual. In current practical use, a steep curve is desired since this allows for easy switching between temporary and permanent shapes. We therefore rank the FJC system as the best in shape recovery, and the RIS system the worst.

From the current results, the simple FJC model can be classified as the best model to represent a shape memory polymer: it shows the largest modulus change across  $T_g$ , the sharpest change in mechanical properties near  $T_g$ , the steepest slope of stretch recovery upon heating, and it appears to hold its shape below  $T_g$  better than the FRC and RIS systems. In Figure 85 we compare the stress during shape-memory cycling of the FJC system in both tension and compression with experimental data from Liu et al. [24]. These authors performed shape memory cycling tests using the DP5.1 epoxy material [23]. This data was chosen for comparison since the sample geometry and test apparatus in Ref. [24] was configured to measure both tensile and compressive stresses during the same test. The initial deformation for the tests in Figure 85 was 9.1% tensile or compressive strain. Although this is much smaller than the simulation, the DP5.1 material also has a smaller maximum extension than the simulated system. It is reasonable to compare the simulation results with the main trends seen during cycling. When cooling, the stress for both the tensile and compressive cases initially decreases in magnitude. Then, below  $T_g$ , an increasing tensile stress develops. This stress is large enough to make compressive stresses become tensile. After stress relaxation at  $T_{low}$ , a peak in the compressive stress is seen below  $T_g$  upon reheating, and then the stress returns to follow behavior close to the path taken during cooling. When the deformation is held during the entire procedure (i.e. the stress is not set to zero at  $T_{low}$ ) each system shows minimal hysteresis. The simulation reproduces all of the trends seen in the experimental data.

## 8.9 VISUALIZATION OF TEMPERATURE-DEPENDENT CHAIN CONFORMATIONS

The molecular behavior of each system above and below  $T_g$  can be visualized by tracking chain conformations over time. Figure 86 shows the time-

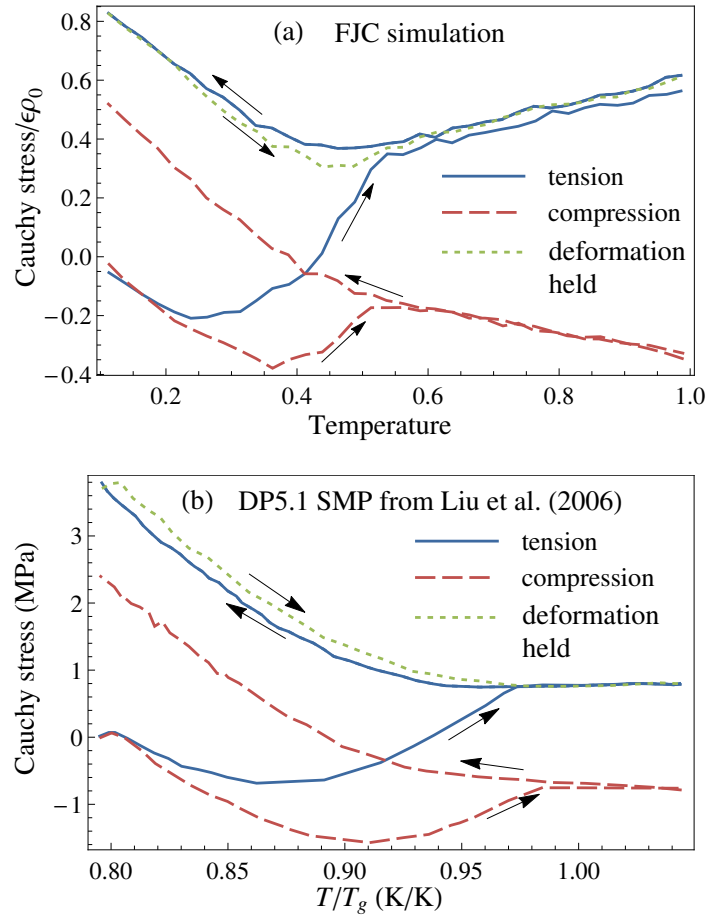


Figure 85: Stress during shape memory cycling after initial tensile and compressive deformations for (a) the simulated FJC-A-NPT system, and (b) the DP5.1 shape memory polymer material [23] tested by Liu et al. [24]. Each plot also shows the thermal cycling response for the tensile case when the deformation was held during the entire procedure (i.e. the stress was not set to zero at  $T_{low}$ ).

averaged chain configuration along with the time-dependent chain configurations tracked over a time of  $5760\tau$  for a representative chain in the FJC, FRC, and RIS systems. Temperatures from  $T_{\text{low}}$  to  $T_{\text{high}}$  in increments of 0.1 are shown. The time each chain was tracked is  $\sim 120$  times the Rouse time for the FJC chain system.<sup>6</sup> At low temperatures, the chain is “caged” by its neighbors and only fluctuates a small amount about an average. The FJC chain system has the smallest magnitude of monomer fluctuations at  $T_{\text{low}}$ , and the RIS system the largest. There are two reasons for this behavior. First, the glass transition temperature, and therefore the designated  $T_{\text{low}}$  temperature,<sup>7</sup> of the RIS system is higher than the FJC system. The RIS chain in Figure 86 therefore has more thermal energy than the freely-jointed chain at  $T_{\text{low}}$ . Additionally, from the results in the previous sections we know that the monomers in the FJC system are able to pack tighter to maximize favorable attractive interactions. The monomer pairs in the FJC system are on average deeper in the minimum of the LJ potential, and require a larger energy to be moved out of this configuration. If thermal energy is not enough to overcome the energy barrier then the magnitude of fluctuations will be very small. Above  $T_g$ , each chain model looks similar in Figure 86 because the thermal energy is high enough to effectively randomize the configurations.

At temperatures near the glass transition each chain model displays different behavior. The magnitude of monomer fluctuations appears to undergo a relatively rapid increase for the FJC model near  $T_g$ . The increase in monomer fluctuations for the FRC and RIS models is more gradual. This is due to the different localization mechanisms responsible for the glass transition in these different systems. The FJC system has a glass transition solely due to attractive monomer interactions. When thermal energy is sufficient to overcome the energy barrier associated with these interactions, monomer fluctuations in the FJC system will increase dramatically. Localization in the RIS system is due to temperature-dependent restrictions on dihedral angle rotation as well as

---

6 The Rouse time is slightly different for the FRC and RIS chains due to the bending and torsional restrictions, since the equivalent freely-jointed chain for these systems has different values of the Kuhn monomer length ( $b$ ) and the number of Kuhn monomers ( $N$ ). However, this difference is not important here.

7 Recall from Section 8.7 that the that the temperatures  $T_{\text{low}}$  and  $T_{\text{low}}$  were defined with respect to the glass transition temperature - see Table 14



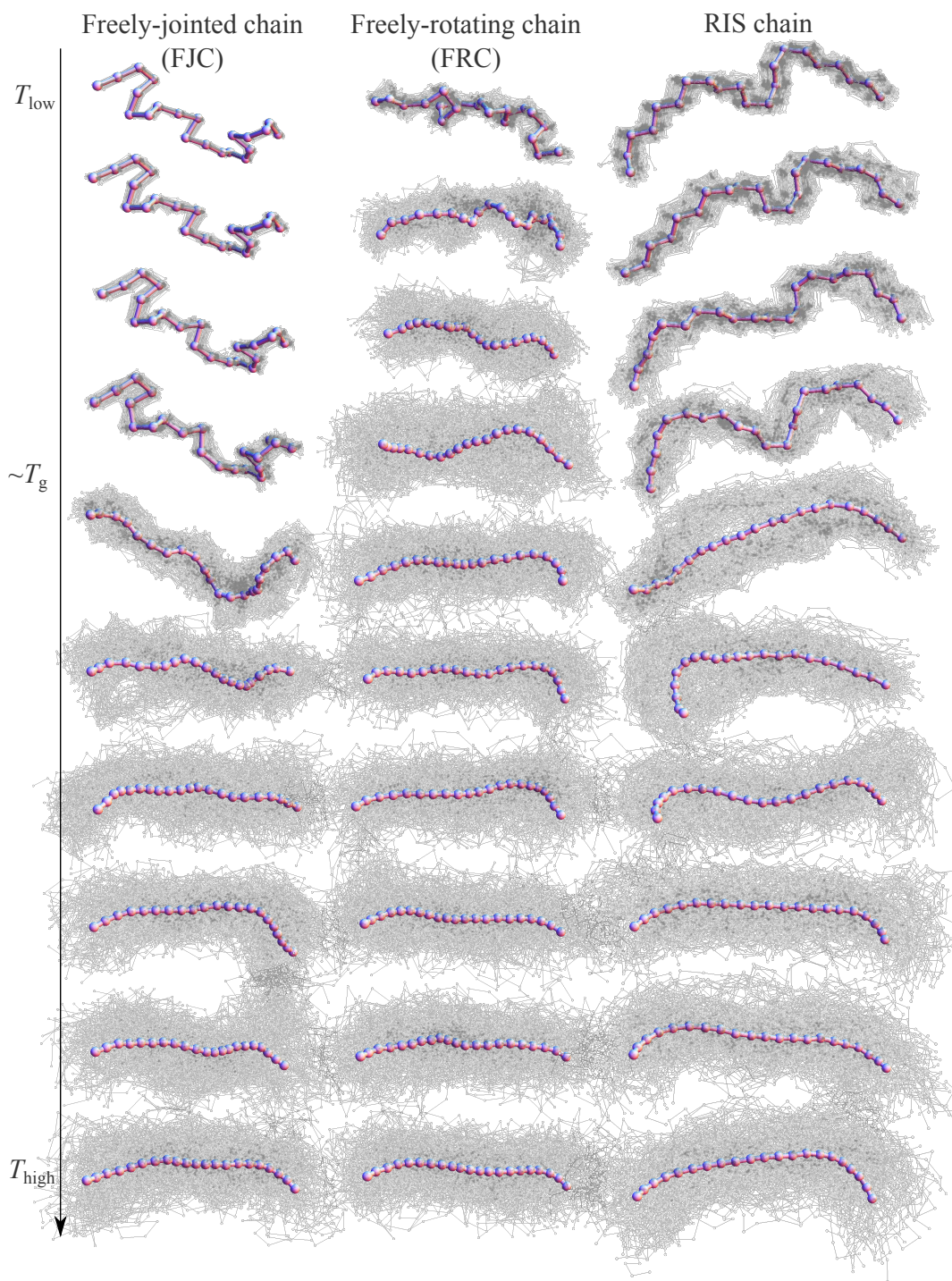


Figure 86: A visualization of time-dependent conformations for each chain model at different temperatures from  $T_{\text{low}}$  to  $T_{\text{high}}$  increments of 0.1. The “same” chain is shown for each system, i.e. this chain has the same bonded connections and intermolecular entanglements for each case. The time-averaged conformation (the connected beads) is shown along with the time-dependent conformations (i.e. the phase space: shown as the shaded region) for each chain at each temperature.

monomer attractions. At low temperatures the dihedral angles stay in one of the minima of  $U_T$ , corresponding to *gauche*<sup>-</sup>, *trans*, or *gauche*<sup>+</sup> states (see Figure 67). The energy difference between *trans* and *gauche* states is  $1.1\epsilon$ , but the height of the energy barrier going from *trans* to *gauche* is  $3.5\epsilon$ . The energy barrier from *gauche* to *trans* is  $2.4\epsilon$ . For comparison, the LJ potential has an energy difference of  $\epsilon$  at the minimum in comparison to the potential at large separation distances (see Figure 35). For an RIS chain, successive bonds must have sufficient rotational kinetic energy to overcome the barrier in order to change to a different dihedral angle. This occurs at temperatures above  $T_g$  for the RIS system, as can be seen in Figure 86. At low temperatures the chain retains fixed dihedral angles. Because there are two mechanisms leading to localization in the RIS system, each with different energy barriers and temperature dependence, the overall result is a broadening of the transition behavior. This can be seen in comparing the chain pictures of the RIS and FJC models in Figure 86, in the temperature-dependent modulus behavior shown in Figure 77, and in the temperature-dependent stretch recovery behavior shown in Figure 84.

The FRC system represents behavior that is somewhat between the FJC and RIS systems. It can be considered as the RIS model in the limit of zero energy barriers between *trans* and *gauche* states. Or, equivalently, as an RIS model case where the energy barrier between dihedral angle changes is much smaller than the energy associated with monomer attraction. For the RIS system simulated here, the energy barrier between dihedral angle changes is greater than the energy associated with monomer attraction. The interplay between these two processes leads to transition behavior, and therefore changing the energy associated with one (or both) will change the temperature dependence. Interestingly, the FRC system appears to have a significant increase in the magnitude of monomer fluctuations below  $T_g$ , while the greatest change for the FJC and RIS systems occurs near  $T_g$ .

Overall, there is a large increase in the magnitude of monomer fluctuations as temperature is increased above  $T_g$ . This behavior can be quantified using the Rouse model. Bennemann et al. [150, 151] calculated mean-square monomer displacements as a function of time and temperature for an uncrosslinked Kremer-Grest FJC system with attractive interactions included (using the NVT

ensemble), and found a very good agreement with Rouse model statistics. Here, we are considering a crosslinked system in the NPT ensemble and have only tracked time-dependent conformations to visualize chain behavior. A detailed analysis of mean-square displacements in comparison with theoretical Rouse model predictions may be a topic for future work.

## 8.10 DISCUSSION

The results in Sections 8.7 and 8.8 showed that temperature-dependent behavior relevant to SMPs can be reasonably represented using the NPT ensemble with LJ attractive interactions included. Indeed, it was shown that the simple FJC model was able to reproduce experimentally observed trends seen during shape memory cycling. This suggests that coarse-grained simulations can play an important role in furthering our understanding of the shape memory effect, developing multiscale models of thermomechanical behavior, and proposing routes for material development. The simulation results are consistent with the concept of temperature-dependent chain mobility, which has its roots in theoretical polymer science [33]. The low temperature deformation behavior in the simulations is consistent with the description of a thermally activated process [213, 214]. Future work will benefit from a comparison of simulation results with these and related theoretical concepts.

The simulated freely-jointed chain (FJC) model displayed the best shape memory properties. A reason for this was discussed in Section 8.7 by comparing the pair-distance correlation function at low temperature for the different chain models (Figure 78). The cohesive energy density in Figure 75 also supports this conclusion: the FJC system is the best shape holder and has the largest modulus change with temperature since the monomers in this system can pack tight to maximize favorable attractive below  $T_g$ . The importance here is in the transition from entropic elasticity above  $T_g$  to energetic elasticity below  $T_g$ . Entropic elasticity depends on network structure and is relatively insensitive to chemical details. Energetic elasticity depends strongly on chemical details and therefore varies for different polymer materials. A material that has extensive monomer interactions below  $T_g$  is likely to be a “good” SMP. In the simulations here, the below  $T_g$  monomer interactions varied only with

the different bending and torsional potentials. Although this suggests that a material with fewer restrictions on chain bending and torsion may perform better as an SMP, it must be noted that in an actual material these characteristics cannot be varied independently. The most important characteristic of a good SMP material is a large change in properties from above to below  $T_g$ , and this change is caused by attractive interactions becoming dominant at temperatures below  $T_g$ .

One way to increase the change in properties from above to below  $T_g$  is to incorporate some sort of molecular mechanism for reversible temperature-dependent bonding. Hydrogen bonds perform exactly this function; indeed, recent work has examined the fabrication of SMPs which contain hydrogen bonds [215, 216]. Another approach is to embed a hydrogen-bonding biopolymer such as DNA into an SMP [217]. Filler particles may function to improve SMP performance via a similar mechanism. A coarse-grained simulation model with spherical filler particles has been developed in other work [136]. Temperature-dependent simulations of this model using the NPT ensemble and attractive monomer interactions could be used to investigate how the molecular mechanisms of SMP behavior are affected by the addition of filler particles.

## 8.11 CONCLUSIONS

In this chapter, we presented the first coarse-grained simulation of thermal shape memory polymer behavior. It was shown that using the NPT ensemble with attractive LJ interactions enabled is sufficient to represent an SMP via molecular dynamics simulation. The results demonstrated that it is important to include attractive interactions and allow for volume changes in order to form a simple SMP simulation model that agrees well with various experimental trends (we compared modulus vs. temperature, volume vs. temperature, and SMP cycling with experimental results). A comparison of simulation results for systems including various levels of restriction in chain motion (FJC, FRC, and RIS models) demonstrated that low temperature attraction, not restrictions on chain bending and torsion, is the most important mechanism leading to “good” SMP behavior. The FJC system was able to pack tightly to maximize favorable

attractive monomer interactions, and therefore had the largest modulus change across  $T_g$ . The FJC system also had the best shape holding ability. These results are important for the development of high-performance SMP materials, since they emphasize the need to maximize the change from entropic to energetic elasticity from above to below  $T_g$  in order to design a “good” SMP. The simulation results support the basic molecular mechanism of temperature-dependent chain mobility as responsible for the shape memory effect. Future simulation work can build on these results to examine the effect of filler particles and temperature-dependent bonding on SMP performance, and to test specific models predictions in the development of a multiscale model of SMP behavior.

## CHAPTER 9

### SUMMARY AND MAIN CONTRIBUTIONS

---

In this work we used physics-based modeling and coarse-grained molecular dynamics simulations to analyze nonlinear elasticity, micro-macro deformation, and the shape memory effect in crosslinked polymers. A new large deformation model of elasticity was derived in Chapter 4; this model can be used within a general continuum mechanics framework, and it was shown that the model can be used to fit experimental data for materials with very different mechanical behavior. The model has 3 parameters that are all tied to the polymer network structure and deformation behavior. Coarse-grained molecular dynamics simulations were performed using the Kremer and Grest [15] bead-spring polymer model. Different simulated polymer networks ranged from short, unentangled chains, to long, entangled chains. A detailed analysis of micro-macro deformation was performed in Chapter 6. We tracked changes in both chain end-to-end length and primitive path length for the different networks, and showed how the affineness of deformation depends on network topology. These results suggest that the primitive path concept can be used to form a consistent description of microscopic chain deformation mechanisms, which applies to networks with different structures (i.e. ranging from short to long chain systems). The model of Chapter 6 accounts for general nonaffine deformations of the polymer network, and it was shown using the simulation results in Chapter 7 how nonaffine deformation affects mechanical properties. The simulated large deformation limiting extensibility behavior was quantified by model fitting, and several different theoretical models were evaluated in terms of their ability to predict property changes for the different networks. Coarse-grained simulations of the shape memory effect were performed in Chapter 8. The simulation model was modified to account

for temperature-dependent polymer behavior, and the results for systems of chains with different molecular mobilities were compared. It was shown that simply including attractive interactions and using the NPT ensemble with the Kremer and Grest [15] model is sufficient to represent a shape memory polymer via coarse-grained MD. The system of chains with the fewest restrictions on molecular motion (i.e. freely-jointed chains) displayed the best shape holding and recovery abilities, and had the largest modulus change across  $T_g$ . This was due to the ability of this system to maximize favorable attractive interactions between monomers. Chain conformations were visualized as a function of temperature to demonstrate the molecular mechanisms responsible for the shape memory effect. The specific contributions from this work are listed below.

#### 9.1 MAIN CONTRIBUTIONS OF WORK

- A new 3-parameter model of large deformation elasticity was derived in Chapter 4. This model is based on generalizing the [5, 6] to include non-phantom deformation and Langevin chain statistics. The model accounts for general nonaffine deformations of chain ends and has parameters that are defined solely by the network structure and deformation behavior. It was shown that the model can fit large deformation elasticity data for materials with very different properties. This model was used to analyze nonaffine chain deformation in Chapter 6, and to analyze the mechanical properties of the different simulated networks in Chapter 7. Ref. [21] is the publication associated with this work.
- The molecular dynamics simulations in Chapter 6 are the first use of primitive path analysis to characterize the deformation of crosslinked polymers. These results show that both chain end-to-end distance and primitive path deformation are linear functions of the applied deformation, even to very large stretch values. The level of affinity of chain end-to-end deformation increases with both chain length and entanglement density, and will become affine for very long, entangled chains. In contrast, the results here show that primitive path deformation is always

nonaffine, even for long, entangled chains, and that the level of affineness is not affected by the network topology.

- The visualization and statistical analysis of Chapter 6 suggests that the primitive path is the correct length scale to quantify microscopic deformation in crosslinked polymers. Although nearly all existing theories of elasticity consider end-to-end chain deformation, the simulations suggest that a multiscale model based on primitive path deformation is the most promising route to link microscopic deformations with macroscopic elastic and viscoelastic properties of crosslinked polymers.
- The molecular dynamics simulations of Chapters 6-7 are the first analysis of the large deformation behavior, and of different deformation states (uniaxial, biaxial, and pure shear) of crosslinked polymers. The large deformation limiting extensibility behavior is quantified by model fitting. By comparing the fit to predicted parameter values for three different models, it was demonstrated that the dominant trend for changes in limiting extensibility is with the number of monomers per chain. Further work is needed to develop a large deformation elasticity model that captures the mechanisms of chain deformation at large stretch and is based on primitive path deformation. These results were discussed in the context of future work in multiscale modeling of the elastic and viscoelastic properties of crosslinked polymer materials.
- The modulus of the different simulation test cases was measured in Chapter 7, and it was shown that the modulus values are correlated with nonaffine deformation.
- Chapter 8 presented the first coarse-grained simulation of shape memory polymer behavior. It was determined that including attractive interactions and using the NPT ensemble with the Kremer and Grest [15] model is sufficient to represent a shape memory polymer.
- The importance of attractive interactions in leading to desirable SMP behavior at low temperatures was demonstrated by comparing simulations of chains with different levels of molecular mobility (the different cases



approximately represented freely-jointed, freely-rotating, and rotational isomeric state chains). The freely-jointed chain system displayed the “best” SMP behavior due to ability to maximize attractive interactions at low temperatures, and it was shown that this system displays the same nonlinear thermomechanical cycling trends seen experimentally. These results give important information as to how to model and understand shape memory polymer materials.

## 9.2 FUTURE WORK AND EXTENSIONS OF CURRENT PROJECTS

- **Nonaffine primitive path deformation: viscoelasticity simulations.** Even for very long chains, the simulation results suggest that quasistatic primitive path length deformation is not affine. Since nonaffine deformation is due to extensive rearrangement, deformations at high strain rates will be more affine if the rate is fast enough to not allow molecular rearrangement to occur. Tracking primitive path length changes for deformations at different applied strain rates is a promising route to elucidate the molecular mechanisms responsible for viscoelasticity. The simulation and analysis methods for such a study would be identical to those used in Chapter 6, except that different applied strain rates would be considered.
- **Nonaffine primitive path deformation: different network structures and monomer densities, and theoretical treatment.** The cases in Chapter 6 were tested at the monomer density of 0.85, which is the typical density used in the Kremer and Grest [15] simulation model. However, it was noted in Chapter 6 that an alternative procedure is to crosslink at different densities and then deform at these densities. For example, crosslink at a monomer density of 0.45 and also deform the system at this density. The nonaffine end-to-end and primitive path coefficients  $\beta_{ee}$  and  $\beta_{pp}$  were listed in Chapter 6 for two test cases deformed using this procedure. A full analysis could be done to generalize and strengthen the conclusions about nonaffine primitive path deformation. This analysis could include randomly crosslinked networks in addition to the ideal endlinked network structures used in this dissertation.

The results in Chapter 6 suggest that  $0.4 \lesssim \beta_{pp} \lesssim 0.5$  can be expected for all cases, regardless of the density and network structure. If this is found to hold for additional simulation cases as well, more attention should be given to the theoretical treatment and why this behavior is seen. A possible starting point is to treat an entanglement as analogous to a four-functional crosslink, and describe the segments between entanglements using the phantom network model. The goal with a combined theoretical and simulation analysis of nonaffine primitive path deformation would be to construct and test a universal description of chain behavior in crosslinked polymer systems which is based on primitive path deformation.

- **Simulating filled materials, interpenetrating polymer networks, and bimodal elastomers** The simulations in this dissertation considered simple, ideal polymer network structures. Filler particles (such as carbon black) are often added to elastomer materials in order to increase the modulus and improve material properties. The simulation methods and chain and primitive path deformation metrics could be used to analyze how chain behavior is affected by the addition of filler particles. Coarse-grained representations of filler particles in polymer systems have been developed [136, 218], and the behavior of chains in uncrosslinked systems has been analyzed. A similar coarse-grained representation could be used as a starting point to analyze the effect of filler particles on chain behavior and mechanical properties of crosslinked polymer materials.

Recent work has examined materials with improved properties obtained via a bimodal distribution of the number of monomers per chain [208] or interpenetrating polymer networks [219, 220]. The analysis methods used in Chapter 6 could be used to examine how chain and primitive path deformation behavior are connected to the mechanical properties of these materials.

## APPENDIX A: MONTE CARLO FITTING PROCEDURE

---

An in-house numerical algorithm was developed for Monte Carlo fitting to multiple datasets. The following procedure was used to obtain the best fit parameters listed in Figures 25 and 27, and in Tables 1, 2, and 8. For a given model applied to a data set, reasonable starting parameter values are chosen and then  $m$  different optimization are started.  $m = 4$  was used to obtain the parameter values in Figures 25 and Figures 27 and Table 8, and  $m = 20$  was used to obtain the parameter values in Tables 1 and 2. The first move of each individual optimization is always accepted and randomly changes the parameters up to 50% of their starting value. Subsequent simultaneous parameter changes are only accepted if they lower the residual, which is calculated as

$$\text{Residual} = \frac{\sum_{\text{all data points}} (\sigma_{\text{model}} - \sigma_{\text{data}})^2}{\sum_{\text{all data points}} (\sigma_{\text{data}})^2}. \quad (146)$$

The maximum step for the changes in parameter values is progressively decreased. Convergence is defined to be when the maximum move size is 0.01% of the parameter values, the previously accepted move changes the residual less than 0.001%, and 100 consecutive random moves have been tried and rejected. Since the first move of each case was defined to be large in order to explore the parameter space, some of the best fits reached a minimum that was obviously wrong (e.g.  $\lambda_{\text{max}} \rightarrow \infty$ ); these were discarded. All of the parameters reported from this fitting procedure are an average of the best fit parameters obtained over the different optimization runs, with the exception of the parameters reported for the micro-sphere model [14] in Table 1. For this model only the single best fit was used since it has 5 parameters and is therefore mathematically over-defined in terms of fitting the presented data.

## APPENDIX B: CODES FOR GENERATING SIMULATION SETUPS AND RUNNING IN LAMMPS

---

### B.1 GENERATING A SIMULATION SETUP

This Mathematica code generate a set of chains as random walks with the backfolding restriction described by Grest [82], and then places them in a simulation box and outputs a data file that can be read as LAMMPS input.

```
(* PARAMETERS *)
Ns=35;
numchains=1000;
density=0.65;
functionality=4;
dir="/media/Chronos/Dropbox/Latex-Current/Dissertation/
  codestoinclude/";
file="startconfig.dat";

(* FUNCTION DEFINITIONS *)
gen[0] = {{0, 0, 0}};
gen[n_] :=
  Append[#, (#/(Sqrt[#1^2 + #2^2 + #3^2] & @@ #)) &[
    RandomReal[{-1, 1}, 3]] + Last[#]] &[gen[n - 1]];
gen[r_, 0] = gen[0];
gen[r_, n_] :=
  Append[#,
    r (#/(Sqrt[#1^2 + #2^2 + #3^2] & @@ #)) &[
      RandomReal[{-1, 1}, 3]] + Last[#]] &[gen[r, n - 1]];
(* with backfolding restriction *)
okgen[r_, last2_] :=
  Module[{n},
```

```

While[EuclideanDistance[
  n = r (#/(Sqrt[#1^2 + #2^2 + #3^2] & @@ #)) &[
    RandomReal[{-1, 1}, 3]] + Last[last2], First[last2
  ]] < 1.02];
n];
gen2[r_, 1] := gen[r, 1];
gen2[r_, n_] := Append[#, okgen[r, Take[#, -2]]] &[gen2[r, n-1]];
placeOneEndInside[chain_, boxvol_] := Function[f, f + # & / @ chain][
  RandomReal[{0, boxvol^(1/3)}, 3]];

(* GENERATE CONFIGURATION AND OUTPUT TO FILE *)
numbeads = Ns + 1;
numcrosslinkers = 2 numchains / functionality;
boxvol = Ns numchains / density;
chains = Table[SeedRandom[]; gen2[0.97, Ns], {i, numchains}];
placed = Map[placeOneEndInside[#, boxvol] &, chains];
type = Prepend[#\[Transpose], ConstantArray[1, Length@#]]\[
  Transpose] & / @ placed;
mlc = Table[Prepend[#\[Transpose], ConstantArray[i, Length@#]]\[
  Transpose] & [type[[i]]], {i, Length@type}];
(* the ones to change into crosslinkers *)
tochange = Take[DeleteDuplicates[Table[{RandomInteger[{1,
  numchains}], RandomChoice[{-1, 1}]], {i, 2 numcrosslinkers}]],
  numcrosslinkers];
(* make the changes to molecules *)
(mlc[[#1, #2, 2]] = 2;) & @@ # & / @ tochange;

atoms = Prepend[#\[Transpose], Range[Length@#]]\[Transpose] &
  @Flatten[mlc, 1];
bonds = Prepend[#\[Transpose], Range[Length@#]]\[Transpose] &
  @Flatten[{ConstantArray[1, Length[#] - 1], Most@#, Rest@#}\[
  Transpose] & [#\[Transpose][[1]]] & / @ Partition[atoms,
  numbeads], 1];

(* format and output to a file *)
numatoms = Length[atoms];

```

```

numbonds=Length[bonds];
endl="\n";
top="# "<>file<>endl;
format[{}]:="\n";
format[list_]:=ToString[NumberForm[First@list,5]]<>" "<>
    format[Rest@list];
output=StringJoin[top,endl,ToString[numatoms],"\tatoms\n",
ToString[numbonds],"\tbonds\n",
endl,
"2\tatom types\n",
"1\tbond types\n",
"4\textra bond per atom\n",
endl,
"0.0000 ",ToString[boxvol^(1/3)]," xlo xhi\n",
"0.0000 ",ToString[boxvol^(1/3)]," ylo yhi\n",
"0.0000 ",ToString[boxvol^(1/3)]," zlo zhi\n",
endl,
"Masses\n\n",
"1\tt1\n",
"2\tt1\n",
endl,
"Atoms\n\n",
format/@atoms,
endl,
"Bonds\n\n",
format/@bonds,
endl
];
out=OpenWrite[dir<>file];
WriteString[out,output];
Close[out];

```

## B.2 SOFT PUSH-OFF

LAMMPS input file for soft push-off step using the soft (cosine) potential of Equation 119.

```
# VARIABLES
variable prefactor equal 4+96*step/(2000*2)

# INITIALIZATION
units          lj
boundary       p p p
atom_style     bond
log            soft.log
read_data      startconfig.dat

# NEIGHBORS, POTENTIALS
neighbor       2 bin
neigh_modify   every 1 one 10000
special_bonds  fene
bond_style     fene
bond_coeff     * 30 1.5 1 1
pair_style     soft 1.122462048309373
pair_coeff     * * 4 #i.e. initially set to the starting
              value

# OUTPUT SETTINGS
thermo_style   custom spcpu step temp press pe ke etotal
thermo        25

# SIMULATION: SOFT POTENTIAL
timestep       0.006
fix            1 all langevin 1 1 2 3416422
fix            2 all nve
fix            3 all adapt 1 pair soft a * * v_prefactor
velocity       all set 0 0 0 units box
run            4000 every 50 &
              "velocity          all set 0 0 0 units box" &
```

```

        "print '${prefactor}'"

# CLEAN UP, AND OUTPUT DATA
unfix 1
unfix 2
unfix 3
variable prefactor delete
write_restart    aftersoft.restart

```

### B.3 EQUILIBRATION AFTER SOFT PUSH-OFF

LAMMPS input file to perform an equilibration run after the soft push off. Note that this code outputs to a directory that is named "LJ", so this directory must exist for the code to run.

```

# VARIABLES
variable n equal 10000000

# INITIALIZATION
units          lj
boundary       p p p
atom_style     bond
log            LJequil.log
read_restart   aftersoft.restart

# NEIGHBORS, POTENTIALS
neighbor       1.5 bin
neigh_modify   every 1 one 10000
pair_style     lj/cut 1.122462048309373
pair_coeff     * * 1 1

# OUTPUT SETTINGS
dump          atoms all custom 100000 LJ/*.atoms id mol
             type x y z
restart       100000 LJ/restart1 LJ/restart2
dump_modify   atoms pad 8

```



```

thermo_style      custom step spcpu temp press pe ke etotal
thermo            10000

# SIMULATION
timestep          0.012
fix               1 all langevin 1 1 0.5 9284829
fix               2 all nve
velocity          all set 0 0 0 units box
run               96000

neighbor 0.65 bin
run $n

# Clean up, data output
unfix 1
unfix 2
write_restart    afterLJ.restart

```

#### B.4 CROSSLINKING REACTION

LAMMPS input file to perform a crosslinking reaction to a functionality of 4. Note that this code outputs to a directory that is named “link4”, so this directory must exist for the code to run.

```

# VARIABLES
variable n equal 5*1000000

# INITIALIZATION
units             lj
boundary          p p p
atom_style        bond
log               link4.log
read_restart      afterLJ.restart

# NEIGHBORS, POTENTIALS
neighbor          0.65 bin

```

```

neigh_modify      every 1 one 10000
special_bonds     fene extra 3
pair_style        lj/cut 1.122462048309373
pair_coeff        1 1 1 1 1.122462048309373
pair_coeff        * 2 1 1 2

# OUTPUT SETTINGS
dump              atoms all custom 100000 link4/*.atoms id mol
                 type x y z
dump_modify       atoms pad 8
compute          bonds all property/local btype batom1 batom2
dump             bonds all local 100000 link4/*.bonds c_bonds
                 [1] c_bonds [2] c_bonds [3]
dump_modify       bonds pad 8
restart          100000 link4/restart1 link4/restart2
thermo_style     custom step spcpu temp press pe ke etotal
thermo           10000

# SIMULATION
timestep         0.012
fix              1 all langevin 1 1 0.5 1948
fix              2 all nve
# every 20 dt, bond 1 to 2 if within rxn radius 1.3 to form
# a bond type 1, with chain (type 1) atoms having a max 2
# bonds and staying as type 1 and crosslink (type 2) atoms
# having a max of 4 bonds and staying as type 2
fix              3 all bond/create 20 1 2 1.3 1 prob 1 232
                 iparam 2 1 jparam 4 2
run              $n

# CLEAN UP, AND OUTPUT DATA
unfix 1
unfix 2
unfix 3
undump atoms

```

```
undump bonds
write_restart afterlink4.restart
```

## B.5 COMPRESS

LAMMPS input file to compress a sample from its initial density to the final density of  $\rho_m = 0.85$  that was used to run the tests. Note that this code outputs to a directory that is named “compress”, so this directory must exist for the code to run.

```
# VARIABLES
variable name          index  compress
log                   ${name}.log
variable startfile    index  afterlink4.restart
variable rho0         equal  0.65
variable rho          equal  0.85
variable dumpdir      index  compress
variable k            equal  100000          # num steps
    to delta lambda = 1
variable r            equal  394873          # random
    number

# INITIALIZATION
units                lj
boundary             p p p
atom_style           bond
read_restart         ${startfile}

# VARIABLES TO CALCULATE STUFF
variable             thermostep    equal  $k/20000 # this
    gives 20000 thermo's per delta lambda = 1
variable             rate          equal  -1/(0.012*$k)
variable             n            equal  1/3*ln(${rho}/${rho0
    })*$k

# NEIGHBORS, POTENTIALS
```

```

neighbor          0.65 bin
neigh_modify      every 1 one 10000
bond_style        fene
bond_coeff        * 30 1.5 1 1
pair_style        lj/cut 1.122462048309373
pair_coeff        * * 1 1 1.122462048309373

# OUTPUT SETTINGS
dump              atoms all custom 100000 ${dumpdir}/*.atoms
                 id mol type x y z
dump_modify       atoms pad 10
thermo_style      custom step spcpu temp press pe ke pxx pyy
                 pzz lx ly lz
thermo            ${thermostep}
restart           10000 ${dumpdir}.restart1 ${dumpdir}.
                 restart2

# DEFORMATION: COMPRESS ALL DIRECTIONS
timestep          0.012
fix               1 all langevin 1 1 0.5 $r
fix               2 all nve
fix               3 all deform 1 x trate ${rate} y trate ${
                 rate} z trate ${rate} units box remap v
run               $n

# Clean up, data output
unfix 1
unfix 2
unfix 3
write_restart     aftercompress.restart

```

## B.6 UNIAXIAL DEFORMATION

LAMMPS input file to apply a uniaxial deformation to a sample, loading and unloading. Note that this code outputs to a directory that is named “uni”, so this directory must exist for the code to run.

```
# VARIABLES
variable name          index    uni
log      ${name}.log
variable startfile    index    aftercompress.restart
variable lambdastart  equal    1
variable lambdaend    equal    1.1
variable lambdaRD     equal    0.05    # restart and dump
      output freq (in delta lambda)
variable lambdathermo equal    0.01    # thermo output freq
      (in delta lambda)
variable dumpdir      index    uni
variable k            equal    1000000 # num steps to delta
      lambda = 1
variable r            equal    284904  # random number

# INITIALIZATION
units          lj
boundary       p p p
atom_style     bond
read_restart   ${startfile}

# VARIABLES TO CALCULATE STUFF
variable       rdstep          equal    $k*${lambdaRD}
variable       thermostep      equal    $k*${lambdathermo}
variable       loadrate        equal    1/(0.012*$k)
variable       unloadrate      equal    -1*${loadrate}/${
      lambdaend}
variable       n                equal    $k*(${lambdaend}-${
      lambdastart})

# NEIGHBORS, POTENTIALS
```

```

neighbor      0.65 bin
neigh_modify  every 1 one 10000
bond_style    fene
bond_coeff    * 30 1.5 1 1
pair_style    lj/cut 1.122462048309373
pair_coeff    * * 1 1 1.122462048309373

# OUTPUT SETTINGS
dump          atoms all custom ${rdstep} ${dumpdir}/*.
             atoms id mol type x y z
dump_modify   atoms pad 8
restart       ${rdstep} ${dumpdir}/*.restart
fix          p all ave/time 2 200 ${thermostep}
             c_thermo_press c_thermo_press[1] c_thermo_press[2]
             c_thermo_press[3]
thermo_style  custom step spcpu temp  f_p[1]  pe      ke
             f_p[2]  f_p[3]  f_p[4]  lx      ly      lz
thermo       ${thermostep}

# DEFORMATION: UNIAXIAL LOADING
timestep      0.012
fix          1 all langevin 1 1 0.5 $r
fix          2 all nve
fix          3 all deform 1 x erate ${loadrate} y volume
             z volume units box remap v
run          $n

# DEFORMATION: UNIAXIAL UNLOADING
unfix        3
fix          3 all deform 1 x erate ${unloadrate} y
             volume z volume units box remap v
run          $n

```

## B.7 GENERATING CHAINS WITH FIXED BOND ANGLES

This Mathematica code can be used to generate chains with specified bond bending angles and random torsional angles.

```
(* DEFINE FUNCTIONS *)
gen[0] = {{0, 0, 0}};
gen[n_] :=
  Append[#, (#/(Sqrt[#1^2 + #2^2 + #3^2] & @@ #)) &[
    RandomReal[{-1, 1}, 3] + Last[#]] &[gen[n - 1]];
gen[r_, 0] = gen[0];
gen[r_, n_] :=
  Append[#,
    r (#/(Sqrt[#1^2 + #2^2 + #3^2] & @@ #)) &[
      RandomReal[{-1, 1}, 3] + Last[#]] &[gen[r, n - 1]];
vrot[v_, k_, th_] :=
  v Cos[th] + Cross[k, v] Sin[th] + k (k.v) (1 - Cos[th]);
triplet[r_, \[Theta]_] :=
  Module[{vectors, \[Theta]0, n},
    vectors = (Rest[#] - Most[#]) &[gen[r, 2]];
    \[Theta]0 = ArcCos[Dot @@ vectors/r^2];
    n = Cross[vectors[[2]], vectors[[1]]]/(r^2 Sin[\[Theta]0]);
    Prepend[
      Accumulate[{vectors[[1]],
        vrot[vectors[[2]], n, \[Theta]0 - \[Theta]]}], {0, 0,
        0}]];
addstep[chain_, r_, \[Theta]_, \[Phi]_] :=
  Module[{trip, vectors, xhat, yhat, new}, trip = Take[chain,
    -3];
    vectors = (Rest[#] - Most[#]) &@trip;
    xhat = #/Sqrt[#.#] &[Cross[vectors[[2]], vectors[[1]]]];
    yhat = #/Sqrt[#.#] &[Last[trip] - First[trip]];
    new = r yhat;
    new = vrot[new, xhat, \[Theta]/2];
    new = vrot[new, #/Sqrt[#.#] &[Last[vectors]], \[Phi]];
    Last[trip] + new];
```

```

anglegen[r_, \[Theta]_, n_] :=
  Module[{chain}, chain = triplet[r, \[Theta]];
  For[i = 1, i <= n - 2, i++,
    AppendTo[chain,
      addstep[chain, r, \[Theta], RandomReal[{0, 2 Pi}]]];
  chain];

(* SET PARAMETERS AND GENERATE A CHAIN CONFIGURATION *)
bondlength = 0.97;
theta = (180 - ArcCos[-0.333]/Degree) Degree;
Ns = 20;
bendingchain = anglegen[bondlength, theta, Ns];

```

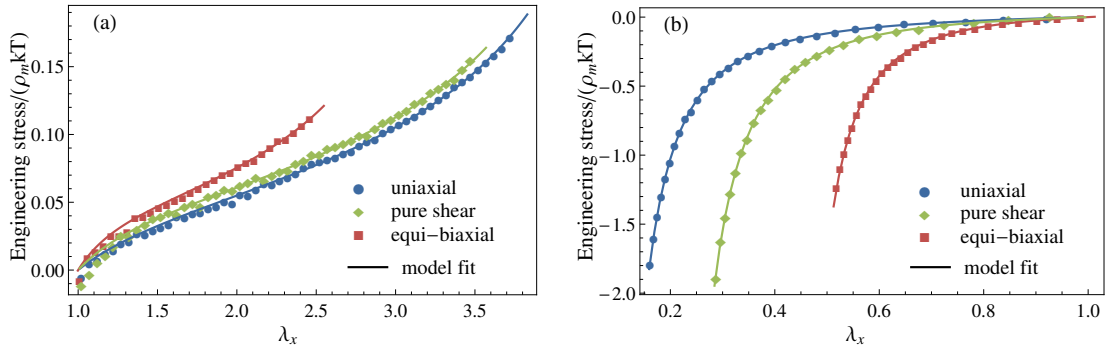


## APPENDIX C: COMPLETE SET OF STRESS-STRETCH DATA FOR THE SIMULATED POLYMER NETWORKS

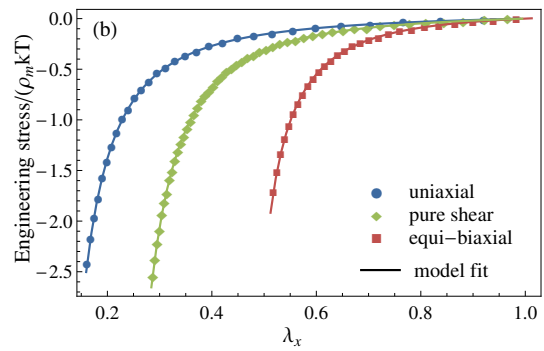
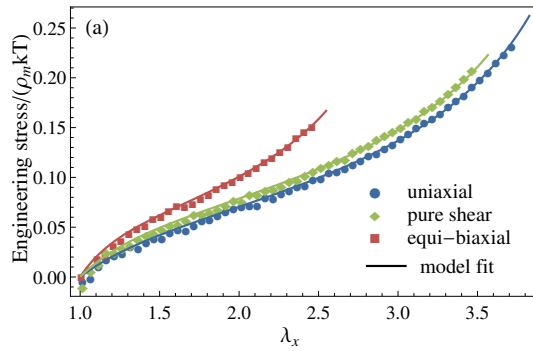
This appendix contains the complete set of simulated stress-stretch data for the 12 simulated polymer networks described in Chapter 5 and analyzed in Chapters 6 and 7. Uniaxial and equi-biaxial tests were performed on all samples, and pure shear tests were performed on most systems, as shown in the figures below. Two plots are shown for each simulated network. Each shows engineering stress-stretch with the nonaffine network model (Chapter 4) fit. Plot (a) is tension data, and (b) is compression data for each. The fit parameters used for each data set are listed in Table 8.

To obtain the compression data, separate simulations were not performed; due to the similarity in boundary conditions, the uniaxial tension test was used to obtain biaxial compression data, the biaxial tension test was used to obtain uniaxial compression data, and the pure shear tension test was used to obtain pure shear compression data.

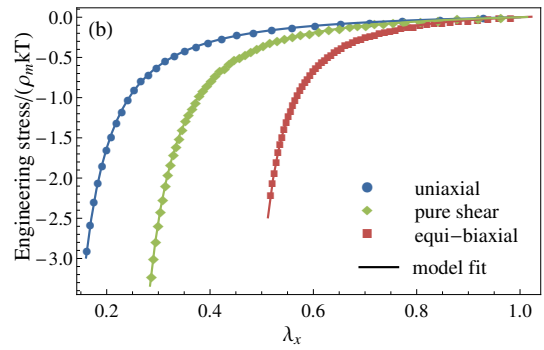
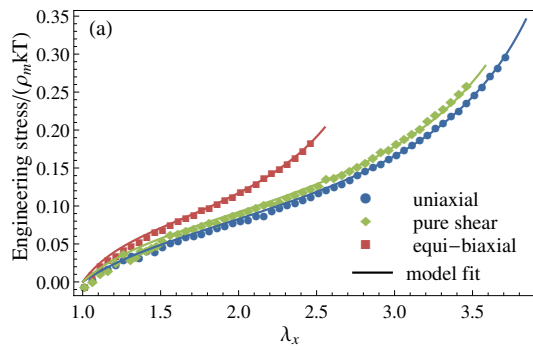
$$N = 20, \rho_{cl} = 0.45$$



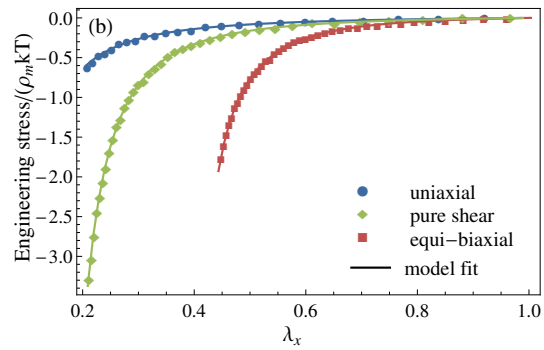
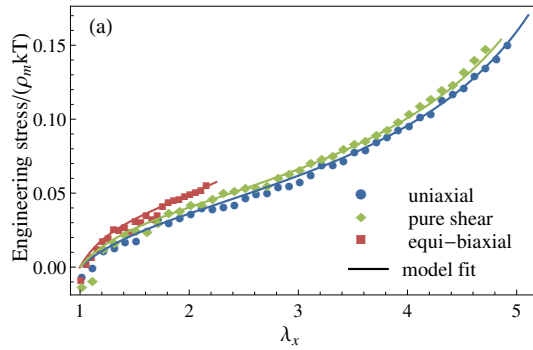
$N = 20, \rho_{cl} = 0.65$



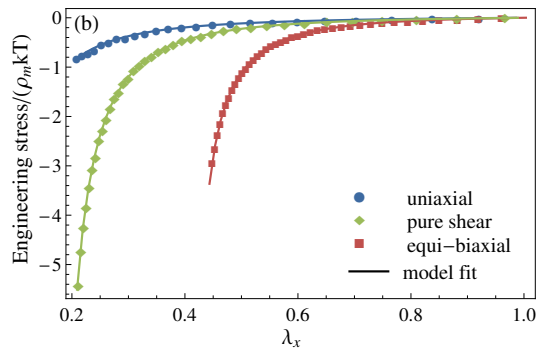
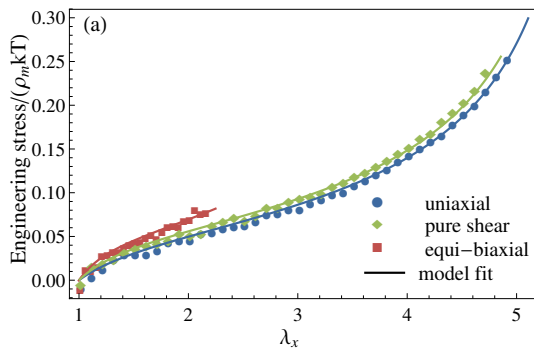
$N = 20, \rho_{cl} = 0.85$



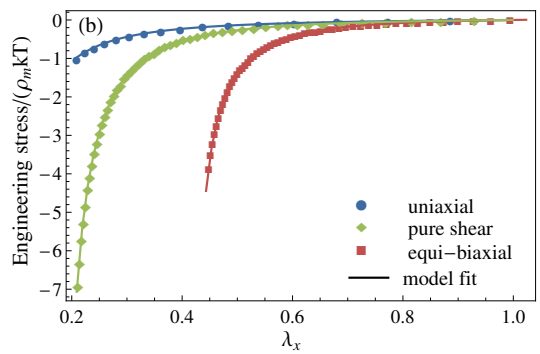
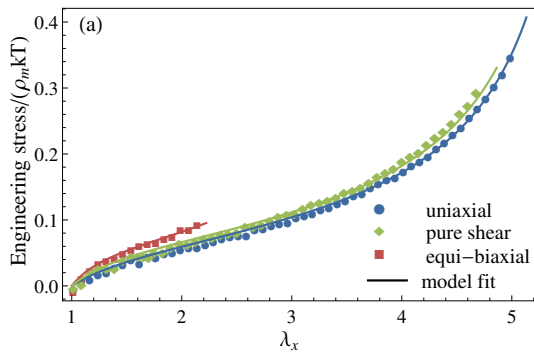
$N = 35, \rho_{cl} = 0.45$



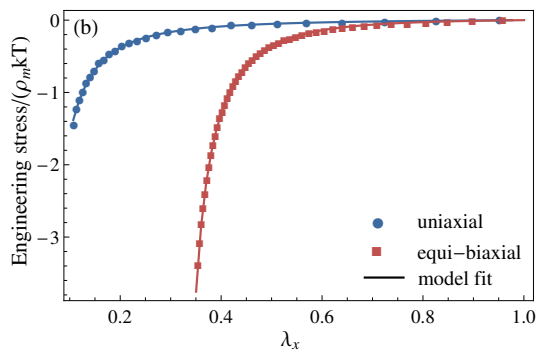
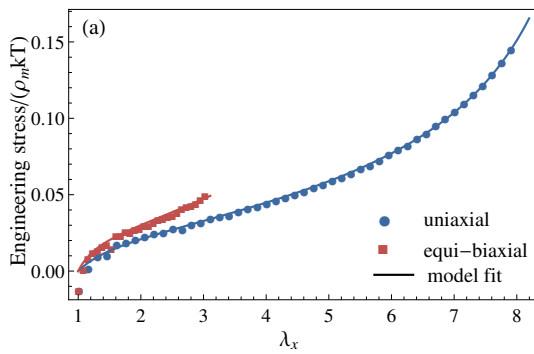
$N = 35, \rho_{cl} = 0.65$



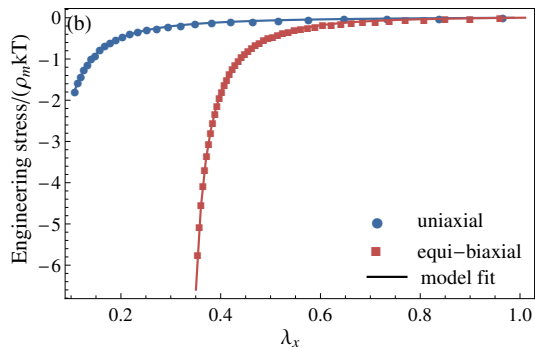
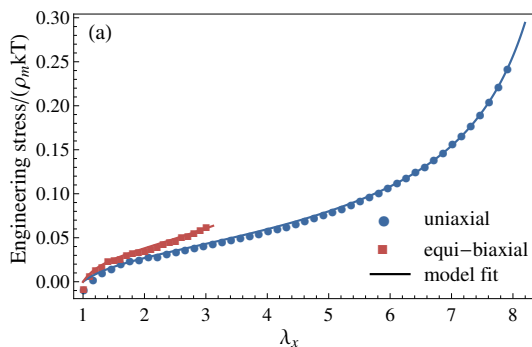
$N = 35, \rho_{cl} = 0.85$



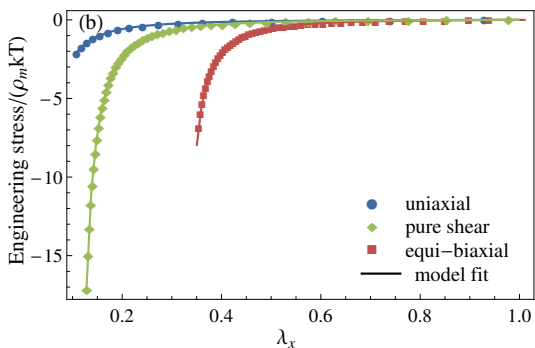
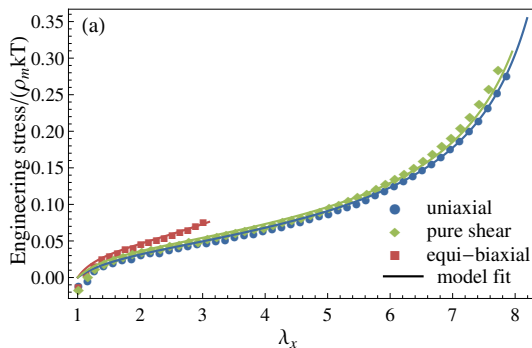
$N = 100, \rho_{cl} = 0.45$



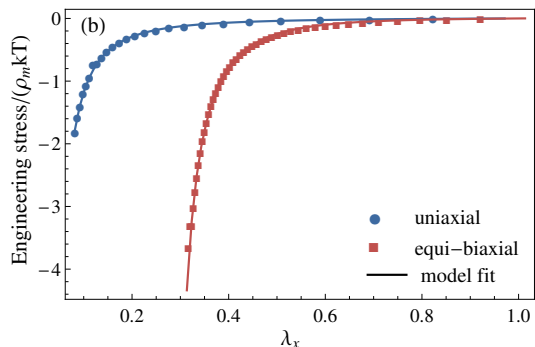
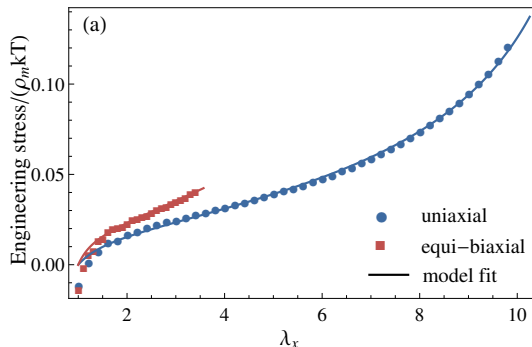
$N = 100, \rho_{cl} = 0.65$



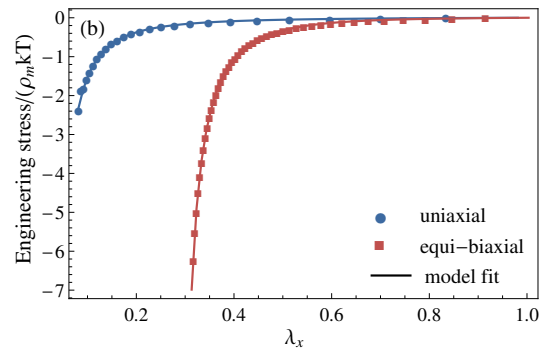
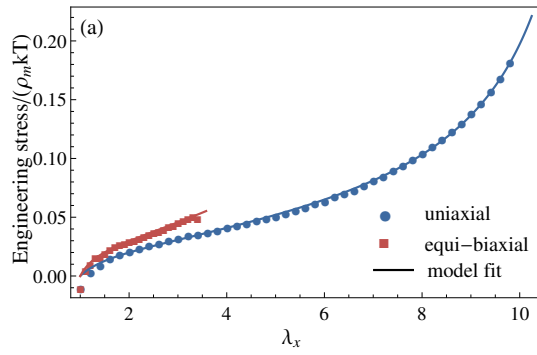
$N = 100, \rho_{cl} = 0.85$



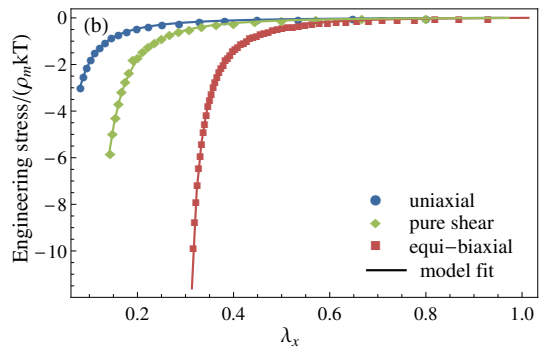
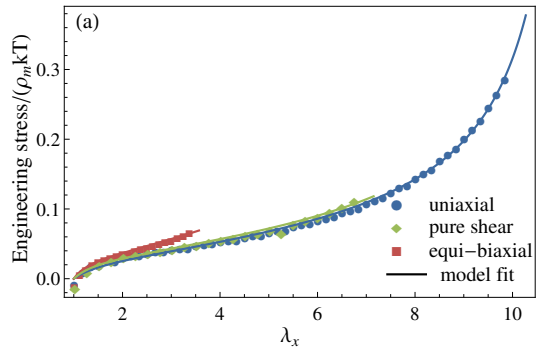
$N = 200, \rho_{cl} = 0.45$



$N = 200, \rho_{cl} = 0.65$



$N = 200, \rho_{cl} = 0.85$



## BIBLIOGRAPHY

---

- [1] L. R. G. Treloar. Stress-strain data for vulcanised rubber under various types of deformation. *Transactions of the Faraday Society*, 40:59–70, 1944.
- [2] J. S. Stenzler. Impact mechanics of PMMA/PC multi-laminates with soft polymer interlayers. Master’s thesis, Virginia Polytechnic Institute and State University, 2009.
- [3] H. J. Qi, T. D. Nguyen, F. Castro, C. M. Yakacki, and R. Shandas. Finite deformation thermo-mechanical behavior of thermally induced shape memory polymers. *Journal of the Mechanics and Physics of Solids*, 56(5):1730–1751, May 2008.
- [4] M. Rubinstein and R. H. Colby. *Polymer physics*. Oxford University Press, July 2003.
- [5] M. Rubinstein and S. Panyukov. Elasticity of polymer networks. *Macromolecules*, 35(17):6670–6686, 2002.
- [6] M. Rubinstein and S. Panyukov. Nonaffine deformation and elasticity of polymer networks. *Macromolecules*, 30(25):8036–8044, Dec. 1997.
- [7] M. C. Wang and E. Guth. Statistical theory of networks of Non-Gaussian flexible chains. *The Journal of Chemical Physics*, 20(7):1144–1157, July 1952.
- [8] E. M. Arruda and M. C. Boyce. A three-dimensional constitutive model for the large stretch behavior of rubber elastic materials. *Journal of the Mechanics and Physics of Solids*, 41(2):389–412, Feb. 1993.
- [9] J. Fox and N. Goulbourne. On the dynamic electromechanical loading of dielectric elastomer membranes. *Journal of the Mechanics and Physics of Solids*, 56(8):2669–2686, Aug. 2008.
- [10] F. Lulei and C. Miehe. A physically-based constitutive model for finite viscoelastic deformations in rubbery polymers based on a directly evaluated micro-macro-transition. In D. Besdo, R. H. Schuster, and J. Ihlemann, editors, *CONSTITUTIVE MODELS FOR RUBBER II*, pages 117–125, 2001. 2nd European Conference on Constitutive Models for Rubber, HANNOVER, GERMANY, SEP 10-12, 2001.

- [11] S. Edwards and T. Vilgis. The effect of entanglements in rubber elasticity. *Polymer*, **27(4):483–492**, Apr. 1986.
- [12] M. Kaliske and G. Heinrich. An extended tube-model for rubber elasticity: Statistical-mechanical theory and finite element implementation. *Rubber Chemistry and Technology*, **72(4):602–632**, Oct. 1999.
- [13] B. Meissner and L. Matejka. A Langevin-elasticity-theory-based constitutive equation for rubberlike networks and its comparison with biaxial stress-strain data. part I. *POLYMER*, **44(16):4599–4610**, July 2003.
- [14] C. Miehe, S. Goktepe, and F. Lulei. A micro-macro approach to rubberlike materials—Part I: the non-affine micro-sphere model of rubber elasticity. *Journal of the Mechanics and Physics of Solids*, **52(11):2617–2660**, 2004.
- [15] K. Kremer and G. S. Grest. Dynamics of entangled linear polymer melts: A molecular-dynamics simulation. *The Journal of Chemical Physics*, **92(8):5057**, 1990.
- [16] R. Auhl, R. Everaers, G. S. Grest, K. Kremer, and S. J. Plimpton. Equilibration of long chain polymer melts in computer simulations. *The Journal of Chemical Physics*, **119:12718**, 2003.
- [17] C. Svaneborg, G. S. Grest, and R. Everaers. Strain-dependent localization, microscopic deformations, and macroscopic normal tensions in model polymer networks. *Physical Review Letters*, **93(25)**, Dec. 2004.
- [18] M. Kröger. Shortest multiple disconnected path for the analysis of entanglements in two- and three-dimensional polymeric systems. *Computer Physics Communications*, **168(3):209–232**, June 2005.
- [19] K. Foteinopoulou, N. C. Karayiannis, V. G. Mavrantzas, and M. Kroger. Primitive path identification and entanglement statistics in polymer melts: Results from direct topological analysis on atomistic polyethylene models. *Macromolecules*, **39(12):4207–4216**, 2006.
- [20] N. C. Karayiannis and M. Kroger. Combined molecular algorithms for the generation, equilibration and topological analysis of entangled polymers: Methodology and performance. *International Journal of Molecular Sciences*, **10(11):5054–5089**, Nov. 2009.
- [21] J. D. Davidson and N. Goulbourne. A nonaffine network model for elastomers undergoing finite deformations. *Journal of the Mechanics and Physics of Solids*, **61(8):1784–1797**, Aug. 2013.

- [22] T. D. Nguyen, H. J. Qi, F. Castro, and K. N. Long. A thermoviscoelastic model for amorphous shape memory polymers: Incorporating structural and stress relaxation. *Journal of the Mechanics and Physics of Solids*, **56(9):2792–2814**, Sept. 2008.
- [23] Elastic memory composite (EMC) material, . URL <http://www.ctd-materials.com/products/emc.htm>.
- [24] Y. Liu, K. Gall, M. L. Dunn, A. R. Greenberg, and J. Diani. Thermo-mechanics of shape memory polymers: Uniaxial experiments and constitutive modeling. *International Journal of Plasticity*, **22(2):279–313**, Feb. 2006.
- [25] R. S. Hoy, K. Foteinopoulou, and M. Kroger. Topological analysis of polymeric melts: Chain-length effects and fast-converging estimators for entanglement length. *Physical Review E*, **80(3):031803**, 2009.
- [26] H. Staudinger. Über polymerisation. *Berichte der deutschen chemischen Gesellschaft (A and B Series)*, **53(6):1073–1085**, 1920.
- [27] P. J. Flory. *Principles of polymer chemistry*. Cornell University Press, Ithaca, N.Y., 1953. 672 p.
- [28] P. J. Flory. *Statistical mechanics of chain molecules*. Interscience Publishers, New York, 1969. xix, 432 p.
- [29] S. F. Edwards. Statistical mechanics with topological constraints: II. *Journal of Physics A: General Physics*, **1:15**, 1968.
- [30] S. F. Edwards. Statistical mechanics with topological constraints: I. *Proceedings of the Physical Society*, **91:513**, 1967.
- [31] S. F. Edwards. The statistical mechanics of polymers with excluded volume. *Proceedings of the Physical Society*, **85(4):613–624**, 1965.
- [32] P. de. Gennes. *Scaling concepts in polymer physics*. Cornell University Press, Ithaca, N.Y., 1979. 324 p.
- [33] M. Doi and S. F. Edwards. *The theory of polymer dynamics*. Clarendon Press, 1988.
- [34] J. Barrat, J. Baschnagel, and A. Lyulin. Molecular dynamics simulations of glassy polymers. *Soft Matter*, **6(15):3430**, 2010.
- [35] P. C. Hiemenz. *Polymer chemistry: the basic concepts*. CRC Press, 1984.



- [36] M. Behl, M. Y. Razzaq, and A. Lendlein. Multifunctional shape-memory polymers. *Advanced Materials*, **22(31):3388–3410**, 2010.
- [37] M. Behl, B. Hiebl, A. Lendlein, and C. Wischke. Shape-memory polymers as a technology platform for biomedical applications. *Expert Review of Medical Devices*, **7(3):357**, 2010. 357.
- [38] A. Lendlein and S. Kelch. Shape-memory polymers. *Angewandte Chemie International Edition*, **41(12):2034–2057**, 2002.
- [39] G. Li and M. John. A self-healing smart syntactic foam under multiple impacts. *Composites Science and Technology*, **68:3337–3343**, Dec. 2008.
- [40] J. A. Rogers, T. Someya, and Y. Huang. Materials and mechanics for stretchable electronics. *Science*, **327(5973):1603–1607**, Mar. 2010.
- [41] M. L. Hammock, A. Chortos, B. C.-K. Tee, J. B.-H. Tok, and Z. Bao. 25th anniversary article: The evolution of electronic skin (e-skin): A brief history, design considerations, and recent progress. *Advanced Materials*, **25(42):5997–6038**, Nov. 2013.
- [42] J. H. Koo, J. Seo, and T. Lee. Nanomaterials on flexible substrates to explore innovative functions: From energy harvesting to bio-integrated electronics. *Thin Solid Films*, **524:1–19**, Dec. 2012.
- [43] C. M. Yakacki, R. Shandas, C. Lanning, B. Rech, A. Eckstein, and K. Gall. Unconstrained recovery characterization of shape-memory polymer networks for cardiovascular applications. *Biomaterials*, **28(14):2255–2263**, May 2007.
- [44] A. A. Sharp, H. V. Panchawagh, A. Ortega, R. Artale, S. Richardson-Burns, D. S. Finch, K. Gall, R. L. Mahajan, and D. Restrepo. Toward a self-deploying shape memory polymer neuronal electrode. *Journal of Neural Engineering*, **3(4):L23–L30**, Dec. 2006.
- [45] Y. Bar-Cohen, editor. *Electroactive Polymer (EAP) Actuators as Artificial Muscles: Reality, Potential, and Challenges, Second Edition*. SPIE, 1000 20th Street, Bellingham, WA 98227-0010 USA, Mar. 2004.
- [46] G. Salbreux, G. Charras, and E. Paluch. Actin cortex mechanics and cellular morphogenesis. *Trends in Cell Biology*, **22(10):536–545**, Oct. 2012.
- [47] J. M. Gosline, M. W. Denny, and M. E. DeMont. Spider silk as rubber. *Nature*, **309(5968):551–552**, June 1984.

- [48] J. M. Gosline, P. A. Guerette, C. S. Oortlepp, and K. N. Savage. The mechanical design of spider silks: from fibroin sequence to mechanical function. *Journal of Experimental Biology*, 202(23):3295–3303, Dec. 1999.
- [49] L. R. G. Treloar. *The physics of rubber elasticity*. Oxford University Press, Nov. 2005.
- [50] W. Kuhn and F. Grun. Beziehungen zwischen elastischen konstanten und dehnungsdoppelbrechung hochelastischer stoffe. *Colloid & Polymer Science*, 101(3):248–271, Dec. 1942.
- [51] A. Cohen. A Pade' approximant to the inverse langevin function. *Rheologica Acta*, 30(3):270–273, 1991.
- [52] W. Kuhn. Dependence of the average transversal on the longitudinal dimensions of statistical coils formed by chain molecules. *Journal of Polymer Science*, 1(5):380–388, 1946.
- [53] H. M. James and E. Guth. Theory of the elastic properties of rubber. *The Journal of Chemical Physics*, 11(10):455, 1943.
- [54] E. M. Valles and C. W. Macosko. Properties of networks formed by end linking of poly(dimethylsiloxane). *Macromolecules*, 12(4):673–679, July 1979.
- [55] K. Urayama. Network Topology-Mechanical properties relationships of model elastomers. *Polymer Journal*, 40(8):669–678, 2008.
- [56] P. J. Flory, M. Gordon, and N. G. McCrum. Statistical thermodynamics of random networks [and discussion]. *Proceedings of the Royal Society of London. A. Mathematical and Physical Sciences*, 351(1666):351–380, Nov. 1976.
- [57] P. Higgs and R. Ball. Polydisperse polymer networks : elasticity, orientational properties, and small angle neutron scattering. *Journal de Physique*, 49(10):27, 1988.
- [58] E. Straube, V. Urban, W. Pyckhout-Hintzen, and D. Richter. SANS investigations of topological constraints and microscopic deformations in Rubber-Elastic networks. *Macromolecules*, 27(26):7681–7688, 1994.
- [59] E. Straube, V. Urban, W. Pyckhout-Hintzen, D. Richter, and C. J. Glinka. Small-Angle neutron scattering investigation of topological constraints and tube deformation in networks. *Physical Review Letters*, 74(22):4464–4467, May 1995.

- [60] S. Westermann, V. Urban, W. Pyckhout-Hintzen, D. Richter, and E. Straube. SANS investigations of topological constraints in networks made from triblock copolymers. *Macromolecules*, **29(19):6165–6174**, 1996.
- [61] W. Schärfl. *Light Scattering from Polymer Solutions and Nanoparticle Dispersions*. Springer, Aug. 2007.
- [62] G. Heinrich and E. Straube. On the strength and deformation dependence of the tube-like topological constraints of polymer networks, melts and concentrated solutions. II. polymer melts and concentrated solutions. *Acta Polymerica*, **35(2):115–119**, Feb. 1984.
- [63] G. Heinrich, E. Straube, and G. Helmis. Rubber elasticity of polymer networks: theories. *Polymer Physics*, **85:33–87**, 1988.
- [64] R. C. Batra. *Elements of Continuum Mechanics*. AIAA, 2006.
- [65] P. J. Flory and J. Rehner. Statistical mechanics of crosslinked polymer networks I. Rubberlike elasticity. *The Journal of Chemical Physics*, **11(11):512–520**, Nov. 1943.
- [66] M. Boyce and E. Arruda. Constitutive models of rubber elasticity: A review. *Rubber Chemistry and Technology*, **73(3):504–523**, Aug. 2000.
- [67] R. W. Ogden. Large deformation isotropic elasticity-on the correlation of theory and experiment for incompressible rubberlike solids. *Proceedings of the Royal Society of London. A. Mathematical and Physical Sciences*, **326(1567):565**, 1972.
- [68] R. Ball, M. Doi, S. Edwards, and M. Warner. Elasticity of entangled networks. *Polymer*, **22(8):1010–1018**, Aug. 1981.
- [69] G. Marckmann and E. Verron. Comparison of hyperelastic models for rubber-like materials. *Rubber Chemistry and Technology*, **79(5):835–858**, Dec. 2006.
- [70] W. Gronski, R. Stadler, and M. Maldaner Jacobi. Evidence of nonaffine and inhomogeneous deformation of network chains in strained rubber-elastic networks by deuterium magnetic resonance. *Macromolecules*, **17(4):741–748**, Apr. 1984.
- [71] G. Ronca and G. Allegra. An approach to rubber elasticity with internal constraints. *The Journal of Chemical Physics*, **63:4990**, 1975.
- [72] P. J. Flory. Theory of elasticity of polymer networks. the effect of local constraints on junctions. *The Journal of Chemical Physics*, **66(12):5720**, 1977.

- [73] A. Kloczkowski, J. E. Mark, and B. Erman. A Diffused-Constraint theory for the elasticity of amorphous polymer networks. 1. fundamentals and Stress-Strain isotherms in elongation. *Macromolecules*, **28(14):5089–5096**, 1995.
- [74] R. Gaylord and J. Douglas. Rubber elasticity: a scaling approach. *Polymer Bulletin*, **18**, Oct. 1987.
- [75] R. J. Gaylord and J. F. Douglas. The localisation model of rubber elasticity. II. *Polymer Bulletin*, **23:529–533**, May 1990.
- [76] B. Mergell and R. Everaers. Tube models for Rubber-Elastic systems. *Macromolecules*, **34(16):5675–5686**, July 2001.
- [77] X. Xing, P. M. Goldbart, and L. Radzihovsky. Thermal fluctuations and rubber elasticity. *Physical Review Letters*, **98(7):075502**, Feb. 2007.
- [78] R. Hansen, A. L. Skov, and O. Hassager. Constitutive equation for polymer networks with phonon fluctuations. *Physical Review E*, **77(1)**, Jan. 2008.
- [79] K. Urayama. An experimentalist's view of the physics of rubber elasticity. *Journal of Polymer Science Part B: Polymer Physics*, **44(24):3440–3444**, Dec. 2006.
- [80] T. Kawamura, K. Urayama, and S. Kohjiya. Multiaxial deformations of End-Linked poly(dimethylsiloxane) networks. 1. phenomenological approach to strain energy density function. *Macromolecules*, **34(23):8252–8260**, Nov. 2001.
- [81] G. A. Holzapfel and R. W. Ogden. On planar biaxial tests for anisotropic nonlinearly elastic solids. a continuum mechanical framework. *Mathematics and Mechanics of Solids*, **14(5):474–489**, July 2009.
- [82] G. S. Grest, M. Pütz, R. Everaers, and K. Kremer. Stress-strain relation of entangled polymer networks. *Journal of non-crystalline solids*, **274(1):139–146**, 2000.
- [83] K. C. Daoulas, D. N. Theodorou, A. Roos, and C. Creton. Experimental and self-consistent-field theoretical study of styrene block copolymer self-adhesive materials. *Macromolecules*, **37(13):5093–5109**, June 2004.
- [84] T. Schlick. *Molecular modeling and simulation: an interdisciplinary guide*, volume 21. Springer, 2010.
- [85] B. J. Alder and T. E. Wainwright. Phase transition for a hard sphere system. *The Journal of Chemical Physics*, **27(5):1208–1209**, Nov. 1957.

- [86] A. Rahman. Correlations in the motion of atoms in liquid argon. *Physical Review*, **136(2A):A405–A411**, Oct. 1964.
- [87] T. H. K. Barron and C. Domb. On the cubic and hexagonal close-packed lattices. *Proceedings of the Royal Society A: Mathematical, Physical and Engineering Sciences*, **227(1171):447–465**, Feb. 1955.
- [88] A. E. Likhtman. Whither tube theory: From believing to measuring. *Journal of Non-Newtonian Fluid Mechanics*, **157(3):158–161**, Apr. 2009.
- [89] C. Baig and V. G. Mavrantzas. From atomistic trajectories to primitive paths to tube models: linking atomistic simulations with the reptation theory of polymer dynamics. *Soft Matter*, **6(19):4603–4612**, June 2010.
- [90] S. L. Mayo, B. D. Olafson, and W. A. Goddard. DREIDING: a generic force field for molecular simulations. *The Journal of Physical Chemistry*, **94(26):8897–8909**, Dec. 1990.
- [91] H. Sun, S. J. Mumby, J. R. Maple, and A. T. Hagler. An ab initio CFF93 all-atom force field for polycarbonates. *Journal of the American Chemical Society*, **116(7):2978–2987**, Apr. 1994.
- [92] W. D. Cornell, P. Cieplak, C. I. Bayly, I. R. Gould, K. M. Merz, D. M. Ferguson, D. C. Spellmeyer, T. Fox, J. W. Caldwell, and P. A. Kollman. A second generation force field for the simulation of proteins, nucleic acids, and organic molecules. *Journal of the American Chemical Society*, **117(19):5179–5197**, May 1995.
- [93] W. L. Jorgensen, D. S. Maxwell, and J. Tirado-Rives. Development and testing of the OPLS all-atom force field on conformational energetics and properties of organic liquids. *Journal of the American Chemical Society*, **118(45):11225–11236**, Jan. 1996.
- [94] H. Sun. COMPASS: an ab initio force-field optimized for condensed-phase applications - overview with details on alkane and benzene compounds. *The Journal of Physical Chemistry B*, **102(38):7338–7364**, Sept. 1998.
- [95] MacKerell, D. Bashford, Bellott, Dunbrack, J. D. Evanseck, M. J. Field, S. Fischer, J. Gao, H. Guo, S. Ha, D. Joseph-McCarthy, L. Kuchnir, K. Kuczera, F. T. K. Lau, C. Mattos, S. Michnick, T. Ngo, D. T. Nguyen, B. Prodhom, W. E. Reiher, B. Roux, M. Schlenkrich, J. C. Smith, R. Stote, J. Straub, M. Watanabe, J. Wiórkiewicz-Kuczera, D. Yin, and M. Karplus. All-atom empirical potential for molecular modeling and dynamics studies of proteins. *The Journal of Physical Chemistry B*, **102(18):3586–3616**, Apr. 1998.

- [96] J. R. Fried. Computational parameters. In J. E. Mark, editor, *Physical Properties of Polymers Handbook*, pages 59–65. Springer New York, Jan. 2007.
- [97] C. Peter and K. Kremer. Multiscale simulation of soft matter systems - from the atomistic to the coarse-grained level and back. *Soft Matter*, **5**(22):4357–4366, 2009.
- [98] E. R. Duering, K. Kremer, and G. S. Grest. Structure and relaxation of end-linked polymer networks. *The Journal of Chemical Physics*, **101**(9):8169, 1994.
- [99] S. J. Barsky, M. Plischke, B. Joós, and Z. Zhou. Elastic properties of randomly cross-linked polymers. *Physical Review E*, **54**(5):5370, Nov. 1996.
- [100] S. A. Dubrovskii and V. V. Vasilev. Effect of the functionality of junctions on the elasticity of polymacromonomer networks: Computer simulation. *Polymer Science Series A*, **53**(6):527–535, June 2011.
- [101] J. Liu, D. Cao, and L. Zhang. Static and dynamic properties of model elastomer with various cross-linking densities: A molecular dynamics study. *The Journal of Chemical Physics*, **131**(3):034903, 2009.
- [102] C. Svaneborg, G. S. Grest, and R. Everaers. Disorder effects on the strain response of model polymer networks. *Polymer*, **46**(12):4283–4295, May 2005.
- [103] D. R. Heine, G. S. Grest, C. D. Lorenz, M. Tsige, and M. J. Stevens. Atomistic simulations of End-Linked poly(dimethylsiloxane) networks: Structure and relaxation. *Macromolecules*, **37**(10):3857–3864, May 2004.
- [104] C. Svaneborg, R. Everaers, G. S. Grest, and J. G. Curro. Connectivity and entanglement stress contributions in strained polymer networks. *Macromolecules*, **41**(13):4920–4928, July 2008.
- [105] Z. Chen, C. Cohen, and F. A. Escobedo. Monte carlo simulation of the effect of entanglements on the swelling and deformation behavior of End-Linked polymeric networks. *Macromolecules*, **35**(8):3296–3305, Apr. 2002.
- [106] D. M. Bhawe, C. Cohen, and F. A. Escobedo. Formation and characterization of semiflexible polymer networks via monte carlo simulations. *Macromolecules*, **37**(10):3924–3933, May 2004.

- [107] D. M. Bhawe, C. Cohen, and F. A. Escobedo. Effect of chain stiffness and entanglements on the elastic behavior of end-linked elastomers. *The Journal of Chemical Physics*, **123(1):014909**, 2005.
- [108] S. Plimpton. Fast parallel algorithms for short-range molecular dynamics. *Journal of Computational Physics*, **117(1):1–19**, Mar. 1995.
- [109] LAMMPS molecular dynamics simulator. URL <http://lammms.sandia.gov/index.html>.
- [110] E. R. Duering, K. Kremer, and G. S. Grest. Relaxation of randomly cross-linked polymer melts. *Physical Review Letters*, **67(25):3531**, Dec. 1991.
- [111] R. Everaers, S. K. Sukumaran, G. S. Grest, C. Svaneborg, A. Sivasubramanian, and K. Kremer. Rheology and microscopic topology of entangled polymeric liquids. *Science*, **303(5659):823–826**, Feb. 2004.
- [112] S. K. Sukumaran, G. S. Grest, K. Kremer, and R. Everaers. Identifying the primitive path mesh in entangled polymer liquids. *Journal of Polymer Science Part B: Polymer Physics*, **43(8):917–933**, Apr. 2005.
- [113] R. S. Hoy and G. S. Grest. Entanglements of an end-grafted polymer brush in a polymeric matrix. *Macromolecules*, **40(23):8389–8395**, 2007.
- [114] R. S. Hoy and M. O. Robbins. Effect of equilibration on primitive path analyses of entangled polymers. *Physical Review E*, **72(6):061802**, Dec. 2005.
- [115] Q. Zhou and R. G. Larson. Primitive path identification and statistics in molecular dynamics simulations of entangled polymer melts. *Macromolecules*, **38(13):5761–5765**, 2005.
- [116] C. Tzoumanekas and D. N. Theodorou. Topological analysis of linear polymer melts: a statistical approach. *Macromolecules*, **39(13):4592–4604**, 2006.
- [117] S. Shanbhag and M. Kroger. Primitive path networks generated by annealing and geometrical methods: Insights into differences. *Macromolecules*, **40(8):2897–2903**, 2007.
- [118] R. G. Larson. Looking inside the entanglement "tube" using molecular dynamics simulations. *Journal of Polymer Science Part B: Polymer Physics*, **45(24):3240–3248**, Oct. 2007.

- [119] J. T. Padding and W. J. Briels. Systematic coarse-graining of the dynamics of entangled polymer melts: the road from chemistry to rheology. *Journal of Physics: Condensed Matter*, **23(23):233101**, June 2011.
- [120] V. A. Harmandaris and K. Kremer. Dynamics of polystyrene melts through hierarchical multiscale simulations. *Macromolecules*, **42(3):791–802**, Feb. 2009.
- [121] R. N. Khaliullin and J. D. Schieber. Analytic expressions for the statistics of the Primitive-Path length in entangled polymers. *Physical Review Letters*, **100(18):188302**, May 2008.
- [122] S. Shanbhag and R. G. Larson. Identification of topological constraints in entangled polymer melts using the Bond-Fluctuation model. *Macromolecules*, **39(6):2413–2417**, 2006.
- [123] C. Tzoumanekas, F. Lahmar, B. Rousseau, and D. N. Theodorou. Onset of entanglements revisited. topological analysis. *Macromolecules*, **42(19):7474–7484**, 2009.
- [124] R. Everaers. Topological versus rheological entanglement length in primitive-path analysis protocols, tube models, and slip-link models. *Physical Review E*, **86(2):022801**, Aug. 2012.
- [125] K. Foteinopoulou, N. C. Karayiannis, M. Laso, M. Kröger, and M. L. Mansfield. Universal scaling, entanglements, and knots of model chain molecules. *Physical Review Letters*, **101(26):265702**, Dec. 2008.
- [126] K. Foteinopoulou, N. C. Karayiannis, M. Laso, and M. Kroger. Structure, dimensions, and entanglement statistics of long linear polyethylene chains. *J. Phys. Chem. B*, **113(2):442–455**, 2008.
- [127] M. Laso, N. C. Karayiannis, K. Foteinopoulou, M. L. Mansfield, and M. Kröger. Random packing of model polymers: local structure, topological hindrance and universal scaling. *Soft Matter*, **5(9):1762**, 2009.
- [128] N. Uchida, G. S. Grest, and R. Everaers. Viscoelasticity and primitive path analysis of entangled polymer liquids: From f-actin to polyethylene. *The Journal of Chemical Physics*, **128(4):044902–044902–6**, Jan. 2008.
- [129] F. Lahmar, C. Tzoumanekas, D. N. Theodorou, and B. Rousseau. Onset of entanglements revisited. dynamical analysis. *Macromolecules*, **42(19):7485–7494**, Oct. 2009.
- [130] J. Hou, C. Svaneborg, R. Everaers, and G. S. Grest. Stress relaxation in entangled polymer melts. *Physical Review Letters*, **105(6)**, 2010.



- [131] R. S. Hoy and M. O. Robbins. Strain hardening of polymer glasses: Effect of entanglement density, temperature, and rate. *Journal of Polymer Science Part B-Polymer Physics*, **44(24):3487–3500**, Dec. 2006.
- [132] J. Kim, B. Edwards, and D. Keffer. Visualization of conformational changes of linear short-chain polyethylenes under shear and elongational flows. *Journal of Molecular Graphics and Modelling*, **26(7):1046–1056**, Apr. 2008.
- [133] C. Baig, V. G. Mavrantzas, and M. Kroger. Flow effects on melt structure and entanglement network of linear polymers: Results from a nonequilibrium molecular dynamics simulation study of a polyethylene melt in steady shear. *Macromolecules*, **43(16):6886–6902**, Aug. 2010.
- [134] F. Leonforte. Evolution of entanglements during the response to a uniaxial deformation of lamellar triblock copolymers and polymer glasses. *Physical Review E*, **82(4)**, Oct. 2010.
- [135] D. K. Mahajan, B. Singh, and S. Basu. Void nucleation and disentanglement in glassy amorphous polymers. *Physical Review E*, **82(1):011803**, July 2010.
- [136] R. A. Riggleman, G. Toepperwein, G. J. Papakonstantopoulos, J. Barrat, and J. J. de Pablo. Entanglement network in nanoparticle reinforced polymers. *The Journal of Chemical Physics*, **130(24):244903–244903–6**, June 2009.
- [137] A. Karatrantos, R. J. Composto, K. I. Winey, M. Kröger, and N. Clarke. Entanglements and dynamics of polymer melts near a SWCNT. *Macromolecules*, **45(17):7274–7281**, Sept. 2012.
- [138] Y. Li, M. Kröger, and W. K. Liu. Nanoparticle effect on the dynamics of polymer chains and their entanglement network. *Physical Review Letters*, **109(11):118001**, Sept. 2012.
- [139] Y. Li, M. Kröger, and W. K. Liu. Nanoparticle geometrical effect on structure, dynamics and anisotropic viscosity of polyethylene nanocomposites. *Macromolecules*, **45(4):2099–2112**, Feb. 2012.
- [140] A. Karatrantos, N. Clarke, R. J. Composto, and K. I. Winey. Topological entanglement length in polymer melts and nanocomposites by a DPD polymer model. *Soft Matter*, **9(14):3877**, 2013.
- [141] J. Qin, J. So, and S. T. Milner. Tube diameter of stretched and compressed permanently entangled polymers. *Macromolecules*, **45(24):9816–9822**, Dec. 2012.

- [142] P. S. Stephanou, C. Baig, G. Tsolou, V. G. Mavrantzas, and M. Kröger. Quantifying chain reptation in entangled polymer melts: Topological and dynamical mapping of atomistic simulation results onto the tube model. *The Journal of Chemical Physics*, **132(12):124904–16**, Mar. 2010.
- [143] P. S. Stephanou, C. Baig, and V. G. Mavrantzas. Toward an improved description of constraint release and contour length fluctuations in tube models for entangled polymer melts guided by atomistic simulations. *Macromolecular Theory and Simulations*, **20(8):752–768**, 2011.
- [144] Y. Li, M. Kroger, and W. K. Liu. Primitive chain network study on uncrosslinked and crosslinked cis-polyisoprene polymers. *Polymer*, **52(25):5867–5878**, Nov. 2011.
- [145] M. Tkachuk and C. Linder. The maximal advance path constraint for the homogenization of materials with random network microstructure. *Philosophical Magazine*, **92(22):2779–2808**, 2012.
- [146] P. M. Goldbart. Heterogeneous solids and the Micro/Macro connection: Structure and elasticity in architecturally complex media as emergent collective phenomena. *Journal of Thermal Stresses*, **33(1):1–8**, Dec. 2009.
- [147] X. Mao, P. Goldbart, X. Xing, and A. Zippelius. Soft random solids and their heterogeneous elasticity. *Physical Review E*, **80(3)**, Sept. 2009.
- [148] E. B. Saff and A. B. Kuijlaars. Distributing many points on a sphere. *The Mathematical Intelligencer*, **19(1):5–11**, 1997.
- [149] J. D. Cloizeaux. Relaxation of entangled polymers in melts. *Macromolecules*, **23(17):3992–4006**, 1990.
- [150] C. Bennemann, W. Paul, K. Binder, and B. Dünweg. Molecular-dynamics simulations of the thermal glass transition in polymer melts: alpha-relaxation behavior. *Physical Review E*, **57(1):843–851**, Jan. 1998.
- [151] C. Bennemann, J. Baschnagel, W. Paul, and K. Binder. Molecular-dynamics simulation of a glassy polymer melt: Rouse model and cage effect. *Computational and Theoretical Polymer Science*, **9:217–226**, Dec. 1999.
- [152] J. S. Bergström and M. C. Boyce. Constitutive modeling of the large strain time-dependent behavior of elastomers. *Journal of the Mechanics and Physics of Solids*, **46(5):931–954**, 1998.
- [153] K. Urayama, T. Kawamura, and S. Kohjiya. Multiaxial deformations of end-linked poly(dimethylsiloxane) networks. 2. experimental tests of molecular entanglement models of rubber elasticity. *Macromolecules*, **34(23):8261–8269**, Nov. 2001.

- [154] J. Diani and K. Gall. Molecular dynamics simulations of the shape-memory behaviour of polyisoprene. *Smart Materials and Structures*, **16**: 1575–1583, Oct. 2007.
- [155] K. Gall, M. Mikulas, N. A. Munshi, F. Beavers, and M. Tupper. Carbon fiber reinforced shape memory polymer composites. *Journal of Intelligent Material Systems and Structures*, **11(11)**:877–886, Nov. 2000.
- [156] M. Lake and D. Campbell. The fundamentals of designing deployable structures with elastic memory composites. volume 4, pages 2745–2756. IEEE.
- [157] D. Campbell, M. S. Lake, M. R. Scherbarth, E. Nelson, and R. W. Six. Elastic memory composite material: an enabling technology for future furlable space structures. In *46 th AIAA/ASME/ASCE/AHS/ASC Structures, Structural Dynamics, and Materials Conference*, pages 1–12, 2005.
- [158] J. Nji and G. Li. A biomimic shape memory polymer based self-healing particulate composite. *Polymer*, **51(25)**:6021–6029, Nov. 2010.
- [159] M. John and G. Li. Self-healing of sandwich structures with a grid stiffened shape memory polymer syntactic foam core. *Smart Materials and Structures*, **19(7)**:075013, July 2010.
- [160] G. Li and N. Uppu. Shape memory polymer based self-healing syntactic foam: 3-d confined thermomechanical characterization. *Composites Science and Technology*, **70(9)**:1419–1427, Sept. 2010.
- [161] D. Campbell, R. Barrett, M. S. Lake, L. Adams, E. Abrahamson, and M. R. Scherbarth. Development of a novel, passively deployed solar array. *AIAA Journal*, **21(9)**:2080–2094, 2006.
- [162] X. Lan, Y. Liu, H. Lv, X. Wang, J. Leng, and S. Du. Fiber reinforced shape-memory polymer composite and its application in a deployable hinge. *Smart Materials and Structures*, **18(2)**:024002, Feb. 2009.
- [163] J. Hu and S. Chen. A review of actively moving polymers in textile applications. *J. Mater. Chem.*, **20(17)**:3346–3355, 2010.
- [164] K. Gall, C. M. Yakacki, Y. Liu, R. Shandas, N. Willett, and K. S. Anseth. Thermomechanics of the shape memory effect in polymers for biomedical applications. *Journal of Biomedical Materials Research Part A*, **73(3)**: 339–348, 2005.

- [165] G. Li and W. Xu. Thermomechanical behavior of thermoset shape memory polymer programmed by cold-compression: Testing and constitutive modeling. *Journal of the Mechanics and Physics of Solids*, **59(6):1231–1250**, June 2011.
- [166] X. Chen and T. D. Nguyen. Influence of thermoviscoelastic properties and loading conditions on the recovery performance of shape memory polymers. *Mechanics of Materials*, **43(3):127–138**, Mar. 2011.
- [167] V. Kafka. Shape memory polymers: A mesoscale model of the internal mechanism leading to the SM phenomena. *International Journal of Plasticity*, **24(9):1533–1548**, Sept. 2008.
- [168] Y.-C. Chen and D. C. Lagoudas. A constitutive theory for shape memory polymers. part i: Large deformations. *Journal of the Mechanics and Physics of Solids*, **56(5):1752–1765**, May 2008.
- [169] Y.-C. Chen and D. C. Lagoudas. A constitutive theory for shape memory polymers. part II: a linearized model for small deformations. *Journal of the Mechanics and Physics of Solids*, **56(5):1766–1778**, May 2008.
- [170] A. M. Ortega, S. E. Kasprzak, C. M. Yakacki, J. Diani, A. R. Greenberg, and K. Gall. Structure-property relationships in photopolymerizable polymer networks: Effect of composition on the crosslinked structure and resulting thermomechanical properties of a (meth)acrylate-based system. *Journal of Applied Polymer Science*, **110(3):1559–1572**, 2008.
- [171] N. Lakhera, C. M. Yakacki, T. D. Nguyen, and C. P. Frick. Partially constrained recovery of (meth)acrylate shape-memory polymer networks. *Journal of Applied Polymer Science*, **126(1):72–82**, 2012.
- [172] A. M. Ortega, C. M. Yakacki, S. A. Dixon, R. Likos, A. R. Greenberg, and K. Gall. Effect of crosslinking and long-term storage on the shape-memory behavior of (meth)acrylate-based shape-memory polymers. *Soft Matter*, **8(28):7381**, 2012.
- [173] C. M. Yakacki, R. Shandas, D. Safranski, A. M. Ortega, K. Sassaman, and K. Gall. Strong, tailored, biocompatible shape-memory polymer networks. *Advanced Functional Materials*, **18(16):2428–2435**, 2008.
- [174] J. Diani, Y. Liu, and K. Gall. Finite strain 3D thermoviscoelastic constitutive model for shape memory polymers. *Polymer Engineering & Science*, **46(4):486–492**, Apr. 2006.
- [175] CRG - Veriflex shape memory polymer, . URL <http://www.crggrp.com/technology/portfolio/veriflex.html>.

- [176] C. Liu, H. Qin, and P. T. Mather. Review of progress in shape-memory polymers. *J. Mater. Chem.*, **17(16):1543–1558**, 2007.
- [177] H. Weintraub, M. Ashburner, P. N. Goodfellow, H. F. Lodish, C. J. Arntzen, P. W. Anderson, T. M. Rice, T. H. Geballe, A. R. Means, and H. M. Ranney. Through the glass lightly. *Science-AAAS-Weekly Paper Edition*, **267(5204):1609–1618**, 1995.
- [178] L. Berthier and G. Biroli. Theoretical perspective on the glass transition and amorphous materials. *Reviews of Modern Physics*, **83(2):587–645**, June 2011.
- [179] A. Lendlein and R. Langer. Biodegradable, elastic shape-memory polymers for potential biomedical applications. *Science*, **296(5573):1673–1676**, May 2002.
- [180] M. Behl and A. Lendlein. Shape-memory polymers. *Materials Today*, **10(4):20–28**, 2007.
- [181] M. Behl, J. Zotzmann, and A. Lendlein. Shape-memory polymers and shape-changing polymers. In *Shape-Memory Polymers*, Advances in Polymer Science, pages 1–40. Springer Berlin / Heidelberg, 2012.
- [182] M. Wolfgardt and K. Binder. On the equation of state for thermal polymer solutions and melts with attractive interaction. *Macromolecular Theory and Simulations*, **5(4):699–712**, 1996.
- [183] M. Wolfgardt, J. Baschnagel, W. Paul, and K. Binder. Entropy of glassy polymer melts: Comparison between gibbs-DiMarzio theory and simulation. *Physical Review E*, **54(2):1535–1543**, Aug. 1996.
- [184] A. R. C. Baljon and M. O. Robbins. Energy dissipation during rupture of adhesive bonds. *Science*, **271(5248):482–484**, Jan. 1996.
- [185] K. Binder, J. Baschnagel, C. Bennemann, and W. Paul. Monte carlo and molecular dynamics simulation of the glass transition of polymers. *Journal of Physics: Condensed Matter*, **11(10A):A47–A55**, Mar. 1999.
- [186] K. Binder, J. Baschnagel, and W. Paul. Glass transition of polymer melts: test of theoretical concepts by computer simulation. *Progress in Polymer Science*, **28(1):115–172**, Jan. 2003.
- [187] M. J. Stevens. Manipulating connectivity to control fracture in network polymer adhesives. *Macromolecules*, **34(5):1411–1415**, Feb. 2001.

- [188] J. Han, R. H. Gee, and R. H. Boyd. Glass transition temperatures of polymers from molecular dynamics simulations. *Macromolecules*, **27(26)**: 7781–7784, Dec. 1994.
- [189] K. Yu, Z. Li, and J. Sun. Polymer structures and glass transition: A molecular dynamics simulation study. *Macromolecular Theory and Simulations*, **10(6)**:624–633, 2001.
- [190] R. Faller, A. Kolb, and F. Müller-Plathe. Local chain ordering in amorphous polymer melts: influence of chain stiffness. *Phys. Chem. Chem. Phys.*, **1(9)**:2071–2076, 1999.
- [191] R. Faller, F. Müller-Plathe, and A. Heuer. Local reorientation dynamics of semiflexible polymers in the melt. *Macromolecules*, **33(17)**:6602–6610, Aug. 2000.
- [192] M. Bulacu and E. van der Giessen. Effect of bending and torsion rigidity on self-diffusion in polymer melts: A molecular-dynamics study. *The Journal of Chemical Physics*, **123(11)**:114901, 2005.
- [193] M. Bulacu and E. van der Giessen. Molecular-dynamics simulation study of the glass transition in amorphous polymers with controlled chain stiffness. *Physical Review E*, **76(1)**:011807, July 2007.
- [194] A. V. Lyulin, B. Vorselaars, M. A. Mazo, N. K. Balabaev, and M. A. J. Michels. Strain softening and hardening of amorphous polymers: Atomistic simulation of bulk mechanics and local dynamics. *Europhysics Letters (EPL)*, **71(4)**:618–624, Aug. 2005.
- [195] J. Rottler, S. Barsky, and M. O. Robbins. Cracks and crazes: On calculating the macroscopic fracture energy of glassy polymers from molecular simulations. *Physical Review Letters*, **89(14)**:148304, Sept. 2002.
- [196] J. Rottler and M. O. Robbins. Shear yielding of amorphous glassy solids: Effect of temperature and strain rate. *Physical Review E*, **68(1)**:011507, July 2003.
- [197] J. Rottler and M. O. Robbins. Growth, microstructure, and failure of crazes in glassy polymers. *Physical Review E*, **68(1)**:011801, July 2003.
- [198] J. Rottler and M. O. Robbins. Unified description of aging and rate effects in yield of glassy solids. *Physical Review Letters*, **95(22)**:225504, Nov. 2005.
- [199] M. Kröger. Rheology and structural changes of polymer melts via nonequilibrium molecular dynamics. *Journal of Rheology*, **37**:1057, Nov. 1993.

- [200] M. Kröger and S. Hess. Rheological evidence for a dynamical crossover in polymer melts via nonequilibrium molecular dynamics. *Physical Review Letters*, **85(5):1128**, July 2000.
- [201] K. Hur, C. Jeong, R. G. Winkler, N. Lacevic, R. H. Gee, and D. Y. Yoon. Chain dynamics of ring and linear polyethylene melts from molecular dynamics simulations. *Macromolecules*, **44(7):2311–2315**, Apr. 2011.
- [202] J. Cao and A. E. Likhtman. Shear banding in molecular dynamics of polymer melts. *Physical Review Letters*, **108(2):028302**, Jan. 2012.
- [203] J. D. Halverson, G. S. Grest, A. Y. Grosberg, and K. Kremer. Rheology of ring polymer melts: From linear contaminants to ring-linear blends. *Physical Review Letters*, **108(3):038301**, Jan. 2012.
- [204] Z. Wang, A. E. Likhtman, and R. G. Larson. Segmental dynamics in entangled linear polymer melts. *Macromolecules*, **45(8):3557–3570**, Apr. 2012.
- [205] Y. K. Gao, X. J. Ding, T. Hu, Y. Li, and S. Z. Wu. Study on the stress relaxation of polychloroprene rubber by molecular dynamics simulation at different temperature. *Advanced Materials Research*, **532-533:311–315**, June 2012.
- [206] D. R. Rottach, J. G. Curro, J. Budzien, G. S. Grest, C. Svaneborg, and R. Everaers. Permanent set of cross-linking networks: Comparison of theory with molecular dynamics simulations. *Macromolecules*, **39(16):5521–5530**, 2006.
- [207] D. R. Rottach, J. G. Curro, J. Budzien, G. S. Grest, C. Svaneborg, and R. Everaers. Molecular dynamics simulations of polymer networks undergoing sequential cross-linking and scission reactions. *Macromolecules*, **40(1):131–139**, Jan. 2007.
- [208] G. D. Genesky, B. M. Aguilera-Mercado, D. M. Bhawe, F. A. Escobedo, and C. Cohen. Experiments and simulations: Enhanced mechanical properties of End-Linked bimodal elastomers. *Macromolecules*, **41(21):8231–8241**, Nov. 2008.
- [209] J. S. Bermejo and C. M. Ugarte. Influence of Cross-Linking density on the glass transition and structure of chemically Cross-Linked PVA: a molecular dynamics study. *Macromolecular Theory and Simulations*, **18(6):317–327**, Aug. 2009.
- [210] J. Gao and J. H. Weiner. Nature of stress on the atomic level in dense polymer systems. *Science*, **266(5186):748–752**, Nov. 1994.

- [211] J. H. Weiner and J. Gao. Simulation of viscoelasticity in polymer melts: effect of torsional potential. *Modelling and Simulation in Materials Science and Engineering*, **2(3A):755–766**, May 1994.
- [212] J. Liu, S. Wu, L. Zhang, W. Wang, and D. Cao. Molecular dynamics simulation for insight into microscopic mechanism of polymer reinforcement. *Physical Chemistry Chemical Physics*, **13(2):518**, 2011.
- [213] H. Eyring. The activated complex in chemical reactions. *The Journal of Chemical Physics*, **3(2):107**, 1935.
- [214] H. Eyring. Viscosity, plasticity, and diffusion as examples of absolute reaction rates. *The Journal of Chemical Physics*, **4(4):283**, 1936.
- [215] W. M. Huang, B. Yang, L. An, C. Li, and Y. S. Chan. Water-driven programmable polyurethane shape memory polymer: Demonstration and mechanism. *Applied Physics Letters*, **86(11):114105**, Mar. 2005.
- [216] G. Liu, C. Guan, H. Xia, F. Guo, X. Ding, and Y. Peng. Novel shape-memory polymer based on hydrogen bonding. *Macromolecular Rapid Communications*, **27(14):1100–1104**, 2006.
- [217] W. G. Liu, J. R. Zhang, and K. De Yao. DNA/lipid complex organogel with shape-memory behavior. *Journal of Applied Polymer Science*, **86(1):259–263**, 2002.
- [218] F. W. Starr, T. B. Schröder, and S. C. Glotzer. Effects of a nanoscopic filler on the structure and dynamics of a simulated polymer melt and the relationship to ultrathin films. *Physical Review E*, **64(2):021802**, July 2001.
- [219] N. C. Goulbourne. A constitutive model of polyacrylate interpenetrating polymer networks for dielectric elastomers. *International Journal of Solids and Structures*, **48(7–8):1085–1091**, Apr. 2011.
- [220] Z. Xuanhe. A theory for large deformation and damage of interpenetrating polymer networks. *Journal of the Mechanics and Physics of Solids*, **60(2):319–332**, Feb. 2012.